Secular Evolution in Galaxies:

Properties of Bars and Bulges as seen with Integral Field Spectroscopy

Justus Neumann

Leibniz-Institut für Astrophysik Potsdam (AIP)

Dissertation
zur Erlangung des akademischen Grades
“doctor rerum naturalium”
(Dr. rer. nat.)
in der Wissenschaftsdisziplin Astrophysik

eingereicht an der
Mathematisch-Naturwissenschaftlichen Fakultät
Institut für Physik und Astronomie
der Universität Potsdam

Potsdam, den 18. September 2019

Tag der Disputation: 23. Oktober 2020

Betreuer:

Dr. Dimitri Gadotti
European Southern Observatory, Garching bei München

Prof. Dr. Lutz Wisotzki
Leibniz-Institut für Astrophysik Potsdam

Prof. Dr. Matthias Steinmetz
Leibniz-Institut für Astrophysik Potsdam

Gutachter:

Prof. Dr. Lutz Wisotzki
Leibniz-Institut für Astrophysik Potsdam

Dr. Dimitri Gadotti
European Southern Observatory, Garching bei München

Prof. Dr. Johan Knapen
Instituto de Astrofísica de Canarias, La Laguna, Tenerife, Spain

Cover photo: barred spiral galaxy NGC 1300
Credit: NASA, ESA, and The Hubble Heritage Team (STScI/AURA); Acknowledgment: P. Knezek (WIYN)

Published online on the
Publication Server of the University of Potsdam:
https://doi.org/10.25932/publishup-48270
https://nbn-resolving.org/urn:nbn:de:kobv:517-opus4-482701

Abstract

Galaxies are gravitationally bound systems of stars, gas, dust and - probably - dark matter. They are the building blocks of the Universe. The morphology of galaxies is diverse: some galaxies have structures such as spirals, bulges, bars, rings, lenses or inner disks, among others. The main processes that characterise galaxy evolution can be separated into fast violent events that dominated evolution at earlier times and slower processes, which constitute a phase called *secular evolution*, that became dominant at later times. Internal processes of secular evolution include the gradual rearrangement of matter and angular momentum, the build-up and dissolution of substructures or the feeding of supermassive black holes and their feedback. Galaxy *bulges* – bright central components in disc galaxies –, on one hand, are relics of galaxy formation and evolution. For instance, the presence of a classical bulge suggests a relatively violent history. In contrast, the presence of a disc-like bulge instead indicates the occurrence of secular evolution processes in the main disc. Galaxy *bars* – elongated central stellar structures –, on the other hand, are the engines of secular evolution. Studying internal properties of both bars and bulges is key to comprehending some of the processes through which secular evolution takes place. The main objectives of this thesis are (1) to improve the classification of bulges by combining photometric and spectroscopic approaches for a large sample of galaxies, (2) to quantify star formation in bars and verify dependencies on galaxy properties and (3) to analyse stellar populations in bars to aid in understanding the formation and evolution of bars. *Integral field spectroscopy* is fundamental to the work presented in this thesis, which consists of three different projects as part of three different galaxy surveys: the CALIFA survey, the CARS survey and the TIMER project.

The first part of this thesis constitutes an investigation of the nature of bulges in disc galaxies. We analyse 45 galaxies from the integral-field spectroscopic survey CALIFA by performing 2D image decompositions, growth curve measurements and spectral template fitting to derive stellar kinematics from CALIFA data cubes. From the obtained results, we present a recipe to classify bulges that combines four different parameters from photometry and kinematics: The bulge Sersic index $n_{\rm b}$, the concentration index $C_{20;50}$, the Kormendy relation and the inner slope of the radial velocity dispersion profile $\nabla\sigma$. The results of the different approaches are in good agreement and allow a safe classification for approximately 95% of the galaxies. We also find that our new 'inner' concentration index performs considerably better than the traditionally used $C_{50;90}$ and, in combination with the Kormendy relation, provides a very robust indication of the physical nature of the bulge. In the second part, we study star formation within bars using VLT/MUSE observations for 16 nearby ($0.01 < z < 0.06$) barred active-galactic-nuclei (AGN)-host galaxies from the CARS survey. We derive spatially-resolved star formation rates (SFR) from Hα emission line fluxes and perform a detailed multi-component photometric decomposition on images derived from the data cubes. We find a clear separation into eight star-forming (SF) and eight non-SF bars, which we interpret as indication of a fast quenching process. We further report a correlation between the SFR in the bar and the shape of the bar surface brightness profile: only the flattest bars ($n_{\rm bar} < 0.4$) are SF. Both parameters are found to be uncorrelated with Hubble type. Additionally, owing to the high spatial resolution of the MUSE data cubes, for the first time, we are able to dissect the SFR within the bar and analyse trends parallel and perpendicular to the bar major axis. Star formation is 1.75 times stronger on the leading edge of a rotating bar than on the trailing edge and is radially decreasing. Moreover, from testing an AGN feeding scenario, we report that the SFR of the bar is uncorrelated with AGN luminosity. Lastly, we present a detailed analysis of star formation histories and chemical enrichment of stellar populations (SP) in galaxy bars. We use MUSE observations of nine very nearby barred galaxies from the TIMER project to derive spatially resolved maps of stellar ages and metallicities, [α/Fe] abundances, star formation histories, as well as Hα as tracer of star formation. Using these maps, we explore in detail variations of SP perpendicular to the bar major axes. We find observational evidence for a separation of SP, supposedly caused by an evolving bar. Specifically, intermediate-age stars ($\sim$ 2-6 Gyr) get trapped on more elongated orbits forming a thinner bar, while old stars ($>$ 8 Gyr) form a rounder and thicker bar. This evidence is further strengthened by very similar results obtained from barred galaxies in the cosmological zoom-in simulations from the Auriga project. In addition, we find imprints of typical star formation patterns in barred galaxies on the youngest populations ($<$ 2 Gyr), which continuously become more dominant from the major axis towards the sides of the bar. The effect is slightly stronger on the leading side. Furthermore, we find that bars are on average more metal-rich and less α-enhanced than the inner parts of the discs that surrounds them. We interpret this result as an indication of a more prolonged or continuous formation of stars that shape the bar as compared to shorter formation episodes in the disc within the bar region.

Zusammenfassung

Galaxien sind gravitativ gebundene Systeme aus Sternen, Gas, Staub und - wahrscheinlich - dunkler Materie. Sie sind die Bausteine des Universums. Die Morphologie von Galaxien ist vielfältig: Einige Galaxien haben Strukturen wie zum Beispiel Spirale, Bulges, Balken, Ringe, Linsen oder innere Scheiben. Die Hauptprozesse, die die Entwicklung von Galaxien charakterisieren, können unterteilt werden in schnelle, heftige Prozesse, die zu früheren Zeiten die Evolution beherrschten, und langsamere Prozesse, die eine Phase bilden, die als säkulare Evolution (*secular evolution*) bezeichnet wird, die zur jetzigen Zeit dominiert. Interne Prozesse der säkularen Evolution sind zum Beispiel die schrittweise Umverteilung von Materie und Drehimpuls, der Auf- und Abbau von Substrukturen oder der Materiezufluss zu supermassereichen Schwarzen Löchern und ihr Feedback. *Bulges* – helle zentrale Komponenten in Scheibengalaxien –, auf der einen Seite, sind Relikte der Entstehung und Entwicklung von Galaxien. Zum Beispiel, lässt das Vorhandensein eines klassischen Bulges auf eine relativ heftige Entwicklung schließen. Im Gegensatz dazu, weist das Vorhandensein eines scheibenähnlichen Bulges auf das Auftreten von säkularen Evolutionsprozessen in der Hauptscheibe der Galaxie hin. Galaxienbalken (galaxy *bars*) - längliche zentrale Sternstrukturen - sind dagegen die Motoren der säkularen Evolution. Eine Untersuchung der Eigenschaften von Balken und Bulges ist der Schlüssel um die Hauptprozesse der säkularen Evolution zu verstehen. Die Hauptziele dieser Arbeit sind (1) das Verbessern der Klassifikation von Bulges durch Kombination von photometrischen und spektroskopischen Ansätzen für eine große Anzahl von Galaxien, (2) das Quantifizieren der Sternentstehung in Balken im Verhältnis zu den Eigenschaften von deren Galaxien und (3) das Analysieren der Sternpopulationen in Balken, um das Verständnis der Entstehung und Entwicklung von Balken zu erweitern. Integrale Feldspektroskopie (*integral field spectroscopy*) ist grundlegend für die vorliegende Arbeit, die aus drei verschiedenen Projekten besteht. Sie wurde im Rahmen von drei verschiedenen Galaxien Surveys – Durchmusterungen von Galaxien – angefertigt: der CALIFA-Survey, der CARS-Survey und das TIMER-Projekt.

Der erste Teil dieser Arbeit befasst sich mit der Charakterisierung von Bulgetypen in Scheibengalaxien. Wir analysieren 45 Galaxien vom CALIFA-Survey unter Benutzung von photometrischer und spektroskopischer Methoden um Eigenschaften von Struktur und Kinematik der Bulges zu identifizieren. Basierend auf den Resultaten präsentieren wir ein Rezept zur Klassifizierung von Bulges, das vier verschiedene Parameter aus Photometrie und Kinematik kombiniert: Der Bulge-Sersic-Index, ein Konzentrationsindex, die Kormendy-Relation und die innere Steigung des Radialdispersionsgeschwindigkeitsprofils. Die Ergebnisse der verschiedenen Ansätze stimmen gut überein und erlauben eine sichere Klassifizierung von ungefähr 95% der Galaxien. Im zweiten Teil untersuchen wir die Sternentstehung in Balken mithilfe von VLT/MUSE-Beobachtungen für 16 nahegelegende Balkengalaxien mit aktiven Kernen (engl. AGN) vom CARS-Survey. Wir berechnen ortsaufgelöste Sternentstehungsraten (engl. SFR) aus Hα Emissionslinienflüssen und führen eine detaillierte Mehrkomponentenanalyse durch photometrische Zerlegung der Galaxien durch. Wir finden eine klare Trennung in acht sternbildende und acht nicht-sternbildende Balken, die wir als Indiz auf ein schnelles Erlöschen von Sternentstehung interpretieren. Des Weiteren, finden wir eine Korrelation zwischen der SFR im Balken und des Helligkeitsprofils des Balkens: Nur die flachsten Balken bilden Sterne. Aufgrund der hohen räumlichen Auflösung von MUSE ist es uns erstmals möglich, die SFR innerhalb des Balkens zu zerlegen und Trends parallel und senkrecht zur Balken-Hauptachse zu analysieren. Die Sternentstehung an der Vorderkante des rotierenden Balkens ist 1,75-mal stärker als an der Hinterkante und nimmt radial ab. Darüber hinaus berichten wir, dass die SFR in Balken nicht mit der AGN Leuchtkraft korelliert. Schließlich, präsentieren wir eine detaillierte Analyse der Sternentstehungsgeschichte und der chemischen Anreicherung von Sternpopulationen (SP) in Galaxienbalken. Wir verwenden MUSE-Beobachtungen von neun nahgelegene Galaxien aus dem TIMER-Projekt und berechnen ortsaufgelöste Karten von Sternenalter und Metallizitäten, [α/Fe]-Häufigkeiten, Sternentstehungsgeschichten sowie Sternentstehung. Anhand dieser Karten untersuchen wir im Detail Variationen von SP in Balken. Wir finden Hinweise für eine Trennung von SP, vermutlich verursacht durch die Präsenz des Balkens. Sterne mittleren Alters bilden einen länglichen dünnen Balken, während alte Sterne einen runderen und dickeren Balken bilden. Diese Beobachtung wird darüberhinaus über ähnliche Resultate in den kosmologischen zoom-in Simulationen des Auriga-Projekts verstärkt. Außerdem finden wir Tendenzen in den jüngsten Populationen, die auf eine kürzliche erfolte oder noch andauernde Sternentstehung entlang der Kanten der Balken hindeuten, mit einem leichten Übergewicht entlang der Vorderkante. Schließlich, finden wir Indiz für eine länger anhaltende oder kontinuierliche Formation von Sternen im Balken verglichen mit kürzeren Formationsepisoden in der Scheibe innerhalb des Balkenradius.

Contents

1 Introduction

It is one of the most marvellous experiences, not only for an astronomer, to look up into the night sky from a dark place on Earth and to see the milky (Greek γαλαξιας) appearance of a huge white band full of stars stretching over a large part of the sky. It is impossible not to recognise its existence, especially at earlier times in history when the Earth was less polluted by light. This was certainly the case as the first written references of this phenomenon date back to the Greek philosophers, more than two thousand years ago. However, it was not until the invention of the telescope in the early seventeenth century that there was proof that the Milky Way (MW) is actually composed of many faint stars. In 1750, Thomas Wright speculated that these stars, including our sun, are part of a confined rotating disc and that the MW and other similar stellar structures are the main building blocks of the Universe. In 1755, Immanuel Kant elaborated on this idea and identified observations of small white fuzzy spots as those building blocks. In the subsequent years, more and more of these systems were observed and were collectively-called 'nebulae'. By 1784, Charles Messier catalogued more than 100 objects along with the Andromeda Galaxy (known as M31). In the 19th century, systematic searches led by William and John Herschel resulted in the publication of the General Catalogue of Galaxies in 1864, which contained more than 5,000 objects. This catalogue was extended by J.L.E. Dreyer to 15,000 objects leading to the creation of the New General Catalogue of Nebulae and Clusters of Stars and the Index Catalogues. At that time, it was still subject to controversy if these nebulae were part of the MW or if they were of extragalactic nature. The discussion culminated in what is now known as the 'Great Debate' between Harlow Sharpley and Herber Curtis in 1920 in the National Academy of Sciences in Washington. The problem was not solved then, but five years later when Edwin Hubble determined distances from Cepheid variables and showed that some of the nebulae are actually extragalactic (Hubble, 1925). This discovery is often understood as the beginning of extragalactic astronomy. As of today, the database of the Sloan Digital Sky Survey contains more than 50 million galaxies (Alam et al., 2015).

1.1 Formation and Evolution of Galaxies

A galaxy is a gravitationally bound system of stars, gas, dust and – probably – dark matter. They can be divided into two main types, namely flattened and rotationally supported disc galaxies and elliptical galaxies that are dominated by random motions. An initial more detailed classification was provided by Hubble (1926, 1936) in the famous 'Hubble Tuning Fork'. However, the morphologies and dynamics of galaxies are much more diverse. Some galaxies have structures such as spirals, bulges, bars, rings, lenses or inner discs, to just name a few (e.g. Buta et al., 2015). They can rotate slowly, fast or can have kinematically decoupled components (e.g. Emsellem et al., 2011; Krajnović et al., 2011; Falcón-Barroso et al., 2017; van de Sande et al., 2017). The cause of the observed diversity of galaxies has its roots in the complexity of their formation and evolution. In this section, I first introduce the most widely accepted theory of galaxy formation before I present main processes that govern their evolution. Subsequently, in the following sections of this chapter, I summarise some aspects of our current knowledge of two main components of galaxies: bulges and bars. Finally, I give an overview of the observational data used in this thesis.

1.1.1 From initial density fluctuations to the first galaxies

According to the currently most widely accepted theory, it all started with a big bang approximately 13.9×10^9 years ago (Planck Collaboration et al., 2016). The theory was proposed by Gamow (1946) and named *Hot Big Bang* by Fred Hoyle.

The basis for this idea was set by the discovery that our Universe is expanding. In 1922, Alexander Friedmann developed models of a static and an expanding Universe based on Albert Einstein's theory of *general relativity* (Einstein, 1916; Friedmann, 1922). Independently, Georges Lemaître derived the same solutions and he was the first to show that the recession velocities of galaxies are linearly correlated with their distances; observational evidence for the expansion of the Universe (Lemaître, 1927). His discovery was largely overlooked, while independently Hubble came to the same conclusion and published what is now known as the *Hubble's law*: $v = H_0\, D$, where H_0 is the *Hubble constant* (Hubble, 1929). Two years later, Lemaître proposed that the initial state of the Universe could have been a single point, a 'Primeval Atom' (Lemaître, 1931). This led to George Gamow's theory in the 1940s.

In the framework of the Hot Big Bang, the Universe started expanding and cooling from an initial hot and dense state. After approximately 10^{-36} s the expansion accelerated exponentially driven by vacuum energy in a quantum field, a period called *inflation* which lasted until $t \approx 10^{-32}$ s (Guth, 1981; Linde, 1982, 1986; Albrecht & Steinhardt, 1982). Quantum density fluctuations in that field, allowed by the *uncertainty principle* (Heisenberg, 1927), were able to grow during the inflation to macroscopic perturbations.

After that, the slower but continuous expansion and cooling of the Universe led to the formation of baryons such as protons and neutrons and eventually to light isotopes, such as helium-3, deuterium and lithium, during the primordial nucleosynthesis (Hoyle & Tayler, 1964; Wagoner et al., 1967). After $\sim 360,000$ years the temperature was sufficiently low ($\sim 3,000$ K) so that protons captured electrons to form neutral hydrogen (Zeldovich et al., 1968; Peebles, 1968). This epoch is usually called *recombination*.

A fundamental consequence of recombination is that Thomson scattering by electrons was much reduced and the Universe became transparent to photons. The decoupling from photons and matter set free a radiation field that traveled through the Universe and cooled down to the present day to ~ 2.7 K. It was predicted by Alpher & Herman (1948) and discovered by Penzias & Wilson (1965) as the *Cosmic Microwave Background* (CMB). A breakthrough in the measurements of the CMB was achieved many decades later by three consecutive satellite missions; the Cosmic Background Explorer (COBE; Smoot et al., 1992), the Wilkinson Microwave Anisotropy Probe (WMAP; Bennett et al., 2003; Hinshaw et al., 2007) and Planck (Collaboration et al., 2011). The maps of the CMB that were delivered from these missions show a very high degree of isotropy on large scales, which confirms the *cosmological principle* of an homogeneous and isotropic Universe. At the same time, however, they present anisotropies of $\Delta T/T \approx 10^{-5}$, which reflect the density fluctuations at the time of recombination.

The initial density perturbations in the early Universe were able to grow by means of gravitational instability: over-dense regions attract matter from under-dense regions and grow even more over-dense. Once the density contrast reaches $\Delta\rho/\rho \approx 1$, the region starts to collapse and structure starts to form. However, a few problems still remain. Most importantly: there is not enough time to grow the structure that we observe today from the initial perturbations at recombination as measured in the anisotropies of the CMB, and the amount of baryonic matter allowed during primordial nucleosynthesis to match the observed abundances of chemical elements is not enough to reach the mass density observed from large-scale structure and preferred by inflationary theories.

These problems are mainly solved in the lambda cold dark matter (ΛCDM) cosmology. It is build upon the assumptions that general relativity is the valid description of gravity, the existence of cold dark matter and a cosmological constant Λ, typically identified with dark energy. First evidence of dark matter was provided by Zwicky (1933), who found a large discrepancy between the required mass to hold galaxy clusters together and the visible mass inferred from the light. In the 1970s and 1980s the debate about the existence of dark matter was fuelled by the emergence of more evidence including measurements of galaxy rotation curves, gravitational lensing and the already mentioned problems in structure formation.

Since then, different dark matter models (and alternative theories as for example *Modified Newtonian dynamics*; MOND; Milgrom 1983) have been discussed, but ΛCDM is now the most widely accepted standard model since it best matches observational constraints. A great contribution to the acceptance was delivered by Riess et al. (1998) and Perlmutter et al. (1999). These authors showed that the cosmic expansion is accelerating by measuring the distance and redshift of type Ia supernovae. Detailed analyses of the CMB power spectrum from WMAP and Planck were able to accurately determine the main parameters of the ΛCDM model, which are in very good agreement with independent measurements of galaxy clustering, weak gravitational lensing and supernova distance-redshift relations (Spergel et al., 2007; Komatsu et al., 2009; Planck Collaboration et al., 2016).

Within the ΛCDM cosmology, dark matter particles decouple from the radiation long before recombination. They grow from the initial density perturbations and eventually collapse in violent relaxation to a quasi equilibrium state forming dark matter halos. After recombination, baryons fall into the potential wells of the halos. The dissipative gas shocks and, if cooling is efficient, fragments and forms stars. Typically both dark and baryonic matter have some initial angular moment acquired from cosmological gravitational torques. When the gas in the dark matter halo cools and flows inwards, it speeds up and settles into a rotating protogalaxy-disc (White & Rees, 1978; Fall & Efstathiou, 1980).

In an early work by Eggen et al. (1962), the authors suggested a model in which disc galaxies are formed in a dark matter halo with large angular momentum, whereas elliptical galaxies are formed from non-rotating gas clouds that consume most of their gas in star formation while it falls in. Therefore, the final collapse is mainly dissipationless and the motion is converted into random motion of stars. Toomre & Toomre (1972), however, pointed out that most elliptical galaxies could be merger remnants. Since then, galaxy formation has been studied in many semi-analytical (e.g. Mo et al., 1998; Kauffmann et al., 1999) and hydrodynamical simulations (e.g. Katz & Gunn, 1991; Katz et al., 1996). While some aspects still remain unclear, a consensual picture has been mostly accepted in which discs are formed in dark matter halos by infalling gas that conserves its initial angular momentum (Fall & Efstathiou, 1980; Mo et al., 1998; Navarro & Steinmetz, 1997; Steinmetz & Navarro, 1999) and ellipticals result from merger events (Toomre & Toomre, 1972; Toomre, 1977; Cole et al., 2000).

1.1.2 Galaxy Evolution

Any theory or simulation of galaxy evolution should have the ultimate goal to match observations of galaxies at all cosmic epochs. In the following paragraph I will summarise some key observational results that we must try to connect and explain with that theory. Afterwards, I will give an overview of the main processes that drive galaxy evolution.

Initial observational constraints of the distribution of structure after recombination at redshift $z \approx 1100$ are provided by the CMB. Direct observations of galaxies start much later in time. With current technology they span the range of $11.1 < z < 0$, i.e. from ~ 400 Myr after the Big Bang, during the epoch of reionisation, until today (see Oesch et al., 2016, for the currently most distant galaxy GN-z11 with spectroscopically confirmed redshift). Galaxies at high redshift appear compact, clumpy and mostly star-forming with turbulent dynamics (e.g. Giavalisco et al., 1996; Stott et al., 2016). In the nearby Universe, galaxies have been observed to be bimodal in many parameters including colour, stellar mass density, star formation rate and concentration (Kauffmann et al., 2003a). They form two groups of blue and active galaxies and big, red and passive galaxies. The cosmic star formation history shows a peak in star formation rate density at $z \approx 1.9$ with an approximately exponential decline to $z = 0$. Half of the total stellar mass observed today was already formed before $z \approx 1.3$ (Madau & Dickinson, 2014). After the peak of star formation, many disc galaxies dynamically settled and grew a wealth of substructures, such as bars, rings and inner discs. A key ingredient to a theory of galaxy evolution is to understand what regulates star formation, what is the role of environment and merger events and how are galaxy dynamics involved in the build-up of galaxy substructure.

The formation and the evolution of galaxies are not two separate epochs in cosmic history. In fact, galaxy formation is still happening today. Some of the same processes are usually discussed within both contexts. The main processes that characterise galaxy evolution can be separated into fast and slow processes and into internal and external evolution (reviews can be found in Kormendy & Kennicutt, 2004; Kormendy, 2013; Sellwood, 2014). At earlier times, galaxy evolution was dominated by fast and violent events, such as dissipative collapse of gas in dark matter halos and merging of galaxies. Today, mergers are still happening, but slower processes have become more important. This phase is called *secular evolution*. The term includes, e.g., the gradual rearrangement of matter and angular momentum, the build-up and dissolution of substructures, the disc growth through accretion of gas, the metal enrichment through gas recycling and the quenching of star formation caused by steady consumption of gas or feedback mechanisms. The responsible processes can be of internal or external nature. External slow processes that drive secular evolution are caused by the environment, for example a steady accretion of gas, minor merger or gravitational tidal torques from fly-by events of other galaxies that can produce warps in the disc, induce bar formation or trigger star formation.

Internal secular evolution is governed by the attempt of a rotating disc galaxy to minimise its energy state. At fixed total angular momentum this is achieved by the outward

transport of angular momentum (Lynden-Bell & Kalnajs, 1972; Tremaine, 1989). As a consequence, outer parts of the disc will grow, while inner parts shrink. Main mechanisms of secular evolution include the formation and evolution of spirals and bars, the radial transport of angular momentum and matter through these structures, the redistribution of gas as response to the gravitational and dynamical changes and the triggered formation of rings or inner discs from that gas, but also the feeding of supermassive black holes (SMBH) and their feedback.

Galaxy bars are one of the main drivers of internal secular evolution since they are very effective in the transport of angular momentum and they induce torques that push gas towards the centre. Galaxy bulges are either built by fast and violent processes or through the assembly of inflowing gas caused by the bar, in which the bulges are more akin inner discs, and are also called pseudobulges. Bulges are perfect relics of the evolution, because they give us information about the nature of evolution that the host galaxies experienced, violent or slow, and they thereby constrain either the merger rate or the formation time of the bar which is connected to the onset of internal secular evolution. The characterisation of these two important galaxy components is the main topic of this thesis.

1.2 Galaxy bulges

In the previous section, I already mentioned discs, bulges, bars and other structural components of galaxies. I will now give a proper introduction into these structures by summarising their formation process as well as some of their main properties, and by explaining how they influence or are influenced by galaxy evolution.

A bulge is literally a structure of bulging nature sitting in the centre of disc galaxies. It is usually brighter than the surrounding disc and, if viewed from edge-on, sticks out of the plane. Since it is therefore easily recognisable, it has been one of the driving characteristics of galaxies in the morphological classification from Hubble (Hubble, 1926, 1936). It was soon recognised that bulges share many similar characteristics with elliptical galaxies (de Vaucouleurs, 1959; Freeman, 1975; Faber, 1977; Whitmore et al., 1979). Nevertheless, with the advance of technology and detailed analyses of bulges, the picture started to change. Some of the objects formerly considered as bulges showed clear deviations in their properties, in particular, they were less alike with ellipticals but rather similar to small discs inside the host disc (Kormendy, 1980; Kormendy & Illingworth, 1982; Kormendy, 1993b). Some other bulge-like objects were found to be the inner parts of bars that buckled vertically out of the disc (Kuijken & Merrifield, 1995; Bureau & Freeman, 1999; Bureau & Athanassoula, 1999, 2005; Athanassoula & Bureau, 1999; Chung & Bureau, 2004). All these three types of central objects can as well co-exist within the same galaxy (Fisher & Drory, 2008; Erwin, 2010; Méndez-Abreu et al., 2014; Erwin et al., 2015).

There is now a consensus in the field that bulges in the historical classification form an ambiguous class of objects. It is widely accepted that the disc-like and bar-like members are indeed different kinds of objects. However, there is still an ongoing debate about the nomenclature, which also depends on the exact definition of a bulge.

1.2.1 Definition of bulge-like objects

Bulge classification is usually a two-step process independently of whether the objects are named one way or the other. The first step is the recognition of bulge-like objects based on a broad and general definition. This definition can be either photometrically: *a bulge is the central component that adds extra light to the inward extrapolation of the disc*; or it can be geometrically: *a bulge is the central component that sticks out of the disc plane when viewed edge-on*. The geometrical definition has the obvious drawback that it only works for edge-on systems. For that reason, the definition of a *photometric bulge* is usually applied. However, it needs a bit of a refinement, since more than the three types of objects that I previously described can produce that extra light, i.e. active galactic nuclei (AGN), nuclear star clusters or bars. These objects can be filtered out by not considering point-like sources (AGN, nuclear star clusters) or clearly elongated objects (bars).

The members of the group defined by this definition are either called directly *bulges* or *bulge-candidates/ bulge-like objects*. The first version is often preferred for historical reasons or for the literal meaning of the term. The second version is sometimes preferred because we now know that some of the objects are not bulges in the classical meaning of an elliptical-like central component. Ultimately, that is just nomenclature and it is secondary to the understanding of the physical processes in galaxy formation and evolution. Throughout this work, I will simply refer to them as bulges and specify whenever I refer to a specific type.

After selecting bulges based on the photometric definition in the first step, they can be classified into the different types by applying one or more selection criteria based on typical characteristics. In the following, I will present the different bulge types and scenarios of bulge formation. Afterwards, I give a short overview of classification approaches that have been used in the literature.

1.2.2 Types and properties of bulges

Classical bulges. These are the elliptical-like objects originally defined as bulges. They have ellipsoidal shapes and their dynamics are dominated by random motion. The stellar populations are usually old. No ongoing star formation in the bulge is observed. The surface brightness profile is steeper than the typically exponential profile of a disc, hence, the mass concentration is also higher. Classical bulges are typically on the massive side of the bulge distribution, but there are suggestions in the literature that small classical bulges may exist (e.g. Erwin et al., 2015). An example of a classical bulge is shown in Fig. 1.1.

Figure 1.1: Classical bulge in M81. Credit: NASA, ESA and the Hubble Heritage Team (STScI/AURA).

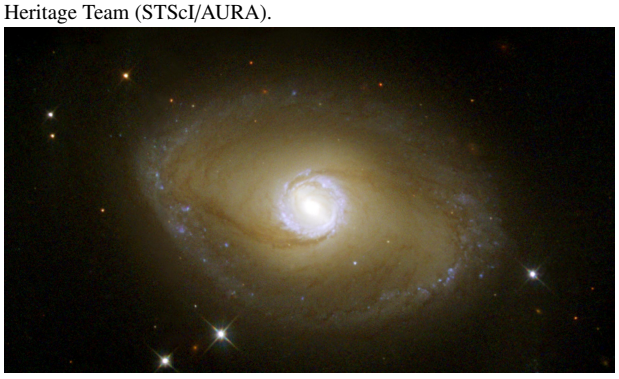

Figure 1.2: Disc-like bulge in NGC 6782. Credit: NASA, ESA and the Hubble Heritage Team (STScI/AURA).

Pseudobulges I or **disc-like bulges** or **inner discs**. These are the objects that are flattened and supported by rotation. They resemble rather discs than ellipticals. They can host morphological substructure similar to the main disc, such as nuclear spirals, nuclear bars or nuclear rings. These inner discs can show star formation and the mean stellar population is often young. However, there are also cases of disk-like bulges of old stars (Gadotti et al., 2015). The slope of the light profile is close to exponential. The concentration is, consequently, typically smaller than that of a classical bulge. Disc-like bulges are rather small, large objects are rarely found. A disc-like bulge can be seen in Fig. 1.2.

Pseudobulges II or **X-shaped bulges** or **boxy bulges** or **box-peanuts**. These are the objects that were identified to be the inner parts of vertically buckled bars seen edge-on. Their stellar content and dynamics resemble those of face-on bars. Some star formation and young stars are possible, but they are usually older than disc-like bulges. It has been suggested that **barlenses** are boxy bulges seen face-on (Athanassoula et al., 2015; Laurikainen & Salo, 2017). An example of a box-peanut bulge with a strong *X* shape is shown in Fig. 1.3.

1.2.3 Formation of bulges

In simulations, *classical bulges* can be formed in three different scenarios, most of which are violent processes that happened early in time. In the first scenario, classical bulges form during the formation of disc galaxies from star-

Figure 1.3: Box-peanut bulge in ESO 597-G036. Credit: NASA, ESA and the Hubble Heritage Team (STScI/AURA).

bursts triggered by the gravitation collapse of small-scale fluctuations, while the disc forms afterwards from fluctuations on larger scales (e.g. Steinmetz & Müller, 1995). In the second scenario bulges form when two galaxies merge and disc stars are stirred into a bulge (Aguerri et al., 2001; Steinmetz & Navarro, 2002; Hammer et al., 2005). In another alternative way of forming a classical bulge, clumps form in the primordial galaxy due to density fluctuations in the disc and spiral rapidly inwards (Noguchi, 1998, 1999; Immeli et al., 2004a; Immeli et al., 2004b; Elmegreen et al., 2008).

The formation of *disc-like bulges* is a slow process and happens in the framework of secular evolution. After a stellar bar has formed due to instabilities in the disc, it exerts gravitational torques on the gas material in the main disc. The inflowing gas gets either stalled in a nuclear ring or builds an inner rotating disc within the inner $\sim$ 100 pc-1 kpc. When the disc or ring becomes massive enough, it begins to form stars which will be observed as a young disc-like bulge (e.g. Athanassoula, 1992b; Kormendy & Kennicutt, 2004; Athanassoula, 2005).

Additional to bars, spirals are also able to transport gas to the centre. This could be one possible explanation to the formation of disc-like bulges that have been observed in unbarred galaxies. However, this process is much slower and requires a substantial amount of time without any merger that would potentially destroy the spiral and form a classical bulge. In a second scenario, the disc-like bulge forms via a bar and the bar is dissolved afterwards leaving behind the bulge in an unbarred galaxy. This can happen if the central bulge grows significantly in mass to weaken or destroy bar-supporting stellar orbits. In simulations, however, this seems to be a rare event (e.g. Shen & Sellwood, 2004).

Box-peanuts are formed due to a buckling instability that leads to a thickening of the bar out of the disc plane. It is caused by strong in-plane radial motions induced by the non-axisymmetric gravitational potential of the bar that destabilise the structure in the vertical direction (Combes & Sanders, 1981; Raha et al., 1991; Martinez-Valpuesta & Shlosman, 2004; Martinez-Valpuesta et al., 2006). As a second mechanism, a bar can also thicken via vertical resonances between the bar and the disc stars (Combes et al., 1990; Pfenniger & Friedli, 1991; Patsis et al., 2002). More details about bar formation and dynamics will be discussed in Sect. 1.3.

1.2.4 Classification of bulges

Measuring the frequency of different types of bulges in the Universe provides important constraints for models of galaxy formation and evolution, as I will explain in the next subsection. Therefore, there has been a great amount of effort in the literature to find the best recipes for bulge classification. In the following, I present a short overview of different approaches.

Probably the most frequently used criteria is the slope of the surface brightness profile. The azimuthally averaged surface brightness profile of a pure disc galaxy is normally best described by en exponential function

$$I(R) = I_0\, e^{(-r/r_0)}. \tag{1.1}$$

Here, I_0 is the surface brightness at $r = 0$ and r_0 is the scale length. The profile of an elliptical galaxy, however, is steeper and it was first found to follow approximately a *de Vaucouleurs profile* (de Vaucouleurs, 1948):

$$I(R) = I_0\, e^{(-r/r_0)^{1/4}}. \tag{1.2}$$

A generalisation of de Vaucouleurs' law is given by the *Sérsic function* (Sérsic, 1963; Sersic, 1968):

$$I(R) = I_0\, e^{(-r/r_0)^{1/n}}. \tag{1.3}$$

Here, n is the *Sérsic index*. This was shown to be a more adequate – because it is more flexible – solution to fit the surface brightness profiles of elliptical galaxies, which in fact cover a range of Sérsic indices (Caon et al., 1994). In accordance with the disc-like and elliptical-like behaviour of pseudobulges and classical bulges, respectively, it was found that pseudobulges (both disc-like and box-penuts) are better fit with near-exponential Sérsic indices while classical bulges have profiles with larger Sérsic indices (Kormendy & Kennicutt, 2004). Essential for these analyses are 2D photometric multi-component decompositions, which will be introduced in more detail in Chapter 2. The same differences seen in the surface brightness profile also manifest themselves in different measures of the mass or light concentration of a galaxy. Namely, galaxies with classical bulges have a higher central concentration than galaxies with pseudobulges.

The Sérsic index or a concentration index is frequently used to classify bulges in studies that include a large number of objects. Unfortunately, there is a large overlap between the distributions of different bulge types and no clear bimodality. Many authors pointed out that multiple criteria and complementary data should be used simultaneously (e.g. Kormendy & Kennicutt, 2004; Fisher & Drory, 2010; Fabricius et al., 2012; Kormendy, 2013). This led, eventually, to a growing list of classification criteria, a selection thereof I present in the following:

- *morphology:* by-eye identification of disc-like features in high-resolution images (e.g. Fisher & Drory, 2010; Erwin et al., 2015),
- *geometry:* reconstructed 3D intrinsic shapes of bulges (Méndez-Abreu et al., 2010a; Costantin et al., 2018),
- *photometry:* Sérsic index and concentration index (Fisher & Drory, 2008; Gadotti, 2009), relative central stellar mass surface density $\Delta\Sigma_1$ within 1 kpc (very recently, by Luo et al., 2019),
- *spectroscopy:* star formation rates (Fisher et al., 2009) and absorption line strength (Peletier et al., 2007; Ganda et al., 2007; Kuntschner et al., 2010)
- *kinematics:* different measurements of velocity and velocity dispersion to measure the rotational support of bulges (Kormendy & Illingworth, 1982; Falcón-Barroso et al., 2006; Méndez-Abreu et al., 2008b; Fabricius et al., 2012; Méndez-Abreu et al., 2014)
- *scaling relations:* how bulges compare to elliptical galaxies in the Kormendy (1977) relation or Faber & Jackson (1976) relation (e.g. Kormendy & Kennicutt, 2004; Gadotti, 2009; Fisher & Drory, 2010).

1.2.5 What do we learn from bulges for galaxy evolution?

One consequence of the ΛCDM model of galaxy formation is the production of a large number of massive classical bulges with steep surface brightness profiles in major merger events (e.g. Navarro & Steinmetz, 2000; Steinmetz & Navarro, 2002; Naab & Burkert, 2003). However, large observational studies of the frequency of bulges in the Local Universe have shown that there is a non-negligible amount of bulgeless galaxies (Böker et al., 2002; Kautsch et al., 2006; Barazza et al., 2008; Weinzirl et al., 2009; Kormendy, 2013) or galaxies where most of the central mass is actually either in disc-like bulges or box-peanuts instead of in a classical bulge (e.g. Kormendy, 2016; Laurikainen & Salo, 2017). A result that challenges the standard cosmological model. One possible alternative solution has been tested in the framework of MOND. In the MONDian cosmology the dynamical friction between and within galaxies is significantly reduced, which results in lower merger rates (Tiret & Combes, 2008) and prevents bulge formation via the coalescence of clumps in the early Universe (Combes, 2014). This offers a much better match to the observed frequency of galaxies without classical bulges. Since the formation scenario of classical bulges and disc-like bulges is fundamentally different, an accurate classification of a large number of bulges is indispensable to constrain simulations using the standard ΛCDM cosmology.

Thus, on one hand, studies of the incidence of classical bulges are important for the fast and violent part of galaxy evolution. On the other hand, studies of disc-like bulges or inner discs help to understand important aspects of secular

evolution. In a barred galaxy, inner discs form from star formation in the gas that was brought to the centre by the bar. This means that the bar had to be there before the first stars formed in the inner disc to push the gas inwards. Therefore, analyses of the oldest stellar ages in inner discs can be used to estimate the minimum formation time of the bar and the age at which the disc had dynamically settled. The feasibility was demonstrated in a pilot study in Gadotti et al. (2015) and it is one of the main goals of the Time Interference with MUSE In Extragalactic Rings project (TIMER; Gadotti et al., 2019). Complementary to that approach, it is also possible to constrain the formation time of bars based on a census of disc-like bulges at higher redshifts. By studying galaxies in HST-COSMOS[1] and SDSS[2], Kruk et al. (2018) found that disc-like bulges started to form at redshifts z = 0.7-0.8. However, these bulges are usually small, which makes them especially difficult to detect (and correctly classify them as disc-like bulges) at higher redshifts. This requires very high spatial resolution.

Finally, insights from studies of extragalactic bulges help us to understand the structural composition of the central part of our own Milky Way. Admittedly, the proximity to the Milky Way bulge allows to resolve single stars and study the dynamics and composition of the bulge in great detail, but it has the major drawback which is that we only see it nearly edge-on from within the disc and through large amounts of interstellar extinction. Studies of the characteristics of extragalactic bulges have provided excellent complementary information to understand the Milky Way bulge. Controversial opinions in the field now seem to converge to the picture that the centre of the Galaxy is dominated by a box-peanut structure as part of a large scale bar (Rich et al., 2007; Shen et al., 2010; Ness et al., 2013a,b; Di Matteo et al., 2014) with a small fraction of stars that seem to be members of a population from an additional classical bulge component (e.g. Babusiaux et al., 2010; Kunder et al., 2016). Moreover, N-body simulations of the formation of box-peanut bulges that try to match the observed chemical and kinematic trends in the Milky Way bulge, have shown to be able to make important predictions about the conditions in disc galaxies before the formation of a bar component (Fragkoudi et al., 2018; Di Matteo et al., 2019).

1.3 Galaxy bars

Just like bulges or spiral arms, bars inherit their name from their shape, a clearly apparent elongated structure in the central part of a disc galaxy. They are *the* dividing morphological property of the two branches in Hubble's famous classification scheme. Furthermore, the incidence of bars is very frequent. Observations in the near-infrared show that bars are found in $\sim$ 70% of disc galaxies (Eskridge et al., 2000; Buta et al., 2015; Erwin, 2018). Bars are very important for galaxy evolution, as I already mentioned in the first sections, because they are one of the main driving forces of secular rearrangement of angular momentum and matter. Thereby, they are responsible for the formation of substructures and the consumption of gas in star formation; leaving their imprint on galaxy morphology and dynamics. In this section, I summarise some of the most important aspects of our current knowledge of bars and their role in galaxy evolution.

1.3.1 Definition and main characteristics

A galaxy bar is a rotating elongated stellar structure in the central part of most disc galaxies. It forms spontaneously from instabilities in the disc. Typical *lengths* of bars are between 1 kpc $< L_{\rm bar} <$ 10 kpc (Gadotti, 2011; Erwin, 2019) with *ellipticities* in the range of $0.4 < \epsilon_{\rm bar} < 0.8$ (Gadotti, 2011). The length of bars is strongly correlated with the size of the disc and, in the case of massive galaxies ($M_\star > 10^{10}\,M_\odot$), with galaxy mass (Erwin, 2019). Models of bar evolution predict that bars slow down and grow over time as natural consequence of angular momentum transport and dynamical friction (Hernquist & Weinberg, 1992; Debattista & Sellwood, 2000; Athanassoula & Misiriotis, 2002; Athanassoula, 2003; Algorry et al., 2017). Bars can also be characterised by the speed at which they rotate, also known as the bar *pattern speed* Ω_b (e.g. Tremaine & Weinberg, 1984), or their *strength* Q_b, which is the maximum gravitational torque induced by the bar (Combes & Sanders, 1981).

1.3.2 Formation scenarios

A thin stellar disc that is supported by rotation is locally stable against axisymmetric gravitational disturbances, if

$$Q = \frac{\sigma_R}{\sigma_{R,crit}} > 1 \quad \text{with} \quad \sigma_{R,crit} = \frac{3.36\,G\,\Sigma}{\kappa} \tag{1.4}$$

$$\Rightarrow \quad Q = \frac{\sigma_R\,\kappa}{3.36\,G\,\Sigma} > 1, \tag{1.5}$$

where σ_R is the radial velocity dispersion, Σ the surface density of the disc, G the gravitational constant and κ the Lindblad epicyclic frequency (*local stability criterion*; Toomre, 1964). The system is globally stable, if the *Toomre parameter* $Q > 1$ everywhere (Kalnajs, 1976). The dependence of Q on σ_R, κ and Σ is physically intuitive, since random motion stabilise the system against gravitational clumping on small scales, rotation on large scales, and the surface density makes it easier for clumping to happen.

Numerous N-body simulations (Hohl, 1971; Ostriker & Peebles, 1973; Sellwood, 1980; Athanassoula & Sellwood, 1986; Combes et al., 1990) and studies of disc stabilities (Kalnajs, 1972, 1978) have shown that models of rotationally supported cool discs are globally unstable, unless additional stabilising components are added. A linear

[1] The Cosmic Evolution Survey (Scoville et al., 2007) based on observations with the NASA/ESA Hubble Space Telescope

[2] The Sloan Digital Sky Survey (York et al., 2000)

instability in the disc leads to the initial formation of a two-armed spiral density wave. The spiral grows through *swing amplification* and by reflection off the galaxy centre and at corotation (CR; see Sect. 1.3.4) it builds a standing wave that eventually forms the bar (Toomre, 1981; Sellwood, 2014).

After the formation of the bar in the plane of the galaxy, the bar is approximately as thin as the disc out of which it formed. However, soon after that, the inner part of the bar thickens vertically (Combes & Sanders, 1981). Due to strong in-plane motions, the bar becomes vertical unstable and buckles out (Toomre, 1966; Raha et al., 1991; Merritt & Sellwood, 1994). This is usually called the *buckling instability* of the bar and it is responsible for the formation of box-peanuts or boxy-bulges (see Sect. 1.2). Alternatively, bars can also thicken due to resonances between the rotating bar and vertical motions of the disc stars (Combes et al., 1990; Pfenniger & Friedli, 1991; Patsis et al., 2002). Resonant heating is, however, much slower than the buckling instability.

There are several mechanisms that can stabilise the disc against bar formation or slow it down, for example (i), increased random motion (Athanassoula & Sellwood, 1986; Athanassoula, 2003), (ii) lower surface density of the disc (Berrier & Sellwood, 2016), (iii) larger gas fraction (Bournaud et al., 2005; Athanassoula et al., 2013; Seo et al., 2019), (iv) unresponsive spherical distributed matter, such as in a dense bulge or halo (Ostriker & Peebles, 1973; Efstathiou et al., 1982; Athanassoula, 2002) or (v) by preventing feedback during swing amplification through the centre by introducing an inner Lindblad resonance (ILR; see Sect. 1.3.4) that absorbs the wave before it can reach the centre, e.g., in the presence of a massive bulge (Toomre, 1981) shown in simulations by Sellwood (1985); Sellwood & Evans (2001); Saha & Elmegreen (2018).

A second mechanism of bar formation is via tidal interaction with satellite galaxies, galaxy clusters or during minor merger events (Noguchi, 1987; Gerin et al., 1990; Łokas et al., 2014, 2016; Łokas, 2018; Peschken & Łokas, 2019). In this scenario, bars can even be formed in globally stable discs through nonlinear trapping of particles (Sellwood, 2014). Finally, bars can grow secularily by orbit trapping from a small seed bar. In this picture, elongated stellar orbits in the disc get slowly aligned into a slowly rotating bar structure (Lynden-Bell, 1979; Polyachenko, 2004, 2013).

1.3.3 Frequency of bars

Galaxies at high redshift ($z \geq$ 1-2) are dynamically hot and morphologically clumpy, while nearby disc galaxies show predominantly a smooth thin structure and they are dominated by rotation. In between, there must be a time when discs cool and dynamically settle. This is also the time when the disc becomes unstable against the formation of bars and, thus, it is the onset of bar-driven secular evolution. One way to determine that time of transition is by studying the dynamics of galaxies at different redshifts (e.g. Förster Schreiber et al., 2009; Wisnioski et al., 2015) or by measuring the formation time of bars in nearby galaxies (Gadotti et al., 2015, 2019). Alternatively, a direct approach to determine the onset of bar formation is to study the incidence of bars over cosmic time.

The presence of bars in disc galaxies in the local Universe has been found to be as high as $\sim$ 70%, but it rapidly decreases as a function of redshift (e.g. Sheth et al., 2008). At $z \approx 1.0$ only 10% of the galaxies host bars (Melvin et al., 2014). However, Sheth et al. (2008) found that the fraction of bars in massive galaxies at $0.60 < z < 0.84$ is on the order of 50%, comparable to the overall abundance in nearby galaxies. This is in agreement with the picture that bars form first in more massive discs as seen in the cosmological zoom-in simulations by Kraljic et al. (2012) and in observations by Sheth et al. (2012). Furthermore, in a comprehensive study of over 800 disc galaxies extending to $z \approx 2$, Simmons et al. (2014) found that the fraction of bars does not decrease significantly between $1 < z < 2$, suggesting that bars can be long-lived and robust objects. Given the small angular size at high redshifts, these studies become increasingly more difficult when probing earlier epochs and even with HST imaging it cannot be excluded that increasing fractions of bars are missed. Nevertheless, they provide important lower-limit estimates of the time when discs start to dynamically settle. Further improvements will be possible once the James Webb Space Telescope (JWST) starts observing.

An alternative approach of studying the fraction of bars is a study as a function of environment instead of time. This gives information about the efficiency of mechanisms that potentially form or destroy bars. Simulations have shown that bars can be formed either via internal processes or stimulated from tidal interactions with neighbouring galaxies, but competing mechanisms are at play and galaxy encounters and mergers can have contrary effects and slow down bar formation or disrupt existing bars (Berentzen et al., 2003; Debattista et al., 2006). It is not yet clear what the combined effect of interactions and mergers is. Elmegreen et al. (1990) found that the fraction of bars in galaxy pairs is higher than in isolated galaxies. Other studies analysed the clustering of bars as function of environment. Some of them found no dependence of environment (Aguerri et al., 2009; Li et al., 2009) while others reported clustering on scales of a few hundred kiloparsec to 1-3 megaparsec (Skibba et al., 2012; Lin et al., 2014). The net environmental effect on the presence of bars has also been studied in nearby (Méndez-Abreu et al., 2010b; Marinova et al., 2012) and intermediate redshift galaxy clusters (Barazza et al., 2009; Marinova et al., 2009). The general consensus is that there is no significant correlation between bar fraction and environment (but see Skibba et al., 2012, for a different perspective). This means that either galaxy interactions do not have a significant effect on the formation of the bar – in contrast to what simulations predict – or that competing mechanisms lead to a zero net

effect.

An interesting question is whether bars formed via interactions are different from those formed spontaneously. For example, from numerical simulations, Noguchi (1996) showed that tidally induced bars have a flat density profile, while isolated galaxies are more exponential. Furthermore, bar formed from interactions were found to have slower patter speeds (Miwa & Noguchi, 1998; Łokas et al., 2016) and have shorter extents (Miwa & Noguchi, 1998). However, Berentzen et al. (2004) report that the dynamical properties of the bars formed in either of the two ways are the same. In summary, there is no clear answer yet to how different the bars are and predictions are based so far on studies of simulations.

1.3.4 Bar dynamics

A star, rotating with the angular frequency Ω_Φ of its guiding centre around the galaxy and the radial frequency Ω_R around the guiding centre, is in resonance with the potential of a non-axisymmetric disturbance, rotating with the constant angular frequency Ω_p, when there are two integer l and m such that

$$\Omega_p = \Omega_\Phi + \frac{l}{m}\,\Omega_R. \tag{1.6}$$

In the epicyclic approximation Ω_R becomes the epicyclic frequency κ and in case of a bar disturbance with the pattern speed Ω_b:

$$m\,(\Omega_\mathrm{b} - \Omega_\Phi) = l\,\kappa. \tag{1.7}$$

For $l = 0$: $\Rightarrow \Omega_\mathrm{b} = \Omega_\Phi$ and the star corotates with the bar (*corotation resonance*; CR). When $m = 2$ and $l = \pm 1$ the star completes one radial oscillations between every encounter with the bar. If $l = -1$, the resonance is well within the CR and $\Omega_\Phi > \Omega_\mathrm{b}$ (*inner Lindblad resonance*; ILR). If $l = +1$, the resonance is outside CR and $\Omega_\mathrm{b} > \Omega_\Phi$ (*outer Lindblad resonance*; OLR). Another important resonance for the secular evolution of a barred galaxy is the *ultrahamonic resonance*, which happens when $m = 4$ and $l = \pm 1$. This resonance is located closer to the CR than the ILR and OLR.

Resonant orbits (often also referred to as periodic orbits) have been studied in great detail in 2D (Contopoulos & Papayannopoulos, 1980; Contopoulos, 1980; Athanassoula et al., 1983) and 3D (Pfenniger, 1984; Skokos et al., 2002b,a). The main 2D orbital family in a bar potential is the $x1$ family. The orbits of this family are elongated parallel to the bar major axis, they are 2:1 orbits, i.e. they complete two radial oscillations for every revolution around the centre. Another family of 2:1 orbits is the $x2$ family which is oriented perpendicular to the major axis. They are found close to the centre and the existence of an ILR is a necessary condition for their appearance (Contopoulos & Papayannopoulos, 1980). Additionally, there are 4:1 orbits,

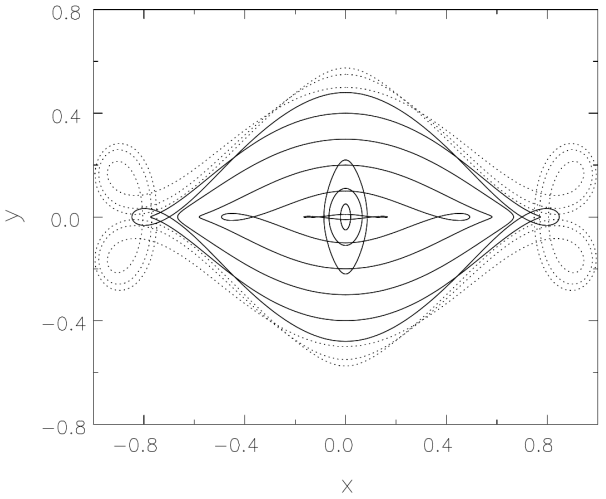

Figure 1.4: Main orbital families in a 2D bar potential. Solid lines represent the $x1$ orbits elongated along the bar major axis, parallel to the x-axis, and the $x2$ orbits in the central region that are perpendicular to the major axis. The dotted lines show three 4:1 orbital families. Figure adapted from Fig. 11 in Sellwood (2014).

which close after four radial oscillations for every revolution in a frame that rotates with the bar. They are elongated along the major axis close to the CR. These orbits may be responsible for the boxy shape of bars. A sketch of these orbital families can be seen in Fig. 1.4. If the periodic orbits are stable, they are able to trap quasi-periodic orbits around them. The conglomeration of stars either on the periodic $x1$ orbits or trapped on quasi-periodic orbits that are wrapped around them build what has been called the 'backbone' of the bar (Contopoulos, 1980).

By using simple calculations of periodic orbits, Contopoulos (1980) demonstrated that bars cannot extend beyond corotation. By using further models of periodic orbits together with hydrodynamical simulations, Athanassoula (1992b,a) found that the ratio between the corotation radius (or the distance to the Lagrange point on the major axis) and the length of the bar $\mathcal{R} = R_\mathrm{CR}/R_\mathrm{bar}$ (Elmegreen, 1996) is 1.2 ± 0.2. Direct (Tremaine & Weinberg, 1984) and indirect (Rautiainen et al., 2008; Buta & Zhang, 2009; Font et al., 2017) estimates of the CR from observational data found that for the vast majority of bars $1.0 \leq \mathcal{R} \leq 1.4$ (Elmegreen, 1996; Rautiainen et al., 2008; Corsini, 2011; Font et al., 2017). Since $R_\mathrm{CR} = V_{R_\mathrm{CR}}/\Omega_\mathrm{b}$, where V_{R_CR} is the circular velocity of the disc at the CR, the parameter $\mathcal{R}$ is anti-propotional to the pattern speed of the bar Ω_b and it can be used to describe its rotation rate. Bars with $\mathcal{R} \leq 1.4$ are usually called 'fast' and bars with $\mathcal{R} > 1.4$ 'slow' (Debattista & Sellwood, 2000). According to this classification, the above mentioned studies haven shown that the majority of bars are fast. However, during the evolution of a bar it not only slows down (in terms of its pattern speed), but it also grows (e.g. Athanassoula & Misiriotis, 2002), and, thus, $\mathcal{R}$ can still be fast even if the pattern speed slows down. There are some extreme cases in the literature where very slow bars have been found, for example in the recent study by Patra & Jog (2019).

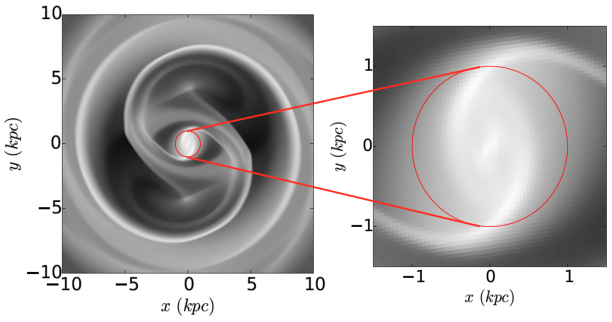

Figure 1.5: Gas surface density in a bar co-rotating frame from high-resolution hydrodynamical simmulations. The bar is parallel to the x-axis. Figure adapted from Fig. 1 in Fragkoudi et al. (2016)

The gas response to the non-axisymmetric gravitational potential of a bar has been studied in detail in various high-resolution hydrodynamical simulations (Athanassoula, 1992a; Piner et al., 1995; Kim et al., 2012; Li et al., 2015; Renaud et al., 2015; Sormani et al., 2015; Fragkoudi et al., 2016) and it is illustrated in Fig. 1.5. In these simulations, gas flows with supersonic speed in thin stream lines along periodic orbits, until they intersect, where shocks are inevitable. When shocks happen, the gas loses angular momentum and energy, and flows inwards. The shocks form along the leading side of the rotating bar and drive the gas towards the inner kpc. In the presence of an ILR, the gas is stalled near that radius in a nuclear ring and it requires additional mechanisms to drive it further inwards, such as nuclear spirals or nuclear bars (Combes, 1996; Sellwood & Wilkinson, 1993; Sellwood, 2014). Observational evidence largely agrees with these models. For example, inflows were observed in Hα in Holmes et al. (2015), dust lanes that trace shocks in the gas are clearly seen on the leading edges of bars (e.g. Gadotti et al., 2019), as well as molecular gas densities and star formation as traced by Hα (e.g. Sheth et al., 2002).

1.3.5 Impact of bars in shaping galaxies

The gas response to the rotating bar in a disc galaxy has important consequences for the evolution. Gas is the fuel for star formation and the rearrangement of gas by the bar changes the position and pace at which stars form. Furthermore, gas may serve to feed SMBHs and an enhanced flow to the centre can potentially ignite or increase the activity of the nucleus.

1.3.5.1 Bars and AGN

The potential of bars to feed AGN has been discussed in the literature for the last three decades since Shlosman et al. (1989, 1990). The idea is simple, bars push gas from kiloparsec-scales, where it is inaccessible to the SMBH, down to parsec-scales building up a reservoir of cool gas that potentially accretes onto the SMBH and triggers or enhances the activity of an AGN.

Additional to hydrodynamical simulations of gas flows in bars (e.g. Piner et al., 1995; Kim et al., 2012; Fragkoudi et al., 2016), observational studies have tried to link the presence of bars to AGN activity by studying the fraction of AGN in barred and unbarred galaxies or the fraction of bars in active and non-active SMBHs. The results are ambiguous, while some studies find a correlation (Knapen et al., 2000; Coelho & Gadotti, 2011; Oh et al., 2012; Alonso et al., 2014; Galloway et al., 2015), others see no differences (Mulchaey & Regan, 1997; Ho et al., 1997; Cheung et al., 2015a). Additionally, some studies compared not only the presence of AGN to bars, but also measured the strength of activity. No evidence that support the AGN feeding scenario was found in Cisternas et al. (2013). In contrast, Alonso et al. (2018) found an excess of nuclear activity in AGN of barred galaxies as compared to that of AGN in unbarred galaxies. It was pointed out that different time scales between long-lived bars and short cycles of AGN activity might complicate the interpretation of these studies. Goulding et al. (2017) approached this problem by stacking X-ray sources as proxy for a time-averaged accretion and found no effect of bars on the nuclear activity.

In addition to different time scales, physical scales of gas flow play a crucial role. García-Burillo & Combes (2012) found that only ~ 35% of 20 AGN host galaxies showed negative torques in the molecular gas in the centre. The positive central torques in the other galaxies kept the gas from falling further in and it was stalled in a ring-like structure at the ILR. In these cases, an additional mechanism is required to drive the gas from a few hundred parsecs further inwards to the central few parsecs where it reaches the sphere of influence of the SMBH and can potentially be accreted. This is possible, e.g., either with magnetic fields or if a trailing nuclear spiral or a small nuclear bar is formed inside the ILR of the large scale bar (Combes et al., 2019). In summary, it seems that bars are capable of pushing a large amount of cool gas from the outer disc towards the central kiloparsec providing the supply for AGN activity but, only in very few cases, the gas directly reaches the SMBH, which makes it difficult to find a direct connection between the presence of bars and AGN.

1.3.5.2 Bars and secularily-built structures

Rings are common structures in galaxies. Nuclear rings with sizes of ~0.2-2 kpc are found in 20 ± 2% of disc galaxies (Comerón et al., 2010), inner rings with diameters between ~2-12 kpc occur in 35 ± 1% of discs and the fraction of outer rings that have sizes between 7-27 kpc is ~ 16 ± 1% (Comerón et al., 2014). It is widely believed that they form from resonant accumulation of gas, but see also Romero-Gómez et al. (2006, 2007), where rings are successfully explained by the manifold theory.

In the resonance theory, the main orbital families are either aligned or perpendicular to the bar major axis and they change orientation by 90° at each resonance. The non-axisymmetric potential of the bar exerts a net tangential torque on the gas that is non-zero between resonance and

zero at each resonance. The sign of the torque changes at each resonance. It is negative between ILR and CR and positive between CR and OLR. Results of hydrodynamical simulations agree with this theory, where in fact inside CR the gas is observed to stream inwards and outside CR outwards (e.g. Athanassoula, 1992a; Kim et al., 2012; Li et al., 2015). It depopulates the CR and accumulates at the OLR outside CR, and at the inner UHR and ILR inside CR. When it gets dense enough at these radii, it starts to form stars, which will be observed as outer rings, inner rings and nuclear rings, respectively.

Inside the nuclear ring further substructure, such as nuclear bars, can develop. Double-barred galaxies have been observed since de Vaucouleurs (1974) and double-bars are present in approximately one third of barred galaxies (e.g. Laine et al., 2002). Two scenarios have been proposed to explain the formation of these independently rotating inner or nuclear bars. In the first scenario, the inner bar forms from a rotating inner disc. The inflow of gas, triggered by the outer bar, increases the central mass which results in a deplacement of the ILR closer to the centre. As a result of the continued inflow of gas, the star-forming ring burns its way towards the centre forming a stellar inner disc or pseudobulge (Kormendy & Kennicutt, 2004). Similarly to the outer main disc, the inner disc may experience spiral and bar instabilities, and form a nuclear spiral or an inner (secondary) bar (Debattista & Shen, 2007; Shen & Debattista, 2009; Du et al., 2015).

A second scenario explains the formation of nuclear structures as a result of decoupling of the gas in the nuclear ring from the outer disc. A necessary condition for this to happen is the existence of two ILR. In that case, the $x2$ orbital family emerges between the two ILR which eventually leads to a phase shifted or decoupled gaseous inner bar inside the inner ILR and stars will follow the potential soon after (Shlosman et al., 1989; Friedli & Martinet, 1993; Combes, 1994; Englmaier & Shlosman, 2004).

Detailed studies of kinematics and stellar populations in double-barred galaxies in de Lorenzo-Cáceres et al. (2012, 2013, 2019) present strong evidence that favour the first scenario in which inner bars form from dynamical instabilities in inner discs. Furthermore, Méndez-Abreu et al. (2019) found for the first time an example of an inner bar that buckled analogous to outer bars, backing up the hypothesis that inner bars are long-lived structures as found in numercal studies by Wozniak (2015).

1.3.5.3 Bars and the cessation of star formation in galaxies

The bimodality in colours and SFR in local galaxies suggests the existence of one or more processes that are responsible for quenching star formation on a global scale, i.e. the cessation of the total SFR in a galaxy as opposed to local processes. Several candidates have been discussed in the literature, including mergers (Peng et al., 2012), morphological quenching (Martig et al., 2013), bar quenching (Haywood et al., 2016; James & Percival, 2018), ram-pressure stripping (Cortese et al., 2011), starvation (Feldmann & Mayer, 2015), harassment (Moore et al., 1996) and AGN feedback (Harrison, 2017). All of these processes are able to lower the global star formation rate and quite possibly it is often a combination of various processes that turns blue star-forming galaxies into red-and-dead galaxies.

The action of bars on the star formation in galaxies is twofold. First, bars redistribute gas into the centre and confined rings, where gas density will be enhanced and star formation accelerated. As a result, gas is consumed faster and the star formation is starved unless there is an external replenishment of gas. Second, bars induce shear in the gas due to the fast flows on different orbits along the bar. The shear prevents the gas from collapsing and forming stars. This process is only able to prevent star formation locally, but, if strong enough, it could have an effect on the global SFR (Phillips, 1996; Verley et al., 2007; Emsellem et al., 2015). Evidence supporting the role of bars in quenching the star formation in galaxies has been provided by both observations (Hakobyan et al., 2016; Haywood et al., 2016; Newnham et al., 2019) and simulations (Spinoso et al., 2017; Khoperskov et al., 2018) .

1.3.6 Internal properties of bars

Stellar and gas dynamics in barred galaxies and their consequences for the evolution of the hosts have been studied in quite detail in the literature. In contrast, quantitative observational studies of internal properties of bars, such as star formation and stellar population within bars, are still scarce. Given the typical width of bars of < 1 kpc, high spatially-resolved spectroscopy is necessary to make these studies feasible. A detailed analysis of star formation and stellar populations in bars is the main focus of the studies that I present in Chapter 3 and 4. In the following, I summarise some of the results from earlier works in the literature.

1.3.6.1 Star formation in bars

Spiral arms, rings or the nucleus are typical locations of star formation in galaxies, which can be seen, for example, in clumpy bright Hα emission. Therefore, the lack of Hα in many of the bars presented in Phillips (1993); Phillips (1996) and García-Barreto et al. (1996) was unexpected. How do bars prevent star formation given that they are the main medium to transport gas towards the centre? In fact, some bars do show Hα along the bar (Sheth et al., 2002). Verley et al. (2007) classified the bars in three categories: Hα bars, non-Hα bars with Hα in the centre and non-Hα bars with no Hα in the centre.

Simulations have shown that shear could impede star formation in the bar (Emsellem et al., 2015; Khoperskov et al., 2018). Alternatively, bars observed as non-star-forming could just have already depleted all the gas in the bar region and, if there is no further external gas falling

in, star formation would cease in these bars. Newnham et al. (2019) recently presented a study of HI morphology of barred galaxies. The authors report the detection of HI holes in the bar region of some dynamical advanced bars, indicating the cessation of gas supply to feed further star formation. However, direct observational evidence that supports one or the other mechanism or quantitative analyses of star formation in bars is still scarce. Furthermore, it is still not well understood how the presence of star formation in bars is connected to the age or evolutionary state of the bar. Do bars form stars at early or late stages? Is it a transient phenomenon? How is that related to other bar properties?

1.3.6.2 Stellar populations in bars

Theories of bar formation and stellar dynamics of bars tell us that during the formation and evolution of the bar stars get trapped in periodic or quasi-periodic orbits in the bar potential, which can have different elongations and orientations. Stars will stay in these orbits unless they are subject to radial migration caused by the exchange of angular momentum at the CR (e.g. Sellwood & Binney, 2002; Minchev & Famaey, 2010). As the bar grows, this process can affect a large part of the disc, but it will be mostly visible outside the bar radius (Friedli et al., 1994; Di Matteo et al., 2013). Observations of the bar region are probably more affected by orbital mixing, where the orbits of stars with different elongations and apocentres cross each other and stellar populations get mixed (Binney & Tremaine, 1987). The result would be a flattening of any gradient that might be present in bars. The amount of flattening partly depends on the spatial resolution of the observation. Stellar population gradients have been studied in observations mostly along the bar major axis as compared to the outer disc or the minor axis of the bar (Pérez et al., 2007, 2009; Pérez & Sánchez-Blázquez, 2011; Sánchez-Blázquez et al., 2011; Seidel et al., 2016; Fraser-McKelvie et al., 2019b). The results still seem somehow ambiguous, but they mostly indicate a flattening along the major axis.

Recent idealised thin plus thick disc *N*-body galaxy simulations by Fragkoudi et al. (2017) show that the kinematically cold stellar component forms a strong and thin bar, while the hot component settles in a rounder and weaker bar (see also Athanassoula et al., 2017; Debattista et al., 2017; Fragkoudi et al., 2018). These results should manifests themselves in observations of bars in stellar population gradients perpendicular to the major axis.

Additionally, from gas dynamics in barred galaxies we know that gas flows inwards in thin stream lines along the leading edges of rotating bars. If gas is present and star formation is not suppressed by shear, star formation is expected to happen along the leading $x1$ orbits. This would induce a new young population of stars along the edges of the bars. However, due to orbital mixing and short dynamical timescales ($\sim$ 100 Myr), the localised effect is expected to be washed out soon.

In summary, observations of stellar populations in bars provide important information about processes during bar formation, capture of stars during bar evolution and star formation in bars. Lower energy orbits within the $x1$ family are more elongated and closer to the major axis, while higher energy orbits are rounder and farther away. From the principle structure of these orbits, as seen in Fig. 1.4, it becomes clear that orbital mixing affects stronger the parts close to the major axis. For that reason, investigations of trends *perpendicular* to the major axis, seem to be best suited to separate stellar populations on different orbits and they should give important insights into the assembly and evolution of stellar bars.

1.4 Integral field spectroscopy with PMAS/ PPak and MUSE

Observational astronomy and astronomical instrumentation closely depend on each other. Big advances in instrumentation continuously push astronomy to new heights. The advent of integral field spectroscopy (IFS) over the last decades has resulted in enormous advances in our understanding of galaxy formation and evolution. The capability of integral field unit (IFU) spectrographs, such as FLAMES (Pasquini et al., 2000), SINFONI (Eisenhauer et al., 2003), SAURON (de Zeeuw et al., 2002) or KMOS (Sharples et al., 2013) to combine the advantages of photometry as well as spectroscopy and spatially resolve spectroscopic features with single observations has significantly increased our understanding of galaxy dynamics, star formation and properties of gas and stars in galaxies.

Integral field spectroscopy is fundamental to the work presented in this thesis, which consists of three different projects as part of three different surveys. The data used is based on observations with the IFU spectrographs PMAS/ PPak (Potsdam Multi-Aperture Spectrophotometer/ PMAS fibre package; Roth et al., 2005; Kelz et al., 2006), mounted on the Calar Alto Observatory (CAHA) 3.5-m telescope in Spain, and MUSE (Multi-Unit Spectroscopic Explorer; Bacon et al., 2010), mounted on UT4 of the Very Large Telescope (VLT) on Cerro Paranal in Chile.

1.4.1 CALIFA survey

A variety of IFU galaxy surveys have emerged over the last years to exploit the power of IFS for large statistical samples including SAURON (de Zeeuw et al., 2002), ATLAS^{3D}[3] (Cappellari et al., 2011), DiskMass (Bershady et al., 2010), CALIFA[4] (Calar Alto Legacy Integral Field Area survey; Sánchez et al., 2012), SAMI[5] (using the Sydney Australian-Astronomical-Observatory Multi-object IFS; Croom et al., 2012), and MaNGA[6] (Mapping Nearby

[3] http://purl.org/atlas3d
[4] http://califa.caha.es
[5] http://sami-survey.org
[6] https://www.sdss.org/surveys/manga/

Galaxies at Apache Point Observatory; Bundy et al., 2015).

The analysis in Chapter 2 of this thesis is based on observations from the CALIFA survey (Sánchez et al., 2012; Husemann et al., 2013b; Walcher et al., 2014; García-Benito et al., 2015; Sánchez et al., 2016). CALIFA is a public legacy survey that provides observations of 667 nearby galaxies ($0.005 < z < 0.03$) using the IFU spectrograph PMAS/ PPak. In comparison with the SAMI and MaNGA survey, which aim to observe 3,600 and 10,000 objects, respectively, the advantage of CALIFA is a high and relatively uniform physical spatial resolution ($\sim$1 kpc) and a large spatial coverage ($\sim 2.5\ r_e$). In this thesis, we use a subsample of 45 galaxies observed with the V1200 high spectral resolution set-up (3650-4840 Å at 2.3 Å FWHM resolution) that allows to measure velocity dispersion down to 40 km s^{-1} (Falcón-Barroso et al., 2017).

1.4.2 CARS survey

The work in Chapter 3 is based on observations from the Close AGN Reference Survey[7] (CARS; Husemann et al., 2017) with the IFU spectrograph MUSE. The main goal of the CARS survey is to unravel the connection between AGN and their host galaxies based on a sample of 40 nearby ($0.01 < z < 0.06$) luminous unobscured AGN. CARS combines a unique massive multi-wavelength data-set of spatially resolved observations from radio to X-ray wavelengths that will aid in a better understanding of processes such as star formation in AGN host galaxies, quenching by AGN-driven outflows and the balance of AGN feeding and feedback.

In this thesis, I use a subsample of 16 barred AGN host galaxies observed with MUSE. The fine spatial sampling of the MUSE instrument ($0.2'' \times 0.2''$) together with a large field of view (FOV, $1' \times 1'$) corresponding to 90,000 spectra per pointing make MUSE the ideal instrument to study spatially resolved star formation in bars and compare them with properties of the host galaxies and test AGN feeding scenarios.

1.4.3 TIMER survey

The analysis of stellar populations in galaxy bars presented in Chapter 4 is part of the Time Inference with MUSE in Extragalactic Rings (TIMER; Gadotti et al., 2019) project. By studying the central structures of 24 nearby ($0.001 < z < 0.01$) barred galaxies with the MUSE IFU spectrograph, TIMER aims at estimating the time when galaxy discs dynamically settle giving rise to the onset of bar-driven secular evolution.

Given the large angular sizes of the very nearby objects in the TIMER sample combined with the fine spatial sampling of MUSE, the TIMER survey provides optimal data for detailed spatially resolved analysis of stellar populations in barred galaxies. In the work presented in Chapter 4, I use a subsample of 9 galaxies to study variations of stellar population within bars with an unprecedented physical spatial resolution.

[7] https://www.cars-survey.org

1.5 Thesis outline

The content of Chapters 2-4 was prepared in a format for publication in the journals *Astronomy & Astrophysics* and *Monthly Notices of the Royal Astronomical Society*. This means that each chapter has its own introduction and conclusion to be self-contained. The main introduction and conclusion of this thesis are written with the aim to provide a broader context of this work.

The global scientific aim of this thesis is to develop a better understanding of how secular evolution of galaxies works, specifically by testing predictions of the secular evolution scenario and elucidating some of the processes through which secular evolution takes place. The main objectives are:

- Improve the classification of bulges by using IFS and combining photometric and spectroscopic approaches for a large sample of galaxies.
- Quantify star formation in bars and verify dependencies on galaxy properties.
- Analyse stellar populations in bars to aid in understanding the formation and evolution of bars.

This work is composed of three separate projects with distinct IFS data-sets drawn from three different galaxy surveys: the CALIFA survey, the CARS survey and the TIMER project. Each sample was chosen for its advantages for the specific project, i.e., a large uniform sample of unbarred galaxies for the classification of bulges in CALIFA, barred AGN host galaxies with different star formation properties observed with MUSE in CARS, and large very nearby barred galaxies observed with MUSE in TIMER. The projects complement each other perfectly. The classification approaches of bulges in the first project help determining the frequency of each type, which sets important constraints on where and how often secular evolution happens. At the same time, it sets constraints on the predicted merger rate in galaxy formation and evolution. The second and third project try to elucidate internal properties and processes of bars, the knowledge of which is still rather rudimentary in the literature. While the second project concerns ongoing and localised star formation, the third project reveals how star formation proceeds in bars on large temporal and spatial scales. The main outline of the thesis is as follows.

In Chapter 2 (Neumann et al., 2017), we investigate the phenomenology of bulges and we provide a combined photometric and kinematic classification approach. We use IFS data from the CALIFA survey together with photometric images from data release 7 of the Sloan Digital Sky Survey (SDSS; York et al., 2000) to perform a photometric

2D multi-component decomposition with the code IMFIT (Erwin, 2015), a determination of concentration indices, and a 2D kinematic analysis by spectral model template fitting with PYPARADISE (Walcher et al., 2015; Husemann et al., 2016). Our sample consists of 45 unbarred, moderately inclined spiral galaxies, for which we provide a final bulge classification based on a combination of four different classification criteria: the bulge Sérsic index $n_{\rm b}$, the new concentration index $C_{20,50}$, the Kormendy relation and the inner slope of the radial velocity dispersion profile $\nabla\sigma$.

In Chapter 3 (Neumann et al., 2019), we use MUSE observations for a sample of 16 barred AGN host galaxies to study the star formation within bars. It had been observed that some bars are absent of star formation while other bars do form stars, but it has never been quantified and set in relation to other bar- and host galaxy properties. We perform a very detailed photometric decomposition with IMFIT including up to 6 different components simultaneously to accurately determine bulge-, bar- and other galaxy parameters. We further use PYPARADISE to fit the spectra and obtain spatially resolved star formation rates (SFR) from dust-corrected Hα emission line fluxes. We show trends of SFR parallel and perpendicular to the bar and compare the total SFR of the bars with properties of the bars and the host galaxies. We further test AGN feeding scenarios.

In Chapter 4 (to be submitted to *Monthly Notices of the Royal Astronomical Society* within a few months), we present a detailed analysis of stellar populations and chemical enrichment in bars based on a subsample of 9 nearby barred galaxies from the TIMER project. For that purpose, we derive and analyse spatially resolved maps of stellar ages and metallicities, [α/Fe] abundances, resolved star formation histories, as well as maps of Hα as tracer of star formation. Additionally, we show results from an analysis of barred galaxies in the cosmological zoom-in simulations from the Auriga (Grand et al., 2017) project and compare them to our observations.

Finally, Chapter 5 summarises the thesis in the context of recent literature and provides a short outlook to potential future projects.

A combined photometric and kinematic recipe for evaluating the nature of bulges using the CALIFA sample

2

J. Neumann, L. Wisotzki, O.S. Choudhury, D.A. Gadotti, C.J. Walcher, J. Bland-Hawthorn, R. García-Benito, R.M. González Delgado, B. Husemann, R.A. Marino, I. Márquez, S.F. Sánchez, B. Ziegler, and CALIFA collaboration

ABSTRACT

Understanding the nature of bulges in disc galaxies can provide important insights into the formation and evolution of galaxies. For instance, the presence of a classical bulge suggests a relatively violent history. In contrast, the presence of an inner disc instead (also referred to as a 'pseudobulge') indicates the occurrence of secular evolution processes in the main disc. However, we still lack criteria to effectively categorise bulges, limiting our ability to study their impact on the evolution of the host galaxies. Here we present a recipe to separate inner discs from classical bulges by combining four different parameters from photometric and kinematic analyses: The bulge Sérsic index $n_{\rm b}$, the concentration index $C_{20,50}$, the Kormendy (1977) relation and the inner slope of the radial velocity dispersion profile $\nabla\sigma$. With that recipe we provide a detailed bulge classification for a sample of 45 galaxies from the integral-field spectroscopic survey CALIFA. To aid in categorising bulges within these galaxies, we perform 2D image decomposition to determine bulge Sérsic index, bulge-to-total light ratio, surface brightness and effective radius of the bulge and use growth curve analysis to derive a new concentration index, $C_{20,50}$. We further extract the stellar kinematics from CALIFA data cubes and analyse the radial velocity dispersion profile. The results of the different approaches are in good agreement and allow a safe classification for approximately 95% of the galaxies. In particular, we show that our new "inner" concentration index performs considerably better than the traditionally used $C_{50,90}$ when yielding the nature of bulges. We also found that a combined use of this index and the Kormendy (1977) relation gives a very robust indication of the physical nature of the bulge.

A version of this chapter is published as Neumann J., et al., *Astronomy & Astrophysics*, 2017, Vol. 604, id. A30, 15 pp.

2.1 Introduction

The traditional picture of disc galaxies consists of two main stellar components, a disc and a central spheroid - the bulge. It is a generally accepted fact that bulges play an essential role for our understanding of galaxy formation and evolution. Gadotti (2009) estimated that in the Local Universe bulges contribute about 28% of the total stellar mass in massive galaxies. From the analysis of the stellar mass budget with the Galaxy and Mass Assembly (GAMA) survey, Moffett et al. (2016) found that 15% of the local total stellar mass density is distributed in S0-Sa bulges. Bulges are closely connected to the strength and length of the bar (e.g. Sellwood, 1981; Aguerri et al., 2009; Laurikainen et al., 2009) and they are correlated with the mass of the supermassive black hole (e.g. Kormendy, 1993a; Gebhardt et al., 2000; Ferrarese & Merritt, 2000; Kormendy & Gebhardt, 2001).

For a long time, bulges were considered to be elliptical-like components embedded in an outer disc, but a significant amount of evidence has shown a dichotomy of bulges (see e.g. Kormendy, 1993b; Kormendy & Kennicutt, 2004; Athanassoula, 2005; Fisher & Drory, 2016, for a review). The bulges that fit into the traditional category of hot central elliptical-like components were henceforth called 'classical bulges' whereas every other bulge-like, but not classical component was called a 'pseudo-bulge' or also disc-like bulge or discy pseudobulge. Photometrically, they satisfy the definition of a bulge since they produce an excess of light over an inward extrapolation of the major disc. But they are considered to be much more like discs, for example they are flattened by rotation, have close to exponential light profiles and are often dominated by young stars. Fisher & Drory (2011) found that the majority of bulges in the Local Universe are in fact pseudobulges. Today we know that not only the overall bulge category, but also the pseudobulges themselves form an inhomogeneous class of objects. Morphologically, nuclear spirals, nuclear rings or nuclear bars can be part of a pseudobulge. Another sub- or equal-level category are boxy or peanut-shaped bulges. They have been shown to be the thick central parts of bars seen edge-on (Kuijken & Merrifield, 1995; Bureau & Freeman, 1999; Bureau & Athanassoula, 1999, 2005; Athanassoula & Bureau, 1999; Chung & Bureau, 2004). The different kinds of bulges can as well coexist (Fisher & Drory, 2008; Erwin, 2010). Méndez-Abreu et al. (2014) found seven out of ten barred galaxies to host composite-bulges. Erwin et al. (2015) predict composite-bulges to be present in at least 10% of barred S0 and early-type spiral galaxies. In this paper, the term pseudobulge will be used to refer to any bulge thought to be made of disc material.

Many photometric criteria have been proposed to identify pseudobulges and classical bulges, for example the morphology, the concentration index, the Sérsic index (Fisher & Drory, 2008), the Kormendy relation (Kormendy, 1977; Gadotti, 2009) or the bulge-to-total light ratio combined with the ratio of the sizes of bulge and disc (Allen et al., 2006), but none of these criteria alone can unambiguously separate the two bulge types. As a consequence, authors have used multiple criteria to improve the accuracy of bulge classification (e.g. Kormendy & Kennicutt, 2004; Fisher & Drory, 2010; Kormendy, 2013).

The kinematics of bulges provided some of the earliest evidence for the dichotomy of bulges. Pseudobulges were found to be more rotationally supported as seen in the $V_m/\langle\sigma\rangle$ - ϵ diagram (Kormendy & Illingworth, 1982) and the central velocity dispersion was used to identify pseudobulges as low-σ outliers from the Faber & Jackson (1976) relation (Kormendy & Kennicutt, 2004). More recently there have been a few studies of kinematic bulge diagnostics that reported correlations between bulge type and radial structure of kinematics (Falcón-Barroso et al., 2006; Méndez-Abreu et al., 2008b; Méndez-Abreu et al., 2014; Fabricius et al., 2012). Yet, a clear quantification of the relations that they found in kinematic behaviour remains an open task. With the advent of big integral field spectroscopy (IFS) surveys, data of a new category become available to do statistically meaningful spatially resolved spectroscopy with a big sample of galaxies (e.g. Krajnović et al., 2011; Falcón-Barroso et al., 2017).

In this paper we present a combination of photometric and spectroscopic bulge indicators derived from two-dimensional analyses of the structure and kinematics of our CALIFA subsample. We use detailed growth curve measurements of the surface brightness distribution, two-dimensional photometric decompositions and kinematic maps to understand their correlation and shed light onto the nature of the bulge dichotomy. Our main aims are: 1) to find a robust concentration index for bulge diagnostic, 2) to use IFS data of a medium-sized sample of galaxies to investigate the bulge kinematics and 3) to provide a prescription based on manifold parameters for bulge classification.

The paper is organised as follows. Section 2.2 describes the sample selection and data used in this work. In Sect. 2.3 we describe our multiple approaches followed by Sect. 2.4 where we present the results. In Sect. 2.5 we provide a recipe for a detailed classification of bulges that we then apply to our sample, and a discussion of various aspects of our analyses. Finally, we summarise our work and main conclusions in Sect. 2.6. Throughout the article we assume a flat cosmology with $\Omega_{\rm m} = 0.286$, $\Omega_\Lambda = 0.714$ and a Hubble constant $H_0 = 69.6\,{\rm km\ s^{-1}\ Mpc^{-1}}$ (Bennett et al., 2014).

2.2 Data sources and sample selection

The Calar Alto Legacy Integral Field Area survey (CALIFA, Sánchez et al., 2012; Walcher et al., 2014) is a large public legacy project that obtained spatially resolved spectra of approximately 600 local galaxies using integral field spectroscopy (IFS). The sample we use in this work is drawn from the sample of 277 galaxies that was observed in the V1200 configuration between the official start of

observation in June 2010 and October 2013.

CALIFA uses the Potsdam Multi-Aperture Spectrophotometer (PMAS, Roth et al., 2005) instrument with the PMAS fibre package (PPak, Kelz et al., 2006) integral field unit (IFU) installed at the Cassegrain focus of the Calar Alto Observatory (CAHA) 3.5 m telescope in Andalucía, southern Spain. The IFU consists of a total of 382 fibres, 331 of them are object-fibres packed in a hexagonal form. Each fibre has a diameter of 2.68″ on the sky, collecting flux from 5.7 arcsec^2. The whole hexagonal arrangement of the object fibres covers a 74×65 arcsec^2 field of view (FoV). The so-called CALIFA mother sample – a pool of 939 galaxies from which the objects to observe were drawn only depending on observability – is primarily diameter limited to ensure a good fit to the FoV of the instrument. It covers a wide range of the luminosity function and all morphological categories. We refer to Walcher et al. (2014) for more details on the sample selection and characteristics. As result of the diameter-limited aspect of the CALIFA sample 97% of the galaxies are covered to more than twice the Petrosian half-light radius, which allows for a detailed study of the bulges and outer disc components.

The data have been reduced with the version 1.5 of the CALIFA pipeline, see Sánchez et al. (2012), Husemann et al. (2013b) and García-Benito et al. (2015) for details. The final data products are two data cubes, one for the low-resolution V500 spectral setup covering the wavelength range 3745-7500 Å with a spectral resolution of 6.0 Å full width at half maximum (FWHM) and the other for the medium-resolution V1200 setup covering the wavelength range 3650-4840 Å with a spectral resolution of 2.3 Å FWHM. Falcón-Barroso et al. (2017) showed that the spectral resolution of the V500 grating is not enough to accurately measure velocity dispersions below $100\,\mathrm{km\,s^{-1}}$, whereas the V1200 grating allows measuring the velocity dispersion down to $40\,\mathrm{km\,s^{-1}}$. We decided to use the V1200 data cubes since we are especially interested in the stellar kinematics of the bulges, which can have very low velocity dispersions if they are of discy nature.

The sample selection for this work was driven by the aim of investigating indicators of the bulge nature in a clean sample of undisturbed, isolated disc galaxies. From the 277 observed galaxies we selected all unbarred disc galaxies with axis ratio $b/a \geq 0.4$. Additionally, we rejected objects with problematic observational data as for example high dust obscuration, bright foreground stars or very low signal to noise (S/N). The final sample contains 45 objects, three of which are bulgeless galaxies for comparative purposes. Choosing unbarred galaxies as objects for our analyses is a simplification. Bars significantly influence bulge parameters like Sérsic index and bulge-to-total light ratio (B/T), if they are not properly accounted for in 2D photometric decompositions (Aguerri et al., 2005; Gadotti, 2008; Salo et al., 2015). They also show kinematic features in both velocity and velocity dispersion profiles (see e.g. Seidel et al., 2015). Here we tried to focus on bulge signatures by avoiding any disturbances which may originate from a bar component. In Fig. 2.1 we show the normalised histograms of absolute SDSS Petrosian r-band magnitudes $M_{r,\mathrm{p}}$[1], redshifts and morphological types of the CALIFA mother sample and the subsample we used in our analysis. We see no fundamental differences in the distribution of our subsample with the CALIFA mother sample, except that we are missing galaxies fainter than $M_{r,\mathrm{p}} = -19$ and very late-type morphological types. The morphlogical types are, by our selection, restricted to disc galaxies. We also have a significantly higher fraction of S0 and Sbc galaxies, but we do not think that these differences affect the way that our analysis can be represented. We conclude that our subsample is representative of massive disc galaxies in the CALIFA mother sample.

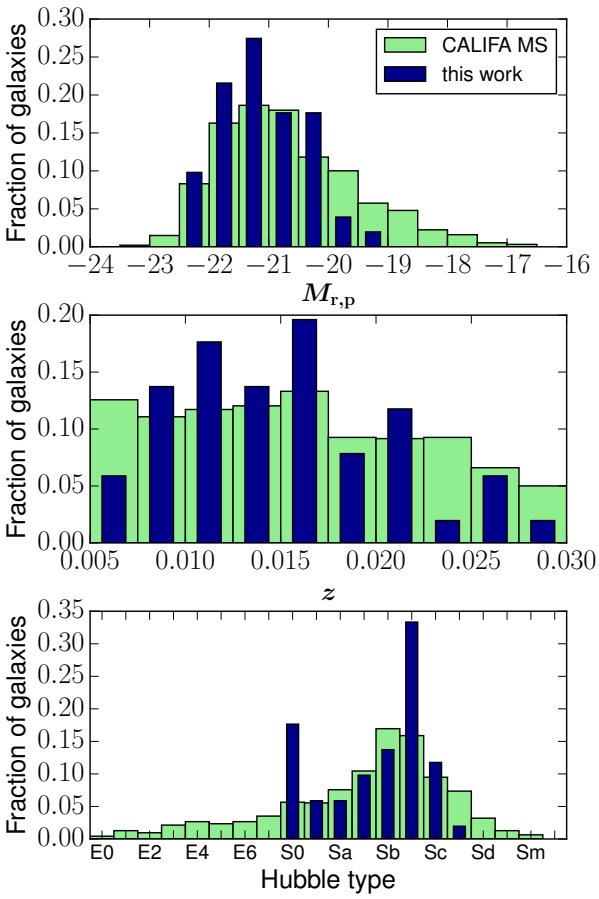

Figure 2.1: Normalised histograms of absolute SDSS Petrosian r-band magnitudes $M_{r,\mathrm{p}}$, redshifts and morphological types of the CALIFA mother sample (MS) and the subsample we used in our analysis.

First we used the complete CALIFA sample for analysing some global structural parameters in Sect. 2.4.1. Subsequently, we determined bulge parameters for our subsample of 45 disc galaxies. We additionally selected a subsample of all isolated elliptical galaxies with good observational data. We used this subsample of 26 galaxies to compare the behaviour of the bulges with respect to the scaling relations built from this sample of ellipticals.

[1] For consistency with Walcher et al. (2014), we show here Petrosian magnitudes instead of total absolute magnitudes that are used in Sect. 2.4.

The CALIFA sample was initially drawn from the photometric catalogue of the data release 7 (DR7, Abazajian et al., 2009) of the Sloan Digital Sky Survey (SDSS, York et al., 2000). This ensures availability of photometric data for every CALIFA galaxy. All photometric analyses in this paper are based on the Sloan *r*-band images. The availability of photometry from SDSS and spectroscopy from CALIFA for a large number of galaxies of all morphological types together with the large spatial coverage of the galaxies in these data makes this sample ideal for a statistical study on properties of bulges with respect to host galaxies.

2.3 Methods

2.3.1 Growth curve analysis and concentration indices

We used the results of the growth curve photometry described in detail in Walcher et al. (2014) for the determination of light concentration indices. Here we simply summarise the basic concept of the method. At first step masks were produced by a combination of an automatic algorithm with SExtractor (Bertin & Arnouts, 1996) and individual inspection by eye. The position angle (PA) and axis ratio (b/a) values were derived from second order moments of the SDSS *r*-band light distribution. The growth curve was then measured within concentric elliptic rings with increasing major axes and fixed b/a and PA.The most delicate and important part is the accurate determination of the sky background and the edge of the galaxy in the presence of sky gradients and incomplete masks. The edge of the galaxy was determined as the major axis at the middle of the current ring where the flux profile slope becomes non-negative, the sky value as the mean of the values within that ring. This method was shown to be sufficiently robust.

From these growth curves it is possible to determine not only the half-light semi-major axes of the galaxies but also any kind of ellipse that encloses a certain percentage of the total light of the galaxy. From here on, we denote the semi-major axis as approximation of the radius r_k that encircles k percent of the total light, for example r_{20} is the radius that encloses 20 percent of the light. The ratio of one of these radii divided by another in any combination can then be used as a concentration index of the galaxy. After exploring a wide range of different options we have chosen $C_{20,50} = r_{20}/r_{50}$ and $C_{50,90} = r_{50}/r_{90}$ as an inner and outer concentration index, respectively. Details on the motivation for that choice and results are presented in Sect. 2.4.1.

2.3.2 Two-dimensional image fitting

Two-dimensional photometric decomposition has become a widely used technique for deriving the structural parameters of galaxies. Multiple codes have been developed to perform image decomposition, such as *GIM2D* (Simard et al., 2002), *GALFIT* (Peng et al., 2002, 2010), *BUDDA* (de Souza et al., 2004) and *GASP2D* (Méndez-Abreu et al., 2008a, 2014). 2D image fitting can be very fast in determining in an automatic way single component parameters such as disc scale length and central surface brightness, but it becomes highly complex and sensitive to initial parameter guesses when fitting in parallel multiple functions to the data. We used *IMFIT* by Erwin (2015)[2] to fit single Sérsic functions to the whole set of 939 galaxies from the CALIFA mother sample. These fits gave us a global Sérsic index for each galaxy that we denote as $n_{\rm g}$.

In addition, we chose to perform a two-component bulge-disc decomposition for our sample of 45 galaxies to derive Sérsic indices $n_{\rm b}$ of the bulge component only. We used a Sérsic function for the bulge and an exponential for the disc. In cases of a Type II (Freeman, 1970) or Type III disc (Erwin et al., 2005) we used either the *BrokenExponential* function of *IMFIT* or we restricted our fit to the central disc component by masking out the outer region of the galaxy. This is a valid approach since we are interested in the central component only. We also checked our sample for evidence of a nuclear component and found no need to fit a central point source. Except for one galaxy that hosts a low-ionization nuclear emission-line region (LINER), none of the objects in our sample hosts active galactic nulei (AGNs). From the best fit model parameters we derived bulge-to-total light ratios (B/T).

Many image fitting codes provide formal uncertainties on the parameter estimates from the Levenberg-Marquardt minimisation technique. In *IMFIT* there is additionally a bootstrap re-sampling option that can be used. The relative uncertainties that we estimated using the bootstrap option for our analysis are of the order of a few per cent. Gadotti (2009) found uncertainties of bulge, disc and bar parameters to be in the range of 5-20% using a different statistical approach with *BUDDA*. However, it has repeatedly been shown that all estimates of statistical errors should be considered underestimates of the true uncertainty of the parameters (e.g. Häussler et al., 2007; Méndez-Abreu et al., 2008a; Gadotti, 2009; Erwin, 2015). One relevant source of uncertainty is the human factor when it comes to select the best model to fit to the data. This is very difficult to account for in a proper error estimation. Additionally, multi-component fits are sensitive to input parameters the more complex the galaxy structure becomes. We therefore conclude that these error estimates are not representative and we chose not to show errorbars for the structural parameters on the individual plots in our paper.

Recently, Méndez-Abreu et al. (2017) (from here on denoted as MA17) published results from photometric decompositions of 404 CALIFA galaxies in the *g*, *r* and *i* SDSS images using the *GASP2D* code. In Fig. 2.2 we compare our best-fit parameters with the results they obtained for the *r*-band images.

The two samples have 40 galaxies in common. We find a relative good agreement between both decompositions.

[2] http://www.mpe.mpg.de/~erwin/code/imfit/

Three of the galaxies were classified in MA17 as purely spheroidal and have therefore $B/T_{\rm MA17} = 1$, and comparitively high $n_{\rm b\ MA17}$ and $r_{\rm e\ MA17}$. The other outliers from the one-to-one relation correspond to either dusty or moderately inclined galaxies or to objects with a more complex structure. Given the overall similarity of the results of both analyses, we will use our decomposition parameters throughout the paper.

2.3.3 Definition of bulge radius

We define the 'bulge radius' as the radius of the ellipse that encloses 90% of the light of the bulge component. This radius is determined by numerical integration of the best fit model Sérsic function from the two-component decomposition. We denote this radius throughout the paper as rb_{90}. This radius is not a demarcation between bulge-dominated and disc-dominated region, but a limit of the bulge extent. This choice was made to trace the whole region of bulge influence. The decision was to use a radius as large as possible, so long as the bulge remains significant.

2.3.4 Velocity dispersion measurement

One key point of this work is to combine photometric bulge indicators with spectroscopic approaches. The CALIFA IFU data offer the great possibility of studying the stellar kinematics in a 2D plane over a large extent of the galaxies. We used the data from the medium resolution V1200 spectral setup to create velocity dispersion profiles from azimuthally averaged stellar kinematic maps for all 45 galaxies of our sample. The procedure is as follows:

We first binned the data cubes spatially using the 2D Voronoi binning method of Cappellari & Copin (2003) to achieve a constant S/N per spatial bin of ≈ 5. This allows for a sufficiently accurate measurement of the velocity and to maintain at the same time enough spatial resolution elements. In the case of five galaxies we had to apply a higher S/N of ≈ 10 to get reliable velocities. This S/N limit is for the velocity measurement only, not the velocity dispersion. Since we are determining only the shift of the spectrum over a wavelength range of 700 Å with good spectral resolution, we consider this S/N limit sufficient. When calculating the noise, we applied weights to the errors in order to take into account the effect of correlated noise of nearby spaxels (Husemann et al., 2013b).

We then estimated the velocities for each bin by fitting model template spectra from the full INDO-US template library (Valdes et al., 2004) to the observed spectra using the code *PyParadise* (Husemann et al., 2016) which is an extended Python version of *paradise* (Walcher et al., 2015). We refer the reader to these references for the details of the algorithm. We used stellar absorption fitting only, since we are only interested in the stellar kinematics. We limited the fit to the wavelength region 4100-4800 Å and masked out strong emission lines. Prior to the fit the stellar templates are smoothed with a 2.3 Å (FWHM) kernel to match the wavelength resolution of the observed CALIFA data. In the *PyParadise* run, a Markov-chain-Monte-Carlo (MCMC) algorithm is used to determine the velocities and related uncertainties.

The next step was to correct every spaxel of the original unbinned data cube to rest-frame and then to the systemic velocity of the galaxy. Afterwards, we binned the cube radially in elliptical rings of one pixel widths which corresponds to 1″ on the sky. Again, we carefully considered the correlated noise during the calculation of the error values. At this point each radial bin is represented by one spectrum. Finally, we ran *PyParadise* again for each radial bin to estimate the velocity dispersions and associated uncertainties.

In Fig. 2.3 we compare our measurements of the central velocity dispersion with the results from Falcón-Barroso et al. (2017) who performed a detailed kinematic analysis of a sample of 300 CALIFA galaxies. Both analyses have 43 galaxies in common. The results are in good agreement, with only one outlier that has a significant higher central velocity dispersion in their measurement. We also conducted a case-by-case comparison between our radial velocity dispersion profiles and theirs. We did not find major differences between the two results.

2.4 Results

In this section we present our findings from the different approaches to characterise bulges and show correlations between the parameters we measured. We highlight the advantages in using the concentration index $C_{20,50}$ and put special effort to combine the photometric approaches with the kinematic measurements. We use both the bulge Sérsic index $n_{\rm b}$ and the concentration index $C_{20,50}$ to separate groups of bulges in the plots. However, we cautiously point out that this is by no means meant to be a final classification of objects as either classical bulge or pseudobulge. In Sect. 2.5.1 we give a recipe using a combination of various parameters for that purpose. The results of our analyses are summarised in Table 2.2 in Appendix 2.B.

2.4.1 Light concentration

In Fig. 2.4 we present concentration indices from the growth curve measurement and global Sérsic indices from the image fitting for the complete set of 939 galaxies that compose the CALIFA mother sample. The global Sérsic index $n_{\rm g}$ is the index obtained from single Sérsic function fits to the galaxies.

We find a very tight correlation of the logarithm of $n_{\rm g}$ with $C_{20,50}$ with a Spearman's rank correlation coefficient of $\rho = -0.8$. A relation between both parameters is expected and has been shown, since they are both estimators of the steepness of the surface brightness profile (e.g. Trujillo et al., 2001; Andrae et al., 2011; Ferrari et al., 2015). Our intention is to show the differences between 'outer' and 'inner' concentration indices. Previous studies (e.g. Gadotti, 2009) have shown that the Petrosian index

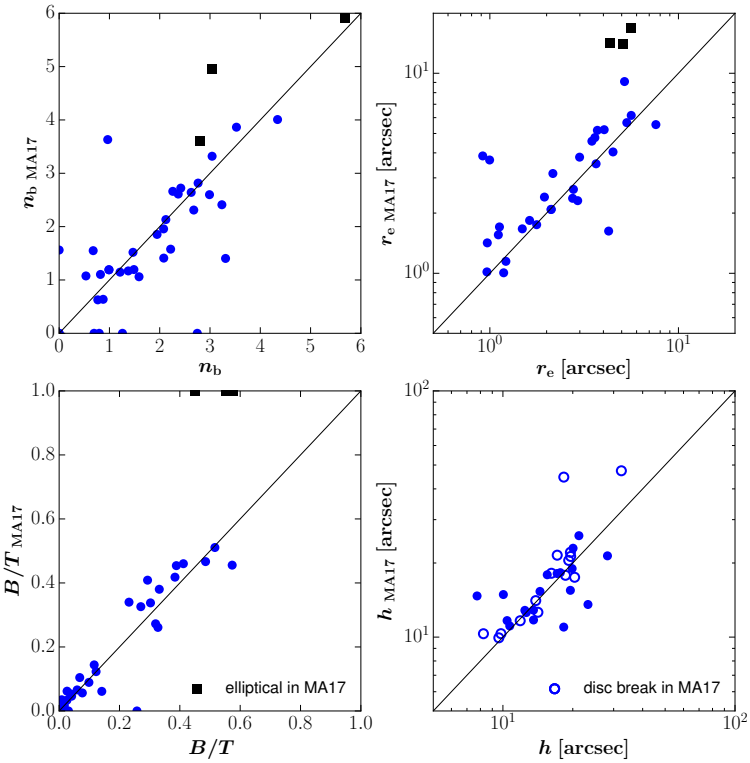

Figure 2.2: Comparison between our decomposition parameters and those obtained from the *GASP2D* r-band decompositions from Méndez-Abreu et al. (2017, annotated as MA17). The two samples have 40 galaxies in common. The left panels show the Sérsic index of the bulge (top) and the bulge-to-total luminosity (bottom). The right panels show the bulge effective radius (top) and the disc scale length (bottom). Galaxies with disc breaks in the decompositions of MA17 are marked by empty circles. In these cases we plot the scale length of the inner disc. Objects with $n_{\rm b} = 0$ in our decomposition are galaxies that were classified as bulgeless. Objects with $n_{\rm b\ MA17} = 0$ in their decomposition were either classified as bulgeless or as having an unresolved bulge. In the latter case, they were modelled by them with a nuclear point source instead. The three objects that have $B/T = 1$ were classified by them as purely spheroidal. There is an overall agreement between both decompositions with moderate scatter.

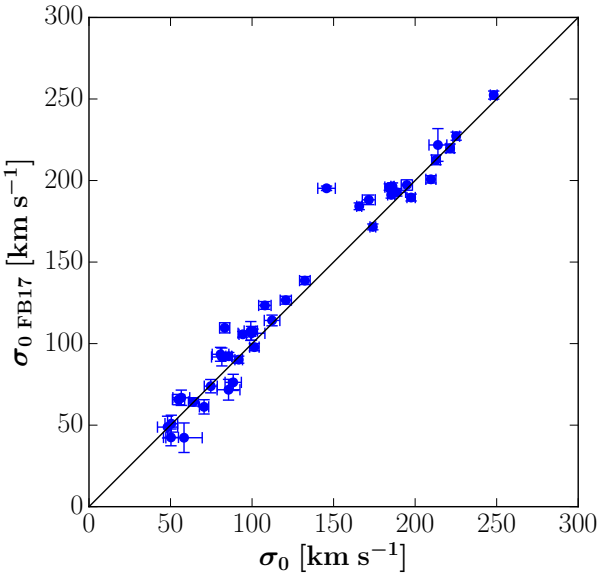

Figure 2.3: Comparison between our central velocity dispersion measurements and those obtained from Falcón-Barroso et al. (2017, annotated as FB17). Overall the results are in good agreement with the exception of one galaxy.

R_{90}/R_{50} correlates with Sérsic index but with considerable scatter. In the bottom panel we see that there is indeed much more scatter in the relation between our measurements of $n_{\rm g}$ and $C_{50,90}$. This clearly favours the usage of the $C_{20,50}$ concentration index as a discriminator between bulge-dominated and disc-dominated galaxies.

It is worth noting that at least part of the reduced scatter using $C_{20,50}$ instead of $C_{50,90}$ might be caused by a smaller uncertainty in the determination of the concentration index. While the radii r_{20} and r_{50} are located on the steeper part of the growth curve, r_{90} is likely to be on the shallower part, where smaller errors in the flux measurement lead to larger uncertainties in the determination of the radius.

We produced the same plots, but with the Sérsic index from the bulge component only for our much smaller sample of 45 galaxies. This is shown in Fig. 2.5. The two plots in this figure suggest that $C_{20,50}$ indicates how much the light or mass of the bulge in a given galaxy is centrally concentrated and it does so better than $C_{50,90}$. The difference is less noticeable than in Fig. 2.4, but still existent (The upper panel shows a Spearman's rank of $\rho = -0.66$, while for the lower panel we measure $\rho = -0.60$). It is also striking that bulgeless galaxies cover a wide range of concentration values when one uses $C_{50,90}$, but are confined to low values when one uses $C_{20,50}$, more in line with the fact that these galaxies have no bulges. This also favours our use of $C_{20,50}$ over $C_{50,90}$ as a reliable bulge parameter.

Pseudobulges were suggested to be more frequent in late-type galaxies whereas classical bulges are more often found in early types (e.g. Kormendy & Kennicutt, 2004). It is therefore interesting to investigate how our $C_{20,50}$ relates to the morphological type. Figure 2.6 shows this relation for the complete CALIFA mother sample. We observe a relatively flat distribution for all elliptical galaxies followed by a continuous decrease in concentration (higher values in $C_{20,50}$) from S0 to Sc, where we find the minimum in the distribution of the concentration, and finally there is a slight increase towards very late types. These results are in line with the expectation given the classification criteria

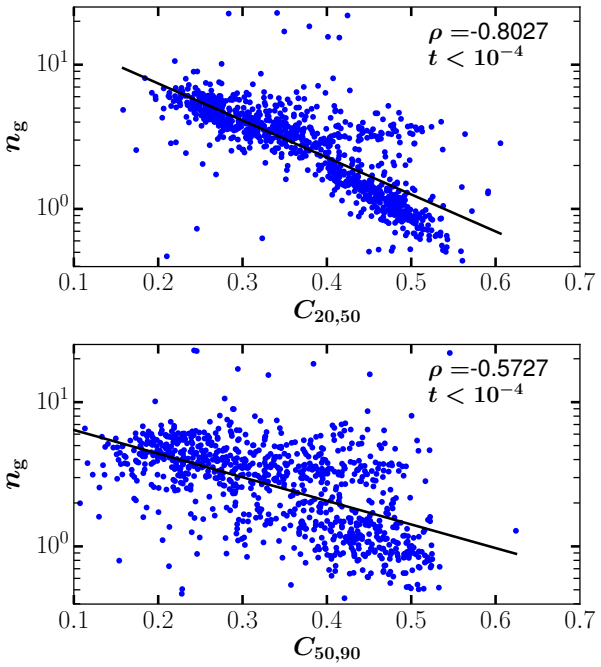

Figure 2.4: Anti-correlation between $\log(n_g)$ and $C_{20,50}$ (upper panel) and $C_{50,90}$ (lower panel). The Spearman's rank correlation coefficient ρ and the value of the null hypothesis significance test t are given in the figure.

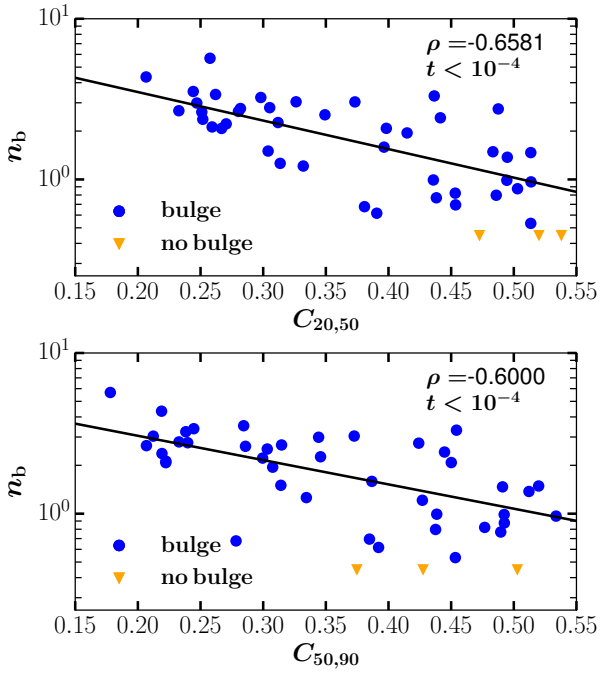

Figure 2.5: Anti-correlation between $\log(n_b)$ and $C_{20,50}$ (upper panel) and $C_{50,90}$ (lower panel). The Spearman's rank correlation coefficient ρ and the value of the null hypothesis significance test t are given in the figure. Bulgeless galaxies are marked by orange triangles for comparison. The y-axis value of the bulgeless galaxies is set to a randomly chosen value for display purposes.

of the morphological types. The increase in concentration for very late types might be surprising, however, the sample statistics are getting lower for these categories. We would like to point out the median concentration for Sb galaxies $\langle C_{20,50} \rangle = 0.398$. Kormendy & Kennicutt (2004) found a sharp transition between the ocurrence of classical bulges and pseudobulges at Hubblte type Sb. Completely independently, we decided to use $C_{20,50} = 0.4$ as demarcation between bulges and inner discs in Sect. 2.5.1 based only on the correlation with other classification criteria. The almost perfect agreement reinforces our decision to use $C_{20,50} = 0.4$ for separating inner discs from classical bulges.

We caution the reader to be aware of the difference between concentration indices derived from growth curve measurements and those extracted from within Petrosian radii. In Appendix 2.A we show the relation between both approaches and provide a conversion factor between our concentration index $C_{20,50}$ and the associated Petrosian concentration.

2.4.2 Structural properties

In this subsection we present bulge and disc component parameters derived from the 2D image decomposition. We show in Fig. 2.7 the relation between bulge-to-total light ratio (B/T) and concentration index $C_{20,50}$. A clear correlation can be seen in the sense that more bulge-dominated galaxies have higher concentrations, reflected as lower values of $C_{20,50}$. This is what one would expect from a theoretical point of view, but the strength of the correlation with a Spearman's rank of $\rho = -0.86$ is surprising and encourages even more the use of $C_{20,50}$ as preferable concentration index.

Additionally, we divided the objects in the upper panel into low-n_b ($n_b \leq 1.5$) and high-n_b ($n_b > 1.5$) galaxies and we observe that the low-n_b galaxies do not populate the region of $C_{20,50} < 0.3$ and $\log(B/T) > -0.5$ and only one outlier has $\log(B/T) > -0.75$. This is an indication that pseudobulges correspond to low B/T fractions.

The lower panel shows the same plot, but the galaxies are separated by $n_b = 2$, a value that has more commonly been used in the literature for bulge separation. With this approach we see a slightly higher fraction of low-n_b galaxies in the region of high concentration and high bulge fraction, which is expected to be populated by classical bulges. A further comparison of both choices with all following bulge diagnostics showed that the bulges of our sample with a Sérsic index between 1.5 and 2.0 are more likely to be classical bulges. We therefore choose $n_b = 1.5$ over $n_b = 2$ as boundary between low- and high-n_b galaxies for the rest of the paper.

2.4.3 Kormendy relation

The Kormendy (1977) relation is a relationship between effective radius r_e and mean effective surface brightness $\langle \mu_e \rangle$ that has been found for elliptical galaxies. It has been used by Gadotti (2009) and Fisher & Drory (2010) to study the location of bulges in a projection of the fundamental plane (Djorgovski & Davis, 1987; Dressler et al., 1987). The authors of both works found that pseudobulges tend to have

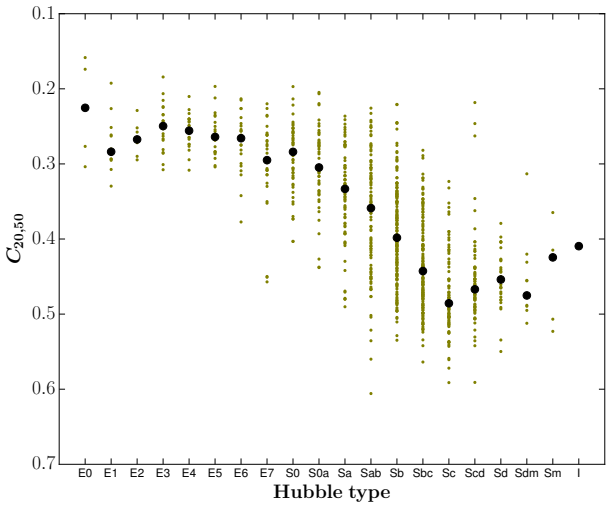

Figure 2.6: Relation between $C_{20,50}$ and morphological type for the complete CALIFA mother sample. Median values for each type are marked by big black dots.

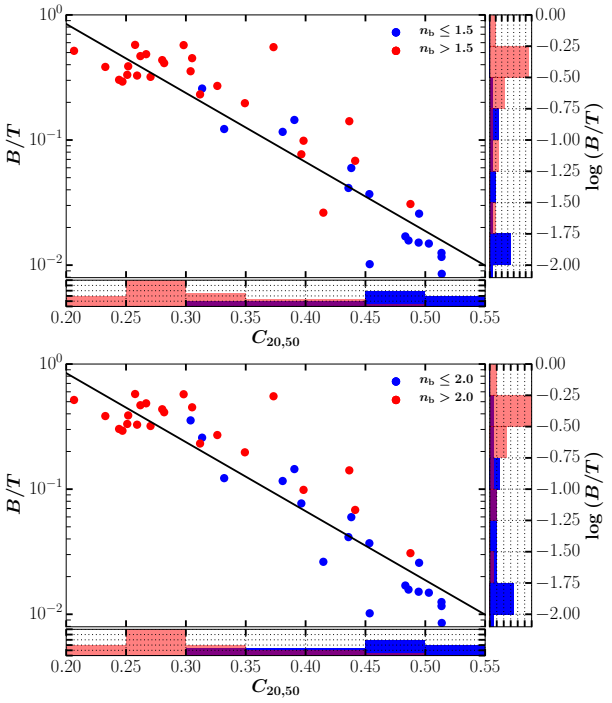

Figure 2.7: Anti-correlation between $\log(B/T)$ and $C_{20,50}$. Blue and red colours correspond to low- and high-n_b values of the associated bulge component. The upper and lower panels compare two different boundaries chosen to separate bulge Sérsic indices. The histograms on the right side show the distribution of the sample in equidistant bins in logarithmic space of B/T. The histograms on the lower side show the distribution of the concentration index.

lower surface brightness than classical bulges or elliptical galaxies of similar sizes. Gadotti (2009) even favoured this criterion for the identification of pseudobulges over the Sérsic index or the bulge-to-total light ratio.

In Fig. 2.8 we present the Kormendy relation for our sample. We observe a relatively clear separation of three independent groups: Ellipticals, high-n_b and low-n_b bulges in the upper panel and ellipticals, low and high concentration galaxies in the lower panel. Nearly all bulges that would be classified as classical based on the Sérsic index and concentration are located within the 2-σ boundaries of the relation found for elliptical galaxies and allmost all pseudobulges are below the relation. The overlap between the two types of bulges is marginal. A co-location with the Kormendy relation demonstrates the similarity of the structure of these bulges with elliptical galaxies. We see that both classifications agree very well with the Kormendy relation criterion. In addition, Fig. 2.8 also indicates that using n_b and $C_{20,50}$ for classifying bulges should yield statistically similar results, a point worth noting, given that $C_{20,50}$ is much more straightforward to derive.

The results confirm the value of the Kormendy relation for bulge diagnostics and we use it in Sect. 2.5.1 for the overall classification.

2.4.4 Faber-Jackson relation

Some bulges of late-type galaxies have been reported to be low-σ outliers from the Faber & Jackson (1976) relation (Kormendy & Kennicutt, 2004). In Fig. 2.9 we present the relation of central velocity dispersion σ_0 with absolute r-band magnitude $M_{r,b}$ of the bulge component for our sample and we added again the subsample of elliptical galaxies from CALIFA to fit the Faber-Jackson relation for ellipticals ($L \propto \sigma_0^\gamma$). In the upper panel we distinguish again between low-n_b and high-n_b galaxies, whereas in the lower panel we divide the galaxies based on the concentration index. We define the central velocity dispersion as the mean velocity dispersion within 1″. This is calculated using the binned radial profiles of σ.

We do not observe any low-σ outliers from the Faber-Jackson relation. In fact, all bulges – independent of their concentration or their shape of the surface brightness profile – do align with the elliptical galaxies within the normal range of scatter. This means that either all bulges have a physical similar structure to the elliptical galaxies and are not inner discs, or the Faber-Jackson relation is not a good instrument to separate inner discs from classical bulges. We believe that the latter is the case. It has been reported that the spread in this relation is usually large and a co-location with the elliptical galaxies does not mean that the object is a classical bulge (e.g. Fisher & Drory, 2016). Moreover, for almost all bulges the Sérsic index and the concentration index agree very well with the concept of having a different physical nature as seen in the Kormendy relation. This indicates that the central velocity dispersion is probably more related to the total mass of the galaxy and not the central component alone. We should instead analyse the radial distribution of the velocity dispersion.

2.4.5 Velocity dispersion gradient

When measuring the velocity dispersion profile it is important to keep in mind that it can be affected in the central region by limits in the spatial resolution. The innermost values would be smeared out to a flat profile.

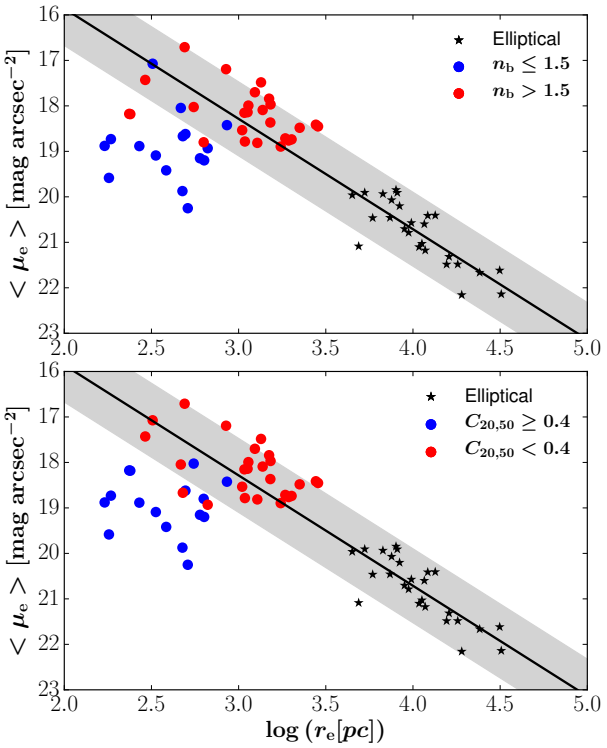

Figure 2.8: Mean effective surface brightness within the effective radius vs. logarithm of the effective radius for bulges and ellipticals. The Kormendy relation is represented by a fit to the elliptical galaxies. The grey shaded region marks the $\pm 2\sigma$ boundaries. The only difference between the two panels is the colour coding. The upper panel shows a separation of the bulges by the Sérsic index, the lower panel shows a separation according to the concentration index. The resemblance between the two plots demonstrates the equal usability of the two parameters n_b and $C_{20,50}$ for bulge classification.

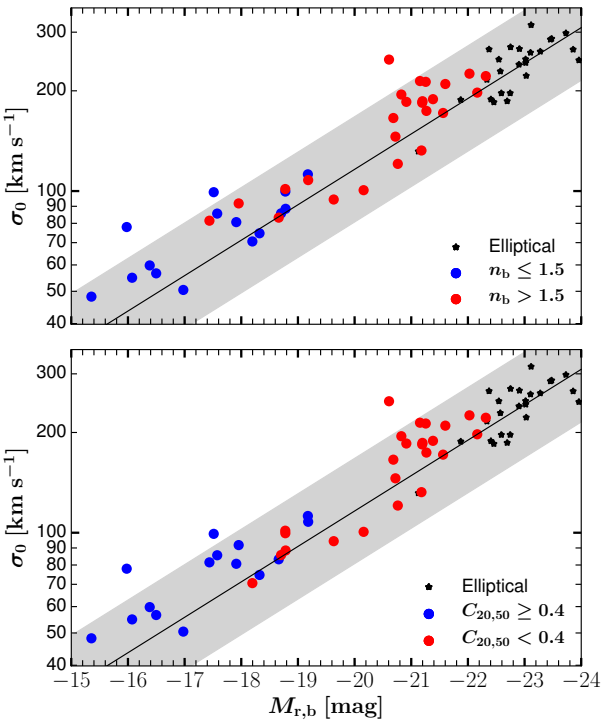

Figure 2.9: Central velocity dispersion vs. absolute r-band magnitude for bulges and ellipticals. The Faber-Jackson relation is represented by a fit to the elliptical galaxies. The grey region indicates the $\pm 3\sigma$ boundaries. Blue and red points show the bulge separation by n_b (upper panel) and $C_{20,50}$ (lower panel).

Gadotti (2008) showed that the structural properties of galaxies can be reliably determined, if the effective radius is larger than 0.8 times the half width at half maximum (HWHM) of the point spread function (PSF). This criterion was estimated for photometric approaches by fitting two-dimensional galaxy images. In spite of that, it should be adaptable for spatially resolved kinematic analyses. The median PSF FWHM of our galaxies is $\approx 2.4''$ (García-Benito et al., 2015). Only four of our galaxies have $r_e \leq 0.96'' = 0.8 \times 1.2''$. They are included in the following figures, but marked as probably unresolved.

In Fig. 2.10 we present the relation between stellar velocity dispersion gradient $\nabla\sigma$ in the bulge region and bulge Sérsic index. The gradient is derived from the radial velocity dispersion profile by first normalising it to the bulge radius rb_{90} and the central velocity dispersion σ_0 and then fitting a linear function to the velocity dispersion within the bulge radius. During the regression process we weight the data values by the associated uncertainties. We denote the slope of that function as $\nabla\sigma$.

We find an anti-correlation between $\nabla\sigma$ and n_b and a correlation between $\nabla\sigma$ and $C_{20,50}$. Low-n_b (high-$C_{20,50}$) bulges have approximately flat profiles whereas high-n_b (low-$C_{20,50}$) bulges have slopes as steep as $\nabla\sigma \approx -0.7$. This result is in good agreement with findings from Fabricius et al. (2012). They observed rather flat profiles for pseudobulges and centrally peaked profiles for classical bulges.

However, these relations must be considered carefully, since they may be significantly influenced by bulge size alone. Let us assume, for example, that all galaxies had identical centrally peaked velocity dispersion profiles, but different bulge sizes. Small bulges would then have comparatively small values for $\nabla\sigma$ whereas for larger bulges we would measure a larger decrease in σ, solely because of the normalisation of the radial profile to the bulge radius. Hence, the distribution of bulge radii alone can theoretically produce the observed relations. As a matter of fact, pseudobulges are usually smaller than classical bulges and there is a correlation between Sérsic index and bulge size. The imprint of the bulge size on the anti-correlation between $\nabla\sigma$ and n_b is thus inevitable.

An alternative is to define a radius that is independent of the bulge, in which we fit the velocity dispersion profile. Figure 2.11 shows the global radial velocity dispersion profiles for all galaxies of the sample averaged within three different groups: low-n_b, high-n_b and bulgeless galaxies. The y-axis is normalised by the velocity dispersion at $0.5\times$ r_{90} and the x-axis by the r_{90} parameter derived from the growth curves, that is, the radius that encloses 90% of the total light of the galaxy. This radius covers the major part of the galaxy and is located far outside the bulge. We note that not all galaxies have kinematic coverage up to r_{90}. The bulgeless galaxies show flat profiles throughout most of

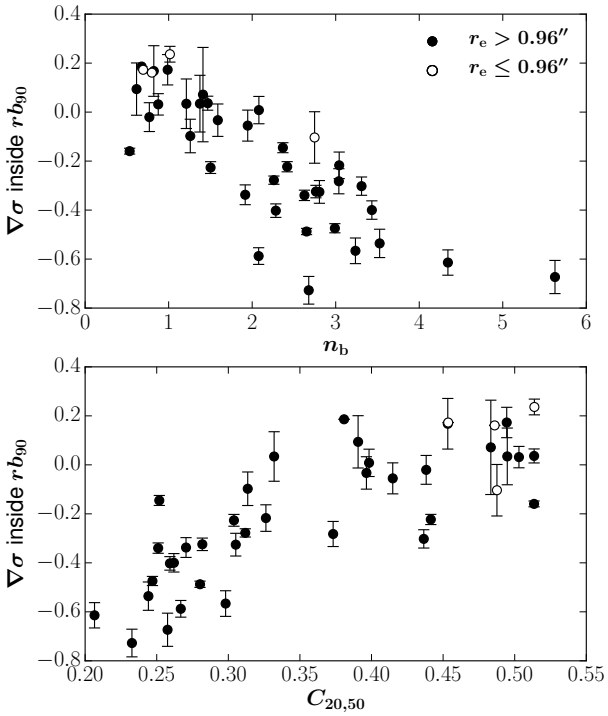

Figure 2.10: Upper panel: anti-correlation between the velocity dispersion gradient inside the bulge radius rb_{90} and the bulge Sérsic index n_b. Lower panel: correlation between the velocity dispersion gradient with the concentration index $C_{20,50}$. The Spearman's rank correlation coefficient is $\rho = -0.80$ in the upper panel and $\rho = 0.81$ in the lower panel. Empty circles mark the bulges that are not well resolved. The error bars indicate the uncertainty of the fit of the velocity dispersion profile.

the radial extent. Galaxies with low-n_b bulges show on average profiles that increase towards the centre by $\approx 20\%$, but are close to flat in the inner $\approx 0.15 \times r_{90}$. Galaxies with high-$n_b$ bulges show a stronger increase up to $\approx 60\%$ with the steepest part in the most central region.

This figure confirms the same trend that we have seen before. The central parts of galaxies with classical bulges tend to have centrally peaked velocity dispersion profiles whereas galaxies that host pseudobulges have profiles that are rather centrally flat, partly similar to the profiles shown by bulgeless galaxies.

In order to quantify the observed trend in the central region of the velocity dispersion profiles, the slope within $0.15 \times r_{90}$ was calculated. The choice of that radius is a compromise between not being too small and lose too much information on the larger bulges and not being too large and then contaminated by too much disc light where bulges are small. We remind the reader that we want to measure the behaviour of the velocity dispersion profile in the central region of disc galaxies, but without being affected by the bulge size. The result is shown in Fig. 2.12 as compared to n_b and $C_{20,50}$, respectively. We see the same trend as before, but with only a mild correlation coefficient of $\rho = -0.53$ in the upper panel and $\rho = 0.64$ in the lower panel and a fair amount of scatter that we will discuss in Sect. 2.5. Furthermore, we observe that bulgeless galaxies (pure discs) behave in this figure like pseudobulges (inner discs) as expected.

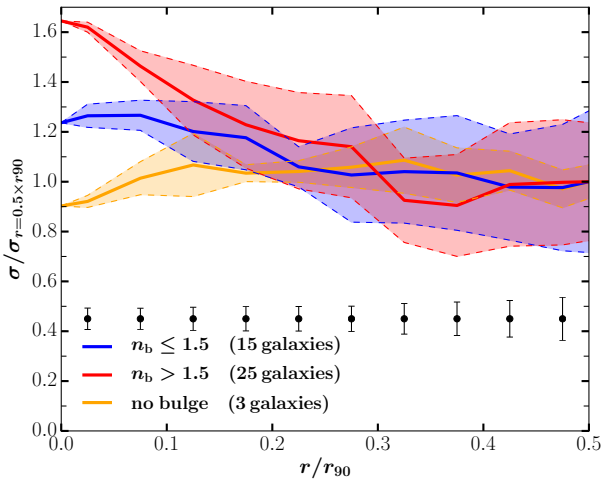

Figure 2.11: Average radial velocity dispersion profiles for low-n_b (blue), high-n_b (red) and bulgeless (orange) galaxies. The thick solid lines represent the median profiles and the dashed lines the median absolut deviations. The velocity dispersion is normalised by σ at $r = 0.5 \times r_{90}$ and the radial distance is normalised by r_{90} – the radius that encloses 90% of the total light of the galaxy. Error bars at the bottom indicate the median uncertainty for each $0.05 \times r_{90}$ bin.

We statistically evaluate the results further in Fig. 2.13, where we show a box plot for low- and high-n_b galaxies. The median $\nabla\sigma$ for low-n_b galaxies is at -0.05 and for high-n_b galaxies at -0.25. The interquartile ranges for both populations are separated with one lower quartile limit coinciding approximately at -0.18 with the other upper quartile limit. If we choose $\nabla\sigma = -0.18$ to divide the bulges into two subsamples we are essentially separating low- and high-n_b bulges by a completely independent method. Following this, we have established a kinematic approach to isolate pseudobulges from classical bulges that we use in combination with traditional and new photometric parameters in Sect. 2.5.1 to classify bulges.

2.5 Discussion

2.5.1 A recipe for separating inner discs from classical bulges

The classification of galaxy bulges into classical bulges (presumably built from violent processes such as mergers), and pseudobulges (thought to be built from dynamical instabilities in the major disc) has become a common task in extragalactic astrophysics, yet there is still no unambiguous way of doing it. While the bulge Sérsic index is probably the most frequently used criterion for bulge type diagnostics in literature, it has been shown to be prone to misclassifications in some cases. Other criteria have been proposed, but the general consensus is that no single criterion should be used alone. For an overview we refer the reader to Kormendy & Kennicutt (2004), Athanassoula (2005) or the very recent review by Fisher & Drory (2016).

As mentioned in the introduction, we use the term 'pseudobulge' to describe the discy bulges in our sample, not only for historical reasons but also because the term

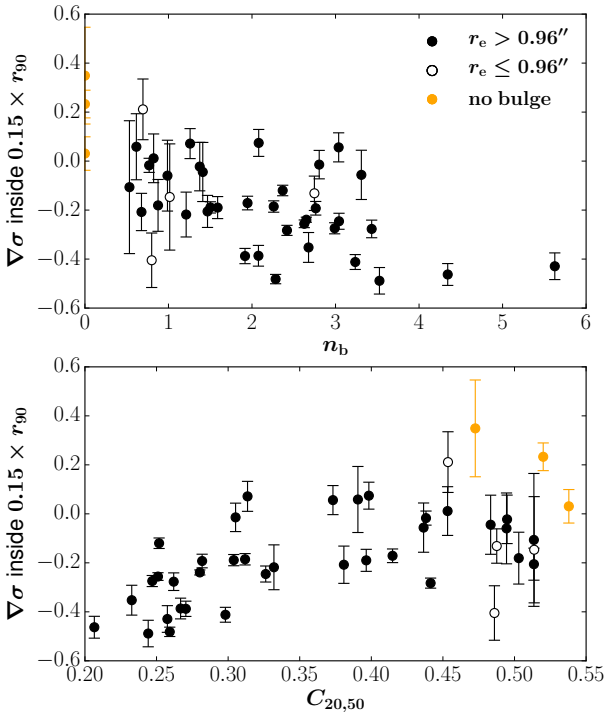

Figure 2.12: Upper panel: anti-correlation between the velocity dispersion gradient inside $0.15 \times r_{90}$ – the radius that encloses 90% of the total light of the galaxy – and the bulge Sérsic index n_b. Lower panel: correlation between the velocity dispersion gradient with the concentration index $C_{20,50}$. The Spearman's rank correlation coefficient is $\rho = -0.53$ in the upper panel and $\rho = 0.64$ in the lower panel. Bulgeless galaxies are marked in orange. Empty circles mark the bulges that are not well resolved. The error bars indicate the uncertainty of the fit of the velocity dispersion profile.

has been largely adopted by the astrophysical community. With this word we are referring to inner discs built from disc material through secular evolution. In this subsection we are trying to give a recipe to separate them from classical bulges. We strongly encourage the use of a combination of photometric and kinematic bulge parameters for a 'safe' classification. In this work we analysed and compared different approaches and determined four parameters that can be used for bulge diagnostics: The bulge Sérsic index n_b, the concentration index $C_{20,50}$, the central velocity dispersion gradient $\nabla\sigma$ and the Kormendy relation.

We decided not to use the B/T light ratio as classification criterion. Considering that pseudobulges are thought to be built from disc material, they are expected to be small fractions of their host galaxies, in contrast to classical bulges which are probably relics from merger events and independent from the disc. Observations confirm that galaxies with pseudobulges have on average smaller B/T light ratios, but they also show that there is a significant overlap (e.g. Drory & Fisher, 2007; Fisher & Drory, 2008; Gadotti, 2009). There is no physical reason for a lower limit of B/T for classical bulges. Hence, the bulge-to-total light ratio can be used for reference, but it should not be included to separate inner discs from classical bulges.

Table 2.1 presents our classification of 45 CALIFA galaxies. It contains all galaxies of the sample classified

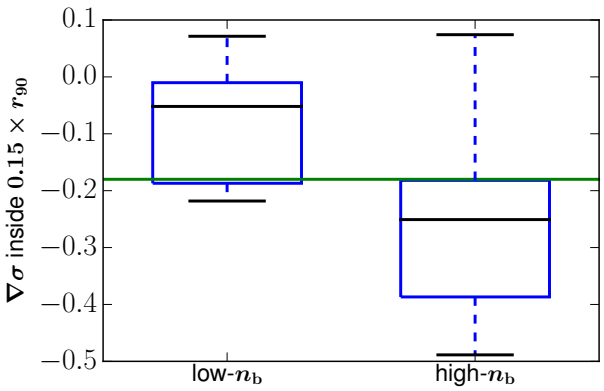

Figure 2.13: Velocity dispersion gradient inside $0.15 \times r_{90}$ for high- and low-n_b galaxies. The blue box marks the interquartile range of the sample, the black line in the box gives the median value. The top and bottom black line stand for the highest and lowest value, respectively. The thick green line at $\nabla\sigma = -0.18$ gives a good demarcation to separate the subsamples based on the velocity dispersion gradient.

by our four different criteria. As mentioned earlier, there are three bulgeless galaxies within the sample and two galaxies have no kinematic data.

The following rules were applied to separate between pseudobulges (*ps*) and classical bulges (*cl*):

$$\text{Sérsic index:} \begin{cases} \text{ps} & \text{if} \quad n_b \leq 1.5 \\ \text{cl} & \text{if} \quad n_b > 1.5 \end{cases}$$

$$\text{Concentration index:} \begin{cases} \text{ps} & \text{if} \quad C_{20,50} \geq 0.4 \\ \text{cl} & \text{if} \quad C_{20,50} < 0.4 \end{cases}$$

$$\text{Velocity dispersion:} \begin{cases} \text{ps} & \text{if} \quad \nabla\sigma \geq -0.18 \\ \text{cl} & \text{if} \quad \nabla\sigma < -0.18 \end{cases}$$

$$\text{Kormendy relation:} \begin{cases} \text{ps} & \text{if the bulge lies below and} \\ & \text{outside } \pm 2\sigma \text{ of the relation} \\ & \text{for elliptical galaxies} \\ \text{cl} & \text{if the bulge lies within} \\ & \text{the } \pm 2\sigma \text{ range} \end{cases}$$

The final classification is built upon a consensus of these parameters. If three out of four criteria agree, we consider the bulge to be safely classified. The division into classical bulges and pseudobulges is an interpretation of these results based on the agreement between the parameters and their physical meaning.

Out of 42 galaxies that host bulges we could reliably classify 40 (95%). Our sample contains at least 16 pseudobulges and 24 classical bulges. If we assume the 40 'safe' classifications to be 'correct'[3], than we can state that the Kormendy relation is the best criterion by achieving 39 out of 40 correct classifications, closely followed by the concentration index $C_{20,50}$ with 38. The velocity dispersion gradient shows the largest amount of scatter among

[3]Since the 'true' physical nature of the bulges is unknown, the parameter performances that we evaluate in this section should be interpreted as relative to each other and not absolute.

the classifiers misclassifying seven bulges.

As seen in Sect. 2.4.5 and also discussed in Sect. 2.5.2 it still remains a difficult task to measure the velocity dispersion distribution accurately. However, despite the fact that it is indeed the weakest of the four criteria in our analysis, it is still strong and yields 82% correct classifications. This means that it was possible to successfully classify 82% of the bulges in our sample using only measurements of the velocity dispersion.

The complexity of galaxy structure and dynamics makes simple classification methods virtually impossible, but by using a combination of photometric and spectroscopic parameters we were able to successfully separate most of the classical bulges from inner discs. We provide in Table 2.1 a classification for a subsample of CALIFA galaxies that can be used for future investigation. We propose the usage of our combined approach as recipe for the diagnostic and separation of galaxy bulges.

2.5.2 Acquisition of kinematic bulge parameters

The traditional picture of a bulge being only a dynamically hot central component that adds an elliptical-like de Vaucouleurs light distribution to the surface brightness profile of the surrounding disc has long been shown to be obsolete. Too much discrepancy has been found between this scenario and observational evidence. A dichotomy of bulges was observed instead. For many galaxies the extra light in the central region was found to follow rather an exponential law, the geometrical appearance was flattened by rotation and disc-like structures like nuclear spirals and nuclear bars were observed. Since then, extensive work has been done and numerous bulge classification criteria have been proposed. Yet the kinematic distinctness of the bulge types could still not been quantified satisfactorily – despite being known over more than three decades (Kormendy & Illingworth, 1982). Fabricius et al. (2012) showed with convincing observational evidence using long-slit spectroscopy that dynamics are indeed part of the bulge dichotomy. Similar results were obtained for a few galaxies by Méndez-Abreu et al. (2014) with IFS data.

In this paper we tried to address this kinematic problem with a larger set of galaxies with IFS observations from the CALIFA survey. We have found similar results to those from previously mentioned works. The stellar radial velocity dispersion gradient is close to flat for pseudobulges and centrally peaked for classical bulges. We see that it is, thus, not only the light profile of a pseudobulge that shows disc similarity, but also the stellar velocity dispersion that resembles disc behaviour. The question is how to quantify what we deduce from the visual inspection of the profiles.

In Fig. 2.10 the gradient of the velocity dispersion profile calculated in the bulge region is plotted versus the bulge Sérsic index and the light concentration. A similar approach has been used by Fabricius et al. (2012). A clear correlation can be seen in that plot, but it has two major caveats: 1) Since the velocity dispersion does not follow a linear profile, the derived slope inside the bulge region depends strongly on the bulge radius. That, on its part, is usually bigger for classical bulges and smaller for pseudobulges, albeit not exclusively. Consequently, the velocity dispersion gradient when derived exactly over the bulge extent is automatically connected to the bulge type. A parameter that is independent from the size of the bulge is desirable. 2) The bulge radii of some pseudobulges are close to the spatial resolution limit of the CALIFA data, whereas all classical bulges are big enough to be very well resolved. Hence, some parts of the bulge-dominated region of these pseudobulges are smeared out to flat profiles.

We tried to address the first problem in Fig. 2.12 by choosing another radial aperture for measuring the velocity dispersion gradient. The radial limit $0.15 \times r_{90}$ ranges between 5″ and 13″ – well beyond the CALIFA PSF FWHM. Using this limit instead of either the bulge radius or, for example, r_{20} has the advantage of being likely not correlated to the bulge size, since it is a fraction of the radius that captures 90% of the total light of the galaxy. At the same time we are ensuring with this approach that we have enough resolution elements within that region.

It is important to keep in mind that Fig. 2.12 tells us about the behaviour of the velocity dispersion profile in the central part of the galaxy and not specifically in the bulge region. The different coverage of the bulge-disc regions – that we caused intentionally – could introduce some additional scatter in that relation.

Pseudobulges are expected to be small objects with low velocity dispersion. Hence, in order to identify pseudobulges reliably, high spectral and spatial resolution is required. Despite the great advantage of IFS observations from surveys like MaNGA (Mapping Nearby Galaxies at APO, Bundy et al., 2015) or SAMI (Sydney-Australian-Astronomical-Observatory Multi-object Integral-Field Spectrograph survey, Croom et al., 2012) to have spectral information over a two-dimensional area on the sky, there is still a deficiency of spatial resolution as compared to data from photometric surveys. CALIFA has the advantage over SAMI and MaNGA to provide a better physical spatial resolution given the lower redshifts by similar projected resolution. As shown in this work, it allowed for a classification of 82% of the bulges using exclusively kinematics.

A separation of bulge types based on their kinematics would physically be a quite convincing approach, since pseudobulges presumably being essentially inner discs should resemble the behaviour of the surrounding discs whereas classical bulges should be observed as hot elliptical-like components. It is therefore desirable to use IFU instruments with even larger spatial resolution such as MUSE (Multi-Unit Spectroscopic Explorer, Bacon et al., 2010) to further decrease the uncertainties of kinematic measurements of bulges.

Table 2.1: Overview of bulge classification.

ID	NED name	B/T	n_b	$C_{20,50}$	$\nabla\sigma$	Kormendy rel	Classification
			≤ 1.5	≥ 0.4	≥ -0.18	low-outlier	
(1)	(2)	(3)	(4)	(5)	(6)	(7)	(8)
2	UGC00005	0.01	ps	ps	cl	ps	pseudo
3	NGC7819	0.12	ps	cl	cl	ps	
6	NGC7824	0.38	cl	cl	cl	cl	classical
8	NGC0001	0.41	cl	cl	cl	cl	classical
20	NGC0160	0.29	cl	cl	cl	cl	classical
31	NGC0234	0.04	ps	ps	ps	ps	pseudo
33	NGC0257	0.10	cl	cl	ps	cl	classical
43	IC1683	0.12	ps	cl	cl	cl	classical
45	NGC0496	bulgeless	bulgeless	ps	ps	bulgeless	bulgeless
47	NGC0517	0.55	cl	cl	ps	cl	classical
119	NGC1167	0.23	cl	cl	cl	cl	classical
147	NGC2253	0.08	cl	cl	cl	cl	classical
275	NGC2906	0.14	cl	ps	ps	ps	pseudo
277	NGC2916	0.07	cl	ps	cl	cl	classical
311	NGC3106	0.30	cl	cl	cl	cl	classical
489	NGC4047	0.03	cl	ps	ps	ps	pseudo
548	NGC4470	bulgeless	bulgeless	ps	ps	bulgeless	bulgeless
580	NGC4711	0.02	ps	ps	ps	ps	pseudo
607	UGC08234	0.58	cl	cl	cl	cl	classical
611	NGC5016	0.01	ps	ps	ps	ps	pseudo
715	NGC5520	0.26	ps	cl	ps	cl	
748	NGC5633	bulgeless	bulgeless	ps	ps	bulgeless	bulgeless
768	NGC5732	0.04	ps	ps	no data	ps	pseudo
769	UGC09476	0.03	ps	ps	ps	ps	pseudo
778	NGC5784	0.39	cl	cl	ps	cl	classical
821	NGC6060	0.06	ps	ps	ps	cl	pseudo
823	NGC6063	0.01	ps	ps	ps	ps	pseudo
826	NGC6081	0.35	cl	cl	cl	cl	classical
836	NGC6155	0.01	ps	ps	ps	ps	pseudo
849	NGC6301	0.01	ps	ps	cl	ps	pseudo
850	NGC6314	0.33	cl	cl	cl	cl	classical
856	IC1256	0.03	cl	ps	ps	ps	pseudo
858	UGC10905	0.52	cl	cl	cl	cl	classical
874	NGC7025	0.44	cl	cl	cl	cl	classical
877	UGC11717	0.20	cl	cl	no data	cl	classical
886	NGC7311	0.32	cl	cl	cl	cl	classical
889	NGC7364	0.45	cl	cl	ps	cl	classical
891	UGC12224	0.02	ps	ps	ps	ps	pseudo
898	NGC7489	0.02	ps	ps	cl	ps	pseudo
912	NGC7623	0.49	cl	cl	cl	cl	classical
913	NGC7625	0.14	ps	cl	ps	ps	pseudo
915	NGC7653	0.27	cl	cl	cl	cl	classical
916	NGC7671	0.33	cl	cl	cl	cl	classical
917	NGC7683	0.57	cl	cl	cl	cl	classical
923	NGC7711	0.47	cl	cl	cl	cl	classical

(1) CALIFA ID, (2) NED name, (3) bulge-to-total light ratio, for reference. We list four different bulge classification criteria in column 4-7: (4) bulge Sérsic index, (5) concentration index, (6) central velocity dispersion gradient, (7) Kormendy relation. (8) Final classification: In the last column we assign each bulge a final classification if and only if at least three out of four criteria are in agreement. With 'pseudo' we are referring to the inner disc of galaxies built through secular evolution, as explained in more detail in the text. The second line of the head of the table shows the boundaries that we have defined to demarcate pseudobulges. If a value of a specific cell in column 4-7 is within these limits it is annotated as 'ps', otherwise it is 'cl', which refers to 'pseudobulge' and 'classical bulge', respectively. The 3 bulgeless galaxies are annotated in column 3, 4 and 7. Two galaxies have no kinematic data, and thus no value in column 6.

2.5.3 Introducing a new concentration index: $C_{20,50}$

The radial light distribution of a galaxy disc is best described by either a single-exponential (Type I) or double-exponential (Type II and Type III) profile. Any additional baryonic component adds light to this distribution. The presence of a bulge can thus be observed by an excess of light in the central part of the galaxy. Classical bulges are usually – but not exclusively – more luminous and in itself more concentrated than pseudobulges. It might seem obvious that one of the first things to do in order to identify and classify bulges is to measure the concentration. The result, however, depends strongly on the method and parametrisation. It is possible to define a concentration index as 1) ratio between two radii that enclose certain percentages of the total light of the galaxy (e.g. r_{50}/r_{25}, r_{75}/r_{50}, r_{75}/r_{25}, r_{80}/r_{20}, de Vaucouleurs, 1977; Kent, 1985) or as 2) ratio of the flux between two correlated isophotes (Doi et al., 1993; Abraham et al., 1994; Trujillo et al., 2001). The final value will also depend on whether the flux was measured within a Petrosian aperture or within the complete extent on the galaxy based on growth curve analysis, as shown in Appendix 2.A.

In this work we have demonstrated the capability of the concentration index defined as $C_{20,50} = r_{20}/r_{50}$ to diagnose the bulge type with great accuracy: 38 out of 40 correct classifications following the recipe in Sect. 2.5.1. We have shown a strong correlation with the logarithm of the global Sérsic index of the galaxy: Spearman's rank correlation coefficient $\rho = -0.80$, and we found correlations with bulge Sérsic index, bulge-to-disc light ratio, Kormendy relation and velocity dispersion gradient. Based on these results, it is evident that $C_{20,50}$ is a powerful indicator of the bulge nature. We thus encourage the use of this index over the widely used r_{90}/r_{50} as it seems to track a more bulge related part of the light distribution of the galaxy.

2.6 Conclusions

In this paper, we derived a set of different photometric and spectroscopic parameters that can be used to separate inner discs from bulges. For that purpose we used growth curve measurements and performed detailed 2D image decomposition of SDSS *r*-band images and spectral fitting to CALIFA IFU data cubes.

We demonstrated that the radial velocity dispersion profile of galaxies can be used to discriminate between pseudobulges and classical bulges. We cautioned on using the bulge radius, which is not independent from the bulge type, to normalise the radial profile. Instead, we found a different quantification of the velocity dispersion based on the global profile that can be used to classify bulges.

We promote the concentration index, defined as $C_{20,50} = r_{20}/r_{50}$, the ratio of the radii that enclose 20% and 50% of the total light of the galaxy, respectively. It correlates well with the widely used bulge Sérsic index n_b and yields statistically similar results when used for bulge classification. We encourage the usage of $C_{20,50}$ given that it is a parameter that can be derived with very little effort.

We showed that the concentration index $C_{20,50}$ and the Kormendy relation are the best classification criteria by achieving over 95% correct classifications (based on the agreement with the other criteria) following our recipe in Sect. 2.5.1. When used in combination, these two criteria should yield a robust indication of the nature of bulges. However, it is important to remember that none of the criteria can undoubtfully separate bulges from inner discs. The more criteria are used, the safer the classification becomes.

We propose a recipe based on four parameters from photometry and spectroscopy to classify bulges. The different parameters are in good agreement and allow a safe classification for approximately 95% of the galaxies.

By using this recipe we provided a detailed bulge classification for a subsample of 45 galaxies from the CALIFA survey. Future IFU surveys should be used to further increase the accuracy and reliability of spectroscopic analyses that are of great importance to unveil the true nature of bulges.

Acknowledgements This study makes uses of the data provided by the Calar Alto Legacy Integral Field Area (CALIFA) survey (http://www.califa.caha.es). Based on observations collected at the Centro Astronómico Hispano Alemán (CAHA) at Calar Alto, operated jointly by the Max-Planck-Institut fur Astronomie and the Instituto de Astrofísica de Andalucía (CSIC). CALIFA is the first legacy survey being performed at Calar Alto.The CALIFA collaboration would like to thank the IAA-CSIC and MPIA-MPG as major partners of the observatory, and CAHA itself, for the unique access to telescope time and support in manpower and infrastructures. The CALIFA collaboration thanks also the CAHA staff for the dedication to this project. We thank the anonymous referee for a careful reading and several comments that helped to improve the paper. RGB and RGD acknowledge support from grants AYA2014-57490-P and JA-FQM-2828. RAM acknowledges support by the Swiss National Science Foundation. IM acknowledges financial support from grants AYA2013-42227-P and AYA2016-76682-C3-1-P. SFS thanks the CONACYT-125180, DGAPA-IA100815 and DGAPA-IA101217 projects for providing him support in this study.

2.A Relation between the Petrosian concentration index and our $C_{20,50}$

The Petrosian radius R_p is defined to be the radius where the Petrosian function $\eta(R)$ equals some fixed value. The Petrosian function gives the average intensity within some projected radius divided by the intensity at that radius. Different multiples of R_p have been used to measure galaxy magnitudes, but they generally underestimate the total flux of the galaxy. Thus any radius r_k, where r_k encloses k percent of the total flux, is also underestimated. Graham et al. (2005) offers correction factors for magnitudes, half-light radii and surface brightness. To provide such a correction factor one has to assume a specific surface brightness distribution of the galaxies. The easiest approach is a single Sérsic profile, which as we know is a precarious simplification for most galaxies. If we adopt from the SDSS consortium the practice of measuring the flux within $2\times R_p$ and $1/\eta(R_p) = 0.2$, we can directly integrate the light profiles and derive the concentration index as a function of n. The discrepancy between the Petrosian concentration index and the concentration derived from integrating the Sérsic function to infinity is illustrated in Fig. 2.14. The conversion factor between our concentration index $C_{20,50}$ and the associated Petrosian concentration can be approximated by

$$C_{20,50}\,(\mathrm{gc}) = a_0 + a_1\,C_{20,50}\,(\mathrm{petro}) + a_2\,C_{20,50}\,(\mathrm{petro})^2, \tag{2.1}$$

where $a_0 = -0.23$, $a_1 = 1.92$ and $a_2 = -0.90$. We emphasise that this approximation is under the assumption that the light profile is well described by a Sérsic function and that the 'edge' of the galaxy is accurately derived from the growth curve measurement.

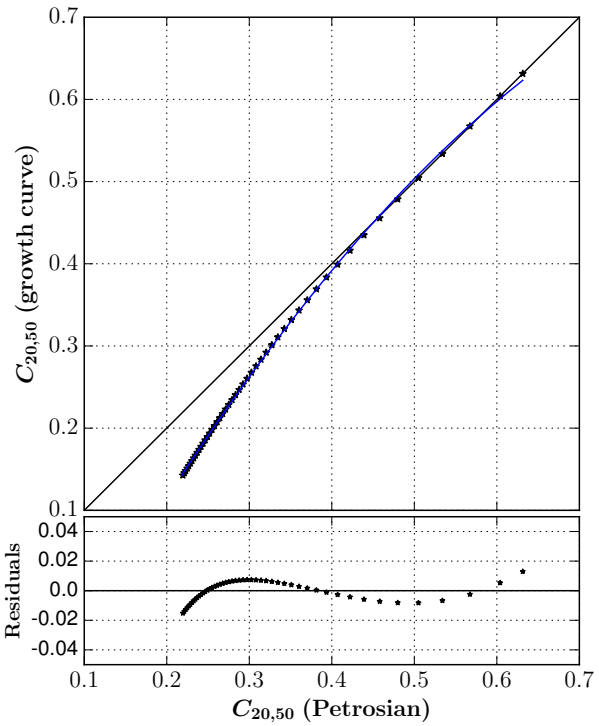

Figure 2.14: Comparison between the concentration index $C_{20,50}$ from growth curve measurement with the associated Petrosian concentration index within the Petrosian aperture $2R_p$. The solid blue line is a polynomial fit to the data, residuals are shown in the bottom panel. The best fit parameters are given in the text.

2.B Parameters of the CALIFA subsample used in this work

Table 2.2: Summary of sample parameters.

ID	NED name	n_g	$C_{20,50}$	B/T	n_b	r_e	$\langle\mu_e\rangle$	rb_{90}	$0.15 \times r_{90}$	σ_0	$\nabla\sigma$
(1)	(2)	(3)	(4)	(5)	(6)	(7)	(8)	(9)	(10)	(11)	(12)
2	UGC00005	0.79	0.50	0.01	0.88	1.22	19.15	2.68	5.40	99.2 ± 4.1	-0.18 ± 0.11
3	NGC7819	7.25	0.33	0.12	1.21	1.95	18.93	4.93	8.90	88.4 ± 5.0	-0.22 ± 0.09
6	NGC7824	5.89	0.23	0.38	2.68	3.66	17.97	14.71	6.41	212.8 ± 2.7	-0.35 ± 0.06
8	NGC0001	5.27	0.28	0.41	2.76	3.48	18.15	14.30	7.98	120.7 ± 3.4	-0.19 ± 0.03
20	NGC0160	8.05	0.25	0.29	2.99	5.62	18.74	24.52	11.36	185.3 ± 2.2	-0.27 ± 0.02
31	NGC0234	0.91	0.45	0.04	0.82	1.62	18.62	3.50	6.78	74.7 ± 4.0	0.01 ± 0.10
33	NGC0257	2.97	0.40	0.10	2.08	2.92	18.53	9.92	7.82	94.3 ± 2.3	0.07 ± 0.05
43	IC1683	3.75	0.38	0.12	0.68	0.97	17.07	1.95	7.48	99.7 ± 8.2	-0.21 ± 0.08
45	NGC0496	1.02	0.47						6.05	58.3 ± 11.2	0.35 ± 0.20
47	NGC0517	5.61	0.37	0.55	3.04	4.31	17.70	19.05	8.20	145.7 ± 5.4	0.06 ± 0.06
119	NGC1167	4.83	0.31	0.23	2.26	5.18	18.90	18.53	12.07	188.8 ± 5.4	-0.19 ± 0.02
147	NGC2253	2.10	0.40	0.08	1.59	1.18	17.43	3.43	6.32	101.4 ± 2.9	-0.19 ± 0.04
275	NGC2906	1.36	0.44	0.14	3.31	4.26	18.80	20.15	6.93	83.2 ± 3.1	-0.06 ± 0.10
277	NGC2916	1.30	0.44	0.07	2.42	2.16	18.03	8.09	9.83	107.9 ± 3.8	-0.28 ± 0.02
311	NGC3106	12.06	0.24	0.30	3.53	3.60	18.37	17.94	12.77	171.6 ± 4.0	-0.49 ± 0.05
489	NGC4047	1.82	0.41	0.03	1.95	1.00	18.18	3.24	8.89	91.8 ± 2.3	-0.17 ± 0.03
548	NGC4470	0.59	0.54						5.98	50.3 ± 4.6	0.03 ± 0.07
580	NGC4711	0.82	0.49	0.02	0.99	0.97	18.88	2.23	5.80	56.6 ± 5.2	-0.06 ± 0.14
607	UGC08234	6.37	0.26	0.58	5.68	5.08	18.41	39.45	7.76	197.5 ± 2.5	-0.43 ± 0.05
611	NGC5016	1.32	0.45	0.01	0.69	0.95	18.88	1.92	7.63	54.9 ± 3.7	0.21 ± 0.12
715	NGC5520	3.02	0.31	0.26	1.26	3.59	18.05 7	9.25	6.26	85.7 ± 1.8	0.07 ± 0.06
748	NGC5633	0.85	0.52						6.04	64.0 ± 3.1	0.23 ± 0.06
768	NGC5732	1.66	0.44	0.04	0.99	1.49	19.42	3.45	5.22		
769	UGC09476	1.00	0.49	0.03	1.37	2.12	19.87	5.69	6.73	50.5 ± 3.9	-0.02 ± 0.10
778	NGC5784	5.56	0.25	0.39	2.37	4.04	17.84	14.91	10.4	209.7 ± 3.1	-0.12 ± 0.02
821	NGC6060	2.76	0.44	0.06	0.77	2.77	18.42	5.84	9.37	112.3 ± 4.8	-0.02 ± 0.03
823	NGC6063	0.66	0.51	0.01	0.97	0.92	19.58	2.01	6.15	48.2 ± 6.2	-0.15 ± 0.22
826	NGC6081	3.79	0.30	0.35	1.50	3.22	18.14	9.07	6.51	194.9 ± 3.4	-0.19 ± 0.02
836	NGC6155	0.95	0.51	0.01	0.53	1.11	18.73	2.09	5.82	78.0 ± 16.2	-0.11 ± 0.27
849	NGC6301	0.77	0.51	0.01	1.47	1.12	19.20	3.12	7.64	80.7 ± 5.1	-0.21 ± 0.07
850	NGC6314	6.20	0.25	0.33	2.63	2.99	17.48	11.86	7.72	174.1 ± 1.8	-0.26 ± 0.02
856	IC1256	1.28	0.49	0.03	2.75	0.73	18.18	3.01	6.31	81.5 ± 6.3	-0.13± 0.07
858	UGC10905	10.35	0.21	0.52	4.34	5.32	18.45	31.83	12.98	221.4 ± 2.5	-0.46 ± 0.04
874	NGC7025	5.32	0.28	0.44	2.65	6.60	18.48	26.36	11.34	225.2 ± 2.1	-0.24 ± 0.01
877	UGC11717	4.35	0.35	0.20	2.53	2.97	18.81	11.46	8.01		
886	NGC7311	4.29	0.27	0.32	2.22	2.75	17.19	6.48	7.33	184.1 ± 2.7	-0.39 ± 0.03
889	NGC7364	3.77	0.31	0.45	2.80	5.59	18.71	23.31	9.54	132.4 ± 3.3	-0.01 ± 0.06
891	UGC12224	0.98	0.48	0.02	1.49	2.11	20.25	5.37	8.18	59.8 ± 9.6	-0.04 ± 0.12
898	NGC7489	1.26	0.49	0.02	0.80	0.79	19.09	1.69	7.22	85.6 ± 7.0	-0.40 ± 0.11
912	NGC7623	4.42	0.27	0.49	2.08	4.50	17.99	15.25	7.86	165.7 ± 1.5	-0.39 ± 0.04
913	NGC7625	1.77	0.39	0.14	0.62	4.26	18.67	8.33	6.03	70.6 ± 2.9	0.06 ± 0.13
915	NGC7653	2.40	0.33	0.27	3.04	3.72	18.78	16.43	5.80	100.6 ± 1.6	-0.25 ± 0.03
916	NGC7671	6.10	0.26	0.33	2.12	1.77	16.71	6.69	8.26	248.2 ± 2.1	-0.48 ± 0.02
917	NGC7683	4.18	0.30	0.57	3.24	7.59	18.76	35.24	10.15	214.0 ± 5.5	-0.41 ± 0.03
923	NGC7711	5.89	0.26	0.47	3.38	4.94	18.09	24.50	10.80	186.1 ± 1.0	-0.28 ± 0.04

(1) CALIFA ID, (2) NED name, (3) global Sérsic index, (4) concentration index, (5) bulge-to-total light ratio, (6) bulge Sérsic index, (7) effective radius in arcsec, (8) mean effective surface brightness in mag arcsec^{-2}, (9) bulge radius as defined in Sect. 2.3.3 in arcsec, (10) $0.15 \times$ the radius that encloses 90% of the total light of the galaxy in arcsec, (11) central velocity dispersion in km s^{-1}, (12) velocity dispersion gradient.

The Close AGN Reference Survey (CARS): Comparative analysis of the structural properties of star-forming and non-star-forming galaxy bars

3

J. Neumann, D. A. Gadotti, L. Wisotzki, B. Husemann, G. Busch, F. Combes, S. M. Croom, T. A. Davis, M. Gaspari, M. Krumpe, M. A. Pérez-Torres, J. Scharwächter, I. Smirnova-Pinchukova, G. R. Tremblay, and T. Urrutia

ABSTRACT

The absence of star formation in the bar region that has been reported for some galaxies can theoretically be explained by shear. However, it is not clear how star-forming (SF) bars fit into this picture and how the dynamical state of the bar is related to other properties of the host galaxy. We used integral-field spectroscopy from VLT/MUSE to investigate how star formation within bars is connected to structural properties of the bar and the host galaxy. We derived spatially resolved Hα fluxes from MUSE observations from the CARS survey to estimate star formation rates in the bars of 16 nearby ($0.01 < z < 0.06$) disc galaxies with stellar masses between 10^{10} $M_\odot$ and 10^{11} $M_\odot$. We further performed a detailed multicomponent photometric decomposition on images derived from the data cubes. We find that bars clearly divide into SF and non-star-forming (non-SF) types, of which eight are SF and eight are non-SF. Whatever the responsible quenching mechanism is, it is a quick process compared to the lifetime of the bar. The star formation of the bar appears to be linked to the flatness of the surface brightness profile in the sense that only the flattest bars ($n_{\rm bar} \leq 0.4$) are actively SF $\left(\mathrm{SFR_b} > 0.5\ M_\odot\ \mathrm{yr}^{-1}\right)$. Both parameters are uncorrelated with Hubble type. We find that star formation is 1.75 times stronger on the leading than on the trailing edge and is radially decreasing. The conditions to host non-SF bars might be connected to the presence of inner rings. Additionally, from testing an AGN feeding scenario, we report that the star formation rate of the bar is uncorrelated with AGN bolometric luminosity. The results of this study may only apply to type-1 AGN hosts and need to be confirmed for the full population of barred galaxies.

A version of this chapter is published as Neumann J., et al., *Astronomy & Astrophysics*, 2019, Vol. 627, id. A26, 26 pp.

3.1 Introduction

One of the main questions that is of great importance in our understanding of the formation and evolution of galaxies is which processes are responsible for quenching and triggering star formation. Bars play a major role in the redistribution of baryons and dark matter, and therefore bars are expected to have a significant effect on where and when star formation can occur.

Galactic bars are commonly observed elongated stellar structures across galaxy discs. These structures have ellipticities and lengths of varying sizes with median values of the order of $\epsilon \approx 0.6$ and $L_{\rm bar} \approx 4.5\,$kpc, respectively (Gadotti, 2011). They form spontaneously from disc instabilities either in secular evolution or induced during a fly-by or merger event. The fraction of bars in disc galaxies in the local Universe is as high as 70%–80% (e.g. Eskridge et al., 2000; Menéndez-Delmestre et al., 2007; Aguerri et al., 2009; Masters et al., 2011; Buta et al., 2015; Erwin, 2018). Bars are very important for many internal processes and work as engine of secular evolution and dynamics of disc galaxies (e.g. Kormendy & Kennicutt, 2004). These structures transfer angular momentum outwards and funnel gas to the centre of the galaxy, where it can build up structures such as nuclear rings and disc-like bulges (Debattista et al., 2006; Athanassoula, 2013; Sellwood, 2014). Bars may feed supermassive black holes and trigger nuclear starbursts, although there is no clear correlation between the presence of a bar and an active galactic nucleus (AGN) (Shlosman et al., 1989; Ho et al., 1997; Coelho & Gadotti, 2011; Cheung et al., 2015a).

The effect of stellar bars on star formation activity in the host galaxy is a widely discussed subject. It has been shown by several authors that bars are responsible for an enhancement of central star formation caused by gas inflow through the bar (e.g. Hawarden et al., 1986; Martinet & Friedli, 1997; Lin et al., 2017; Catalán-Torrecilla et al., 2017). Yet, the global star formation rate (SFR) seems not to depend on the presence of a bar (Kennicutt, 1994) or might even be lower for barred galaxies (Cheung et al., 2013; Kim et al., 2017). These observations are in agreement with a theory in which bars transport gas towards the centre, where it triggers star formation and the gas reservoir gets depleted, which is followed by a decrease of the global SFR.

In this study, we shed light on another local aspect of the interplay between bars and star formation. An interesting phenomenon was observed and discussed in García-Barreto et al. (1996), Phillips (1993), and Phillips (1996): some galaxies show a significant amount of star formation within the bar component itself, while others have bars that are quiescent. These studies also point out that late-type spiral galaxies preferably have star-forming (SF) bars, while early-type spirals have non-star-forming (non-SF) bars. Ryder & Dopita (1993) found a reciprocal relationship between the number of H II regions in the bar and in an inner ring component. Verley et al. (2007) proposed three different classes of barred galaxies with respect to its star formation activity based on Hα measurements: (1) galaxies with strong central star formation, star formation at the ends of the bar and in the spiral arms, and no star formation within the bar; (2) smooth galaxies with no central star formation; and (3) galaxies with star formation within the bar region. These authors explained these categories with an evolutionary sequence from (3) via (1) to (2), where gas is driven towards the centre and subsequently consumed. Interestingly, they could not reproduce the quiescent bars in category (1) with simulations. In these simulations, SFR calculations are mainly based on gas densities. So, how is the star formation inhibited in these bars?

In a study of CO(1-0) observations of the barred galaxy NGC1530, Reynaud & Downes (1998) found strong velocity gradients in the molecular gas in the bar, which coincide with regions of weak Hα. These velocity gradients perpendicular to the bar major axis cause a shearing effect on the gas. The authors argued that the shear could prevent gas clouds that are travelling along the bar to collapse and form stars. These observed velocity gradients agree with simulations in which they are associated with straight dust lanes on the leading edge of strong bars (e.g. Athanassoula, 1992b). In a sub-parsec resolution Milky Way-like simulation Emsellem et al. (2015) showed the distribution of shear, gas density, and star formation across the galaxy. In summary, these authors found that stars are forming in regions of high gas density and low shear, that is at the end of the bar and in the spiral arms, while along the central part of the bar the shear is strongest and no stars are formed. Using the same type of simulation, Renaud et al. (2015) pointed out that the tangential velocity gradient is much smaller at the edge of the bar than in the innermost region, which makes star formation more likely to occur at the edges. Additionally, orbital crowding at the tip of the bar leads to enhanced star formation in these regions. Simulations by Khoperskov et al. (2018) have shown how the presence of a bar in massive gas-rich galaxies quenches the SFR over time both globally and within the radial extent of the bar. These authors have detected an increasing velocity dispersion within the bar region through shear during the bar formation phase that is seemingly responsible for the reduction of the SFR.

These observations and simulations provide a theory that explains the inhibition of star formation in stellar bars caused by shear. Yet, it is still not understood why some galaxies may have these velocity gradients while others may not (given that they show SF bars). If shear is the explanation of the differences seen in star formation activity in bars, then how is the presence of shear related to structural properties of the bar and the host galaxy? How is this changing during the evolutionary development of the bar?

The present work intends to contribute to a better understanding of the nature of star formation in galaxy bars by investigating major structural properties of the bars and their host galaxies in relation to the star formation activity within

the bar. It makes use of spatially resolved spectroscopic data from the Multi-Unit Spectroscopic Explorer (MUSE; Bacon et al., 2010), which is essential for accurately measuring emission line fluxes and being able to pinpoint the location where they were emitted. Hence, this allows us to separate star formation within the bar region from star formation outside the bar. We perform a 2D image decomposition to obtain basic parameters of the different components of the galaxy and use Hα flux from emission line fitting as tracer of star formation. We then compare the various parameters and discuss the implications of our results. Throughout the paper we assume a flat topology with a Hubble constant of $H_0 = 67.8\,\mathrm{km\,s^{-1}\,Mpc^{-1}}$ and $\Omega_m = 0.308$ (Planck Collaboration et al., 2016).

3.2 Data and sample

As part of the Close AGN Reference Survey (CARS; Husemann et al., 2017)[1], this work makes use of multiwavelength observations of 41 nearby ($0.01 < z < 0.06$) luminous type-1 AGN host disc galaxies drawn from the Hamburg/ESO survey (HES; Wisotzki et al., 2000). The analysis presented in this work is almost exclusively based on data from integral field spectroscopy (IFS) observed with MUSE on the Very Large Telescope (VLT) at Paranal. The MUSE instrument covers a 1 squared arcmin field of view (FOV) with a spatial sampling of $0.2''$/pixel. It covers almost the full optical wavelength range from 470 nm to 930 nm with a mean spectral resolution of $R \sim 3000$. The large FOV combined with the fine spatial sampling makes MUSE the ideal instrument to study spatially resolved spectral properties of galaxies, such as SFRs in different structural components. In addition, this study makes use of complementary infrared imaging data from SOAR/SPARTAN[2] (proj. ID: 2015B-Yale/0617), NTT/SOFI[3] (proj. ID: 083.B-0739(A)), and LBT/LUCI[4] (see Busch et al., 2014), which are only included to aid in morphological galaxy classification as well as to perform sanity checks during the photometric fitting procedure.

From the CARS sample of 41 objects 37 galaxies have been observed with MUSE. We selected all galaxies that host a bar component based on our own visual classification by two of the authors, Neumann and Gadotti, in consultation with each other. Some bars may have been missed, especially very weak bars or bars in galaxies at high inclination or small apparent size. These are typical challenges and limitations that affect the studies of bars in general. However, the high quality of the data used for the classifications, namely the high signal-to-noise (S/N) images from the MUSE collapsed cubes in combination with the infrared images that are less affected by dust obscuration, favour an optimal search for bars. That selection gave us 19 barred galaxies, 2 of which had to be excluded because they did not have MUSE data and 1 galaxy was not entirely covered by the MUSE FOV and was therefore not useful for our analysis either. Our final sample comprises 16 barred galaxies of Hubble types between SBa and SBcd, with stellar masses ranging from 10^{10} to $10^{11}\,M_\odot$ and inclinations between approximately $0° < i < 63°$. Visual Hubble type classification was performed by two of the authors, Neumann and Gadotti, independently and then averaged. The subsample of non-barred CARS galaxies is not remarkably different from the barred galaxy sample in terms of Hubble types. Besides 9 ellipticals and 2 irregular/merger galaxies, this subsample comprises 11 galaxies of Hubble types from S0 to Sc compared to the 16 barred galaxies of types Sa to Scd. The stellar masses were estimated from $(g - i)$ colours and i-band absolute magnitudes following the empirically calibrated relation in Taylor et al. (2011). We used simple point-source/host-galaxy decompositions on g- and i-band collapsed MUSE images to integrate the magnitudes on the AGN-subtracted broadband images.[5] The inclination is estimated from the observed axial ratio of the disc component in the multi-component decomposition described in Sect. 3.3 assuming an intrinsic thickness of $q_0 = 0.2$ (e.g. Cortese et al., 2014). All of the galaxies in the CARS survey were selected to host type-1 AGNs, however, owing to misclassification, 1 of our 16 galaxies (HE0045-2145) does not host an AGN. Fig. 3.1 shows collapsed i-band images from the MUSE cubes overlaid with Hα contours of all galaxies in our sample. An overview of the main parameters of our sample can be found in Table 3.2.

The implications of the presence of an AGN on our analysis constitute an interesting and important topic. If bars are responsible for fueling AGN by driving gas inflows and if the nuclear activity depends on certain bar characteristics, then the selection of AGN host galaxies for this work could possibly introduce a bias on the type of bars and the hosts they are residing in. While we leave a full analysis with a control sample of AGN-free barred galaxies for a future paper, it is important to discuss some of the implications the selection could have on the results of this study.

We point out that our investigation of star formation along bars uses a type-1 AGN sample that avoids potential AGN misclassification depending on the Baldwin, Phillips, & Terlevich diagram (BPT diagram; Baldwin et al., 1981, see also Sect. 3.5) selection critera for type-2 AGN as used in many previous papers studying the effect of bars on AGN fueling (Oh et al., 2012; Alonso et al., 2014; Galloway et al., 2015; Alonso et al., 2018). Some BPT classifications for type-2 AGN are prone to be contaminated by low-ionisation nuclear emission-line region (LINER)

[1] `https://www.cars-survey.org`

[2] The Spartan Infrared Camera (SPARTAN; Loh et al., 2004) mounted on the Southern Astrophysical Research (SOAR) Telescope.

[3] The Son OF Isaac (SOFI; Moorwood et al., 1998) on the New Technology Telescope (NTT).

[4] The Large Binocular Telescope Near-infrared Utility with Camera and Integral Field Unit for Extragalactic Research (LUCI; Seifert et al., 2003) on the Large Binocular Telescope (LBT).

[5] Emission lines were not masked when collapsing the cubes. Since the calibrated relation was established from broadband imaging of a large sample of galaxies, their contribution to the flux is already accounted for.

Table 3.1: Overview of model components used in the photometric decomposition.

Model component	Function
Point source	Gaussian with a 0.1 px width
Bulge	Sérsic
Disc	Exponential
Bar1	Sérsic with generalised ellipses
Bar2	Sérsic with generalised ellipses
Bar3	Sérsic with generalised ellipses
Ring	Gaussian ring
Background	FlatSky

The three bar components given are all parts of the same bar. In detail, bar1 is the main long part of the bar, bar2 is the broadened inner part of the bar, and bar3 is the very thin and long part (see text for details).

galaxies which do not necessarily host AGN (e.g. Singh et al., 2013). In addition, the CARS sample was drawn from the Hamburg/ESO survey selecting the most luminous AGN within a certain redshift range without applying any specific criteria on the host galaxy properties. Therefore, it is hard to study trends as a function of AGN luminosity, and the results from this study may only apply to type-1 AGN hosts. Further work is needed to confirm whether these results can be extended to the full population of barred galaxies.

The selection of barred galaxies from this sample did not introduce any obvious additional bias regarding Hubble types or galaxy properties. The presence of an AGN implies that there must be some gas in the centre of the galaxy that somehow must have been pushed inwards. However, different temporal and spatial scales of the activity of the nucleus and a large-scale bar do not permit a direct conclusion about a correlation that extends to kiloparsec scales. We elaborate on this discussion further and test an AGN feeding scenario in Sect. 3.7.2 and briefly address AGN feedback in Sect. 3.8. A deeper study of AGN feeding and feedback in CARS galaxies will be the subject of upcoming papers from the collaboration.

3.3 Photometric decomposition

Two-dimensional image decomposition has become a widely used technique to retrieve structural properties of galaxies. The accuracy, but also the degeneracy of the results depend on many factors such as the amount of detail that is desired to model, the quality of the observations, and the human based decision on which galaxy components to include in the modelling. The most basic approach is to fit a two-component bulge-disc model, which is simple enough to be conducted in an automatic way for a large sample of objects and – to some extent – good enough to get rough estimates of parameters such as disc scale length, bulge-to-total light ratio (B/T), or bulge Sérsic index (n_b) (e.g. Allen et al., 2006). However, it becomes rapidly more complex, if a higher accuracy of these parameters is desired. For example, the neglect of bars, when fitting barred galaxies, can lead to an overestimation of B/T by a factor of 2 (Gadotti, 2008; see also Aguerri et al., 2005; Salo et al., 2015). Similarly, not considering a point source in an AGN host galaxy, results on average in larger B/T and n_b and smaller effective radii of the bulge $r_\mathrm{e,b}$ (Gadotti, 2008). This bias is strongest in bright type-1 AGN. Moreover, the majority of galaxies have been found to have disc breaks (Erwin et al., 2005; Pohlen & Trujillo, 2006; Erwin et al., 2008; Marino et al., 2016). Ignoring the disc break in the fit can lead to an underestimation of B/T and bar-to-total light ratio (Bar/T) by $\sim$ 10% and 25%, respectively, and differences in the disc scale length (h) of $\sim$ 40% (Kim et al., 2014; see also Gao & Ho, 2017). Hence, it is indispensable to analyse carefully which components to include in the model.

In recent decades many programs have been made publicly available to perform 2D photometric decomposition, such as GIM2D (Simard et al., 2002), GALFIT (Peng et al., 2002, 2010), BUDDA (de Souza et al., 2004), and GASP2D (Méndez-Abreu et al., 2008a). For our analysis, we used IMFIT (v.1.5) by Erwin (2015)[6]. The most important component for this work is the bar of the galaxy, for which we are not only interested in the basic parameters, as for example Sérsic index (n_bar), ellipticity (ϵ_bar), and Bar/T, but we also want to determine the exact region from the position, length, ellipticity, and position angle (PA) that is covered by the bar. This is important information to distinguish between the star formation that is happening within the bar and outside the bar. Bars have been modelled in 2D decompositions either with Sérsic (Sérsic, 1963) or Ferrer (Ferrers, 1877; Binney & Tremaine, 1987) functions (e.g. Laurikainen et al., 2005, 2007, 2010; Gadotti, 2008; Weinzirl et al., 2009; Peng et al., 2010; Méndez-Abreu et al., 2017). Kim et al. (2015) and Gao & Ho (2017) showed that both profiles can describe the main shape of the bar and the results should not be influenced by the choice of the fitting function. In our model we call this component our main bar component (bar1).

Kim et al. (2015) also stressed that bars should ideally not be modelled as a single component. It is known that during the evolution of the bar it experiences a buckling instability phase that leads to a vertical thickening of the inner part of the bar with respect to the equatorial plane, as shown for example in Combes et al. (1990), Kuijken & Merrifield (1995), Athanassoula & Bureau (1999), Bureau & Athanassoula (1999), Bureau & Athanassoula (2005), and Athanassoula (2005). In edge-on galaxies, this has been observed as boxy-, peanut-, or x-shaped feature (Jarvis, 1986; de Souza & Dos Anjos, 1987) and it is even visible in only moderately inclined galaxies (Athanassoula & Beaton, 2006; Erwin & Debattista, 2013). It appears that the same physical component manifests itself morphologically also as a barlens when seen face-on (Laurikainen et al., 2011; Athanassoula et al., 2015; Laurikainen & Salo, 2017). We thus adopted a two-component bar model for all the galaxies where an inner boxy bar or barlens is clearly visible; in our model, this is denoted as bar2.

[6] http://www.mpe.mpg.de/~erwin/code/imfit/

Table 3.2: Summary of the main parameters from the 2D decomposition, bar length measurement, and morphological classification.

Galaxy	Type	Incl[°]	PS/T	B/T	Bar/T		R/T	D/T	h [″]	$n_{\rm bar1}$	$n_{\rm bar2}$	$n_{\rm bar3}$	$L_{\rm bar}$ [″]
(1)	(2)	(3)	(4)	(5)	(6)		(7)	(8)	(9)	(10)	(11)	(12)	(13)
HE0021-1819	SBab	16	0.03	0.20	0.08	(100/0/0)	0.10	0.59	3.44	0.76	–	–	2.84
HE0045-2145	SBab	5	0.16	0.02	0.23	(68/0/32)	–	0.59	6.89	0.34	–	0.16	8.30
HE0108-4743	SBc	13	0.10	–	0.10	(100/0/0)	–	0.80	4.02	0.97	–	–	4.98
HE0114-0015	SBab	40	0.05	0.14	0.27	(75/0/25)	–	0.54	4.23	0.28	–	0.06	3.60
HE0119-0118	SBab	2	0.23	–	0.12	(100/0/0)	–	0.65	3.37	0.37	–	–	4.84
HE0253-1641	SBab	30	0.39	–	0.16	(100/0/0)	–	0.45	5.80	0.75	–	–	9.16
HE0433-1028	SBcd	57	0.19	0.06	0.21	(77/0/23)	–	0.54	6.00	0.09	–	0.05	14.78
HE0934+0119	SBab	38	0.45	–	0.18	(73/0/27)	–	0.36	4.98	0.22	–	0.05	6.78
HE1011-0403	SBb	26	0.42	0.02	0.17	(100/0/0)	–	0.39	4.51	0.50	–	–	6.59
HE1017-0305	SBc	54	0.24	0.02	0.16	(65/9/26)	0.01	0.58	6.83	0.38	0.05	0.18	5.37
HE1029-1831	SBab	38	0.15	0.26	0.15	(100/0/0)	–	0.44	4.45	0.21	–	–	3.78
HE1108-2813	SBc	51	0.17	–	0.22	(46/23/31)	–	0.62	5.38	0.26	0.24	0.07	9.35
HE1330-1013	SBc	40	0.06	0.02	0.18	(82/18/0)	0.06	0.69	11.20	0.64	0.26	–	11.56
HE2211-3903	SBbc	4	0.20	0.02	0.17	(52/36/12)	0.01	0.60	7.12	0.60	0.39	0.05	8.44
HE2222-0026	SBa	7	0.42	–	0.15	(100/0/0)	–	0.44	2.06	0.55	–	–	3.25
HE2233+0124	SBb	63	0.13	0.11	0.14	(100/0/0)	–	0.62	5.22	0.73	–	–	4.52

(1) Galaxy name; (2) Hubble type from our own visual classification by two of the authors, Neumann and Gadotti; (3) inclination of the galaxy calculated from the ellipticity of the disc component in the decomposition assuming an intrinsic thickness of the disc of $q_0 = 0.2$; (4)-(8) luminosity fractions of point source, bulge, bar, ring and disc, respectively; in (6) we are additionally showing the relative contribution in percentage of each bar component (bar1/bar2/bar3) to the total luminosity of the bar; (9) disc scale length; (10)-(12) Sérsic indices of the main, second (broadened) and third (narrow) bar component, respectively; (13) length of the bar.

Furthermore, in many cases there is evidence for a very elongated light excess in the residual image of the bar after the fit. It has approximately the length of the outer part of the bar, but is much thinner. It can be seen in Fig. 3.2 and in residual images of previous works (e.g. Gadotti, 2008; Athanassoula et al., 2015). For these galaxies, we decided to add a third bar component in the model. This decision is purely empirically motivated. We stress these are all parts of the same bar. From 2D and 3D orbital theory we know that bars are built from families of periodic orbits with different extents, elongations, and orientations. (e.g. Contopoulos & Papayannopoulos, 1980; Athanassoula et al., 1983; Pfenniger, 1984; Skokos et al., 2002a,b). While the usual single bar component fits the main orbits that constitute the backbone of the bar, the very narrow extra component in the residual might be a signature of very elongated orbits along the bar major axis. We include this component in our model when necessary; we call this in our model bar3. Additionally, a ring was fitted when present. This is important to accurately determine the Sérsic index of the main bar component.

In summary, we fit a selection of the galaxy components given in Table 3.1 and we only include a component if we have clear visual indications of its presence. Out of the 16 galaxies 8 were modelled with a single bar component, 5 needed two components, and 3 galaxies were fitted with all three bar components.

All fits were performed independently on pseudo SDSS *i*-band images from the MUSE data cubes and on *R*-band or *J*-band images from either SOAR/SPARTAN, NTT/SOFI, or LBT/LUCI. During the fitting of the *R*-band and *J*-band images, we identified some problems to model accurately the point-spread function and some of the images were taken with rather short exposure times. Furthermore, only observations from MUSE were available for the complete sample, which gives us the advantage of consistency. After a careful comparison, we opted to use only the results performed on the MUSE *i*-band images. However, the decompositions on the broadband images were a useful control set to tune the initial parameter values and evaluate intermediate results during the fitting procedure. The point-spread function was determined by fitting Moffat profiles to at least two point sources in the FOV of each image. The stripes in the background of the images as seen for example in Fig. 3.1 – a known effect from the integral field unit – are very shallow and do not affect the decomposition.

Fig. 3.2 shows for the galaxy HE 1108-2813 from left to right the collapsed *i*-band image from MUSE, the model, residual image, and surface brightness profile. The profile was derived by fitting ellipses to the isophotes in the images with the IRAF[7] task ELLIPSE. In a first step, we fitted the data image with the parameters for PA and ellipticity left free. Leaving these parameters free has the advantage that the surface brightness profile highlights at each distance the predominant source that contributes to the total surface brightness. Then, we used the same set of values from the first fit to perform the same task on the model images in non-fitting mode just measuring the surface brightness on the same ellipses. This can be done via the INELLIP option. A summary of the parameters from the decomposition is given in Table 3.2.

[7] IRAF is distributed by the National Optical Astronomy Observatories, which are operated by the Association of Universities for Research in Astronomy, Inc., under cooperative agreement with the National Science Foundation.

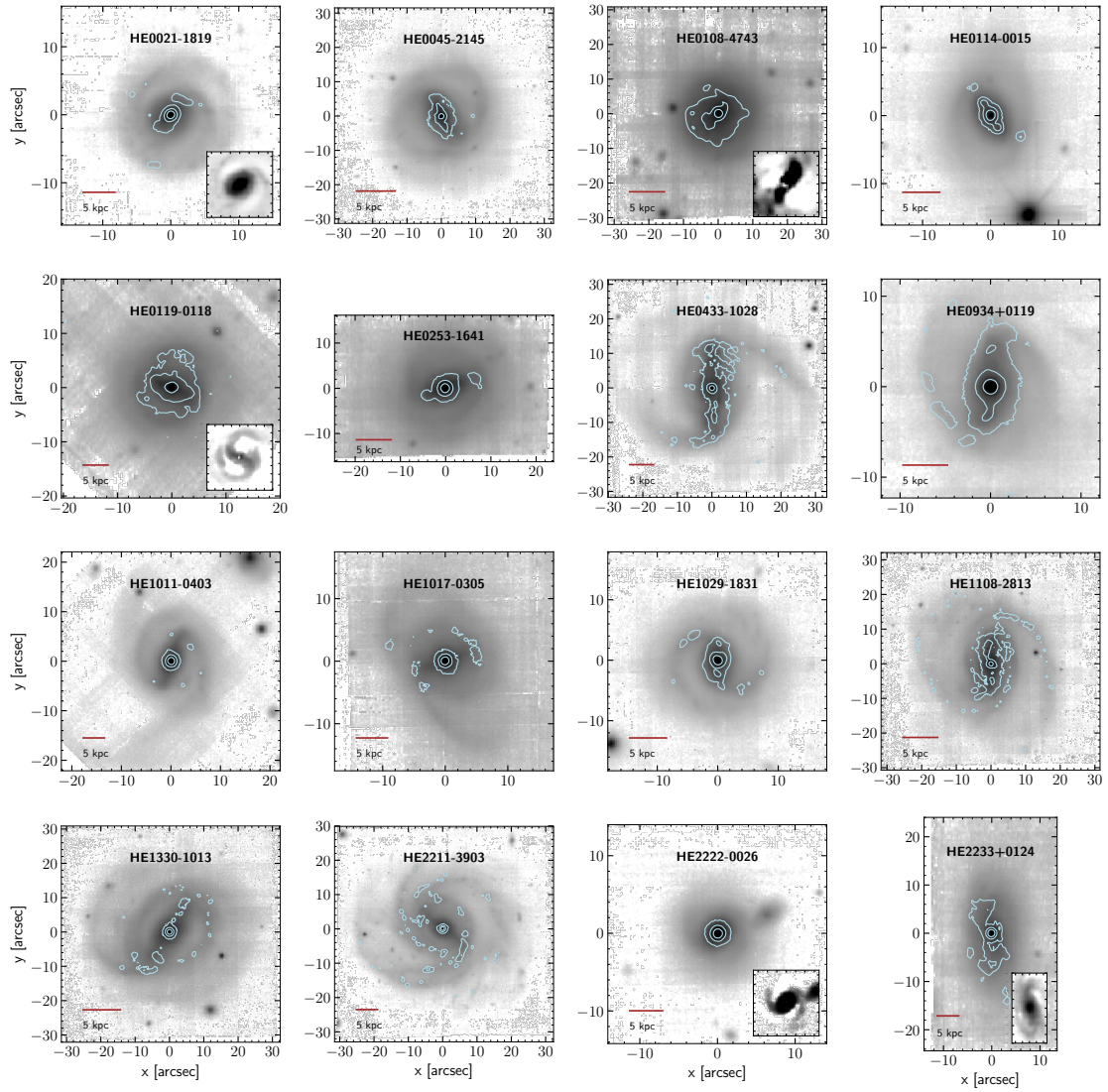

Figure 3.1: MUSE collapsed *i*-band images overlaid with contours of continuum subtracted Hα emission from the original data cubes (AGN+host). This figure shows our complete sample. Inset plots are added for galaxies where bars are difficult to recognise. These inset plots present residual images when subtracting a simple point source + exponential disc model from the galaxy.

3.4 Measuring the length of the bar

There is no unambiguous way to determine the length of the bar, and authors have determined this value in many different ways in the past; there is no sharp transition, but bars join smoothly the outer disc. A common approach is to use the isophotal ellipticity profile of the galaxy and define the bar length as the distance from the centre (on the x-axis) at the first maximum ellipticity (on the y-axis; see Wozniak & Pierce, 1991). We call this $L_{\rm peak}$. This maximum is usually associated with the ellipses close to the end of the bar, after which the bar transitions into the disc causing the ellipticity to drop. If the bar is strong, this drop may be very fast, but weak bars tend to show a slow decline in ellipticity (e.g. Gadotti et al., 2007).

Many different approaches of measuring the length of the bar for simulated galaxies were tested and compared in Athanassoula & Misiriotis (2002). These authors found that the maximum ellipticity method generally provides the smallest value for the bar length. Alternatively, the first minimum after the ellipticity peak ($L_{\rm min}$) or a sudden change of the PA ($L_{\rm PA}$) can be used (Erwin & Sparke, 2003). Erwin (2005) showed that L = minimum($L_{\rm min}$, $L_{\rm PA}$) correlates very well with $L_{\rm peak}$ with a Spearman correlation coefficient of $\rho = 0.96$ and the average of both values matches best the visual bar size measurement ($L_{\rm vis}$).

In this work, we derived an estimate by a combination of different proxies for the bar length, such as ellipticity peak and minimum, the change in PA and – in specific cases – the radius of an inner ring, as explained below. We performed the fitting of the isophotes with the IRAF task ELLIPSE as described in the previous section. We then determined, where it was possible, the location of the ellipticity peak $L_{\rm peak}$ and the location of the proximate minimum after the drop $L_{\rm min}$. We further used the radial profile of the PA to identify sudden changes in the PA after

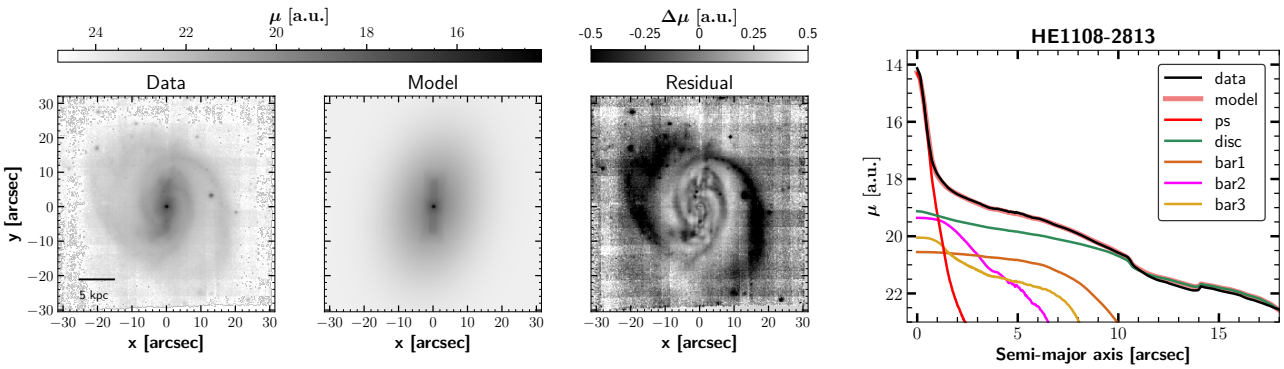

Figure 3.2: Photometric decomposition of MUSE collapsed *i*-band image of galaxy HE 1108-28138. From *left* to *right*: data image, model, residual=data-model, and surface brightness profile from isophotal fitting. The colour map in the residual image is stretched to show faint details. The surface brightness profiles in the right-most panel show a separation into all components that were included in the fit. The thick coral line shows the sum of all model components and the black line the observed data. A set of figures that shows the decomposition of the complete sample can be found in the Appendix 3.C.

the ellipticity peak. The position where the PA changed about 10° as compared to the PA at $L_{\rm peak}$ is denoted as $L_{\rm PA}$. Our first estimate of the bar length is defined as follows:

$$L_{\rm bar,0} = {\rm AVG}(L_{\rm peak}, {\rm MIN}(L_{\rm min}, L_{\rm PA})). \quad (3.1)$$

It is not always possible to determine the length of the bar with the ellipticity or the PA profile. Sometimes the end of the bar transitions smoothly into a ring or spiral arms of the galaxy and no clear ellipticity drop or change in PA can be identified. In other cases the ellipticity can get distorted in the presence of strong dust lanes. Hence, a careful case-by-case evaluation including a visual inspection of the image is necessary. The final bar estimate is

$$L_{\rm bar} = {\rm MIN}(L_{\rm bar,0}, L_{\rm ring}) \quad \text{or} \quad L_{\rm vis}. \quad (3.2)$$

We only had to use a visual estimation in the case of HE2233+0124. A typical ellipticity profile of a galaxy is exemplarily shown for HE2211-3903 in Fig. 3.3

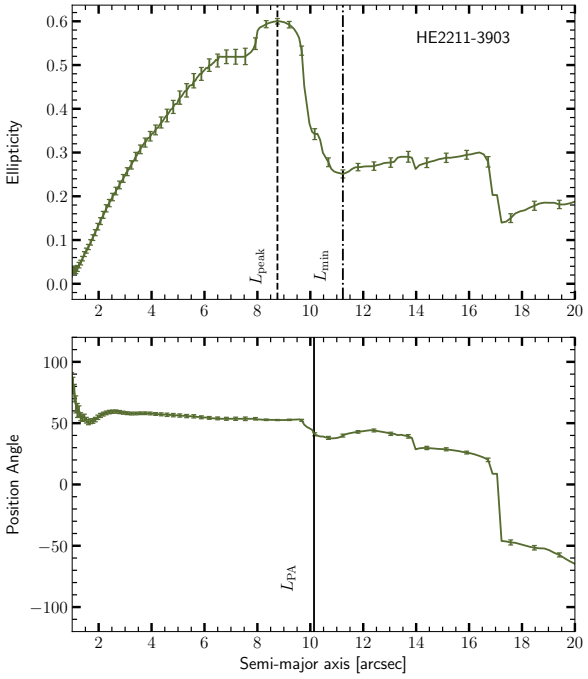

Figure 3.3: Results from the isophotal fitting routine ELLIPSE in IRAF for the MUSE collapsed *i*-band image for galaxy HE 2211-3903 to estimate the bar length. The vertical lines show the different estimates of the length of the bar as described in more detail in the text.

3.5 Derivation of SFR from dust-corrected Hα emission lines

Since individual stars are unresolved in our galaxy sample, measurements of star formation activity rely on tracers of star formation in the spectrum of integrated light. A big pool of diagnostic methods across the electromagnetic spectrum from ultraviolet (UV) to far-infrared has been established over the years (for a review, see Kennicutt, 1998; Kennicutt & Evans, 2012). While the young stellar population can be directly observed in UV emission, this method has the disadvantage that a significant fraction of the UV light is absorbed by dust and re-emitted in the far-infrared. Furthermore, for the analysis of nearby galaxies this method is limited to space telescope observations. Alternatively, recombination lines in the optical that trace the re-emission of ionised hydrogen in H II regions can be used. The Hα line has become very popular for a measurement of the SFR. This is one of the strongest emission lines and it is less affected by dust obscuration than UV tracers. For local galaxies, Hα is within the MUSE spectral range (470-930 nm). In this section, we describe the procedure for getting spatially resolved SFR maps from the MUSE observations.

Prior to the emission line analysis, a deblending of AGN and host galaxy is performed using the software QDEBLEND3D (Husemann et al., 2013a, 2014). The stellar continuum and emission lines are then modelled on the AGN-substracted cubes with the code PYPARADISE (Walcher et al., 2015; Husemann et al., 2016) that uses a linear combination of stellar template spectra convolved

with a Gaussian line-of-sight velocity kernel. The fitting is done in three steps. First, the continuum is fitted for co-added spectra in Voronoi bins with target S/N~10. Second, the continuum is fitted on a spaxel-by-spaxel basis with fixed kinematics according to the underlying Voronoi cell. Finally, the emission lines are modelled in the residual spectra using a single Gaussian component. A Monte Carlo simulation is used to estimate errors by refitting the data 100 times after modulating the input data by the formal errors (for more details of the functionality of PyParadise, see also De Rosa et al., 2018; Weaver et al., 2018).

The Hα flux has to be corrected for dust attenuation to derive accurate SFRs. Since the intrinsic ratio of the emission lines Hα/Hβ (Balmer decrement) is in ideal conditions set by quantum mechanics, it has been commonly used as a measure of the effect of dust on the source spectrum of interest. The attenuation is wavelength dependent and thus changes the observed ratio. Following Calzetti et al. (1994) and Domínguez et al. (2013) the intrinsic luminosity $L_{\rm int}$ can be obtained by

$$L_{\rm int}(\lambda) = L_{\rm obs}(\lambda)\ 10^{0.4\ k(\lambda)\ E(B-V)}. \quad (3.3)$$

In this equation, $L_{\rm obs}$ is the observed luminosity and $k(\lambda)$ is the reddening curve. In this work we use the reddening curve from Calzetti et al. (2000). $E(B-V)$ is the colour excess that is given by

$$E(B-V) = 1.97\ \log_{10}\left(\frac{(\mathrm{H}\alpha/\mathrm{H}\beta)_{\rm obs}}{2.86}\right). \quad (3.4)$$

After this analysis, it is possible to compute a spatially resolved dust-corrected Hα map for each galaxy. We clean this map by considering only spaxels, where $\mathrm{S/N}_{\mathrm{H}\alpha} > 3$, $\mathrm{S/N}_{\mathrm{H}\beta} > 3$, $V_{\rm err} < 20\,$km/s, and $\sigma_{\rm err} < 30\,$km/s.

The presence of an AGN can contaminate the measurement of Hα-based SFRs. It is no longer possible to convert Hα flux to SFRs under the assumption that all Hα is caused by star formation. In contrast, a new source of photoionisation has to be considered. The AGN and star formation ionisation can be seen on emission line diagnostic diagrams, such as the traditional BPT diagram (Baldwin et al., 1981; Veilleux & Osterbrock, 1987). While the BPT diagram has been widely used to classify galaxies as whole systems (e.g. Kauffmann et al., 2003b), more recently this diagram has also been applied to analyse different regions of the galaxies with data from IFS surveys (Singh et al., 2013; Belfiore et al., 2016; Federrath et al., 2017).

The main idea behind our analysis is to not only classify each pixel to one or the other ionisation source because the sources can be mixed and pixels form the so-called mixing sequence on a BPT diagram, but to define a fraction of Hα per pixel caused by one mechanism or the other. We performed an emission line diagnostic that is based on an analysis described in Davies et al. (2016) with modifications necessary for analysing more complicated BPT diagrams. We defined a number of AGN and SF basis pixels based on their spatial distribution and BPT position. To fit the mixed pixels and disentangle the AGN fraction we treated the pixels as vectors of emission line fluxes and fitted a linear combination using a Markov chain Monte Carlo (MCMC) algorithm as follows:

$$\begin{pmatrix} \mathrm{H}\alpha \\ \mathrm{H}\beta \\ [\mathrm{O\,III}] \\ [\mathrm{N\,II}] \\ [\mathrm{S\,II}] \end{pmatrix}_{\rm mixed} = f_{\rm SF} \times \begin{pmatrix} \mathrm{H}\alpha \\ \mathrm{H}\beta \\ [\mathrm{O\,III}] \\ [\mathrm{N\,II}] \\ [\mathrm{S\,II}] \end{pmatrix}_{\rm SF} + f_{\rm AGN} \times \begin{pmatrix} \mathrm{H}\alpha \\ \mathrm{H}\beta \\ [\mathrm{O\,III}] \\ [\mathrm{N\,II}] \\ [\mathrm{S\,II}] \end{pmatrix}_{\rm AGN}, \quad (3.5)$$

where $f_{\rm SF}$ and $f_{\rm AGN}$ are SF and AGN fractions and these values obey the assumption of no other excitation mechanisms $f_{\rm SF} + f_{\rm AGN} = 1$. In the fitting procedure we varied the fractions and the basis vectors, parameterised with metallicity of SF basis and the [N II]/Hα ratio of AGN basis.

We show in Fig. 3.4 the spatially resolved emission line diagnostic for the galaxy HE 1108-2813. Each point in the left panel of this figure corresponds to one spectrum in the MUSE cube. The right panel shows the spatial location of the data points from the BPT diagram overplotted on the *i*-band image of the galaxy. Regions are coloured according to the fraction of Hα that comes from star formation. For comparison, we also show the theoretical-based maximum starburst line from Kewley et al. (2001) and the empirically motivated division line from Kauffmann et al. (2003b). We note that [S II] is included in the fitting, but not shown on this BPT. The figure shows that all spaxels that are most affected by the AGN are centrally concentrated and the Hα from the bar region and the spiral arms is almost exclusively caused by star formation.

For each spaxel, we multiplied the dust-corrected Hα flux by the star formation fraction and converted it into SFR assuming a Salpeter initial mass function (Salpeter, 1955) and using the Kennicutt (1998) relation

$$\mathrm{SFR}\,[M_\odot\,\mathrm{yr}^{-1}] = 7.9\times10^{-42}\,L(\mathrm{H}\alpha)\,[\mathrm{erg\,s}^{-1}]\times f_{\rm SF}. \quad (3.6)$$

The final SFR map for the galaxy HE 1108-2813 overplotted with the bar region is shown in Fig. 3.5. The extent of the bar is defined by the parameters of the photometric decomposition and the measurement of the bar length. As approximation, we used a rectangle with the two sides *a* and *b* having the length of the major and minor axis of the bar. We split the bar further into 3×9 subregions. A collection of these plots for the entire sample can be found in Appendix 3.D.

Finally, to estimate the total SFR in the bar region ($\mathrm{SFR_b}$), we rebinned the original spectra in the AGN-subtracted MUSE cubes within each of the 27 bar subregions and repeated subsequently the complete analysis as described above. The decision was made to increase the S/N and get more accurate measurements of the SFR in the bar, especially in regions of low signal. Additionally,

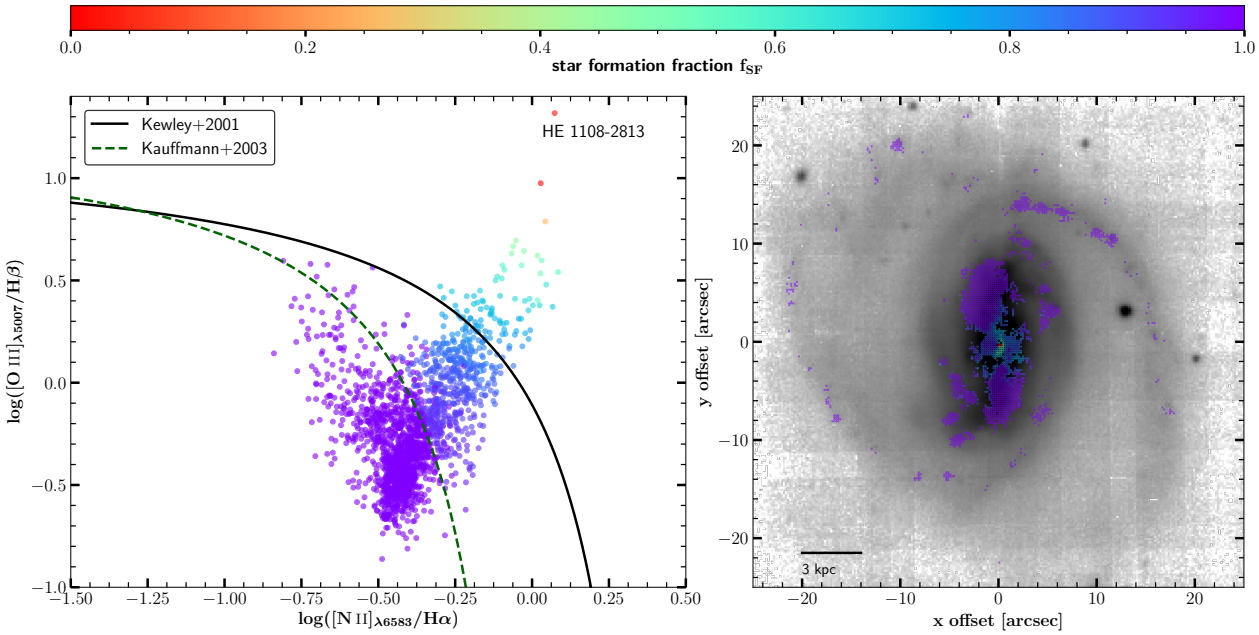

Figure 3.4: *Left panel*: Emission line diagnostic for galaxy HE 1108-2813. Data points are coloured by the fraction of Hα that comes from star formation. The black solid line is adopted from the theoretical line from Kewley et al. (2001) and the green dashed line from the empirically derived separation from Kauffmann et al. (2003b). We show only points where S/N > 3 for all four emission lines. *Right panel*: Collapsed MUSE *i*-band image overplotted with the data points from the left panel to show the spatial location of these spectra.

we divided the SFR by the stellar mass to derive specific star formation rates (sSFR). Throughout the analysis we used two different measures of the sSFR:

$$\begin{aligned} {}_{\rm t}{\rm SFR}_{\rm b} &= {\rm SFR}_{\rm b}/M_{\rm t}, \\ {}_{\rm b}{\rm SFR}_{\rm b} &= {\rm SFR}_{\rm b}/(M_{\rm t} \times {\rm Bar/T}), \end{aligned} \tag{3.7}$$

where $M_{\rm t}$ is the total stellar mass of the galaxy that we estimate from *g*- and *i*-band magnitudes as explained in Sect. 3.2 and $M_{\rm b} = M_{\rm t} \times {\rm Bar/T}$ is the approximate stellar mass of the bar component only. To get one clean value to characterise the star formation activity in the bars, we calculated the $\rm SFR_b$, ${\rm _tSFR_b}$, and ${\rm _bSFR_b}$ within the rows −3 to −1 and 1 to 3 as annotated in Fig. 3.5 that we call the intermediate region of the bar. A summary of the SFRs for all galaxies can be found in Table 3.3.

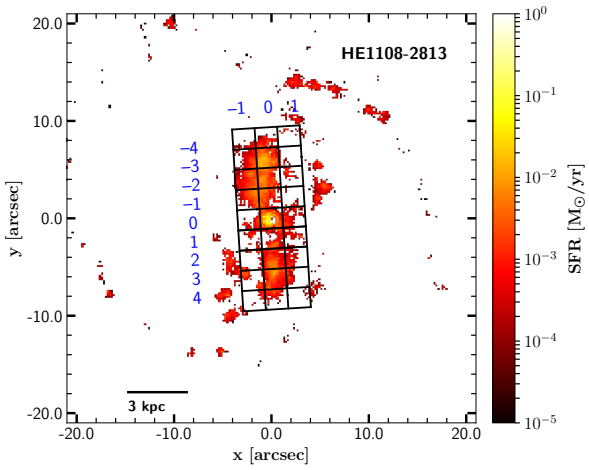

Figure 3.5: Spatially resolved map of SFRs in the galaxy HE1108-2813. On top, we show the bar mask for that galaxy, created from the parameters of the image decomposition and ellipse fitting. The mask is divided into 3×9 subcells to analyse how the SFR changes over the bar region. A set of these maps for the complete sample with additional *i*-band contours can be found in Appendix 3.D.

3.6 Results

The purpose of this work is to investigate whether there is a connection between the presence or absence of star formation activity in the bar region and structural properties of the bar or the host galaxy. Our aim is to search for relations between the parameters that represent these properties of the bar and to analyse whether there is a clear separation into two types of bars or if we observe rather a continuous diversity.

3.6.1 Star-forming versus quiescent bars

In Fig. 3.6 we present the distribution of star formation activity in the intermediate bar region that excludes the outermost and innermost rows of the bar mask. This is to ensure we exclude contamination from spiral arms or remaining Hα emission from the AGN. The upper panel shows the SFR of each galaxy bar against the total stellar mass of the galaxy. The uncertainties of the SFRs are propagated from the errors of the emission line fluxes. A clear separation between bars with almost zero star formation and bars with clear star formation activity becomes evident in that plot. We choose $\rm SFR_b = 0.5\ M_\odot/yr$ to be the demarcation between SF and quiescent (non-SF) bars,

Table 3.3: Summary of the SFRs from dust-corrected and AGN-masked Hα emission in the intermediate bar region.

Galaxy	SFR_b $M_\odot\,yr^{-1}$	$\log(s_tSFR_b/yr^{-1})$	$\log(s_bSFR_b/yr^{-1})$
(1)	(2)	(3)	(4)
HE0021-1819	0.10 ± 0.01	-11.11 ± 0.11	-9.99 ± 0.11
HE0045-2145	1.87 ± 0.19	-9.93 ± 0.11	-9.29 ± 0.11
HE0108-4743	< 1.10	< -10.60	< -9.61
HE0114-0015	2.16 ± 0.22	-10.16 ± 0.11	-9.60 ± 0.11
HE0119-0118	3.77 ± 0.38	-10.12 ± 0.11	-9.21 ± 0.11
HE0253-1641	0.47 ± 0.05	-10.93 ± 0.11	-10.14 ± 0.11
HE0433-1028	7.72 ± 0.77	-9.95 ± 0.11	-9.28 ± 0.11
HE0934+0119	1.34 ± 0.13	-9.92 ± 0.11	-9.19 ± 0.11
HE1011-0403	0.14 ± 0.02	-11.57 ± 0.11	-10.80 ± 0.11
HE1017-0305	< 0.11	$- < 11.54$	< -10.74
HE1029-1831	8.37 ± 0.84	-9.44 ± 0.11	-8.62 ± 0.11
HE1108-2813	2.53 ± 0.25	-9.88 ± 0.11	-9.22 ± 0.11
HE1330-1013	0.08 ± 0.01	-11.55 ± 0.11	-10.81 ± 0.11
HE2211-3903	0.35 ± 0.04	-11.17 ± 0.11	-10.40 ± 0.11
HE2222-0026	0.11 ± 0.01	-11.07 ± 0.11	-10.24 ± 0.11
HE2233+0124	0.16 ± 0.02	-11.27 ± 0.11	-10.41 ± 0.11

(1) Galaxy name; (2) SFR in the bar region; (3) logarithm of the sSFR considering the total stellar mass of the galaxy; (4) logarithm of the sSFR considering only the stellar mass of the bar component. All measurements of star formation are integrated within the intermediate bar region (rows −3,−2, −1, 1, 2, 3) as defined in the text and in Fig. 3.5. The SFR in galaxy HE0108-4743 is derived from real detections, but considered as upper limit because of possible contamination from other physical processes (see Sect. 3.6.2 for details).

represented by the vertical solid line. The next two panels below show histograms of the logarithm of s_bSFR_b and s_tSFR_b. Both histograms independently confirm a well-defined separation into two categories of star formation activity. The absence of an intermediate population indicates that the quenching process must be quick as compared to the lifetime of SF and non-SF bars. The limited range in stellar mass may be responsible that the plot does not change much when using sSFR or SFR alone. Therefore, in our case it does not make a difference which parameter is used to divide between SF and non-SF bars, but s_bSFR_b might be in general the preferred discriminator.

3.6.2 Bar Sérsic index

Our results show no obvious correlations between star formation activity and structural parameters as for example B/T, Bar/T, n_{bulge}, L_{bar}/h, h or the type and number of parameters included in the fit, except for the bar Sérsic index n_{bar}, which is shown in Fig. 3.7. The parameter n_{bar} is the Sérsic index of the main bar component *bar1*. In this figure, we plot the specific SFR of the intermediate region of the bar against n_{bar}. First of all, we observe that all bars have Sérsic indices smaller than 1, which is typical for a bar component. A Sérsic function with an index less than 1 produces a concave function that shows little variation in the central part and bends down towards larger radii. The smaller the Sérsic index the sharper is the drop at the end of the bar and the flatter is the central part of the profile. The term flat is often used to describe shallow surface brightness profiles in a log-linear plot. Furthermore, the applied separation into SF and non-SF bars that we adopt from Fig. 3.6 concurs with a trend from very low to larger Sérsic indices, respectively. One outlier from this observed trend is discussed separately in the end of this subsection. A statistical test for a correlation between these two parameters yields a Spearman's rank correlation coefficient of $\rho = -0.72 \pm 0.05$, which clearly indicates the presence of a strong correlation. Kim et al. (2015) found that massive galaxies mainly have flat bars with $n_{bar} < 0.4$, while less massive galaxies have close to exponential ($n_{bar} \geq 0.8$) light profiles. Our comparison of galaxy mass and Sérsic index presented in Fig. 3.8 shows that all galaxies in our sample are predominantly massive ($M_\star > 10^{10}\,M_\odot$) and there is no correlation between n_{bar} and $M_\star$. The scatter in n_{bar} for the given mass range does not disagree with the presented results in (Kim et al., 2015, their Fig. 2). We conclude that the observed correlation of the Sérsic index with the sSFR in our analysis cannot be explained by galaxy mass.

In order to address the question whether the light from recently formed hot young stars in SF bars is responsible for flattening the light profile of the bar, we performed an additional multiband fit for a test case using the galaxy with the flattest and SF bar HE0433-1028. We ran a simultaneous decomposition on the collapsed *g*-, *r*-, *i*-, and *z*-band images from the MUSE cube using GALFITM (Häußler et al., 2013) a modified version of GALFIT. The Sérsic index did not change across the four bands within a small interval of $\Delta n_{bar} = 0.02$. Given this result, it should be safe to assume that additional light due to ongoing star formation is not a dominant cause of flat bars.

The estimation of uncertainties for parameters from 2D image decompositions is usually a difficult endeavour.

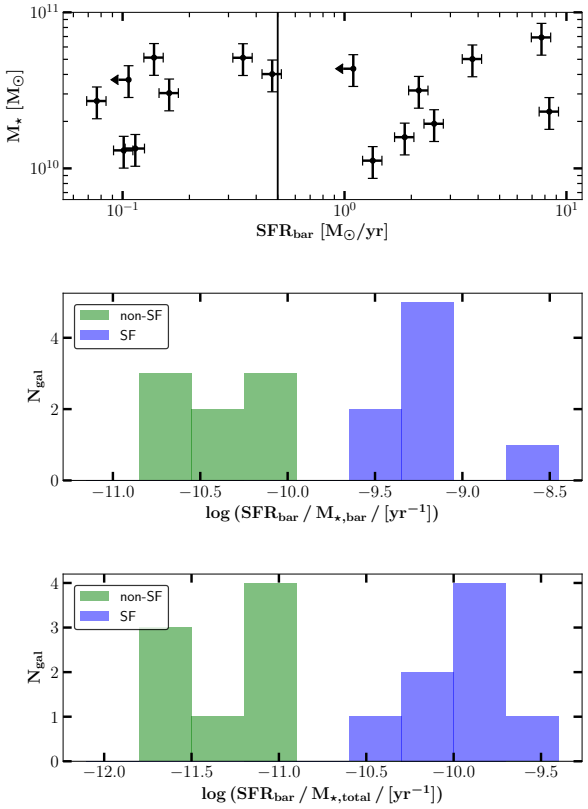

Figure 3.6: Total integrated SFRs in the intermediate bar region of each galaxy that includes the rows −3 to −1 and 1 to 3 as defined in Fig. 3.5. *Upper panel:* SFR_b for each galaxy vs. total stellar mass. A separation between almost zero SFRs and $SFR_b \gtrsim 1\ M_\odot$/yr is clearly apparent. A vertical black line at $SFR_b = 0.5\ M_\odot$/yr shows our classification into SF and non-SF bars. *Middle panel:* Histogram of sSFRs when accounting only for the mass of the bar. In light green and light blue we show non-SF and SF bars according to their location in the upper panel. Going from SFR_b to s_bSFR_b does not change the separation. *Lower panel:* The same as the middle panel but dividing SFR_b by the total stellar mass of the galaxy. Again, the classification does not change.

Especially an increasing number of model components augments the degeneracy between the parameters and concurrently the human factor becomes more important. Most of the available codes provide a χ^2 value to measure the goodness of fit. This has been shown generally to underestimate the uncertainty (e.g. Häussler et al., 2007; Gadotti, 2009; Erwin, 2015) in galaxy decompositions and, if at all, can only be used as a lower limit. To date, there is no common method that has been proven to give robust estimates of the error budget. In Appendix 3.A.1, we discuss two different methods: one that is based on bootstrap resampling and one that follows a MCMC approach. Individual error bars for both methods can be seen and compared in Fig. 3.14, where we also discuss that the errors from MCMC are probably too large and the bootstrap error should be preferred. In Fig. 3.7, 3.8, and 3.10 we show only the more reliable bootstrap errors. Both bootstrap and MCMC are implemented functionalities in IMFIT.

The galaxy HE0108-4743 stands out from the general trend found for the other galaxies in the sample. Despite a rather large Sérsic index, it shows high star formation activity in the bar region. However, the Hα found in this galaxy is not limited to the bar region or spiral arms, but rather seems to be a continuous feature across the whole galaxy. Possibly, there has been a burst of star formation that occurred everywhere in the galaxy. This could mean that different processes are in place as compared to just the typical evolution of star formation in galaxy bars. The SFR of the bar should therefore be considered as an upper limit.

Another special case is HE2222-0026. In contrast to the other galaxies with non-SF bars in our sample, in this galaxy we do not observe any Hα in the outer disc and we only observe very little along the bar. Furthermore, the total molecular gas mass is rather low $M(H_2) = 0.5 \times 10^9\ M_\odot$ (Bertram et al., 2007). In this special case, the absence of star formation in the bar is simply explained by a global lack of fueling gas.

3.6.3 Bar surface brightness profile

The Sérsic function seems to yield satisfying results when it is used to fit bar components, but there are weaknesses that are important to keep in mind. The difference between Sérsic profiles in the central flat part of functions with very low Sérsic indices is small, as a result of which the Sérsic index of the model is very sensitive to small variations in the data for flat bars. It is mainly governed by the strength of the cut-off in the profile, hence the end of the bar. This is problematic in the case of weak bars or the presence of inner rings or smooth transitions into spiral arms.

To test our bar fits for such cases, we chose a direct examination of the light profile as best approach. Unfortunately, the total integrated surface brightness profile confronts us with a sum of light that originates from all galaxy components. Even in the radial range where the bar dominates the light profile, it is not straightforward to recognise the light distribution of the bar only. For example, the presence of a central point source, an inner ring or strong spiral arms can alter substantially the surface brightness profile of the galaxy across a range of radii. The most appropriate solution seems to be to use our multicomponent decomposition yet having the major drawback that it already assumes certain model functions for the various components. The extent to which our assumption influences our result is determined by how much the specific bar model constrains the fit of the other galaxy components in the decomposition.

We calculated the residual light profiles of the bar by subtracting all model components from the data image except the bar itself. For example, if the galaxy was best fitted with a ps+bulge+bar+disc, then we calculate $\text{residual}_{bar} = \text{data}_{total} - (\text{model}_{ps} + \text{model}_{bulge} + \text{model}_{disc})$. In Fig. 3.9, we show the bar residuals together with the disc profiles for each galaxy. For comparison, we also

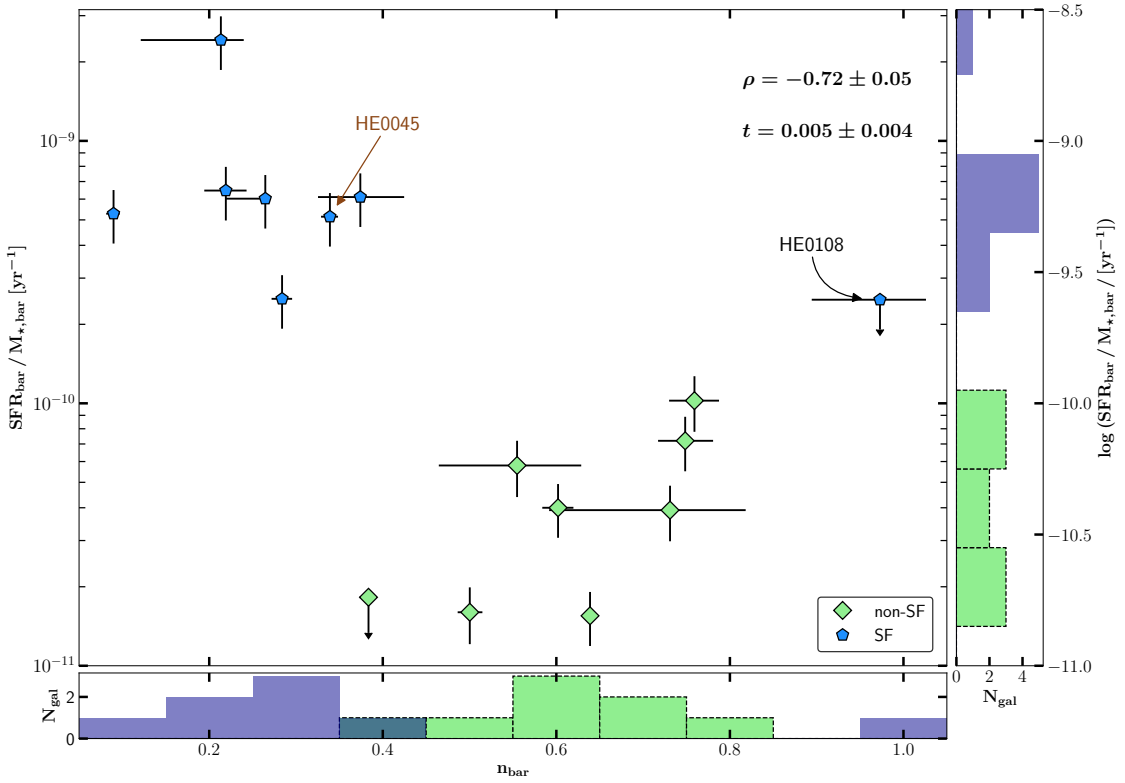

Figure 3.7: Comparison between the sSFR and the Sérsic index of the bar. The s_bSFR_b is the SFR normalised by the stellar mass of the bar in the intermediate bar region that includes the rows −3 to −1 and 1 to 3 as defined in Fig. 3.5. The index n_{bar} is the Sérsic index of the main bar component *bar1*. The objects are divided into non-SF (green) and SF (blue) according to the classification in Fig. 3.6. The *bottom* and *right panels* present histograms for both parameters. There is a clear separation in $\log(s_bSFR_b)$ as we have seen before. The separation is also apparent in n_{bar} with only marginal overlap. The galaxy HE0108-4743 annotated in black is discussed separately in the text. HE0045-2145 (indicated with a brown arrow) is the only galaxy not hosting an AGN in the sample. The error bars for n_{bar} show the 68% confidence intervals from the posterior distribution of our bootstrap resampling method. More details about the uncertainties can be found in the main text and Appendix 3.A.1. In the top right corner, we show the Spearman's rank correlation coefficient ρ and the t-value for a null-hypothesis test.

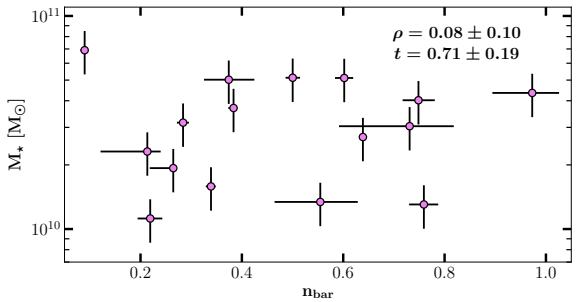

Figure 3.8: Comparison between total stellar mass and bar Sérsic index. Error bars show bootstrap errors on the x-axis and 0.1 dex uncertainties from the calibration in Taylor et al. (2011) on the y-axis. The Spearman's rank correlation coefficient ρ and the t-value for a null-hypothesis test are given in the top right corner. The results show no indication for a correlation between the two parameters in the given mass range.

plot the Sérsic model of the bar. In the case of multiple bar components in our fit, we show only the main component *bar1*. All non-SF bars are on the left side and all SF accordingly on the right side.

While keeping in mind the special case of HE0108-4743 the following observations can be made. For non-SF bars, the bar profiles are approximately exponential within the bar extent. The scale length of the bar is smaller than that of the disc. Considering the smaller scale length of the bar and a generally larger central surface brightness as compared to the disc, both profiles of the bar and the disc are in the majority of the cases crossing.

For SF bars, the variation of the profiles with radial distance is generally higher than among the non-SF bars. The inner parts tend to be flatter with a scale length of similar size to that of the disc. Further out, the profiles show a sharp drop that usually starts before the measured end of the bar.

In summary, the surface brightness profiles of SF bars are similar to those of their corresponding discs in the inner 50–80% of their lengths, where they reach a drop-off point. In contrast, non-SF bars have much smaller scale lengths with no clear down bending at the end or near the end of the bar. Compared to the bar Sérsic index, we note that both methods are able to make the same

distinction between both classes of objects. However, the results of $n_{\rm bar}$ give the impression that non-SF bars are more similar to their discs by having close to exponential Sérsic indices; yet the direct observations of the profiles yield contrary conclusions since their scale lengths are substantially shorter than the scale lengths of their host discs. All in all, $n_{\rm bar}$ can be used as a measure of the flatness of the bar, but a bar with a close-to-exponential index should not be considered to be more similar to the disc than a bar with a smaller index.

3.6.4 Morphology of host galaxy

Some previous studies have reported that the aforementioned bar features correlate with the morphological type of the host galaxy. Early-type disc galaxies have been found to have flat (e.g. Elmegreen & Elmegreen, 1985; Elmegreen et al., 1996; Ohta, 1996) and non-SF bars (e.g. Phillips, 1996). In contrast, late-type discs have supposedly exponential and SF bars.

We performed a classification into Hubble types (see Sect. 3.2 and Table 3.2) and compared them with the parameters $n_{\rm bar}$ and $s_{\rm b}SFR_{\rm b}$ in Fig. 3.10. The distributions show no significant differences between early-type (Hubble type $T \leq 3$, 10 objects) and late-type ($T > 3$, 6 objects) spiral galaxies for either of the parameters. A k-sample Anderson-Darling test shows that they are consistent with being drawn from the same parent population.

Our sample comprises four galaxies with an inner ring (HE0021-1819, HE1017-0305, HE1330-1013, and HE2211-3903). An inner ring is usually defined as the ring-like structure that lies just outside the bar. Interestingly, all four galaxies are non-SF within the bar, while they show some star formation along the ring. However, not all non-SF bars co-exist with inner rings. Inner rings may be connected to the star formation activity in the bar (or absence thereof), but their presence is not a necessary condition for non-SF bars.

3.6.5 Spatial distribution of star formation

In addition to distinguishing between star formation that is happening inside or outside the bar, we can also pinpoint the direct location (in 2D projection) of SF sites within the bar. In Fig. 3.5 we showed the bar mask used for this measurement. Instead of using the total sum of star formation in the bar, it is also possible to plot a radial profile of SFR for each galaxy. Fig. 3.11 shows the SFR along the bar major axis (row number −4 to 4 in Fig. 3.5). Each bin shows the sum of the three columns −1 to 1, it is therefore not a cut across the major axis, but contains the whole SFR within the width of the bar.

In addition to the applied method to disentangle Hα flux from AGN and star formation, we also excluded the central bin from this plot. We do not observe any significant difference between both sides of the bar. On average, the figure shows a trend of decreasing SFR with radial distance for SF bars, although the scatter is large and some individual objects show the opposite trend. The cause of that could be an effect of gas density or other local variables. This trend agrees with findings of radial decreasing numbers of core-collapse supernovae (e.g. Hakobyan et al., 2009; Herrero-Illana et al., 2012), which have been found to follow Hα distributions in SF galaxies (Anderson & James, 2009).

A look at the distribution across the three columns of the mask (going perpendicular to the bar major axis) helps us to understand whether the star formation is preferentially happening either on the leading or the trailing edges of the bar. We define the direction of rotation of the bar under the assumption that spiral arms are trailing in our galaxies. In Fig. 3.12 we plot the SFR of the leading edge against the SFR of the trailing edge. We recognise that for all but one bar the star formation is stronger on the leading edge. There is an even strong indication for a correlation between the SFR on both edges. A Pearson test for linear correlation yields a correlation coefficient of $\rho = 0.96 \pm 0.01$. The result of a linear regression is given by $SFR_{\rm trailing} = (0.58 \pm 0.09) \times SFR_{\rm leading} + (0.00 \pm 0.01)$. The prevalence of star formation on the leading edge of the bar is in good agreement with previous observations (e.g. Sheth et al., 2002) and simulations (Athanassoula, 1992b; Renaud et al., 2015). Observationally, molecular gas clouds are predominantly found on the leading edges. This has been confirmed in simulations by converging flows and large-scale shocks that yield higher gas densities. Additionally, Renaud et al. (2015) found that tangential velocity gradients are less strong on the leading edge that makes it easier for the gas clouds to collapse and form stars. The spiral-like pattern that can be seen in the SFR maps in Fig. 3.5 and Figs. 3.21 to 3.23 is typical. This pattern follows the leading edges of the bar (frequently traced by dust lanes), which is built inside corotation from the *x1* orbits parallel to the bar. If there are two inner Lindblad resonances (ILR) there are *x2* orbits perpendicular to the bar, and a possible nuclear bar inside a nuclear ring, to trigger further gas infall to the centre of the galaxy. (Athanassoula, 1992b; see also Kim et al., 2012; Sormani et al., 2015; Fragkoudi et al., 2016).

3.7 Discussion

3.7.1 Comparison with previous works

3.7.1.1 Flatness of the bar

In Elmegreen & Elmegreen (1985), the authors classified 15 barred galaxies into bars with flat and exponential-like surface brightness profiles based on *I*-band surface photometry on photographic plates. A bar is described as flat if the major axis profile is flatter than the outer profile along the spiral arm and it is exponential if it is similar or even steeper than the spiral profile. They further subdivide the flat bars into a group of bars with flat interbar intensity profiles and a group with much faster interbar intensity decrease. When compared to Hubble types, flat bars are

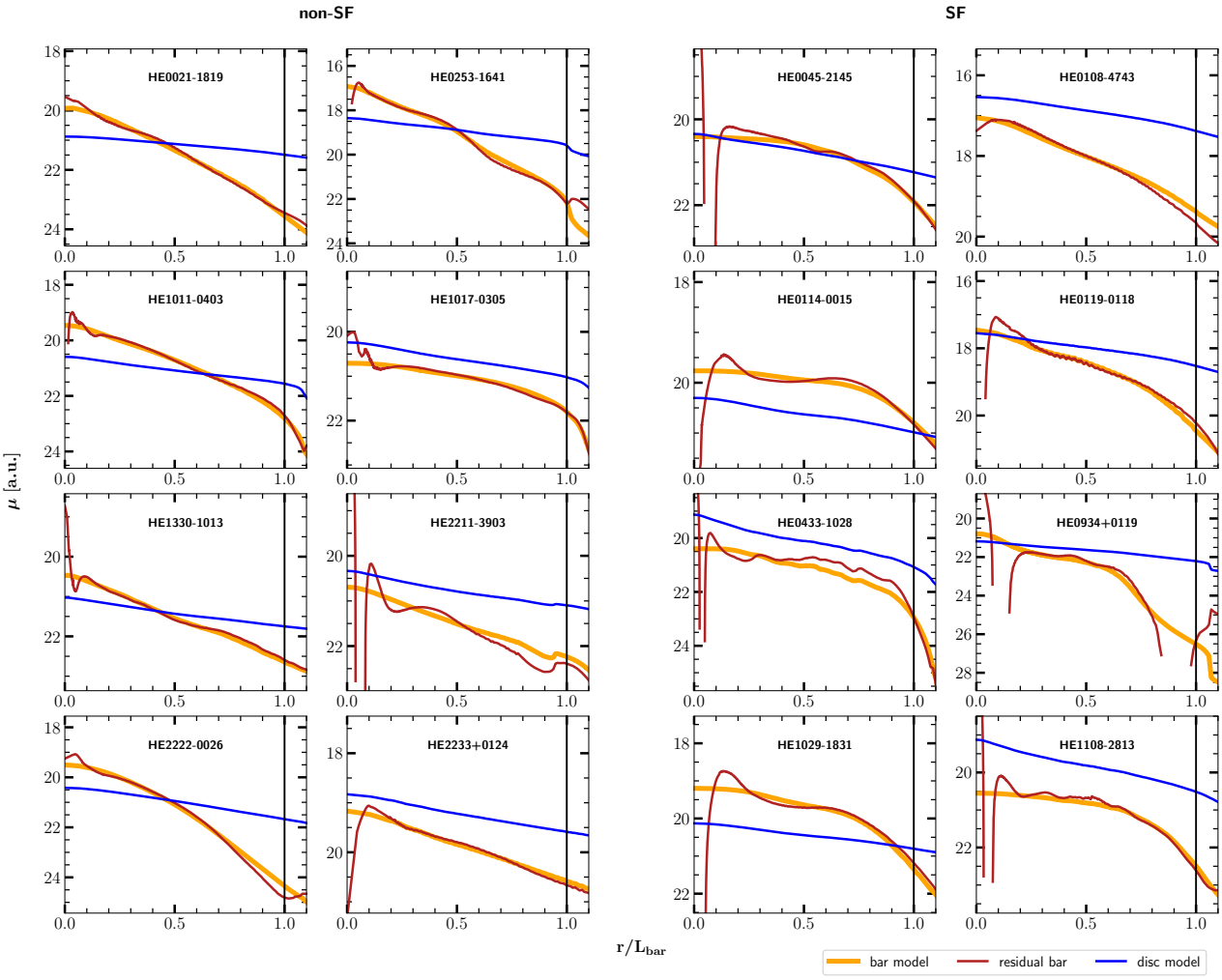

Figure 3.9: Residual surface brightness bar and disc profiles. On the x-axis we plot the radial distance from the centre of the galaxy along the bar major axis normalised by the bar length. The latter is shown by a vertical black line. On the y-axis we plot the surface brightness. The bar residuals are indicated in red. The orange line shows the surface brightness of the model bar component using a Sérsic profile. The blue line shows the exponential disc profile. All profiles were extracted from the 2D image using the ellipse fitting method. The subplots are grouped according to our classification into SF and non-SF bars.

preferably found in early-type spiral galaxies, while late-type spirals tend to have exponential bars. These findings were confirmed in Elmegreen et al. (1996) with a (partially overlapping) sample of 19 barred galaxies in the *B*, *I*, *J*, and *K* band on CCD detectors. In the latter work, they do not use the spiral arm profiles, but a straight continuation of the major axis profiles into the disc. They also plot minor axis profiles instead of interbar averages. The main result is that flat bars are located in SBb-SBc galaxies and exponential bars in SBc-SBm types.

In this work, we do not find a correlation between Hubble type and flatness of the bar. Our estimate of the flatness is based on the Sérsic index of the main bar component from a 2D photometric decomposition. A comparison of this estimate with residual bar light profiles in Sect. 3.6.3 confirmed our classification. In addition, for the purpose of a cleaner comparison to Elmegreen & Elmegreen (1985), we constructed major and minor axis light profiles for our sample shown in Fig. 3.16. By purely examining the major axis profiles, we find only four bars that are exponential-like, i.e. HE0021-1819, HE0108-4743, HE2222-0026, and HE2233+0124. The Sérsic indices of these bars are between $0.55 \leq n_{\rm bar} \leq 0.97$, thus, they are among the larger values. Their Hubble types range from SBa to SBc. All other bars have flatter profiles. This analysis confirms our result that there is no preferred Hubble type for a flat or for an exponential bar. Both types of bars occur from SBab to SBc. However, we do not cover types later than SBcd.

Given the limited sample sizes and the subjectivity of Hubble type classification, we refrain from claiming global statements, but with our detailed analysis of surface brightness profiles of galaxy bars using high quality data, we caution that a relation between the flatness of the bar and Hubble type is not as simple as hitherto thought.

3.7.1.2 Star formation within the bar

A correlation between Hubble type and star formation along the bar was reported in Phillips (1993), Phillips

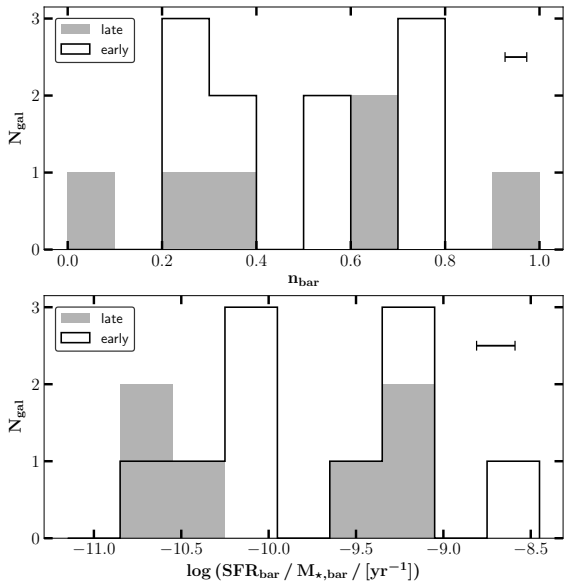

Figure 3.10: Morphology of the host galaxies. Comparison between early-type (Hubble type $T \leq 3$, 10 objects) and late-type ($T > 3$, 6 objects) spiral galaxies. *Upper panel:* Distribution of the Sérsic index of the primary bar component $n_{\rm bar}$. *Lower panel*: Distribution of the sSFR in the bar region s_bSFR_b. The median errors of $n_{\rm bar}$ and $\log(s_bSFR_b)$ are shown in the upper right corner. A typical error of Hubble type classifications for spiral galaxies is $\sigma = 1.01$ T-types (based on ¿700 classification of 5 observers, Walcher et al., 2014). A k-sample Anderson-Darling test yields that the hypothesis that the early- and late-type galaxy samples are drawn from the same parent distribution cannot be rejected for either the Sérsic index nor s_bSFR_b with significance levels of 92% and 55%, respectively.

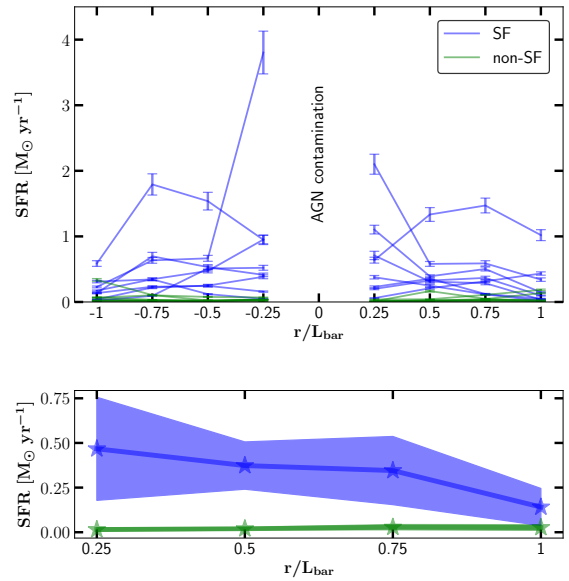

Figure 3.11: *Upper panel:* Distribution of the SFRs across the bar parallel to the bar major axis. Each data point shows the integrated SFR (y-axis) within the corresponding row (x-axis) in the bar mask as indicated in Fig. 3.5. Each line corresponds to one object. The SF bars are shown in blue and non-SF bars are indicated in green. The central row is not shown since the SFR is very uncertain, because of over or under subtraction of AGN contamination. *Lower panel:* Median of both sides of the bar and all objects within each category. The shaded regions show the median average deviation (MAD). On average, the SFR of SF bars is decreasing with distance.

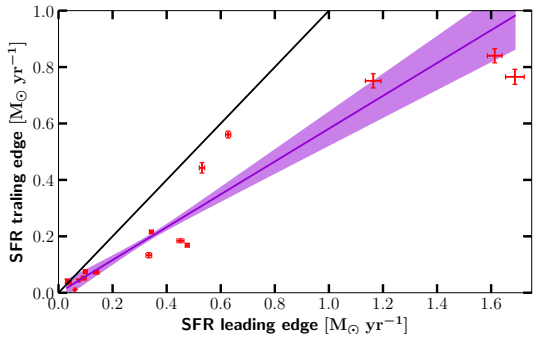

Figure 3.12: Comparison between the SFR on the leading and on the trailing edge of the bar. The black solid line shows a hypothetical one-to-one correlation. The data suggest a linear correlation that was tested with the Pearson correlation coefficient that yields $\rho = 0.96 \pm 0.01$. The violet solid line shows a linear regression of the form $y = m \cdot x + c$ with the parameter estimates $m = 0.58 \pm 0.09$ and $c = 0.00 \pm 0.01$. On average, the SFR is stronger on the leading edge of the bar by a factor of 1.76.

(1996) and García-Barreto et al. (1996). In these works the authors use narrowband Hα images to analyse the distribution of SF sites in the galaxies. The sample in Phillips (1993) comprised 15 barred spiral galaxies of SBb to SBc Hubble types. He found that SBb galaxies have moderate to no star formation along the bar, while SBc galaxies have luminous H II regions within the bar. In Phillips (1996), in addition to the previously mentioned sample the author included Hα observations from the literature (without precise specification), concluding that galaxies of SBb and earlier types show no star formation in the bar, whereas bars in SBbc and later galaxies are actively SF. Similarly, García-Barreto et al. (1996) found that 18 out of 52 barred spiral galaxies in their sample show star formation within the bar. Five of these 18 galaxies are SBb or earlier and 13 galaxies are SBbc or later.

In this work, we conducted a detailed measurement of SFRs based on dust-corrected and AGN-star formation deblended Hα measurements in spatially resolved, well-defined regions within the bar. Our Fig. 3.10 shows no correlation of star formation activity in the bar with Hubble type. In fact, galaxies of the same type can host both SF and non-SF bars. A nice example shows the comparison of HE1108-2813 with HE1017-0305. Both galaxies are classified as SBc, yet the former is actively SF ($SFR_b = 2.53\ M_\odot\ yr^{-1}$) within the bar and the latter is not ($SFR_b < 0.11\ M_\odot\ yr^{-1}$). This can clearly be seen already in the Hα contours in the images in Fig. 3.1. In summary, we show that bars of all Hubble types between SBa and SBcd can be SF and non-SF.

3.7.2 AGN feeding

Simulations have succesfully shown that the gravitational potential of a large-scale bar induces gas inflow towards the centre of the galaxy through torques and angular momentum transfer. Thereby they are able to provide the fuel for nuclear activity (Shlosman et al., 1989, 1990; Piner et al., 1995; Fragkoudi et al., 2016). Such inflows have

been seen observationally in Holmes et al. (2015), who finds non-circular flows in Hα velocity fields in 12 out of 29 galaxies with 11 of 12 stemming from bars.

Observational evidence trying to link the presence of a bar to AGN activity is still not conclusive. To test the scenario of bar-driven AGN feeding, studies have compared the incidence of bars in active and non-active galaxies as well as the incidence of AGN in barred and unbarred galaxies. While some of these studies report results that support the hypothesis that bars fuel AGN (Knapen et al., 2000; Coelho & Gadotti, 2011; Oh et al., 2012; Alonso et al., 2014; Galloway et al., 2015), others find no significant correlations (Mulchaey & Regan, 1997; Ho et al., 1997; Cheung et al., 2015a). Oh et al. (2012) point out the importance of breaking degenerate correlations between bar effects and galaxy properties.

Additionally, the influence of bars on AGN has also been studied by measuring the strength of the nuclear activity as compared to the presence and strength of the bar. Cisternas et al. (2013) studied the activity of low-luminosity AGN in 41 barred host galaxies with Chandra X-ray observations and near-infrared Spitzer data and found no correlation between nuclear activity and bar strength, irrespective of galaxy luminosity, stellar mass, Hubble type, and bulge size. Goulding et al. (2017) approached the problem that AGN activity changes on much smaller timescales compared to the lifetime of bars by stacking Chandra X-ray sources as proxy for a time-averaged accretion. These authors also concluded that bars have little or no effect on the nuclear activity. Another possible explanation for a lack of correlation in some studies apart from different timescales is provided by Fragkoudi et al. (2016) who found in their simulations that boxy/peanut bulges reduce the gas inflow rate by more than an order of magnitude. By contrast, in an extensive study of $\sim$ 5000 AGN Alonso et al. (2018) have found that AGN in barred galaxies show an excess of nuclear activity (as measured from $L_{[\mathrm{O\,III}]}$) and accretion rate as compared to AGN in unbarred galaxies.

In this context, it is interesting to investigate whether the capability of a bar to transport gas to the centre and fuel AGN depends on bar properties other than the bar strength. The non-SF and SF bar types in our sample might reflect the dynamical state and age of the bar or its gas content. In the following we test if the star formation activity in the bars of our sample correlates with nuclear activity.

In the upper panel of Fig. 3.13 we plot $\mathrm{SFR_b}$ against the AGN bolometric luminosity (L_{bol}) which we derive from the host-subtracted (see AGN-host deblending procedure, explained in Sect. 3.5) monochromatic luminosity λL_λ (5100 Å) at rest-frame wavelength of 5100 Å following Wandel et al. (1999) and Kaspi et al. (2000). The lower panel shows $\mathrm{s_bSFR_b}$ against the Eddington ratio ($L_{\mathrm{bol}}/L_{\mathrm{edd}}$). There is no indication for a correlation between these parameters in either of the two plots. However, the restricted range in AGN luminosities ($\sim$ 1 dex) and Eddington ratios ($\sim$ 1.5 dex) limits an optimal comparative study. Although bars may enhance the nuclear activity,

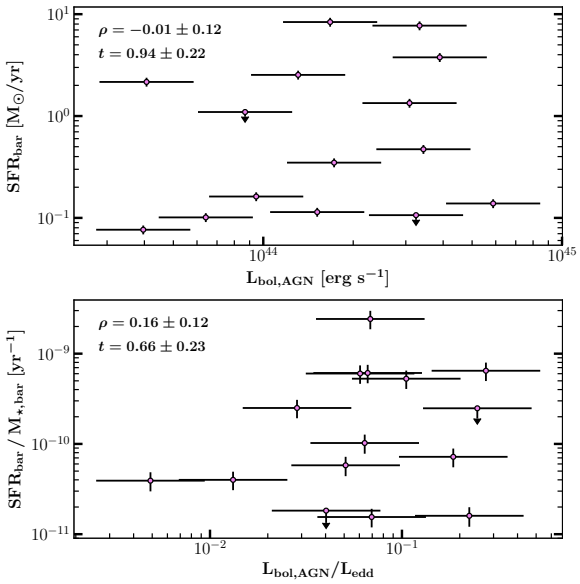

Figure 3.13: Testing AGN feeding: comparison between star formation activity in the bar and nuclear activity in the host galaxy. *Upper panel:* SFR in the bar region against bolometric luminosity of the AGN. *Lower panel:* sSFR in the bar against Eddington ratio. The Spearman's rank correlation coefficient ρ and its t-value for a null-hypothesis are given in the top left corner of each panel. HE0045-2145 is not included because it does not host an AGN.

the effect of SF and non-SF bars does not show clear differences. Nevertheless, a causal connection between bars and AGN activity is difficult to observe owing to the different timescales of long-living stellar bars, variable AGN activity, and tracers of ongoing star formation such as Hα.

3.7.3 Implications on the evolution of stellar bars

Stellar bars form spontaneously from instabilities in the galactic disc (e.g. Athanassoula, 2013). It seems reasonable to assume that as they form from the disc material, they start with similar properties as the underlying disc in terms of radial surface brightness profile (exponential) and ongoing star formation activity (SF) in the early stages of their formation and evolution. As they evolve, bars grow stronger and longer and eventually must stop forming stars because of depletion of gas, as long as there is no external replenishment. Additionally, other processes such as shear may be in place that restrict star formation locally and accelerate the quenching process in the bar. This scenario can be seen for example in the simulation of Khoperskov et al. (2018).

In the present paper, we show that the flattest bars ($n_{\mathrm{bar}} \lesssim 0.4$) – those with very shallow profiles in the log-linear radial surface brightness diagram – are actively SF and bars that are less flat ($0.4 \lesssim n_{\mathrm{bar}} \lesssim 0.8$) are non-SF. If bars evolve from one type into the other, this suggests either that young bars have shallower profiles that grow steeper over time or that non-SF bars can start forming stars at later stages of their evolution. The non-correlation of SFR in the bar with B/T and Hubble T-type can be

explained by a variability of gas in the bar during the evolution.

If we look at the parameters of our sample, we see that this study is missing low-mass galaxies $\left(M_\star < 10^{10}\ M_\odot\right)$, exponential bars ($n_{\rm bar} > 0.8$) , and very late Hubble types (SBcd-SBm). Exponential bars have been connected to low-mass galaxies (Kim et al., 2015) and late-type spirals (Elmegreen & Elmegreen, 1985). Late-type galaxies of low stellar masses with exponential bars, which have been associated with star formation in the bar, could be an important population of bars to complement the evolutionary picture. Nevertheless, our results indicate that the SF bars in our sample are not part of that population. In other words, earlier-type spirals in massive galaxies can host flat and SF bars.

Another important part of the puzzle is the presence of inner rings. Ring-like structures in disc galaxies are often associated with dynamical orbital resonances; but see also Romero-Gómez et al. (2006, 2007) in which the manifold theory is employed to explain such structures. The most important resonances in a barred galaxy are the outer Lindblad resonance (OLR), the corotation resonance (CR) and the inner Lindblad resonance (ILR). Usually the OLR is located at about twice the bar length, the CR just outside the bar region and the ILR well within the bar region (e.g. Comerón et al., 2014). The non-axisymmetric potential of a barred galaxy induces gravitational torques that drive gas outside the CR outwards where it accumulates at the OLR. Gas inside the CR is driven inward towards the ILR and/or the inner 4/1 resonance, which is also called ultra-harmonic resonance (UHR) just inside corotation (Schwarz, 1984; Buta & Combes, 1996). This resonant accumulation of gas can lead to the formation of outer rings at the OLR, inner rings between the UHR, and the CR and nuclear rings at the ILR (see also Buta, 1986; Rautiainen & Salo, 2000)

All four galaxies with inner rings in our sample host non-SF bars. However, not all non-SF bars host inner rings (see Sect. 3.6.4). This indicates that the conditions for a galaxy to quench star formation in the bar might be necessary, but they are not sufficient conditions to develop an inner ring. It could also be a timescale effect. During the evolution of the bar it depletes itself from gas, hence the star formation decreases, while at the same time gas accumulates near the UHR fueling an inner ring. After the formation of the ring it becomes more difficult to replenish the bar region with gas, especially if the galaxy is relatively isolated. This scenario is in agreement with the reciprocal relationship of H II regions between the bar and an inner ring found by Ryder & Dopita (1993). A similar relationship should also be observable between star formation in bars and nuclear rings and would be an interesting subject for a future work.

3.8 Conclusions

We have used MUSE/VLT IFS data from the CARS survey to accurately photometrically decompose a sample of 16 local barred spiral galaxies including up to 7 different components. We additionally derived spatially resolved SFRs from dust-corrected Hα line fluxes and analysed the total amount and the spatial distribution of star formation within the bar component. From a detailed comparison of the obtained parameters, we summarise the following conclusions:

1. There are two classes of galaxy bars: those that show significant star formation (SF bars) and those that have very little to no star formation activity (non-SF bars). A third category of bars with fading star formation in the centre as proposed by Verley et al. (2007) could not be probed because of AGN dominated photoionisation in the central region. The clear separation in s_bSFR_b between SF and non-SF bars indicates that the quenching process must be fast as compared to the lifetime of SF and non-SF bars.

2. The SFR_b and s_bSFR_b correlate with the Sérsic index $n_{\rm bar}$ of the main bar component; in fact, we observe a separation between SF and low-index ($n_{\rm bar} \lesssim 0.4$) bars and non-SF and high-index ($0.4 \lesssim n_{\rm bar} \lesssim 0.8$) bars.

3. We find that SF bars are flatter and have profiles that have a similar slope to that of the underlying disc up to a radius where the brightness suddenly drops, whereas non-SF bars have closer to exponential profiles with a smaller scale length than the disc and no clear downturn within the bar length. The flatness of a bar is a term that has been used in the literature to describe the surface brightness profile of some stellar bars. It is, however, misleading since a flat bar can still be exponential, but with a larger scale length, up to the radius where it turns down. Flat bars might actually be more similar to their discs than exponential bars.

4. There is no significant difference in the distribution of sSFR of the bar (s_bSFR_b) or bar Sérsic index ($n_{\rm bar}$) between early-type and late-type disc galaxies. Both earlier and later types can have star formation or not and can be flat or exponential. This is in contrast to previous reports (Elmegreen & Elmegreen, 1985; Elmegreen et al., 1996; Ohta, 1996; Phillips, 1993; Phillips, 1996). Compared with this literature the range of Hubble types of our sample is similar and we only miss the very late types SBd to SBm, which are however the types previously reported to host exponential bars. Most of the bars in our sample are indeed rather flat. Furthermore, neither the samples in the aforementioned literature nor our sample are of statistically significant size to make global statements, but – given the depth of our analysis – this is a cautionary note: a plain correlation between Hubble type and flatness or star formation activity

might be too simple. Early-type spirals in massive galaxies can host flat and SF bars.

5. The radial distribution of SFR of SF bars is decreasing with increasing distance from the centre.
6. Star formation activity is about 1.75 times stronger on the leading edge than on the trailing edge of the bar, in good agreement with previous works (e.g. Athanassoula, 1992b; Sheth et al., 2002; Renaud et al., 2015).
7. The presence of non-SF bars might be related to the presence of inner rings.
8. The SFR_b is not correlated with the bolometric luminosity of the AGN, nor is s_bSFR_b correlated with the Eddington ratio. Hence, there is no evidence that the star formation activity in the bar affects AGNs feeding. However, given the potential unknowns of the effects of selecting luminous type-1 AGN and the therefore restricted range of AGN luminosities and Eddington ratios, the conclusions from this work may only apply to type-1 AGN hosts. Further work is required to confirm whether they can be extended to the full population of barred galaxies.

Our analysis is by construction based on a sample of AGN host galaxies, which raises the question whether the presence of the AGN affects the SFRs in the bars measured in this work. There is no obvious answer to that. Not only different and uncertain timescales when AGN feedback becomes visible, but also the radial range it affects is still under debate (e.g. Gaspari & Sądowski, 2017; Harrison, 2017). The impact on the results presented in this work is frankly unknown. One of the galaxies, HE0045-2145, which was first misclassified to host an AGN, does not show exceptional results in any way in our analysis. We suggest a comparable study with an AGN-free control sample in the future, but until then there is no reason to believe that barred galaxies without AGN would yield different results. Further papers from the CARS collaboration will address the effect of feedback in the future.

Acknowledgements We thank the anonymous referee for the constructive feedback that helped to improve this paper. We thank Darshan Kakkad, Peter Erwin, and Bruce Elmegreen for useful comments on method and content. TAD acknowledges support from a Science and Technology Facilities Council Ernest Rutherford Fellowship. M.G. is supported by the *Lyman Spitzer Jr.* Fellowship (Princeton University) and by NASA Chandra GO7-18121X and GO8-19104X. MK acknowledges support by DLR 50OR1802.

3.A Uncertainties of the 2D photometric decomposition

3.A.1 Uncertainty of n_{bar}

In this subsection, we discuss two different approaches to estimate the uncertainties of 2D image decompositions; both are implemented in the code IMFIT. The first method uses a bootstrap technique after finding the best fit result. Per iteration, it resamples and replaces a fraction of the data points and repeats the fit using the fast Levenberg-Marquardt minimisation algorithm given the best fit parameter values as initial guesses. We perform the bootstrapping with 1,000 iterations and take the inner 68% range of the posterior distribution as error. The other approach is based on a MCMC analysis. It starts with multiple walkers that explore the parameter space that is given by the user as input. It is completely independent from the best fit result. We choose to equal the number of walkers to the number of free parameters (which range between 11 and 34 depending on the number of model components in the fit) as suggested in the documentation of the code; we used a 5,000 step burn-in phase and an upper limit of 100,000 steps to terminate the script if no convergence is reached. Again, the inner 68% range of the posterior distribution is used as an estimation of the error of the best fit. Given the large number of free parameters, the fit did not converge within a reasonable time for most galaxies even on a multiple-core machine. This is one reason why the MCMC error bars are probably too large for many galaxies. The results of both approaches are shown in Fig. 3.14. We only plot the n_{bar} parameter. It is clearly visible that the MCMC error bars are much larger than the errors derived with the bootstrap approach.

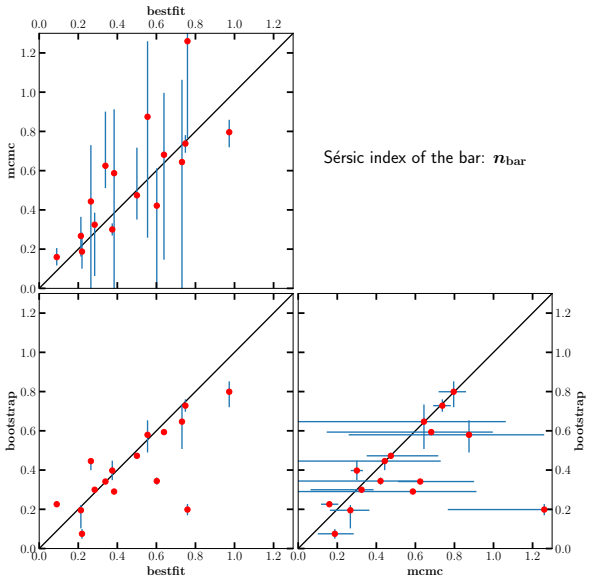

Figure 3.14: Comparison between different methods to fit multicomponent galaxy models to the collapsed 2D MUSE *i*-band images. This plot only shows results for the parameter n_{bar}. The label *best fit* is the best fitting result using the Nelder-Mead simplex minimisation technique and a χ^2 fit statistic for minimisation. The label *bootstrap* gives the result of resampling the pixel values in the data image with 1,000 iterations after the best fit. For time-saving reasons it uses the Levenberg-Marquardt minimisation algorithm. The red data points given in the plot indicate the median value of the 1,000 fits; the error bars show the 0.16 and 0.84 quantiles. The label *mcmc* is the result of applying a MCMC analysis to the data image instead of searching for the best fit model. The data points in the plot indicate again the median value of the posterior distribution; the error bars show the 0.16 and 0.84 quantiles.

For the interpretation of these results it is important to keep in mind that the more components are added to the fit the more degenerate it becomes. Therefore, it is more likely to be trapped in local minima in the χ^2 landscape. The MCMC method strongly differs from the bootstrap technique in the sense that it explores the whole parameter space completely independently from the best fit values. However, because of the degeneracies, in many cases the fit did not converge within a reasonable amount of steps. On the contrary, the bootstrap method with Levenberg-Marquardt minimisation starting at the best fit values is apparently not very likely to get out of a local minimum. The main question that we should probably ask ourselves is what kind of error we want to estimate: uncertainties from observational data, uncertainties from a mismatch between model and reality, or uncertainties from human-made choices for certain model components and initial parameter values. In this context, the results from the MCMC approach demonstrate the spread of possible solutions, if as little assumptions as possible are made. On the other side, bootstrap provides the error given a specific model.

The reason why some of the points in the lower left, best fit bootstrap panel are off the one-to-one line is most probably caused by the different minimisation techniques. The best fit results come from using the slower but more robust Nelder-Mead simplex minimisation while bootstrap uses the fast Levenberg-Marquardt technique. The exact explanation as to why the different algorithms lead to these offsets still needs to be explored in more depth given the complexity of the decompositions. We trust our measurements from the best fit result.

3.A.2 Modelling a synthetic galaxy image

Another way to estimate the accuracy of the photometric decomposition fitting procedure is to create synthetic images of galaxies and subsequently fit these in the exact same manner as was done for the real galaxies. We show as an example the results for one synthetic galaxy that demonstrates how the input parameters can be retrieved satisfactorily.

The image was created using the MAKEIMAGE module of IMFIT. It takes the same component functions that can be used to fit an image and generates a new image. A psf image can be provided to convolve with the object image before the final output (for further details see Erwin, 2015). We selected six input components: a point source, a bulge, three bar components, and a disc. Additionally, we added a flat sky background. The input values for the model parameters were generated randomly within certain limitations to ensure a realistic galaxy image (for example relative sizes and luminosities). After generating the image with MAKEIMAGE we added on top Poisson noise using the MKNOISE function of IRAF.

With no a priori knowledge of the input values, we started the fitting procedure exactly like we did for the real galaxies with a simple point source + exponential disc model. After inspecting the residual images we added other components to the next fit if we had clear visual indications of their presence. As last step we performed bootstrapping with 200 iterations to estimate error intervals. In Table 3.4 we summarise the results. In Fig. 3.15 we show the image of the generated artificial galaxy, the best fitting model and the residual image.

We note that most parameters were successfully retrieved within a range of $\sim 5\%$ deviation including specifically the main bar component *bar1* and its Sérsic index. Only the bulge and the thick bar component *bar2* show larger deviations from the true values. This can be explained by similar sizes and luminosities of both components and thus degeneracies between the corresponding parameters. We point out, however, that the uncertainties in the photometric fits so derived should be considered as lower limits. This is because the structural components of the synthetic images follow the exact same models employed by the fitting software. This assumption might not necessarily hold in real galaxies.

Table 3.4: Synthetic galaxy: Input and best fit values for all model parameters.

Parameter	Model component	Input value	Best fit value	Error	Rel. dev. from input	Within errors 1=true, 0=false
(1)	(2)	(3)	(4)	(5)	(6)	(7)
X0	Position	158.598	158.597	0.003	0.00%	1
Y0		153.462	153.462	0.001	0.00%	1
PA [°]	Point source	0	fixed	fixed	fixed	fixed
ell		0	fixed	fixed	fixed	fixed
I_0 [counts]		167000	169900	4985	1.74%	1
σ		0.1	fixed	fixed	fixed	fixed
PA [°]	Bulge	70.970	85.154	52.559	19.99%	1
ell		0.031	0.235	0.284	646.91%	1
n		1.800	1.646	2.240	8.53%	1
I_e [counts]		17.140	16.942	21.102	1.16%	1
r_e [px]		3.200	3.848	4.295	20.26%	1
PA [°]	Bar1	113.450	113.489	0.088	0.03%	1
ell		0.730	0.731	0.002	0.19%	1
c0		2.000	1.957	0.134	2.16%	1
n		0.320	0.314	0.007	1.92%	1
I_e [counts]		5.200	5.163	0.073	0.71%	1
r_e [px]		32.170	32.321	0.166	0.47%	1
PA [°]	Bar2	113.450	113.451	2.112	0.00%	1
ell		0.160	0.125	0.036	21.94%	1
c0		24.200	30.707	66.273	26.89%	1
n		0.500	0.794	0.191	58.85%	0
I_e [counts]		9.200	14.577	4.075	58.45%	0
r_e [px]		5.100	4.776	0.486	6.36%	1
PA [°]	Bar3	113.450	113.570	0.070	0.11%	0
ell		0.900	0.898	0.002	0.22%	1
c0		1.240	1.301	0.255	4.96%	1
n		0.160	0.154	0.010	3.87%	1
I_e [counts]		7.250	7.234	0.125	0.23%	1
r_e [px]		27.530	27.409	0.253	0.44%	1
PA [°]	Disc	70.970	71.316	0.287	0.49%	0
ell		0.140	0.139	0.001	0.41%	1
I_0 [counts]		20.000	20.021	0.073	0.11%	1
h [px]		28.900	28.774	0.050	0.43%	0
I_{sky} [counts]	Background	0.0010	0.0004	0.0006	59.92%	1

The synthetic galaxy was created with six different structural components and a flat sky background. Poisson noise was added afterwards, but before the fitting procedure. This table gives an overview of the input values as well as all 31 simultaneously fitted free parameters and 3 fixed parameters. (1) Parameter; (2) structural component of the model; (3) input value to create the synthetic galaxy; (4) best fit value; (5) 1σ error estimate from bootstrapping with 200 iterations; (6) relative deviation of the best fit value from the input value; and (7) check whether the input value lies within the 1σ interval of the best fit result.

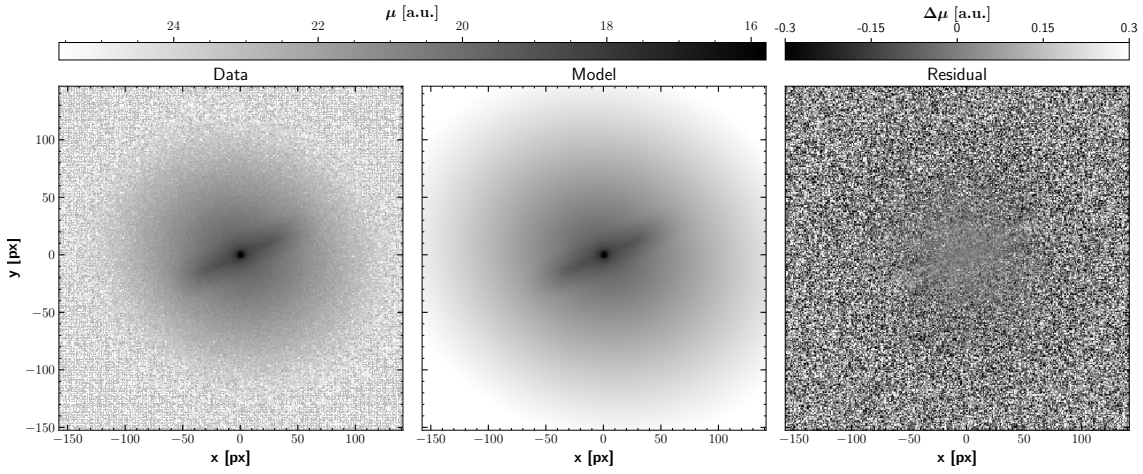

Figure 3.15: Photometric decomposition of generated artificial galaxy image. From *left* to *right*: data image, model, and residual=data-model. The greyscale mapping in the residual image is stretched in order to show faint details.

3.B Major and minor axis surface brightness profiles

In Fig. 3.16 we present surface brightness profiles along the major and minor axis of the stellar bars. These were directly extracted from the collapsed *i*-band images of the MUSE cubes. We used these profiles to mimic an analysis similar to Elmegreen & Elmegreen (1985) and Elmegreen et al. (1996) and compare our results with theirs; see Sect. 3.7.1.1 for further details.

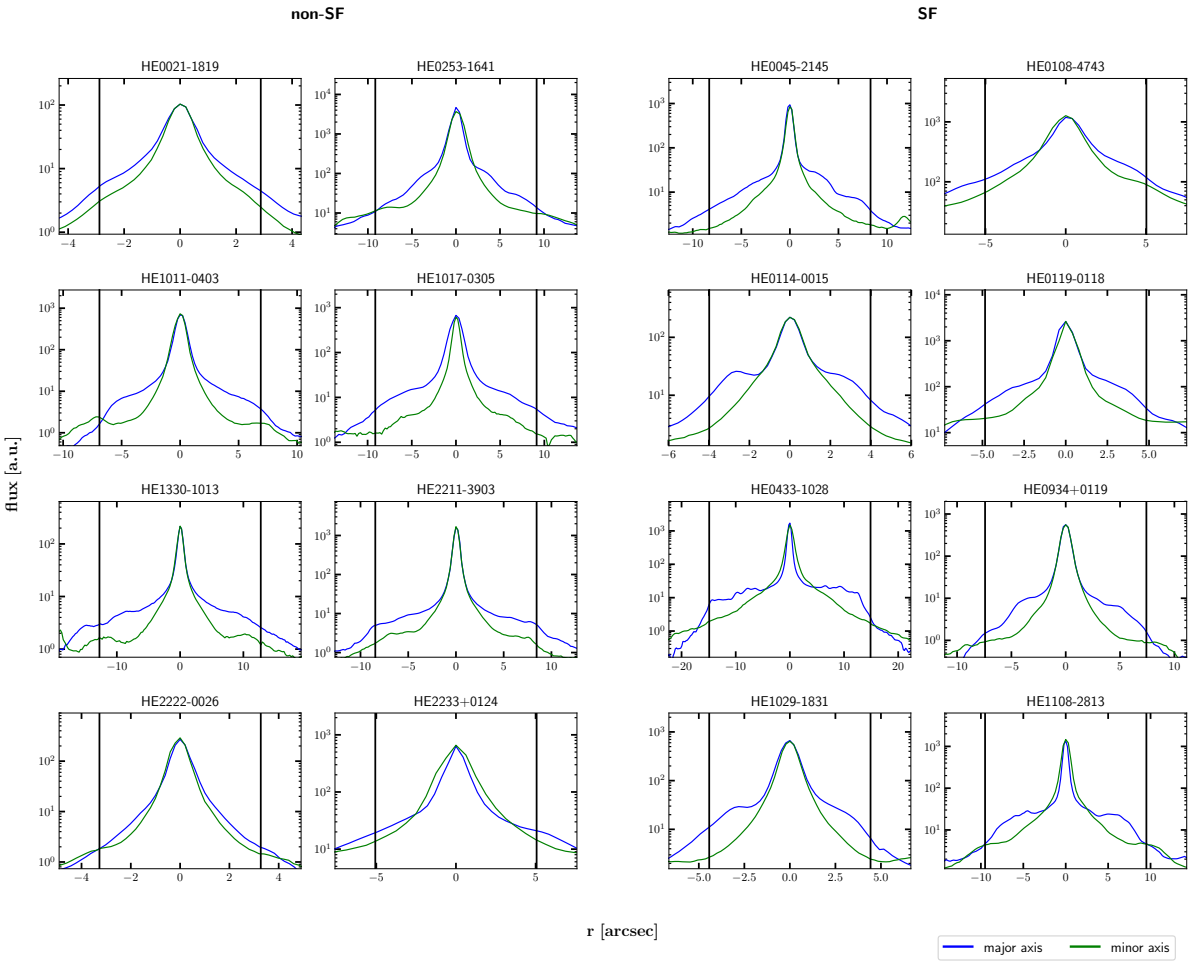

Figure 3.16: Radial surface brightness profiles along the major (blue) and minor (green) axes of the bar and continued into the disc. The distance on the x-axis is deprojected and scaled to the galaxy plane. The length of the bar is denoted by vertical black lines

3.C Photometric image decomposition

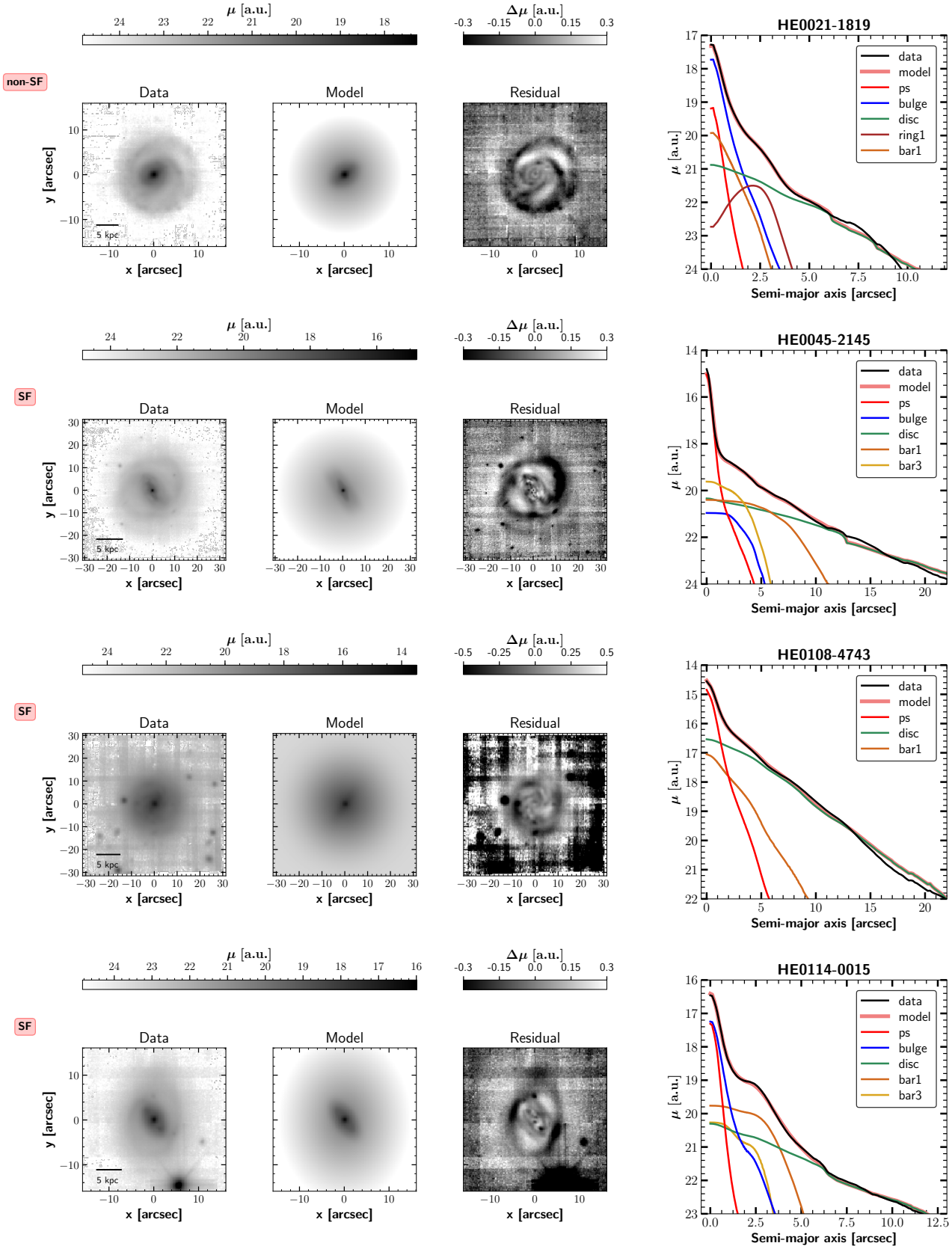

Figure 3.17: Same as Fig. 3.2. Photometric image decomposition of the complete sample.

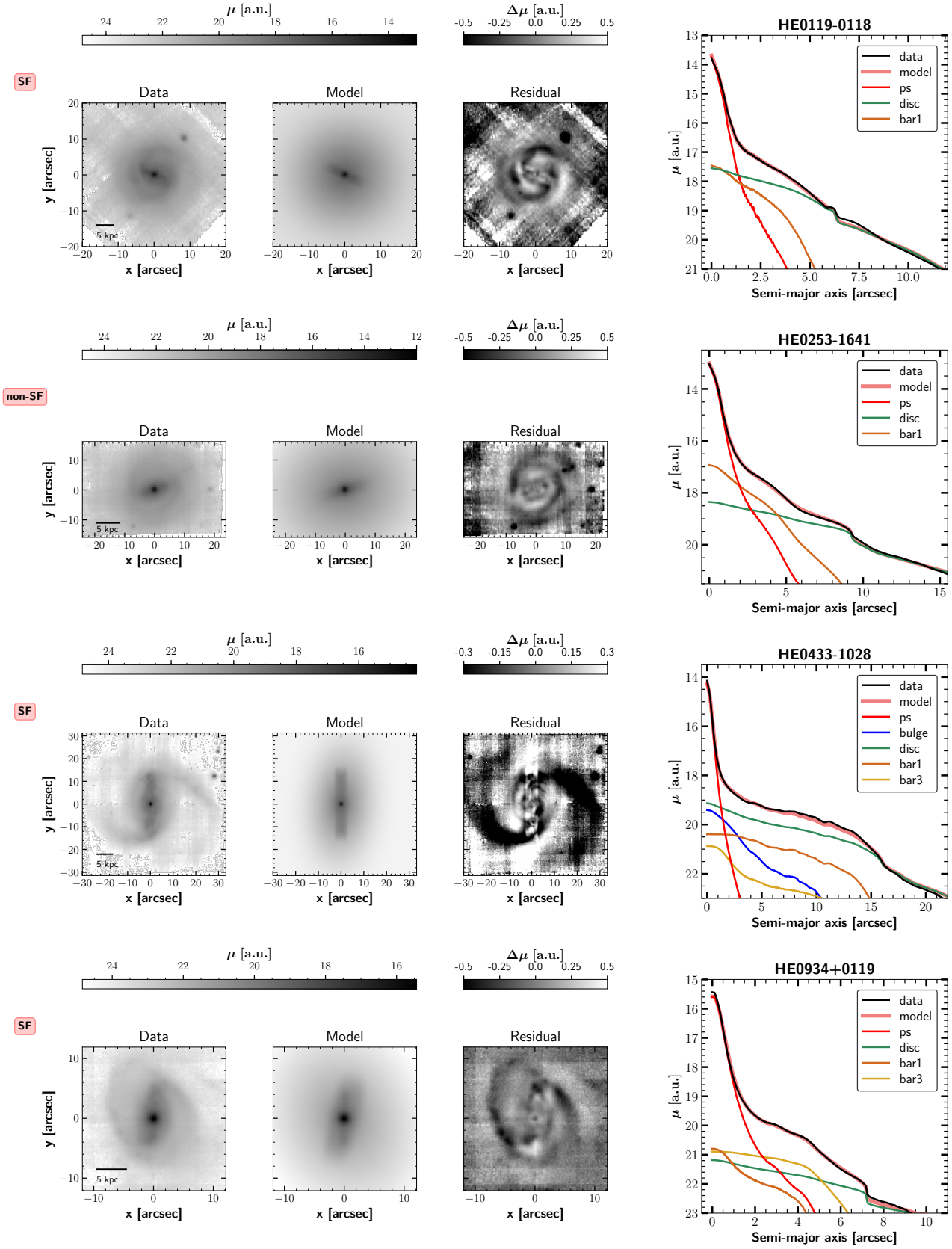

Figure 3.18: continued.

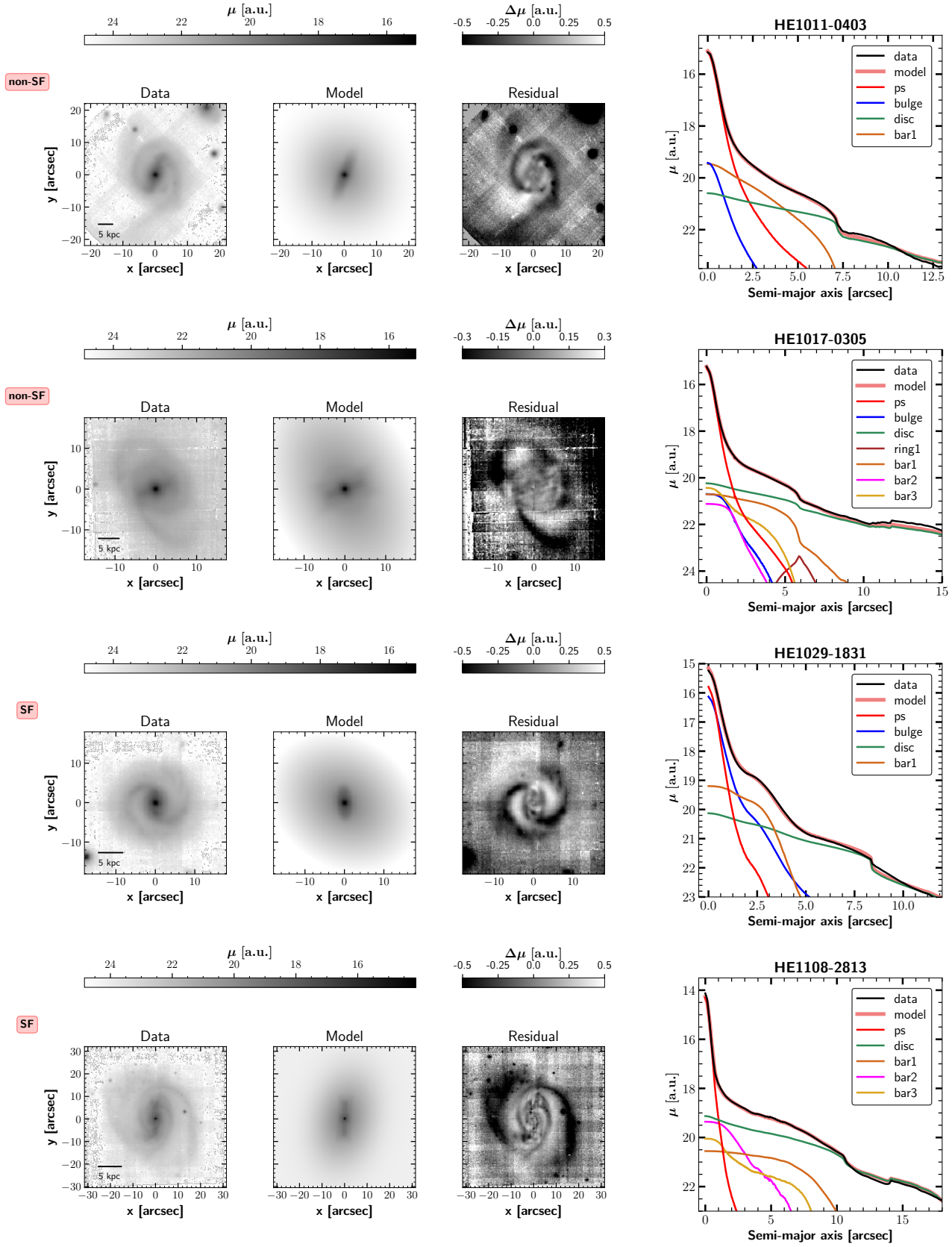

Figure 3.19: continued.

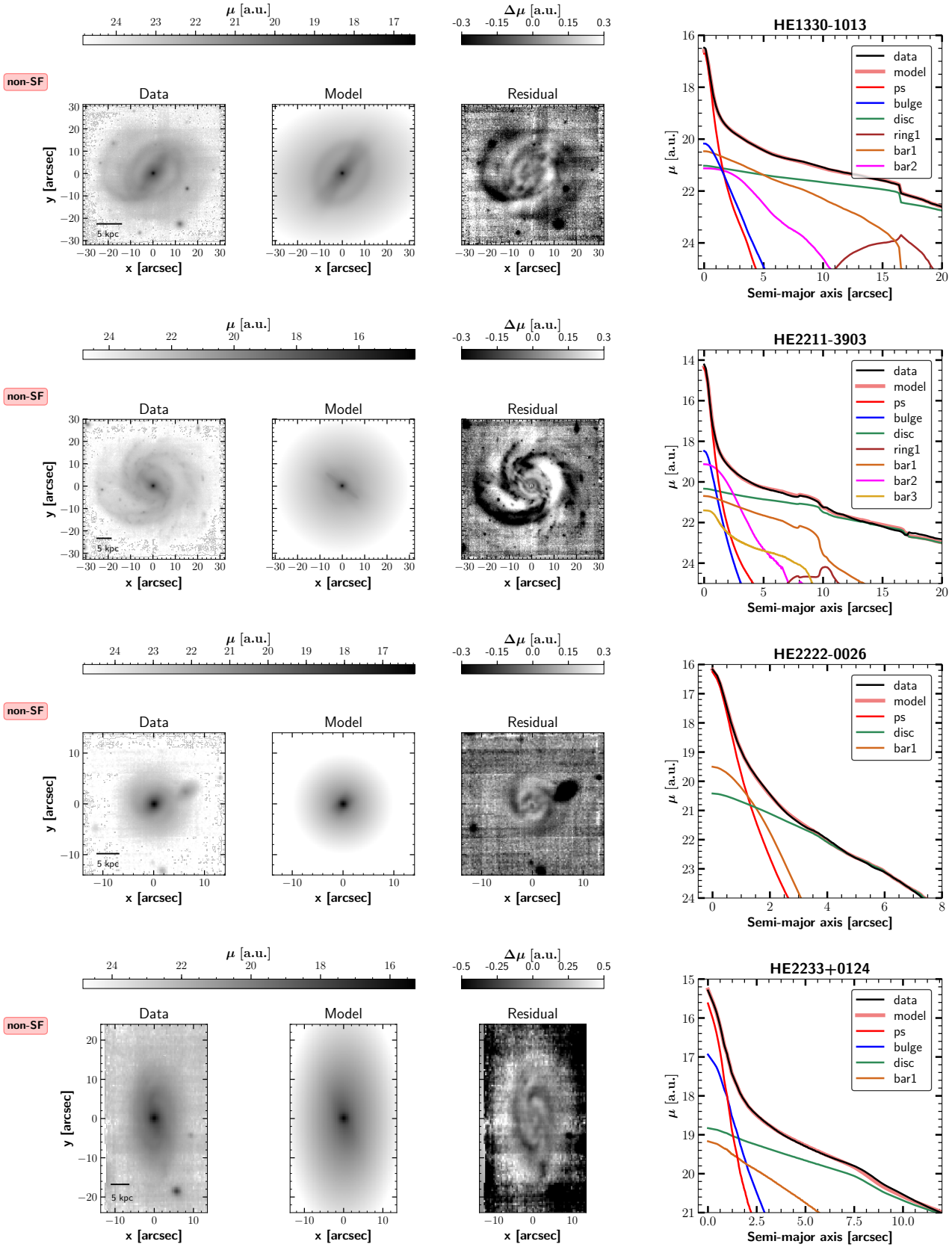

Figure 3.20: continued.

3.D Spatial distribution of star formation

In this section we show the spatial distribution of star formation for the entire sample used in this work. The figures are of the same format as Fig. 3.5. The coloured pixels are showing the SFR per spaxel in the MUSE cube overplotted with a 3×9 grid outlining the region of the bar. This grid is used in the next step of the analysis to rebin the spectra in each cell and estimate the corresponding SFR per bin as described in Sect. 3.5. Additionally to Fig. 3.5, here, we also show in blue isophotal contours from the *i*-band image of the galaxy. In the case of galaxy HE1108-2813, the PA of the grid has been adjusted carefully (by 7 deg counterclockwise) to capture fully the star formation that clearly comes from the bar and avoid as much as possible contaminant star formation from spiral arms. This is caused by the offset of the PA of Hα as compared to the stellar bar towards the leading edge as discussed in Sect. 3.6.5. The spiral-like pattern seen in many SFR maps follows the typical pattern of infalling gas along the *x1* and *x2* orbits of the bar.

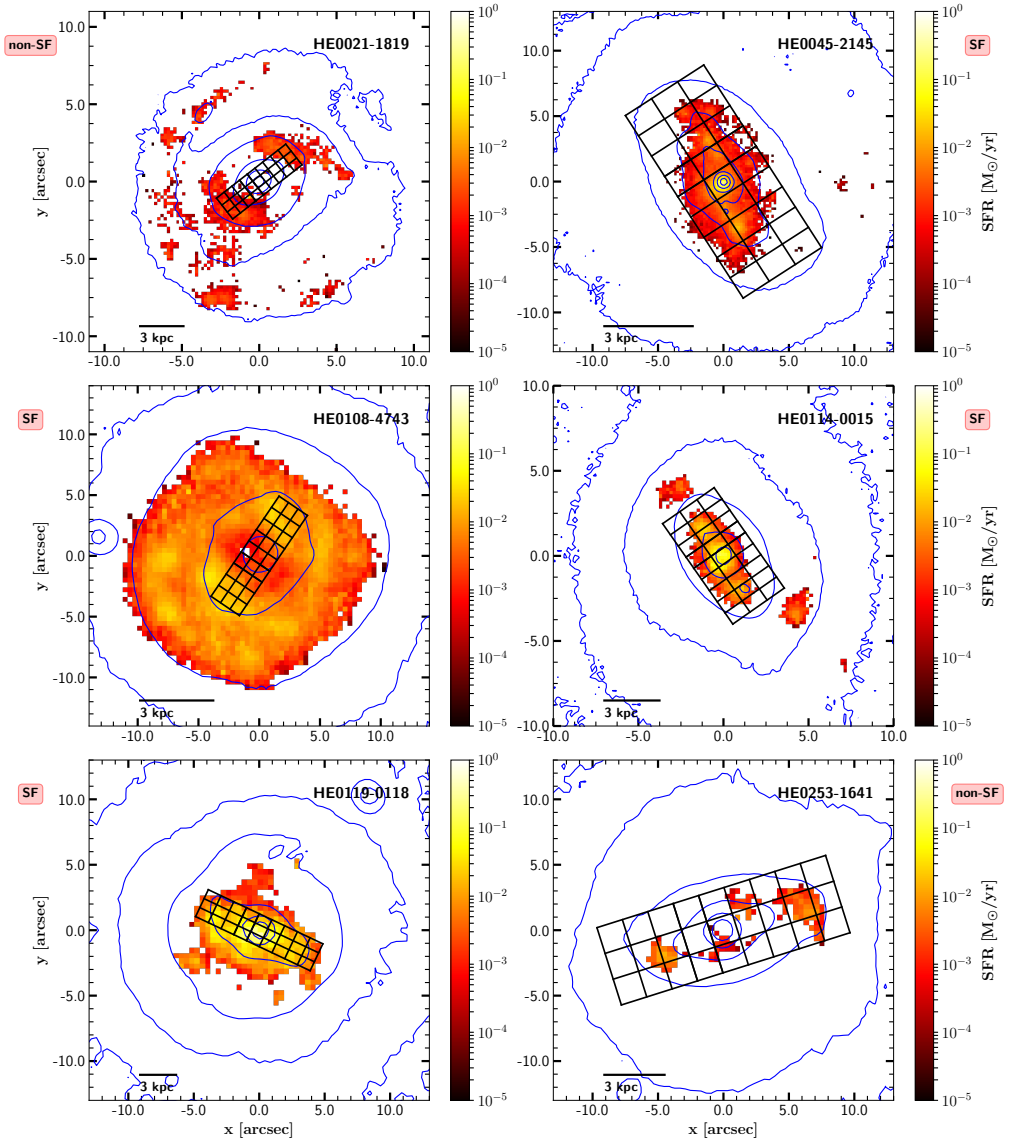

Figure 3.21: Same as Fig. 3.5. Spatial distribution of SFR of the complete sample. We also show blue contours of the *i*-band image of the galaxy.

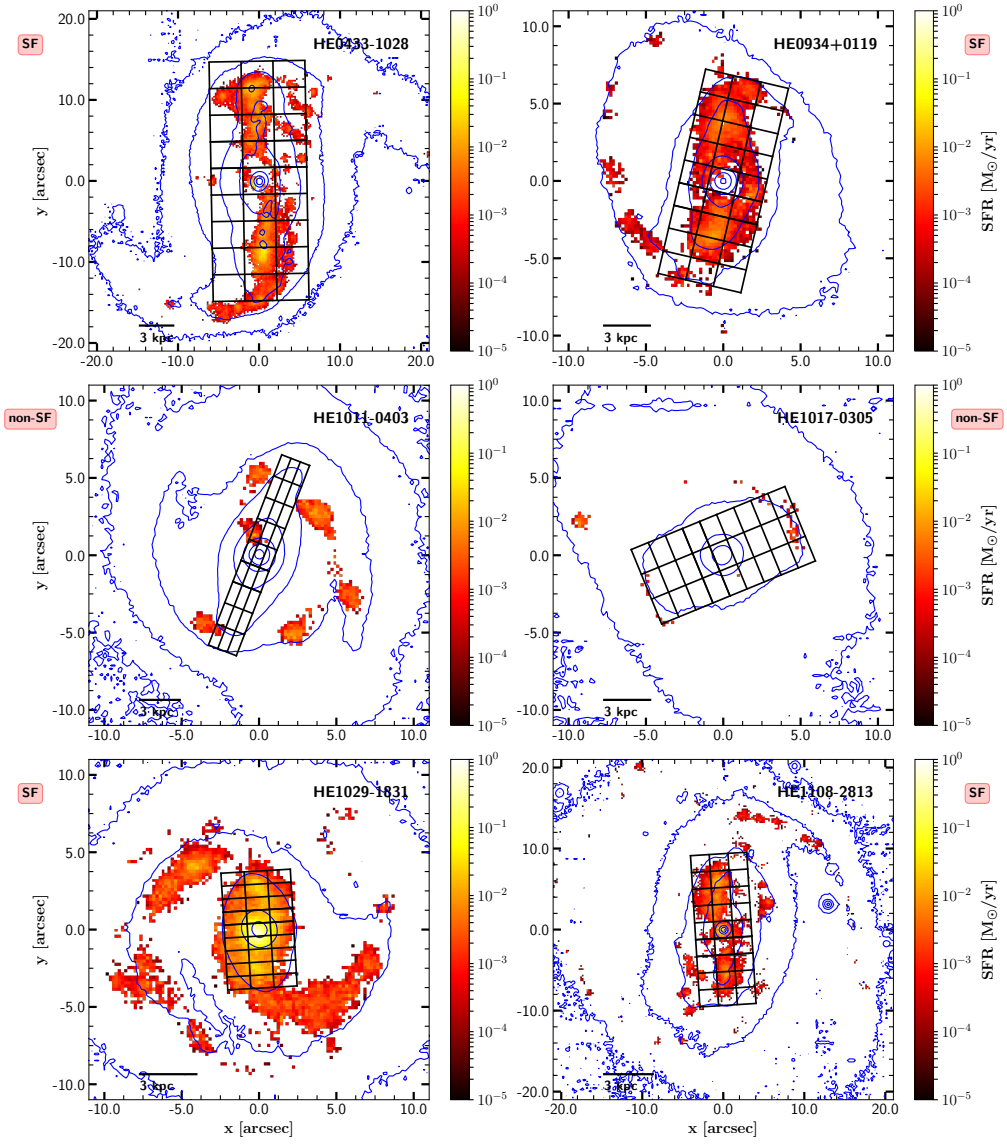

Figure 3.22: continued.

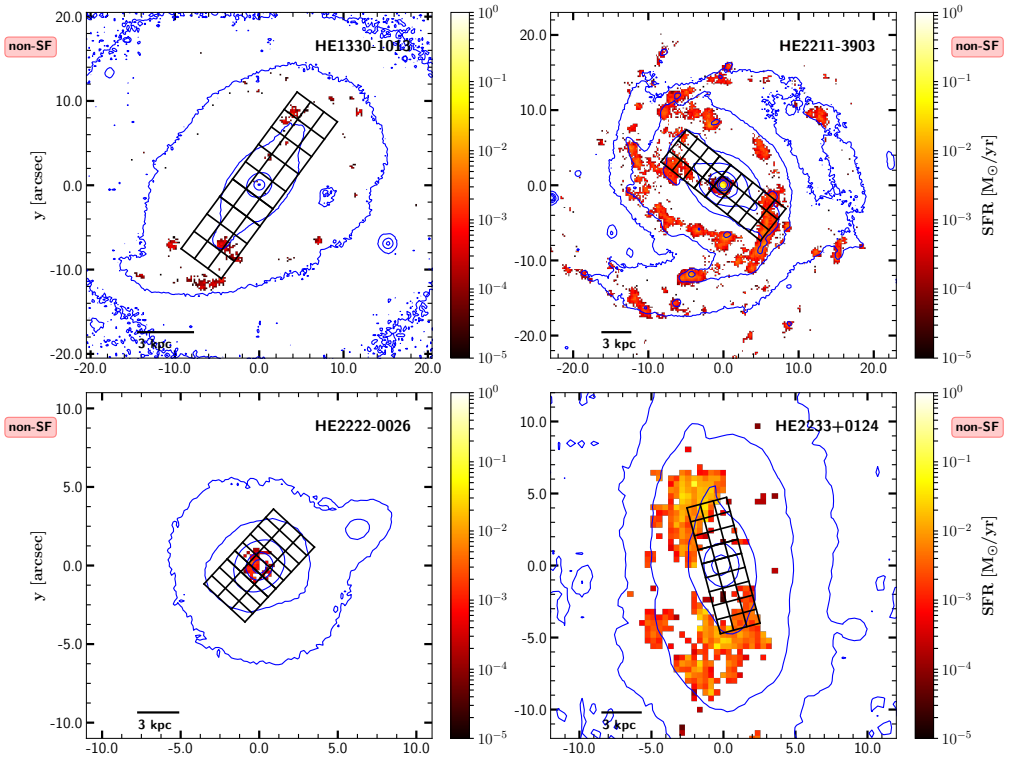

Figure 3.23: continued.

4 Stellar populations across galaxy bars in the TIMER project

J. Neumann, F. Fragkoudi, I. Pérez, D.A. Gadotti, J. Falcón-Barroso, P. Sánchez-Blázquez, A. Bittner, B. Husemann, C.E. Donohoe-Keyes, Taehyun Kim, A. de Lorenzo-Cáceres, Marie Martig, Jairo Méndez-Abreu, Glenn van de Ven et al.

ABSTRACT

We present a detailed analysis of star formation histories and chemical enrichment of stellar populations in galaxy bars. We use integral field observations with the MUSE instrument of nine nearby barred galaxies from the TIMER project to derive spatially resolved maps of stellar ages and metallicities, [α/Fe] abundances, star formation histories, as well as Hα as tracer of star formation. We find observational evidence that supports the concept that in a bar potential intermediate-age stars ($\sim$ 2-6 Gyr) get trapped on more elongated orbits forming a thinner bar, while old stars ($>$ 8 Gyr) form a rounder and thicker bar. This evidence is further strengthened by very similar results obtained from barred galaxies in the cosmological zoom-in simulations from the Auriga project. Additionally, we find imprints of typical star formation patterns in barred galaxies on the youngest population ($<$ 2 Gyr), which continuously becomes more dominant from the major axis towards the sides of the bar. This observation coincides with the appearance of star formation at the sides of the bar while it is mostly absent within all bars in the sample. The effect is stronger on the leading edge. Stellar metallicities in the bars are on average higher than in the disc. Except for a pronounced peak in the centre, however, the gradients are shallow and mostly negative when light-weighted and scattered around zero when mass-weighted ($-0.15 < \Delta$[Z/H] < 0.15). Finally, we find that bars are less α-enhanced than the inner parts of the discs that surround them.

A version of this chapter is published as Neumann J., et al., *Astronomy & Astrophysics*, 2020, Vol. 637, id. A56, 28 pp.

4.1 Introduction

Most disc galaxies in the nearby Universe are barred. Numerous observational studies find fractions on the order of 70-80% (Eskridge et al., 2000; Menéndez-Delmestre et al., 2007; Aguerri et al., 2009; Masters et al., 2011; Buta et al., 2015; Erwin, 2018). In principle, one would expect this number to be even larger, since bars are long-lived (Gadotti et al., 2015) and it is extremely difficult to avoid bar-forming instabilities in the disc in galaxy simulations (e.g. Berrier & Sellwood, 2016; Bauer & Widrow, 2019). These statistics already demonstrate that studying the ubiquitous bars is essential for the global understanding of galaxy evolution.

Bars are very efficient in the radial redistribution of matter and angular momentum and thereby drive the formation of nuclear structures such as nuclear bars (de Lorenzo-Cáceres et al., 2012, 2013), nuclear rings or inner discs (Debattista et al., 2006; Athanassoula, 2013; Sellwood, 2014), as well as outer structures like inner and outer rings (see also Buta, 1986; Buta & Combes, 1996; Rautiainen & Salo, 2000). At the same time they are believed to intensify the global cessation of star formation in late stages of galaxy evolution (Hakobyan et al., 2016; Haywood et al., 2016; Khoperskov et al., 2018; George et al., 2019). The role of bars in feeding active galactic nuclei (AGN) by transporting gas inwards is a heavily discussed subject and still somehow inconclusive (Ho et al., 1997; Coelho & Gadotti, 2011; Oh et al., 2012; Cheung et al., 2015a; Galloway et al., 2015; Goulding et al., 2017; Alonso et al., 2018). The ambiguous results of studies that tried to find correlations between bars and AGN activity is partly explained by the difficulty to account for the different time scales of the different processes and the need for additional mechanisms to drive the gas from the inner Lindblad resonance (ILR; at scales of $\sim$ 100 pc) to the supermassive black hole (at scales of $\sim$ 10 pc; Shlosman et al. 1989, 1990; Piner et al. 1995; Regan & Teuben 2004; Kim et al. 2012; Fragkoudi et al. 2016).

The study of stellar populations in bars helps us to understand the formation and evolution of these structures. While bars manage to push gas inwards fast and easily through gravitational torques, the dynamics of the stellar component are governed by different processes. Sellwood & Binney (2002) have shown that, when spiral arms are present in a galaxy, stars can gain or lose angular momentum at the corotation resonance without heating the disc. This process can be enhanced by coupling with a bar potential (Minchev & Famaey, 2010). As a consequence, stars migrate radially which would result in a flattening of the stellar abundance gradient. With a growing bar this process can affect large parts of the disc, but will be mostly visible outside corotation, i.e. outside the bar region (e.g. Friedli et al., 1994; Di Matteo et al., 2013). In observations, however, this has not yet been confirmed. Sánchez-Blázquez et al. (2014) find no differences in the age and metallicity gradients between barred and unbarred galaxies studying 62 galaxies form the Calar Alto Legacy Integral Field Area (CALIFA) survey (see also Cacho et al., 2014 and Cheung et al., 2015b who studied the influence of bars on bulge and global age and metallicity properties).

Additionally to radial migration in the disc, the gradients along bars can be flattened due to orbital mixing (Binney & Tremaine, 1987). Bars are confined elongated structures. In any spatial resolution element within the bar, stellar orbits with different elongations and apocentres cross or come very close together. This would result in mixing and flattening of measured stellar population gradients along the bar.

Observational studies of the metallicity gradient in the bar have found ambiguous results, but recent papers tend to agree on a flattening along the bar. In detail: in analyses of line-strength indices from long-slit spectroscopy along bars, gradients were found to have all kinds of slopes from positive to negative depending on mean stellar ages and central velocity dispersion (Pérez et al., 2007, 2009). Sánchez-Blázquez et al. (2011) found that two of the bars in Pérez et al. (2009) are flatter in age and metallicity as compared to the gradients along the major axis of the discs they are residing in. Pérez & Sánchez-Blázquez (2011) reported that bulges of barred galaxies are more metal-rich than bulges of unbarred galaxies. The mean metallicity of the bulges and bars are well correlated while the gradients in the bar have different slopes. Seidel et al. (2016) studied 16 barred galaxies from the Bars in Low Redshift Optical Galaxies (BaLROG) sample with integral field unit (IFU) data from the SAURON instrument (Bacon et al., 2001). They found that gradients of age, metallicity and [Mg/Fe]-abundance along the bar major axis are flatter than the gradients along the minor axis, which are similar to those in discs of an unbarred control sample. They also point out that in many cases the gradient in the central region ($<$ 0.15$\times$bar length) is considerably steeper, which highlights the importance of carefully considering central components. These results were confirmed in Fraser-McKelvie et al. (2019b) studying 2D bar and disc regions of 128 strongly barred galaxies from the MaNGA survey (Bundy et al., 2015).

At least part of the mixing and, hence, of the flattening is a result of limited spatial resolution. The bigger the spatial resolution element, the more different orbits get mixed. Furthermore, better spatial resolution allows to better separate central components such as inner discs or nuclear rings from the bar. It also provides more detail across the width of these thin elongated structures. Such a detailed study of stellar populations in extragalactic bars has the potential to provide important information that could also help understanding the bar of the Milky Way.

In this work, we present spatially resolved stellar populations analyses of nine barred galaxies from the **T**ime **I**nference with **M**USE in **E**xtragalactic **R**ings (TIMER) project studied with the Multi-Unit Spectroscopic Explorer (MUSE; Bacon et al., 2010) on the Very Large Telescope (VLT). We specifically concentrate on the bar region, while

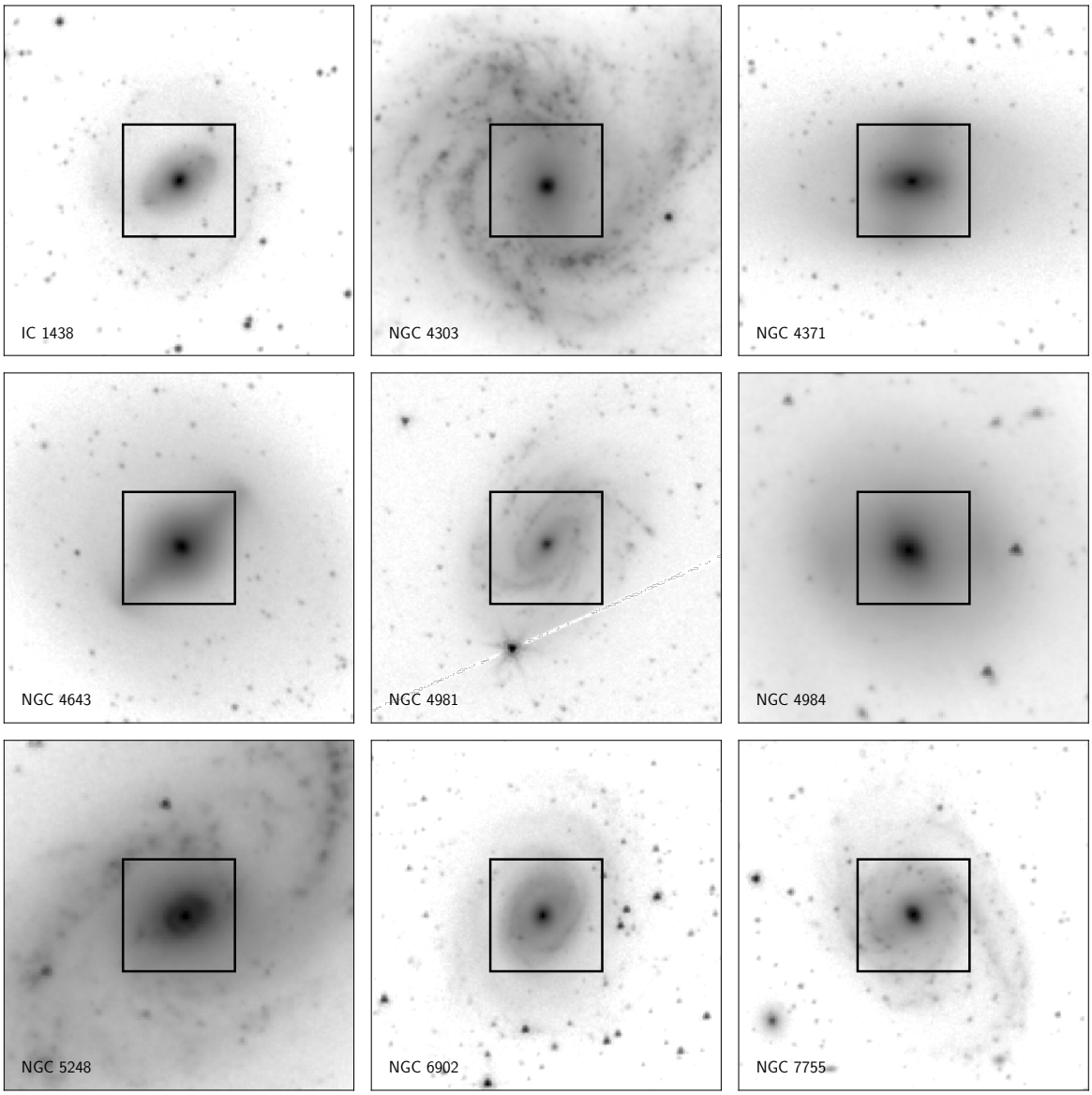

Figure 4.1: S^{4}G images at 3.6 µm for the complete sample. The black squares show the approximate MUSE FOV.

other components of the galaxies will be analysed in future papers by the collaboration. Additionally to stellar ages, metallicities and [α/Fe]-abundances, we present a detailed analysis of star formation histories (SFH) across bars.

The outline of the paper is as follows. In Sect. 4.2, we present the TIMER sample, the selection of our subsample and the observations with MUSE. Sect. 4.3 shows our analysis of Hα emission line fluxes. Subsequently, in Sect. 4.4, we present a detailed analysis of stellar population parameters in bars, starting with a short description of the derivation of the parameters, followed by a presentation of the results in terms of ages, metallicities, star formation histories and alpha-enhancements. Finally, we discuss some of the most important results in Sect. 4.5, where we also compare our observations to simulations from the Auriga project, and conclude the work in Sect. 4.6.

4.2 Sample selection and MUSE observations

The present work is part of the TIMER project (Gadotti et al., 2019, hereafter Paper I), a survey with the MUSE IFU spectrograph that aims at studying the central structures of 24 nearby barred galaxies. One of the main goals of the project is to estimate the epoch when galactic discs dynamically settle, which leads to the formation of bars. The feasibility was demonstrated in a pilot study of the galaxy NGC4371 (Gadotti et al., 2015).

The parent sample of the TIMER project is that of the Spitzer Survey of Stellar Structures in Galaxies (S^{4}G; Sheth et al., 2010) and includes only nearby ($d < 40$ Mpc), bright ($m_B < 15.5$) and large ($D_{25} > 1'$) galaxies. From this catalogue, TIMER galaxies were selected based on

Table 4.1: Summary of the main parameters of the sample.

Galaxy	Type	i	d	$M_\star$	$M_{\rm HI}$	$Q_{\rm bar}$	$L_{\rm bar}$	$PA_{\rm bar}$	$\epsilon_{\rm bar}$
		deg	Mpc	$10^{10}\,M_\odot$	$10^{10}\,M_\odot$		arcsec	deg	
(1)	(2)	(3)	(4)	(5)	(6)	(7)	(8)	(9)	(10)
IC 1438	$(R_1)SAB_a(r', \underline{l}, nl)0/a$	24	33.8	3.1	0.12	0.178	23.8	121.0	0.51
NGC 4303	$SAB(rs, nl)b\underline{c}$	34	16.5	7.2	0.45	0.535	36.1	178.0	0.69
NGC 4371	$(L)SB_a(r, bl, nr)0^{0/+}$	59	16.8	3.2	0.08	0.234	36.6	157.0	0.25
NGC 4643	$(L)SB(\underline{r}s, bl, nl)0^{0/+}$	44	25.7	10.7	0.03	0.272	49.9	133.0	0.47
NGC 4981	$SA\underline{B}(s, nl)\underline{bc}$	54	24.7	2.8	0.35	0.093	18.9	147.0	0.57
NGC 4984	$(R'R)SAB_a(l, bl, nl)0/a$	53	21.3	4.9	0.03	0.176	30.0	94.0	0.30
NGC 5248	$(R')SAB(s, nr)bc$	41	16.9	4.7	0.40	0.138	27.4	128.0	0.36
NGC 6902	$(R')S\underline{A}B(\underline{r}s, nl)\underline{a}b$	37	38.5	6.4	2.34	0.045	16.2	132.5	0.36
NGC 7755	$(R')SAB(rs, nrl)\underline{bc}$	52	31.5	4.0	0.65	0.401	24.6	125.0	0.56

Column (1)-(6) are extracted from Table 1 in Paper I. For details, we refer to that paper. (1) Galaxy name; (2) morphological type by Buta et al. (2015); (3) inclination of the galaxy; (4) distance to the galaxy; (5) total stellar mass; (6) total H I mass; (7) bar maximum gravitational torque from Díaz-García et al. (2016). Column (8)-(10) are taken from Herrera-Endoqui et al. (2015): (8) bar length; (9) position angle of the bar; (10) ellipticity of the bar.

mass ($M_\star > 10^{10}\,M_\odot$), inclination ($i < 60°$) and the presence of a bar and prominent central structures, such as nuclear rings or inner discs. The latter was judged consulting the morphological classification in Buta et al. (2015).

Out of the 24 nearby barred galaxies in the TIMER sample, 21 galaxies have been observed with MUSE up to date. From these 21 objects we selected all galaxies where almost the entire bar (80% of the semi-major axis of the bar) is covered by the MUSE field-of-view (FOV). This choice was made as a compromise between sample size and having enough of the bar covered for the analysis. The final sample consists of nine galaxies, the bars of six of them completely fit into the MUSE FOV. In Fig. 4.1, we show infrared 3.6 µm S^{4}G images of the sample superimposed with the approximate outline of the MUSE FOV. The main parameters of the sample are summarised in Table 4.1. This table includes parameters for the bars from the S^{4}G analyses in Herrera-Endoqui et al. (2015) and Díaz-García et al. (2016) that we will use to constrain the bar position and to compare with results from the TIMER observations.

Observations of eight of the galaxies were performed during ESO Period 97 from April to September 2016. NGC 4371 was subject to our science verification programme for MUSE (Gadotti et al., 2015) and observed between the 25th and the 29th of June 2014. The MUSE instrument covers a 1 squared arcmin FOV with a spatial sampling of 0.2″ and a spectral sampling of 1.25 Å per pixel. We used the nominal setup with a wavelength coverage from 4750 Å to 9350 Å at a mean resolution of 2.65 Å (full-width-at-half-maximum, FWHM). The typical seeing during observations was 0.8″-0.9″. The data was reduced with the MUSE pipeline v1.6 (Weilbacher et al., 2012) applying the standard calibration plan. Details of the TIMER sample selection, the observations and the data reduction can be found in Paper I.

4.3 Recent star formation as traced by Hα

To get a complete picture of the stellar population properties in bars, it is important to study the star formation history (SFH) as well as ongoing star formation in these structures. A detailed investigation of star-forming and non-star-forming bars was conducted for a different sample in Neumann et al. (2019). Our present work is focused on ages, metallicities and SFHs. However, to characterise the bars in light of the results of Neumann et al. (2019) and to aid in understanding the stellar population properties, we derived Hα maps as tracer of H II regions and thus star formation for the complete set of galaxies.

The extraction of emission line fluxes for all TIMER galaxies was performed by employing the code PyParadise, an extended version of paradise (see Walcher et al., 2015). One of the advantages of PyParadise is that it propagates the error from the stellar absorption fit to the emission line analysis. The procedure was done on a spaxel-by-spaxel basis to retrieve the fine spatial structure of the gas component. This is possible owing to the generally high signal in the emission lines. The stellar absorption features, however, are usually less pronounced. For that reason, we Voronoi binned the cubes to estimate the underlying stellar kinematics. For self-consistency and to make use of the internal error propagation, we did not use the kinematics derived with pPXF that we describe in the next subsection, but performed an independent analysis with PyParadise.

The procedure can be summarised in three steps, further details can be found in Paper I. First, the stellar kinematics are measured by fitting a linear combination of stellar template spectra from the Indo-US template library (Valdes et al., 2004) convolved with a Gaussian line-of-sight velocity kernel to the Voronoi-binned spectra in the cube. Second, in each spaxel, the continuum is fitted with fixed kinematics according to the underlying Voronoi cell. Finally, the emission lines are modelled with Gaussian

functions in the continuum-subtracted residual spectra. To estimate uncertainties, the fit is repeated 30 times in a Monte Carlo simulation after modulating the input spectra by the formal errors and by using only 80% of the template library.

The extracted Hα fluxes have to be corrected for dust attenuation. For that purpose, we used the ratio of Hα/Hβ = 2.86 (Balmer decrement from case B recombination), which is intrinsically set by quantum mechanics. Since the attenuation is wavelength dependent, the observed ratio changes and can thus be used to correct for the effect of dust on the emission line fluxes. We used the prescription by Calzetti et al. (2000) to account for the wavelength dependent reddening.

In Fig. 4.2 we plot Hα maps for all galaxies in the sample. This figure shows that most galaxies have ongoing star formation in the outer disc, for example, along spiral arms (e.g. NGC 4303, NGC 4981, NGC 5248), at the tips of the bar (IC 1438) or in a ring-like feature (e.g. NGC 6902, NGC 7755). Additionally, in many cases there are nuclear structures present such as nuclear rings or inner discs that cause strong star formation in the central region.[1] That being mentioned, there is a clear lack of star formation between the centre and the end of the bar for all bars. Some galaxies show star formation at the edges of the bar while others none at all. The galaxy NGC 5248 is a peculiar case. Seen in Hα, it seems to have a large nuclear disc with spiral-like features attached to it inside the bar region. It will show as an outlier in the subsequent plots in this paper.

4.4 Stellar population analysis

4.4.1 Derivation of stellar population parameters

A detailed description of the extraction of stellar population parameters for the whole set of TIMER galaxies is given in Paper I. Here we summarise the main steps of the procedure.

To secure a high quality of the analysis, the spectra in each cube were spatially binned using the Voronoi method of Cappellari & Copin (2003) to achieve a minimum signal-to-noise (S/N) of ≈ 40 per spatial element. The spectrum of each Voronoi bin was then analysed as follows.

First, the stellar kinematics were determined employing the penalized pixel fitting code pPXF by Cappellari & Emsellem (2004) with the E-MILES single stellar population (SSP) model library from Vazdekis et al. (2015). Subsequently, with fixed stellar kinematics, the nebular emission was fitted and removed with the code GANDALF (Sarzi et al., 2006; Falcón-Barroso et al., 2006). Afterwards, we modelled ages, metallicities and star formation histories (SFH) on the emission-free residual spectra employing the code STECKMAP (STEllar Content and Kinematics via Maximum A Posteriori; Ocvirk et al., 2006a,b) with the E-MILES library and assuming a Kroupa (2001) initial mass function (IMF). In the model, we employed the BaSTI isochrones (Pietrinferni et al., 2004, 2006, 2009, 2013) with stellar ages ranging from 0.03-14.0 Gyr and metallicities from 0.0001 to 0.05. We refer to Paper I for further technical details.

Uncertainties in the derivation of mean stellar ages and metallicities with STECKMAP were studied for a set of 5000 spectra from the TIMER data in Appendix A of Paper I. Typical values are 0.5-1 Gyr for age, and 0.005-0.010 for metallicity (Z).

Since STECKMAP is not capable of measuring [α/Fe] values, we exploit the pPXF routine to derive those values in a similar but slightly optimized set-up. The implementation of this analysis is based on the GIST pipeline[2] (Bittner et al., 2019) and further details of the analysis are described in Bittner et al. (in prep.). A comparison between the results obtained from STECKMAP and pPXF is currently conducted within the TIMER collaboration and will be published soon. Differences are found to be minimal. In the following, we summarise the main steps of exploiting the pPXF routine.

In order to obtain reliable estimates of the [α/Fe] values, in this analysis, we spatially bin the data to an approximately constant S/N of 100. We note that all spaxels which surpass this S/N remain unbinned while those below the isophote level that has an average S/N of 3 are excluded from the analysis. As line-spread function of the observations we adopt the udf-10 characterisation of Bacon et al. (2017).

We employ the wavelength range of 4800 Å to 5800 Å together with the MILES model library from Vazdekis et al. (2010), covering a large range in age and metallicities, and two [α/Fe] values of 0.00 and 0.40. The models employ the BaSTI isochrones (Pietrinferni et al., 2004, 2006, 2009, 2013) and the revised Kroupa initial mass function (Kroupa, 2001). In order to account for differences between observed and template spectra, we include an 8th-order, multiplicative Legendre polynomial.

The analysis is performed in three steps: we first derive the stellar kinematics with pPXF with emission lines masked, before modelling and subtracting any gaseous emission with pyGANDALF – a python implementation of GANDALF. Then, we perform a regularised run of pPXF to estimate the population properties, while keeping the stellar kinematics fixed to the results from the unregularised run. The used strength of the regularisation is the one at which the χ^2 of the best-fitting solution of the regularised run exceeds the one from the unregularised run by $\sqrt{2N_{\rm pix}}$, with $N_{\rm pix}$ being the number of spectral pixels included in the fit. This criterion is applied to one of the

[1] The ionised gas in the centre can of course also be caused by photoionisation triggered by an AGN and the central Hα flux that we observe is in some cases most probably a mixture of that process, shocks and star formation. In fact, in Paper I, we show that almost all TIMER galaxies have AGN-like ionisation in the central arcsecond. However, it is unlikely that the AGN is responsible for the Hα in the outer disk and is safe to account that to star formation (see also Neumann et al., 2019).

[2] https://abittner.gitlab.io/thegistpipeline

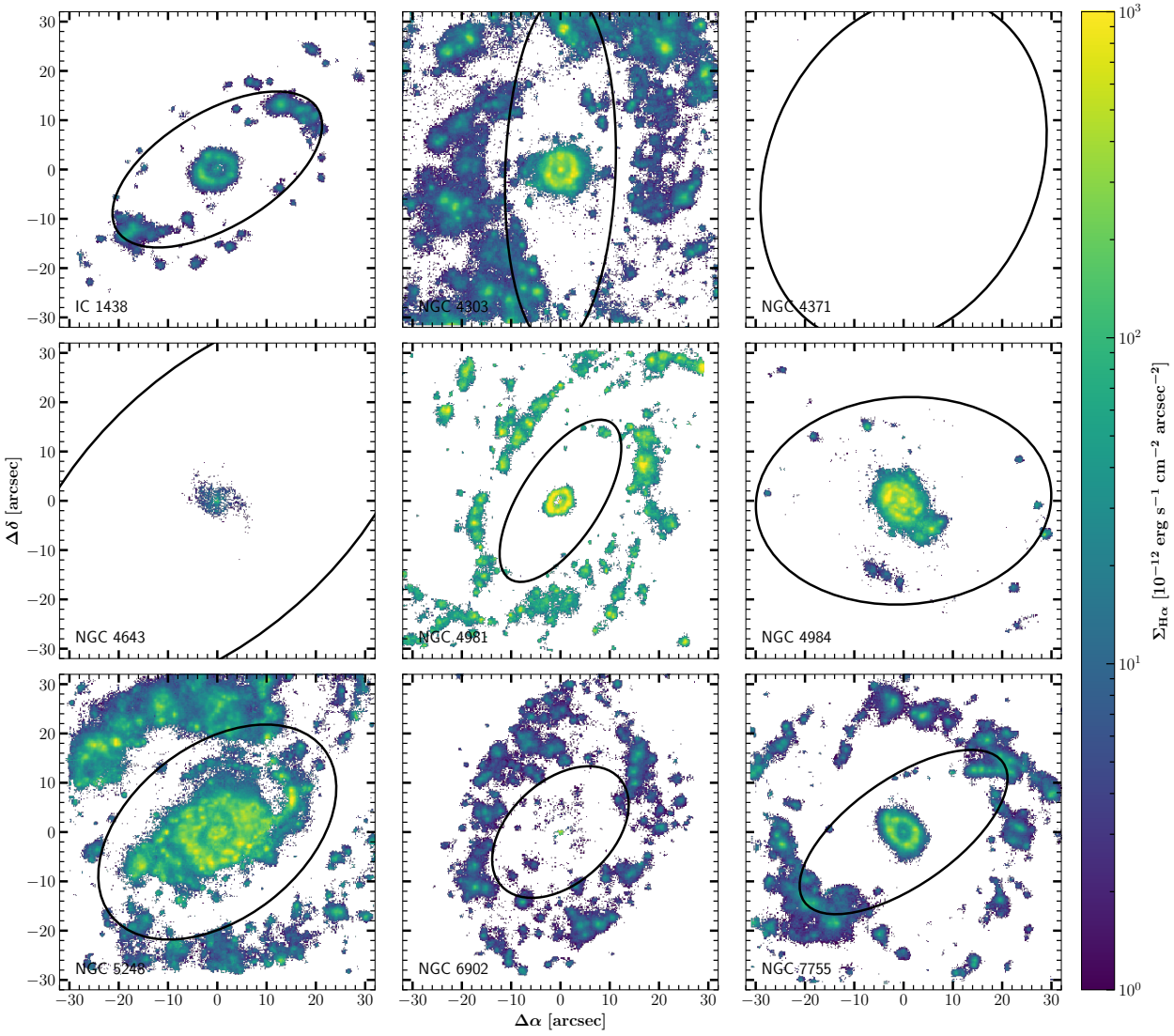

Figure 4.2: Dust-corrected Hα maps for the complete sample. Only fluxes with $S/N_{H\alpha} > 5$ and $S/N_{H\beta} > 5$ are shown. Black ellipses outline the approximate extent of the galaxy bar. NGC 4371 does not have any Hα above the S/N cut.

central bins with high signal-to-noise and then used for the entire cube (Press et al., 1992; McDermid et al., 2015).

4.4.2 Mean ages and metallicities

From the output of STECKMAP, we are able to reconstruct the SFH as well as the metallicities for each spatial bin. In this subsection, we will first look at light-weighted and mass-weighted mean ages and metallicities.

4.4.2.1 Profiles along the bar major and minor axis

So far, most research on stellar populations in bars has focussed on 1D profiles along the bar major axis and compared either to the disc (Sánchez-Blázquez et al., 2011; Fraser-McKelvie et al., 2019b) or the bar minor axis (Seidel et al., 2016). Before we present our results of a different approach, we first show gradients of ages and metallicities along the bar major and minor axis for the sake of comparison with previous studies.

We derived the major/minor axis profiles from pseudo slits of 2″ width on top of the Voronoi-binned 2D mean age and metallicity maps for each galaxy. The spatial scale was deprojected to the plane of the galaxy using the inclination of the disc together with the position angle of the axes with respect to that of the disc. Fig. 4.11 in Appendix 4.A shows an example for the galaxy NGC 4303. Clear breaks in the profiles are apparent in the inner regions of all galaxies, in agreement with Seidel et al. (2016). These authors reported breaks commonly at 0.13 ± 0.06 bar length. We typically find two breaks: the first break is typically at or near the position of a nuclear structures such as an inner disc or nuclear ring; afterwards follows presumably a transition zone that ends at the second break. The second break in our sample is located at $r = 0.29 \pm 0.09$ bar length. We chose the range between that break and the bar length

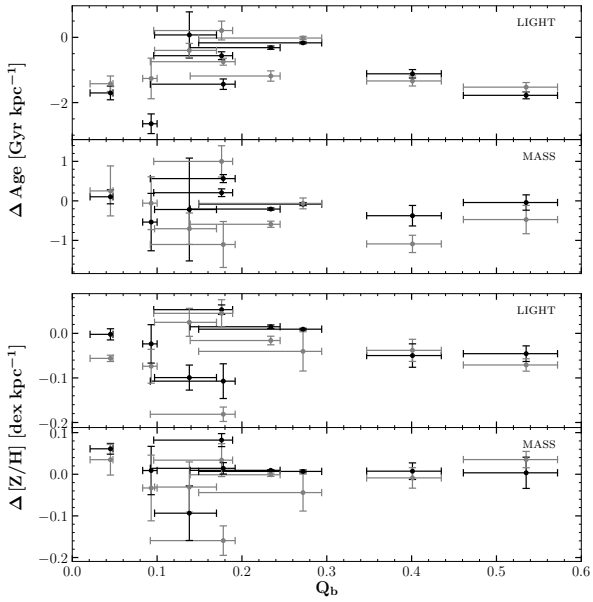

Figure 4.3: Gradients of deprojected age and metallicity profiles for light- and mass-weighted mean values along the bar major and minor axis. An example of such profiles is shown in Fig. 4.11. Gradients are measured between the second inner break and the bar length as seen in the aforementioned figure and discussed in the text. Major axis gradients are shown in black and minor axis gradients in grey. The minor axis is extended into the disc within the bar radius. The x-axis shows the bar strength.

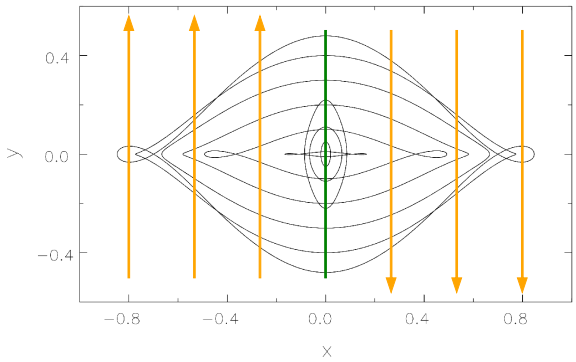

Figure 4.4: Important periodic orbits in a rotating bar potential. The bar major axis is horizontal. Orbits elongated parallel to the major axis are members of the $x1$ family. Orbits elongated perpendicular to the major axis form the $x2$ family. The figure is adopted from Sellwood (2013). We show superimposed on that figure a sketch of the anti-parallel vectors along which the stellar populations are binned and averaged.

to measure the gradients along the bar major and minor axis. The implication is that what we call 'gradient of the minor axis' is typically measured in the disc along the extension of the minor axis.

In Fig. 4.3, we present the age and metallicity gradients along the bar major axis and along the extension of the bar minor axis into the disc. We plot them against the bar strength Q_b taken from Díaz-García et al. (2016). In none of the four panels there is a clear indication for a correlation with Q_b. Light-weighted age gradients are negative with no systematic difference between major and minor axis. Mass-weighted age gradients are flatter with a mean of -0.07 ± 0.31 Gyr kpc^{-1} for the major axis and -0.31 ± 0.64 Gyr kpc^{-1} for the minor axis. Gradients in [Z/H] are shallow and on average negative for light-weighted values and slightly flatter, in some cases becoming positive, for mass-weighted means. The mean mass-weighted metallicity gradient along the major axis is $+0.01 \pm 0.05$ dex kpc^{-1} and for the minor axis -0.02 ± 0.06 dex kpc^{-1}.

In summary, light-weighted age and metallicity gradients are on average negative, while mass-weighted gradients are flatter and in some cases positive. There is no correlation with bar strength and we see no systematic differences between the gradients along the bar major axis and along the extension of the minor axis into the disc, except for a flatter mass-weighted age gradient along the major axis as compared to the disc.

4.4.2.2 *Profiles across the width of the bar*

The stellar bar as we observe it in 2D projection is a superposition of stars that are trapped in mainly elongated orbits around the galaxy centre. Analyses of orbital structure in the gravitational potential of a barred disc galaxy reveal that bars are built from families of periodic and quasi-periodic orbits with different extents, elongations, and orientations (e.g. Contopoulos & Papayannopoulos, 1980; Athanassoula et al., 1983; Pfenniger, 1984; Skokos et al., 2002a,b). One of these families is comprised of the $x1$ orbits, which are elongated parallel to the bar major axis and build the backbone of the bar. Within the $x1$ family, higher energy orbits are rounder and reach further into the disc and farther away from the bar major axis, whereas lower energy orbits are more elongated and closer to the bar major axis. Our aim is to investigate whether there are differences or trends in stellar populations across different orbits in the $x1$ family that could help us to understand the formation and evolution of the bar.

We approached this problem by constructing a series of 1D cuts perpendicular to the bar major axis[3]. We used four cuts to both sides of the minor axis: a central cut on top of the minor axis, two cuts at the distances of one third and two thirds of the bar length, respectively, and one cut at the end of the bar. Afterwards, every pair of equidistant cuts with respect to the minor axis were averaged in anti-parallel direction. The procedure is illustrated in Fig. 4.4. This approach ensures to average the leading edge of a rotating bar with the opposite leading edge, and the trailing edge with the opposite trailing edge. The result is a set of four profiles going from the leading to the trailing edge cutting across the widths of the bar at different distances from the centre.

[3]We note that the bar minor axis and the cuts are not perpendicular to the bar major axis in the projection on the sky, if the galaxy is not seen face-on. The angles are calculated such that they are orthogonal in the galaxy plane.

In Figs. 4.12-4.20 in Appendix 4.B, we present light- and mass-weighted mean ages and metallicities for all galaxies. These figures show 2D maps as well as the four previously described profiles. Additionally, along the cuts, we plot Hα densities and total surface brightness. In the discussion in this section we will refer to some general trends seen in the profiles. We refer the reader to the appendix for more detail on single objects. From these plots we measured the gradients of light- and mass-weighted mean stellar ages and metallicities across the widths of the bars. For this measurement, we selected the cut at the distance of two thirds of the bar length to the centre as it is less contaminated by the central region. The result is presented in Fig. 4.5 for ages and Fig. 4.6 for metallicities. We compare the gradients from the leading to the trailing side as well as the light-weighted and mass-weighted quantities.

The profiles of the light-weighted mean ages show a clear peak close to the bar major axis with a decrease towards both edges of the bar. In Fig. 4.5 this is clearly apparent as almost all gradients are negative and located in the bottom-left quadrant. Furthermore, we see that for most objects the gradient is steeper on the leading edge. This is true for all galaxies that also show some Hα on the edges. Additionally, in Figs. 4.12-4.20 we see that the peak is shifted towards the trailing side for all objects were it was possible to determine the sense of rotation. NGC 5248, on the bottom-right quadrant of Fig. 4.5, is a clear outlier. These results are clear indication for the presence of young stellar populations on the edges of the bar with a slight predominance on the leading side. This is in agreement with the general picture that, if there is star formation in a bar, it is preferentially happening on the leading side (e.g. Sheth et al., 2008; Neumann et al., 2019), but it is the first time this is seen in stellar populations.

If we inspect the mass-weighted ages, the observed gradients change. Almost all galaxies show positive gradients on both sides. Light-weighted mean parameters are dominated by the light of luminous young stellar populations. This effect is much reduced in mass-weighted quantities, which rather show differences in the intermediate to old ages.[4] The positive gradients indicate that the stellar populations close to the bar major axis are younger than at the edges. This result will be strengthened by more details in the SFH and discussed in the following section.

The metallicity gradients in Fig. 4.6 are shallow (between -0.15 and 0.15 dex kpc^{-1}) and mostly negative. Mass-weighted gradients are a bit flatter or even slightly positive in some cases. There are no obvious differences between the leading and trailing edge.

In terms of absolute values, from the 2D maps in Figs. 4.12-4.20, we deduce that the stellar populations in bars are on average more metal-rich than in the discs. The difference is more pronounced in light-weighted maps. Typical light-weighted metallicities of bars are sub-solar (-0.3 to 0 dex), while mass-weighted they are in the range of -0.2 to $+0.2$ dex. Two exceptions are the bars of NGC 4371 and NGC 4643, which are very old with [Z/H] between $+0.2$ and $+0.4$ dex, both light- and mass-weighted. In all metallicity maps a strong peak prominently features in the centre of the galaxies that stands out from the otherwise rather flat profiles. In light-weighted ages, the stellar populations of bars are generally older than in their discs. This is probably caused by very young populations in the disc which, due to suppression or cessation of star formation within the bar, are less dominant in the bar. The effect vanishes in the maps of mass-weighted ages where both bars and discs are usually old (~8-10 Gyr).

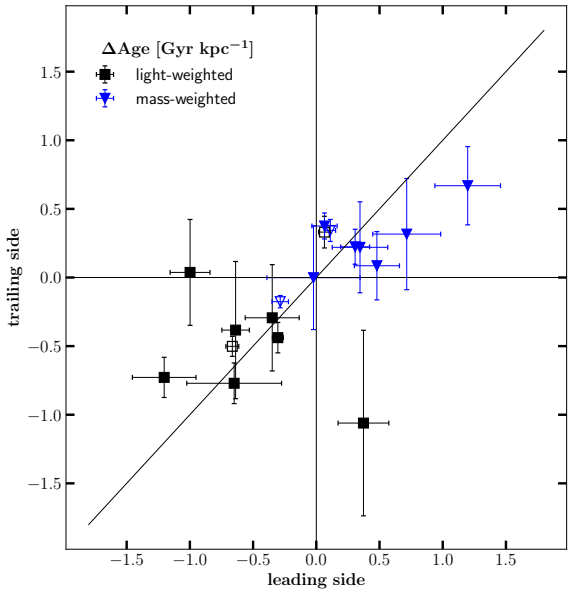

Figure 4.5: Gradients of light- and mass-weighted mean stellar age profiles along the third cut perpendicular to the bar major axis as shown in Figs. 4.12-4.20 and described in the text. Shown are the gradients from the major axis towards the leading (x-axis) and trailing (y-axis) edge of the bar. The sense of rotation was determined assuming that spiral arms are trailing. Empty markers show galaxies for which the rotation is not clear.

4.4.3 Star formation histories

One single observation with the MUSE instrument of a galaxy provides tens of thousands of spectra each of which contains information that makes it possible to disentangle, inter alia, the composite of young and old stellar populations, as well as metal-poor and metal-rich. The presentation of the full wealth of information from the spatially resolved SFH of a galaxy is a multi-dimensional problem and it is a challenge to best illustrate important aspects. Two-dimensional maps of mean ages and metallicities, as shown in the previous subsection, embody projections that keep the spatial information but average the parameters along the axis of time. In this subsection, we present how stars of different ages shape the stellar bars that we observe.

[4] However, the light-weighted ages are directly derived from observations whereas the mass-weighted ages depend on the models and are based on the same observations of light. This has to be kept in mind when drawing conclusions from these kind of parameters.

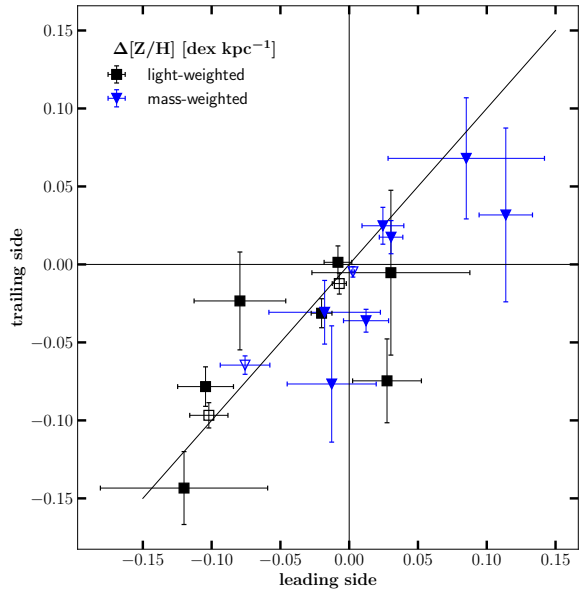

Figure 4.6: Same as Fig. 4.5 but for mean stellar metallicities.

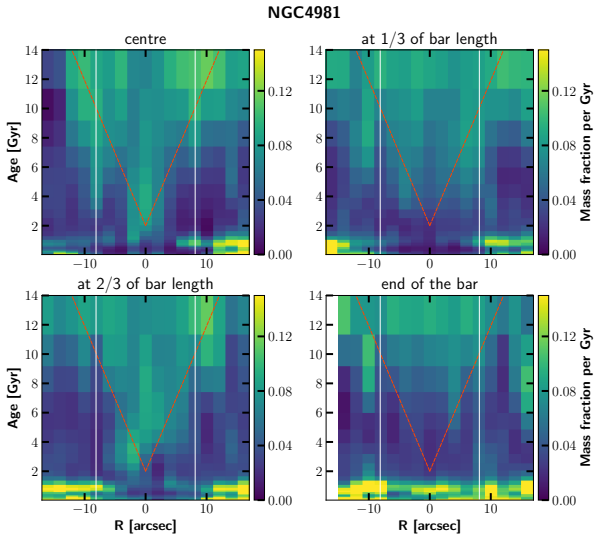

Figure 4.7: SFHs of NGC 4981 along the cuts illustrated in the sketch in Fig. 4.4. and in the Figs. 4.12-4.20. Each panel shows one of the four cuts. The x-axis shows the distance to the bar major axis along the cut and the y-axis the age of the population. Colour-coded is the fraction of stellar mass that was formed at a certain position at a certain time. The mass is normalised within each spatial bin (vertically in that diagram). The mass fractions are further divided by the size of the bin on the y-axis to correct for non-equally spaced bins on the linear age axis. White vertical lines indicate the edges of the bar. Red lines are plotted on top to indicate the 'V-shape' discussed in the text.

In the figures of SFH, we will use the same spatial binning scheme along the cuts perpendicular to the bar major axis as presented previously.

The SFHs are shown as an example for NGC 4981 along the four cuts in four different panels in Fig. 4.7. The last panel shows the profile at the end of the bar. We see a very young and an old population with not much variation across the cut, which highlights that there is not much difference between the ends of the bar and the disc. We now address the second and third panel, which contain information of less contamination from the nuclear structure and the outer disc. The plots present clear evidence of a very young stellar population in the main disc, here seen as bright features of less than 1 Gyr left and right to the edges of the bar. Additionally, we recognise a 'V-shape' in the ages above 2 Gyr, where stars at intermediate ages between 2-8 Gyr are more concentrated close to the major axis, while the oldest population (> 8 Gyr) is spread across the whole spatial range. This feature is not exclusive for this galaxy but can be seen in at least 5 out of 9 galaxies in our sample. Plots of SFHs for the complete set of galaxies can be found in Fig. 4.21 in Appendix 4.C. A consequence of the 'V-shape' is a positive age gradient from the major axis outwards that we observed indeed for all but one galaxy in the mass-weighted mean ages in Fig. 4.5.

These results that indicate that intermediate age stellar populations are concentrated on more elongated orbits closer to the bar major axis are consistent with the findings from idealised thin (kinematically cold/young) plus thick (kinematically hot/old) disc *N*-body galaxy simulations in Fragkoudi et al. (2017). In their Fig. 2, they show that the colder components form a strong and thin bar, while the hotter component forms a weaker and rounder bar. (see also Athanassoula et al., 2017; Debattista et al., 2017; Fragkoudi et al., 2018).

4.4.4 Alpha-enhancement

The measurement of [α/Fe] abundance ratios can shed further light on the formation process of different components in a galaxy. This ratio is usually used as time-scale indicator of the star formation history. While α-elements are produced in short-lived massive stars and are released in core-collapse supernovae, Fe-elements come from type Ia supernovae over much longer time-scales. A low [α/Fe] value points towards an extended period of continuous star formation. A high α-enhancement, however, indicates rapid formation (e.g. Thomas et al., 1999).

We present our measurements of [α/Fe] in Fig. 4.8. We notice that [α/Fe] in the bar is on average similar to that in the inner disc or ring component, while the surrounding disc is more α-enhanced. This is in accordance with the results found for inner bars as compared to the inner discs in the double-barred galaxies NGC 1281 and NGC 5850 in the TIMER project (de Lorenzo-Cáceres et al., 2019) and supports the picture in which outer and inner bars are formed in similar ways.

Interestingly, Seidel et al. (2016) found that in the BaLROG sample the outer discs are less α-enhanced than the bars. However, the [α/Fe] of the discs in their sample is measured outside the bar radius. In contrast, the disc region that our measurements in TIMER cover is, for most of the galaxies, restricted to be within the radial range of the bar. This region, which encompasses the part of the disc that is within the bar radius but outside of the bar, is typically termed 'star formation desert' (SFD; James et al., 2009; James & Percival, 2016). It seems that star

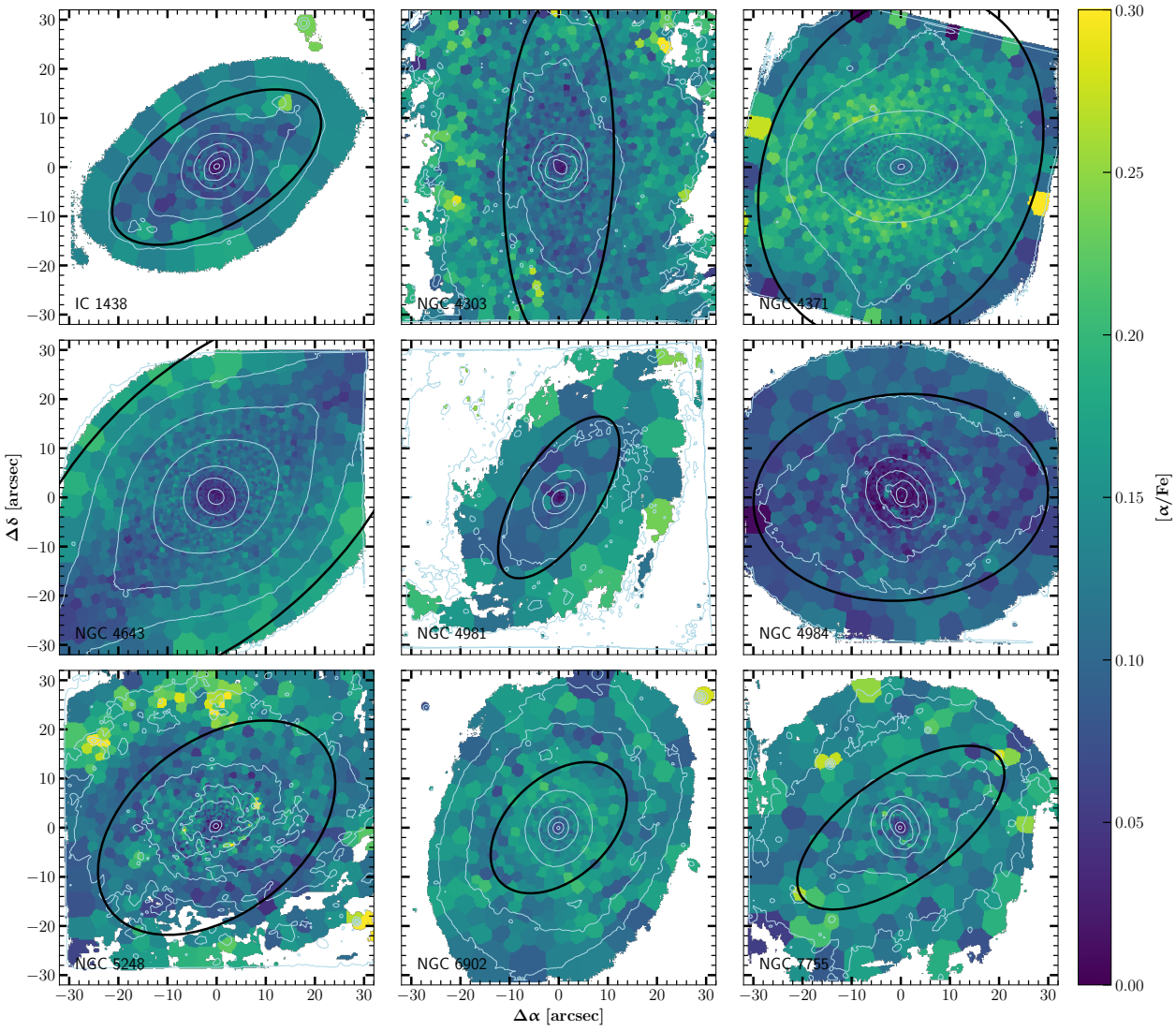

Figure 4.8: Spatially resolved Voronoi-binned maps of [α/Fe]. Contours of the surface brightness distribution from the MUSE whitelight images are shown in white. The positions of the bars are shown in black, approximated by ellipses.

formation is being suppressed by the bar in the SFD. In fact, a truncation of the SFH in SFDs has been found in observations (James & Percival, 2016, 2018) and, as a more gradual decline, in cosmological zoom-in simulations (Donohoe-Keyes et al., 2019). In this work we, thus, find higher [α/Fe] abundances in the SFDs than in the bars. This result can be explained by a rapid suppression of star formation in the SFD after the formation of the bar and a more extended SFH along the bar. An even more extended period of star formation in the disc outside the radius of the bar, as reported by Seidel et al. (2016), fits well within the same picture, in which many bars quench star formation within the bars themselves, while the outer discs are still forming stars (e.g. Neumann et al., 2019).

4.5 Discussion

4.5.1 V-shaped age distribution: Comparison to Auriga simulations

As discussed in Section 4.3, the SFHs along the minor axis of the bar, shown in Figure 4.7, have a distinctive V-shape, when examining age versus distance along the minor axis of the bar. To better understand the origin of this V-shape we explore the SFHs in bars in the Auriga magneto-hydrodynamical cosmological zoom-in simulations Grand et al. (2017). These are simulations of isolated Milky Way mass halos (10^{12}-$2 \times 10^{12} M_{\odot}$), which run from redshift $z = 127$ to $z = 0$, with a comprehensive galaxy formation model (see Grand et al. 2017 and references therein for more details on the simulations). These simulations form disc-dominated galaxies with a significant fraction having prominent long-lived bars, with properties similar

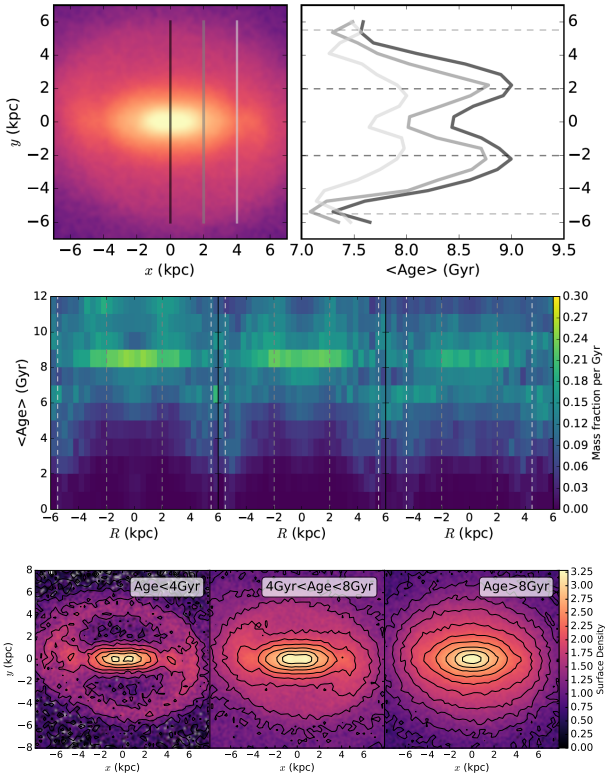

Figure 4.9: Results from Auriga simulations. The top-left panel shows the face-on surface density map of halo 18 from the Auriga sample, overplotted with three vertical lines that indicate the cuts to extract the data shown in the other panels. The bar major axis is horizontal. The top-right panel shows the mean stellar age profiles along the cuts. The middle row presents SFHs diagrams for each of the cuts (left panel corresponds to the dark slit and rightmost panel corresponds to the light grey slit). The axis and the colour-coding are the same as in our observations shown in Fig. 4.7. The red dashed lines mark the edges of the bar and the white dashed lines the location of an inner ring. The bottom row shows face-on surface density projections of stars in the bar in three different age bins as indicated in the top right corner of each panel. We see that younger ages cluster along the bar major axis compared to older ages which have a rounder shape.

to those of barred galaxies in the local Universe (see Fragkoudi et al. in prep., Blazquez-Calero et al. submitted).

In the top left panel of Figure 4.9, we show a face-on surface density projection of the model, where we clearly see a prominent bar with an inner ring. We trace pseudo-slits along the minor axis of the bar in three different locations, as we did for the observations, and calculate the mean age of stars along the slits. These are shown in the top right panel of the figure, where we see that within the bar region (dark dashed lines) there is a dip towards younger ages along the bar major axis. In the second row of the Figure, we plot the SFH in each slit with the leftmost panel corresponding to the black slit and the rightmost panel corresponding to the light grey slit (outer part of the bar). We see that inside the dark grey dashed lines, which outline the edge of the bar, there is a characteristic V-shape as the one seen in our observations. The light dashed lines indicate the location of the inner ring of the galaxy where there is constant star formation and therefore younger stars. Therefore the simulations show a similar V-shape inside the bar region as the observations do.

To understand the origin of the V-shape, in the bottom panel of Fig. 4.9, we show the face-on surface density projections of stars in the model in three different age bins: for stars younger than 4 Gyr (left), stars with ages between 4 and 8 Gyr (middle) and stars older than 8 Gyr (right panel). We see that the youngest population has an elongated bar shape, much more so than the oldest population which is rounder. This difference in the shape of the bar according to the age and kinematics of the underlying population was shown using idealised simulations in Fragkoudi et al. (2017); Athanassoula et al. (2017) and was termed *kinematic fractionation* by Debattista et al. (2017). Therefore we see that the younger populations are more clustered along the bar major axis than the oldest populations due to kinematic fractionation, giving rise to the V-shape we see in the observations.

4.5.2 V-shaped age distribution: How do stars separate that form after the bar?

The unprecedented physical spatial resolution of stellar populations in TIMER galaxies, by observing very nearby objects with MUSE, led for the first time to observational evidence for a separation of stellar populations by the bar, as it was recently predicted from simulations. In this concept, initially co-planar cold-and-young and hot-and-old stellar populations separate when the bar forms.

It is still an open question how stars, which form *after* the bar, get separated. The key for the morphological separation is the kinematics of the stellar populations or the gas out of which they form, since the bar doesn't have a different gravitational pull on stars just because they are young or old. One possibility is that gas settles into dynamically colder configurations over time. The stars that are formed in that gas get, thus, also trapped into colder and, hence, more elongated orbits. An interesting question is whether there is a second mechanism in which a star that forms in cold orbits after the bar would heat, for example through interactions, and therefore migrate to higher energy orbits, i.e. to rounder bar orbits that are further away from the bar major axis.

To shed light on these mechanisms, it would be very interesting to determine the time of bar formation for the galaxies in this sample. This is, in fact, one of the main goals of the TIMER project and it is currently work in progress. The result will give us a vertical line on the SFHs shown in Figs. 4.7 and 4.21. Everything above that line would have been formed before the bar and everything below the line after bar formation. It will be interesting to see how much of the V-shape is on either side and whether the V-shape is continuous before and after the formation of the bar.

4.6 Conclusions

We have conducted a detailed analysis of spatially resolved stellar populations in galaxy bars within the TIMER project. We have combined Hα measurements as star formation tracer with mean ages and metallicities, SFHs and [α/Fe] abundance ratios. We have shown 2D maps as well as averages along pseudo-slits perpendicular to the bar major axis that helped us to separate stellar populations across the width of the bars. We have further compared one of our main observational results with cosmological zoom-in simulations from the Auriga project. Our main results can be summarised as follows:

- Diagrams of SFHs perpendicular to the bar major axis in the MUSE TIMER observations show noticeable 'V-shapes' in the intermediate to old population (> 2 Gyr) which also manifest themselves in positive gradients in profiles of mass-weighted mean ages from the major axis outward. The same shapes are found in the barred galaxies from the cosmological zoom-in simulations from the Auriga project. We believe they are the result of younger stars being trapped on more elongated orbits forming a thinner bar and older stars forming a thicker and rounder bar.

- We showed the imprints of typical star formation processes in barred galaxies on the young age distribution (< 2 Gyr) in the stellar populations. Light-weighted mean stellar ages decrease from the major axis towards the edges of the bar with a stronger decrease towards the leading side. This behavior is especially observed for galaxies that show traces of Hα on the edges of the bar. Furthermore, none of the galaxies in our sample shows significant Hα in the bar region except for the presence in central components such as inner discs or nuclear rings, at the ends or at the edges of the bar. This result is explained by recent and ongoing star formation in the main disc and at the edges of the bar, but not in the region of the bar close to the major axis. A stronger effect on the leading side is in accordance with stronger star formation in that region.

- We found stellar populations in the bars to be on average more metal-rich than the discs. Except for a prominent peak in the very centre, mass-weighted gradients of mean [Z/H] in the bar are rather shallow with no systematic trends, both along the major axis and perpendicular to it. The gradients become more negative, but still shallow, for light-weighted means.

- Major axis gradients are not very distinct from the gradients along the extension of the minor axis into the disc within the bar radius.

- Bars are less α-enhanced than the surrounding disc as seen by [α/Fe] measurements. The region of the disc that we probe is mostly within the radius of the bar, which is often called 'star formation desert'. We find that [α/Fe] is similar in bars to that of inner secularly-built structures but lower than in the SFD. This is indication for a more prolonged or continuous formation of stars that shape the bar structure as compared to shorter formation episodes in the surrounding SFD.

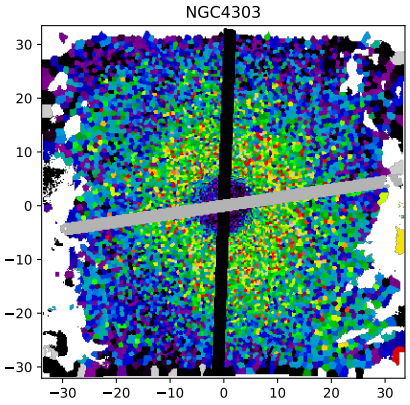

Figure 4.10: Sketch to visualise the procedure of extracting age and metallicity profiles along the bar major and minor axis. Shown is here a map of light-weighted Voronoi-binned mean ages from NGC 4303. Overplotted are pseudo-slits that were used to extract the profile of the major axis (black stripe) and minor axis (grey stripe).

Acknowledgements Based on observations collected at the European Organisation for Astronomical Research in the Southern Hemisphere under ESO programmes 097.B-0640(A) and 060.A-9313(A).

4.A Details on mean ages and metallicities along the bar major and minor axis

As discussed in Sect. 4.4.2.1, we derived mean age and metallicity profiles along the bar major and minor axis for all galaxies in the sample. Here, we show one example in Fig. 4.11 and discuss a few more details of the procedure.

Starting points are the 2D Voronoi-binned maps of mean ages and metallicities derived with STECKMAP. On these maps we determined the position of the major and minor axis of the bar, shown in Fig. 4.10. Note that these axes are not exactly perpendicular to each other on the maps, since we required them to be at 90° on the deprojected galaxy plane. The deprojection scales were derived from the relative PAs of the axes to the PA of the disc and from the inclination. The average profile was then calculated within pseudo-slits of 2″ width in bins of 2″ distance along the slit.

An example of these profiles is shown in Fig. 4.11 for NGC 4303. The distance r along each profile to the centre is the deprojected distance in the galaxy plane and it is divided by the deprojected length of the bar. Two clear breaks are noticeable in all four profiles of this galaxy. The inner break coincides with the position of a nuclear lens

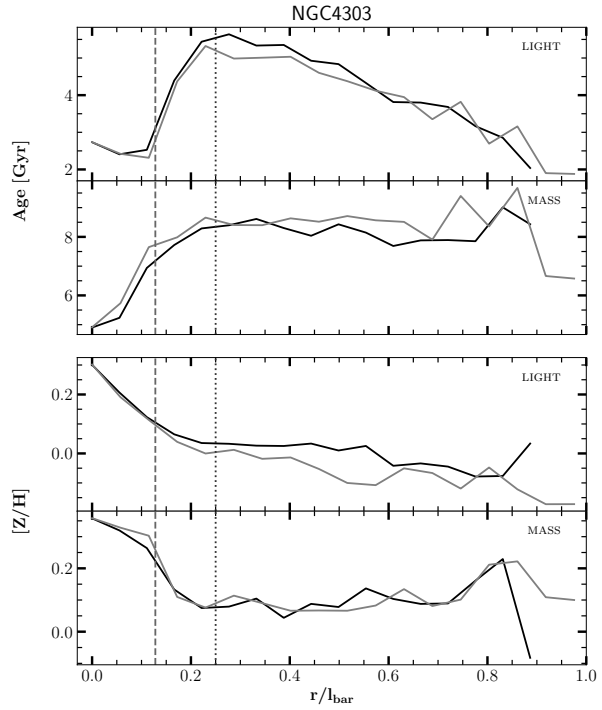

Figure 4.11: Mass- and light-weighted mean age and metallicity profiles along the bar major (black) and minor (grey) axis, extended into the disc. This is an example for galaxy NGC 4303. The vertical dashed line shows the position of the nuclear lens component (Herrera-Endoqui et al., 2015) and coincides with the first break in the profile. The vertical dotted line marks the position of the second break.

component (Herrera-Endoqui et al., 2015). Afterwards follows a transition zone leading to a second break. These breaks are observed in all of our galaxies. In order to measure the slope of each profile (the results of which we showed in Fig. 4.3) we decided to use the range of the profile between the second break and the length of the bar. Note that the profiles along the minor axis do not stop at the edge of the bar but continue into the disc.

4.B Details on mean ages and metallicities perpendicular to the bar major axis

In Figs. 4.12-4.20 we present our detailed analysis of ages and metallicities along four cuts perpendicular to the bar major axis for the complete sample. The main results from the gradients of these profiles were discussed in Sect. 4.4.2.2.

Equally to the extraction of major and minor axis profiles described in the previous appendix, we start with the 2D maps of light- and mass-weighted mean ages and metallicities as derived from STECKMAP. On these maps we define the bar major and minor axis in projection as previously outlined. Additional to a central cut along the bar minor axis, we define 3 pairs of cuts equally spaced to both sides of the minor axis, such that the last cuts are at the end of the bar. The cuts have a width of 4″ and equally spaced bins along the cut every 2″. Stripes of the same colour in the figures are averaged in anti-parallel direction. The motivation and a sketch were presented in Sect. 4.4.2.2.

Additionally, along the cuts, we plot Hα densities and total surface brightness. The former is measured along the same cuts from the Hα maps in Fig. 4.2. The latter is extracted from the total flux within each Voronoi bin during the measurement of the stellar kinematics with PPXF (see Sect. 4.4.1). For convenience, in order not to overload the figure, we show Hα only in the panels of the left side and the total surface brightness only on the right side, but both can equally be considered for the opposite side as well.

Dust lanes are signatures of cold gas inflows, they are clearly present for most of the galaxies in this sample and can be seen as dark features in the colour maps in Fig. 2 of Paper I. In our figures, we mark them for reference as grey shaded areas at the approximate position along the profiles.

In Figs. 4.12-4.20 we present detailed results from this analysis separately for every galaxy in the sample. We do not show individual errorbars on the age and metallicity profiles, since an estimation of the uncertainties of the fits with STECKMAP was not performed for all bins within all galaxies. As mentioned in the main text, general uncertainties were studied for a set of 5000 spectra from the TIMER data in Appendix A of Paper I. Typical values are 0.5-1 Gyr for age, and 0.005-0.010 for metallicity.

4.C Details on star formation histories

Star formation histories were derived along the same four cuts perpendicular to the bar major axis for the complete sample. An example was shown for NGC 4981 in Fig. 4.7, where we also highlighted the apparent ‘V-shape’. In Fig. 4.21, we show the SFH for all galaxies in the sample. Each row shows one object.

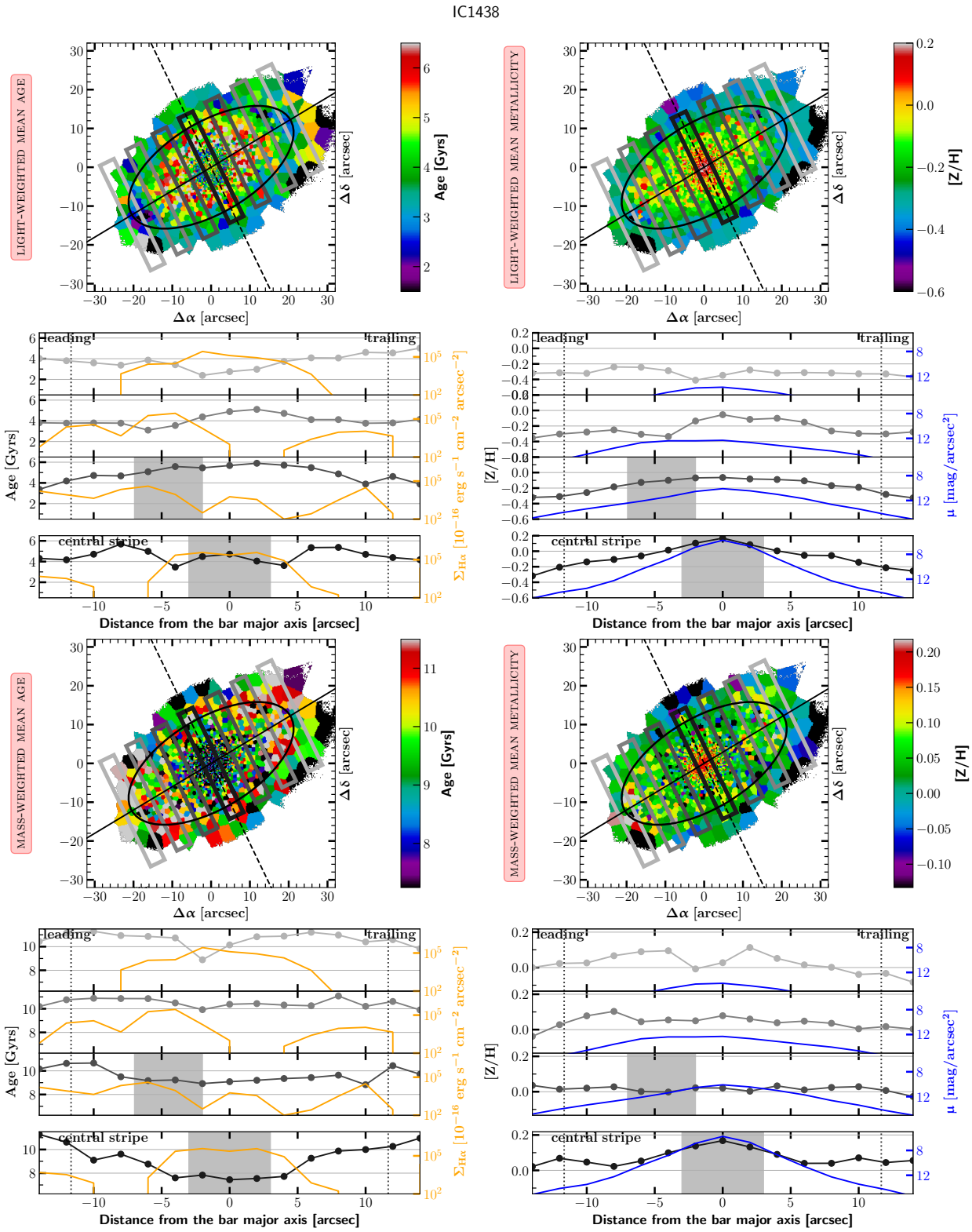

Figure 4.12: Light- and mass-weighted mean ages and metallicities. The figure splits into four quarters. On the left we show ages and on the right we show [Z/H]. The top shows light-weighted values, the bottom mass-weighted. In each quarter we show a 2D map of Voronoi-binned mean values overplotted with an outline of the bar (black ellipse), the bar major axis (solid line), the minor axis (dashed line) and outlines of the cuts from which we derive the profiles shown below (empty rectangles). Below each map, in four panels, we plot averaged profiles extracted from the corresponding cuts shown in the map. The shades of grey of the profiles correspond to the grey of the rectangles in the map. Also shown are Hα (orange line), total surface brightness (blue line) and the approximate position of dust lines (grey area). Vertical grey dotted lines mark the edge of the bar assuming for simplicity a rectangular shape. Further details can be found in the text.

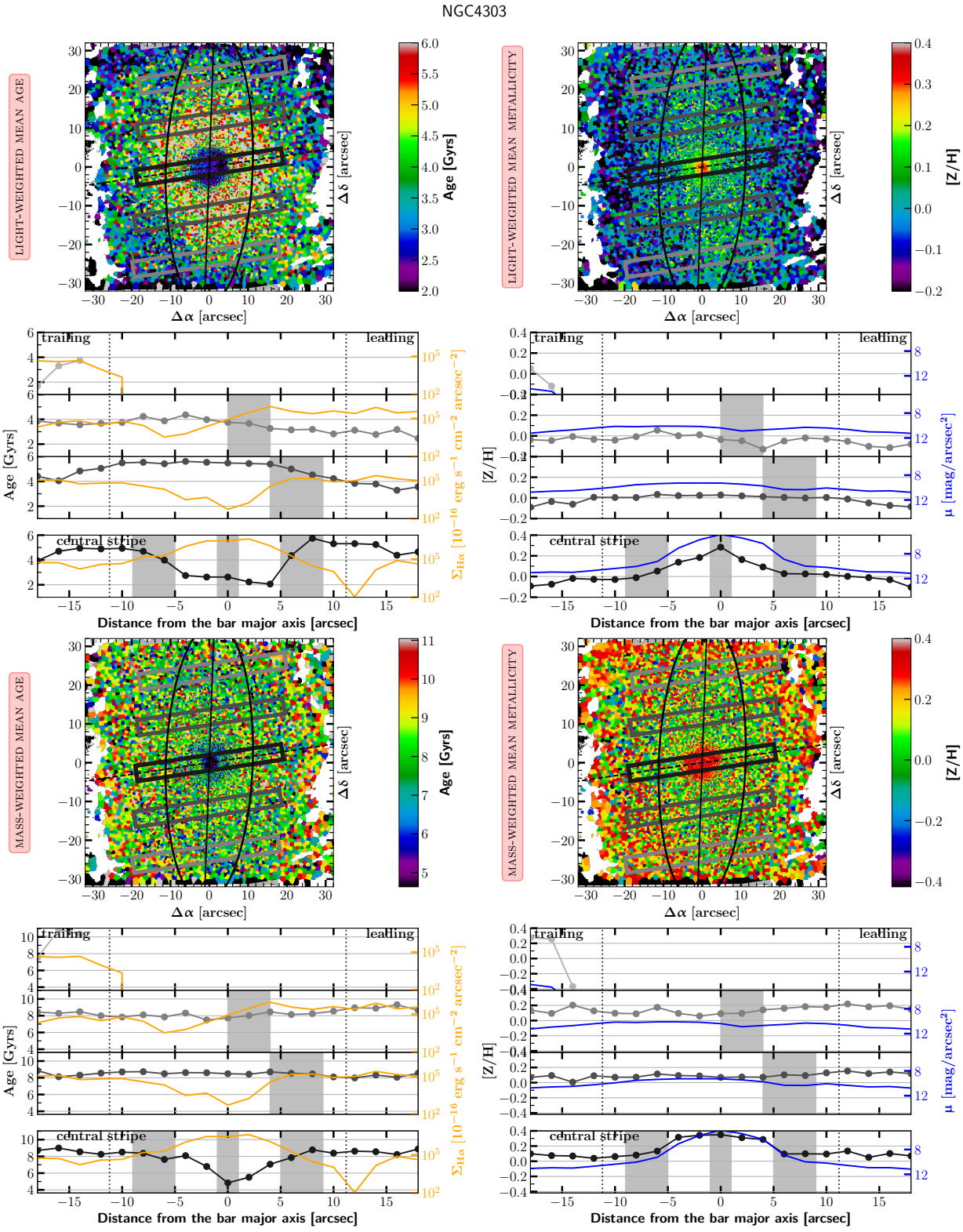

Figure 4.13: Same as 4.12.

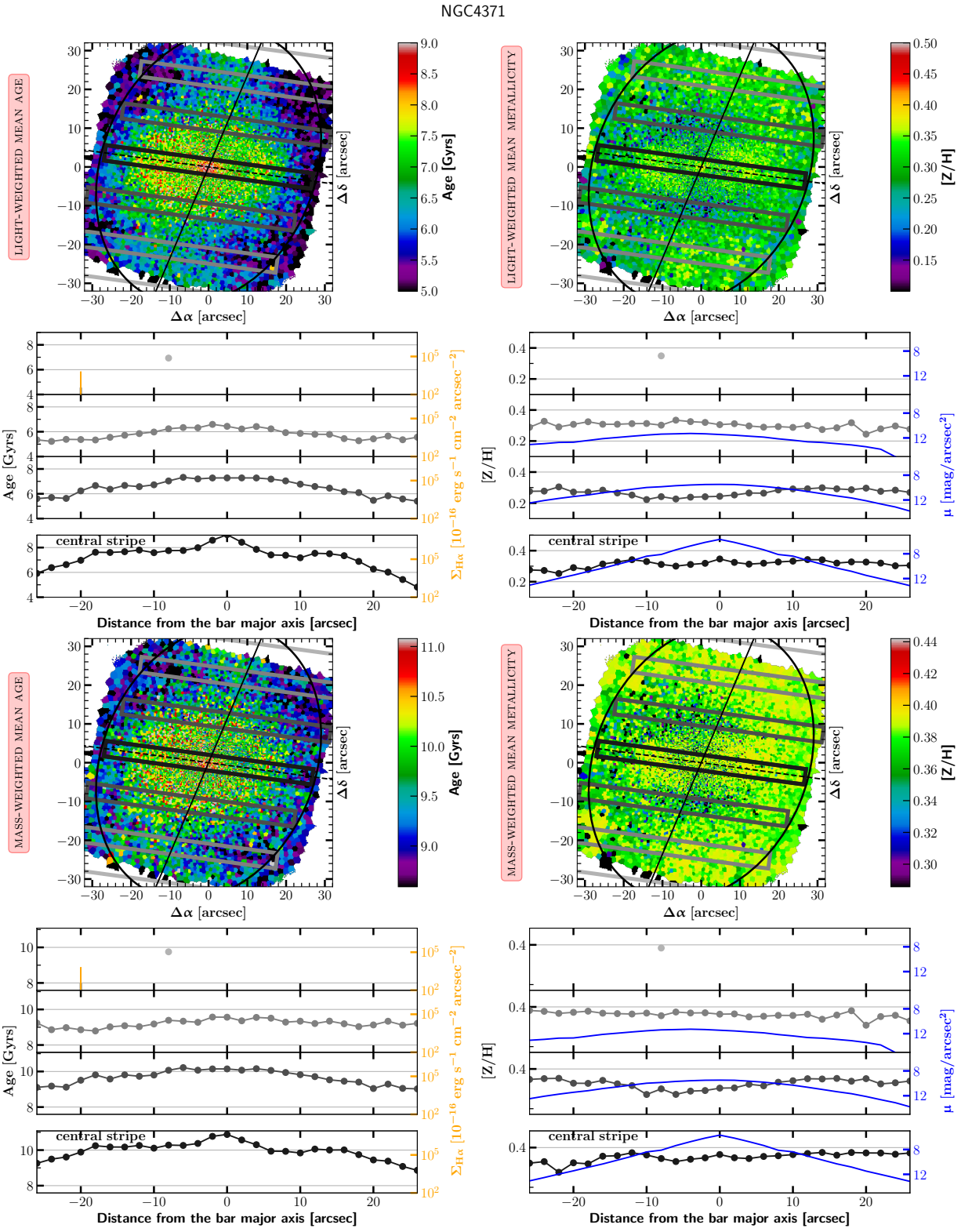

Figure 4.14: Same as 4.12.

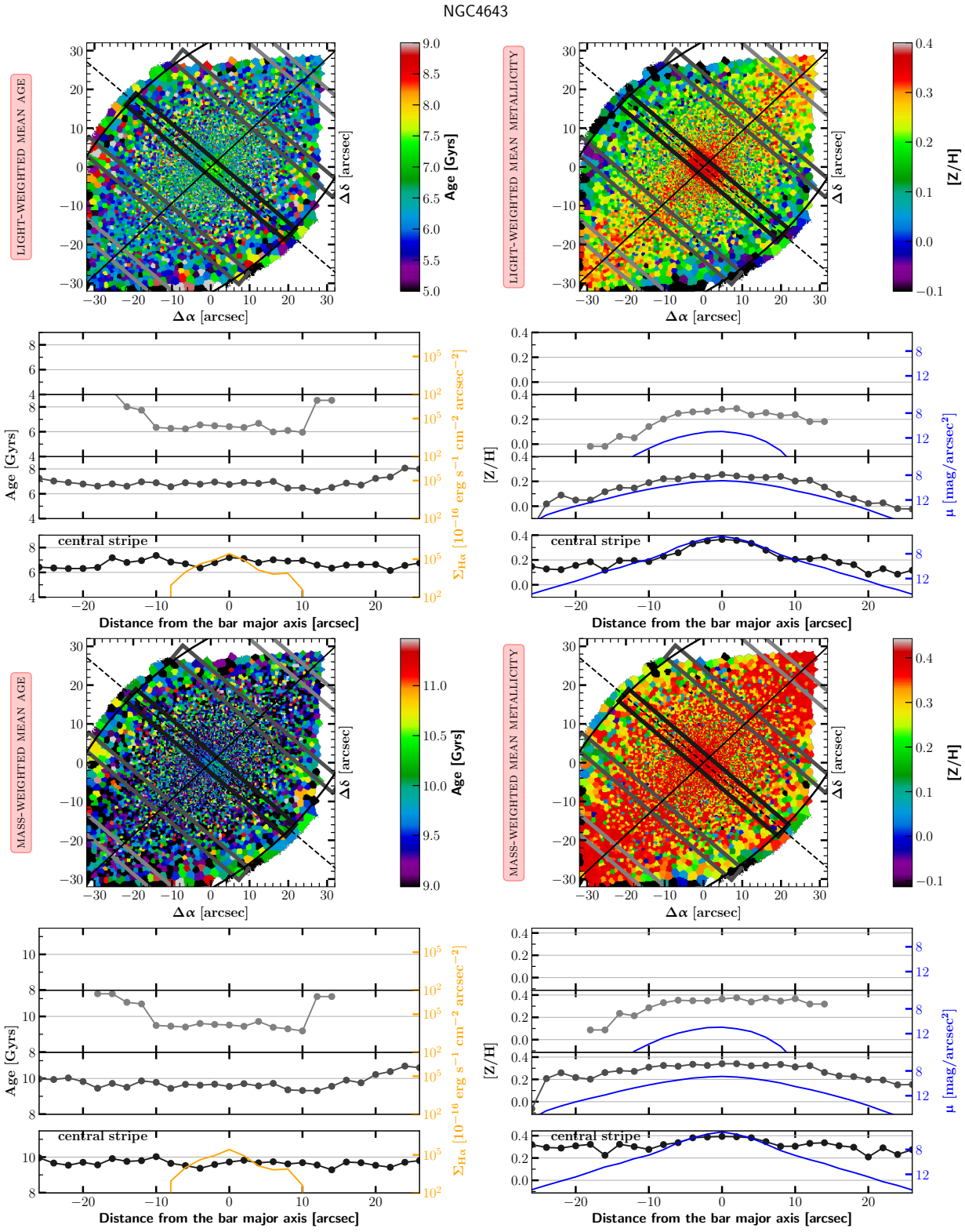

Figure 4.15: Same as 4.12.

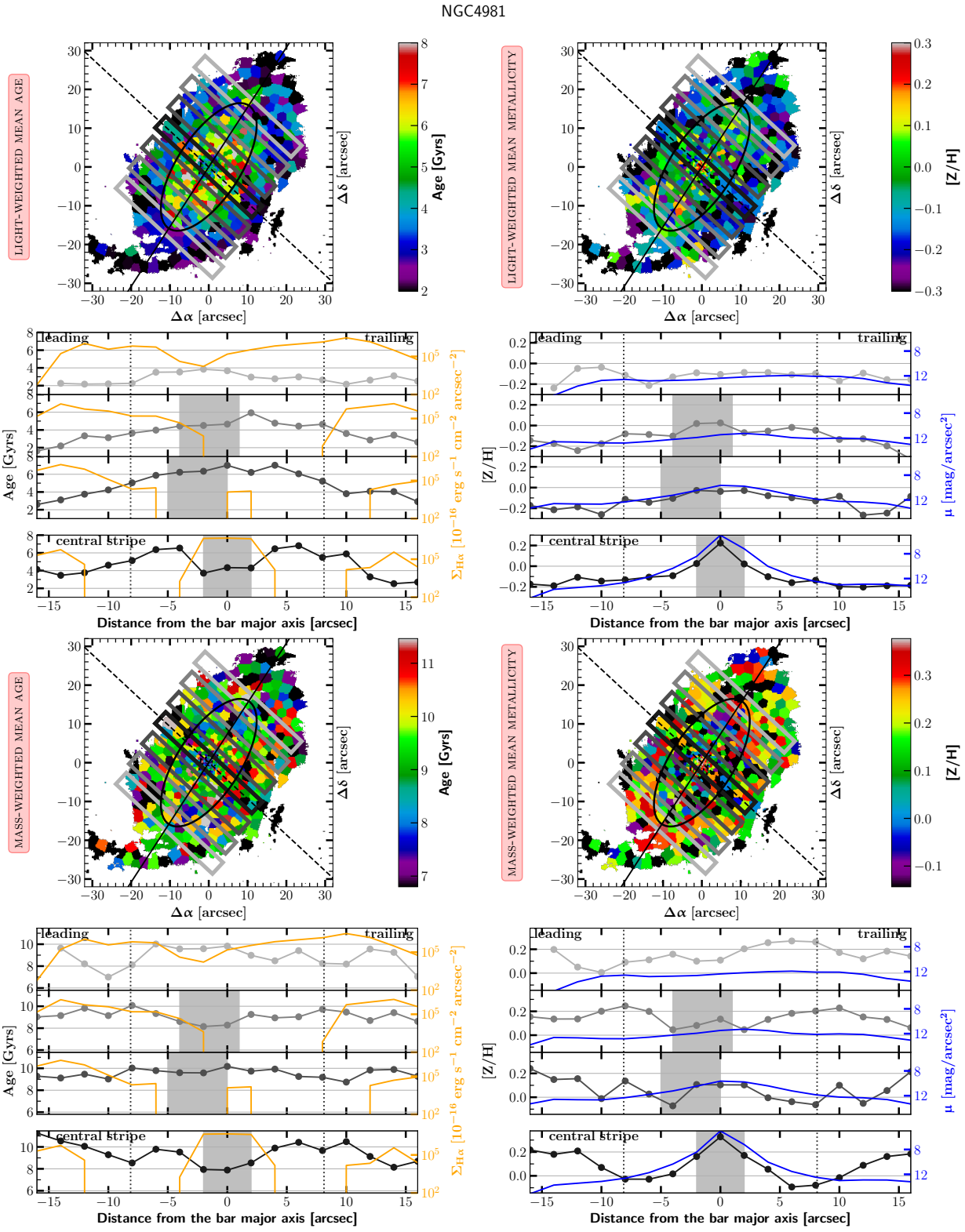

Figure 4.16: Same as 4.12.

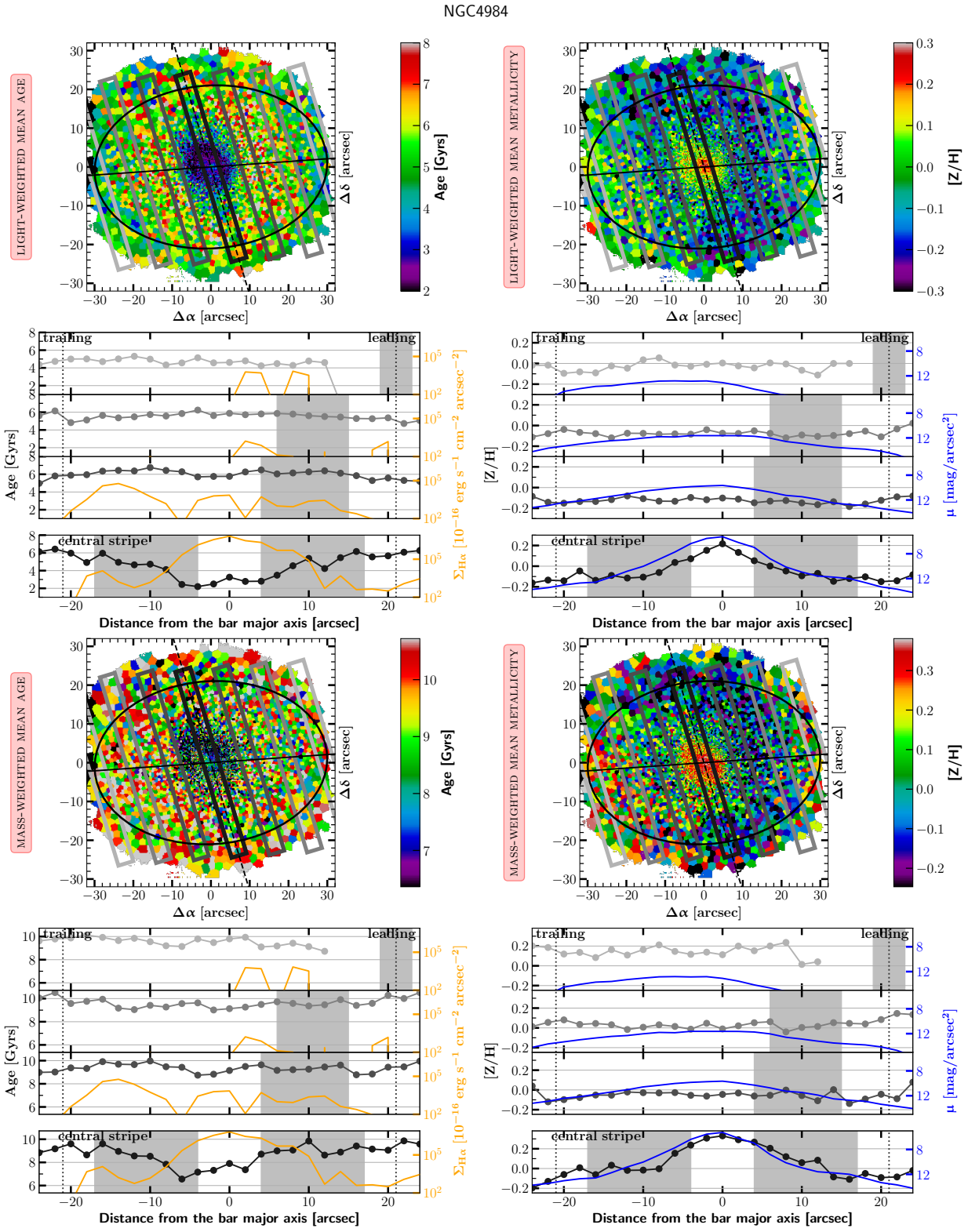

Figure 4.17: Same as 4.12.

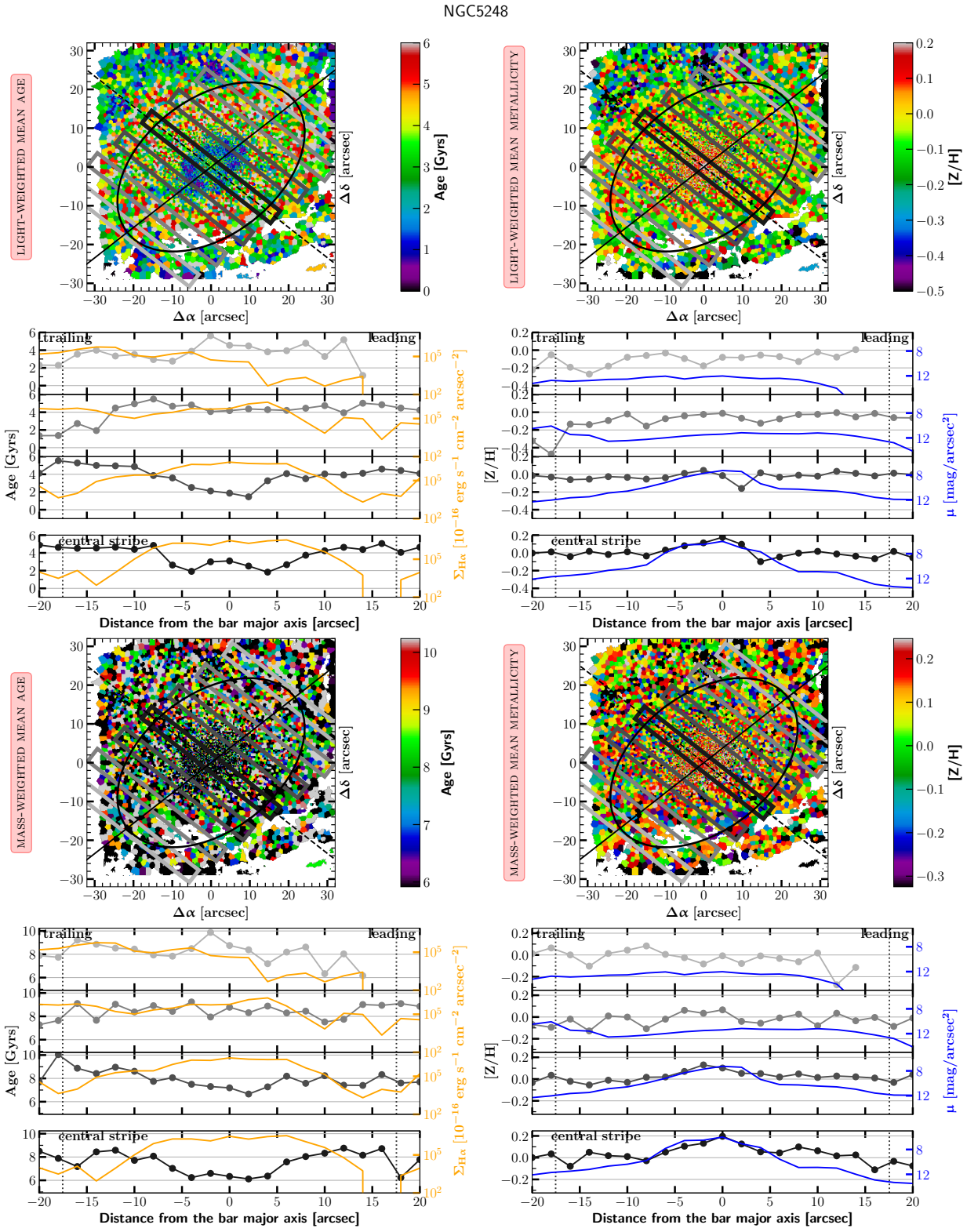

Figure 4.18: Same as 4.12.

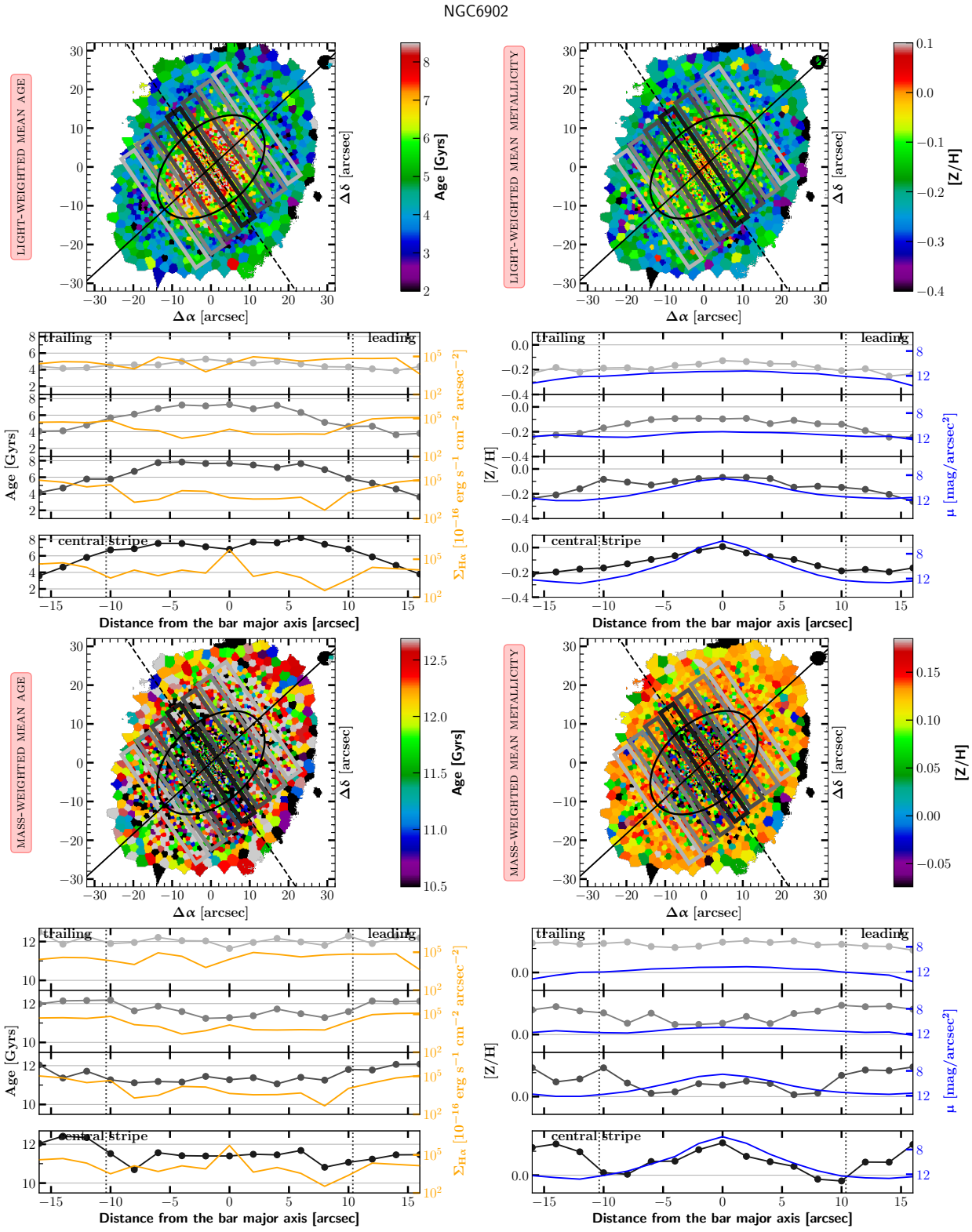

Figure 4.19: Same as 4.12.

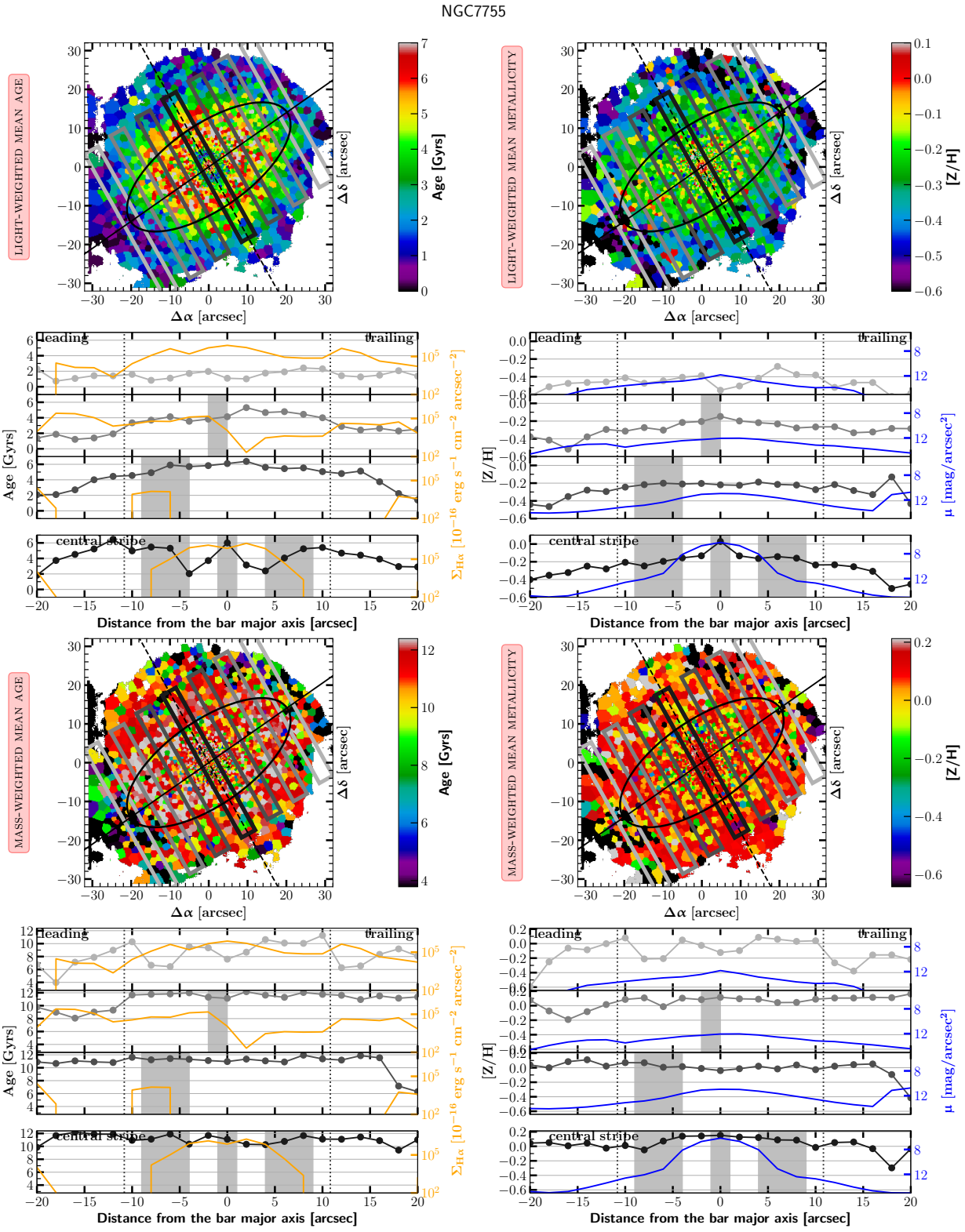

Figure 4.20: Same as 4.12.

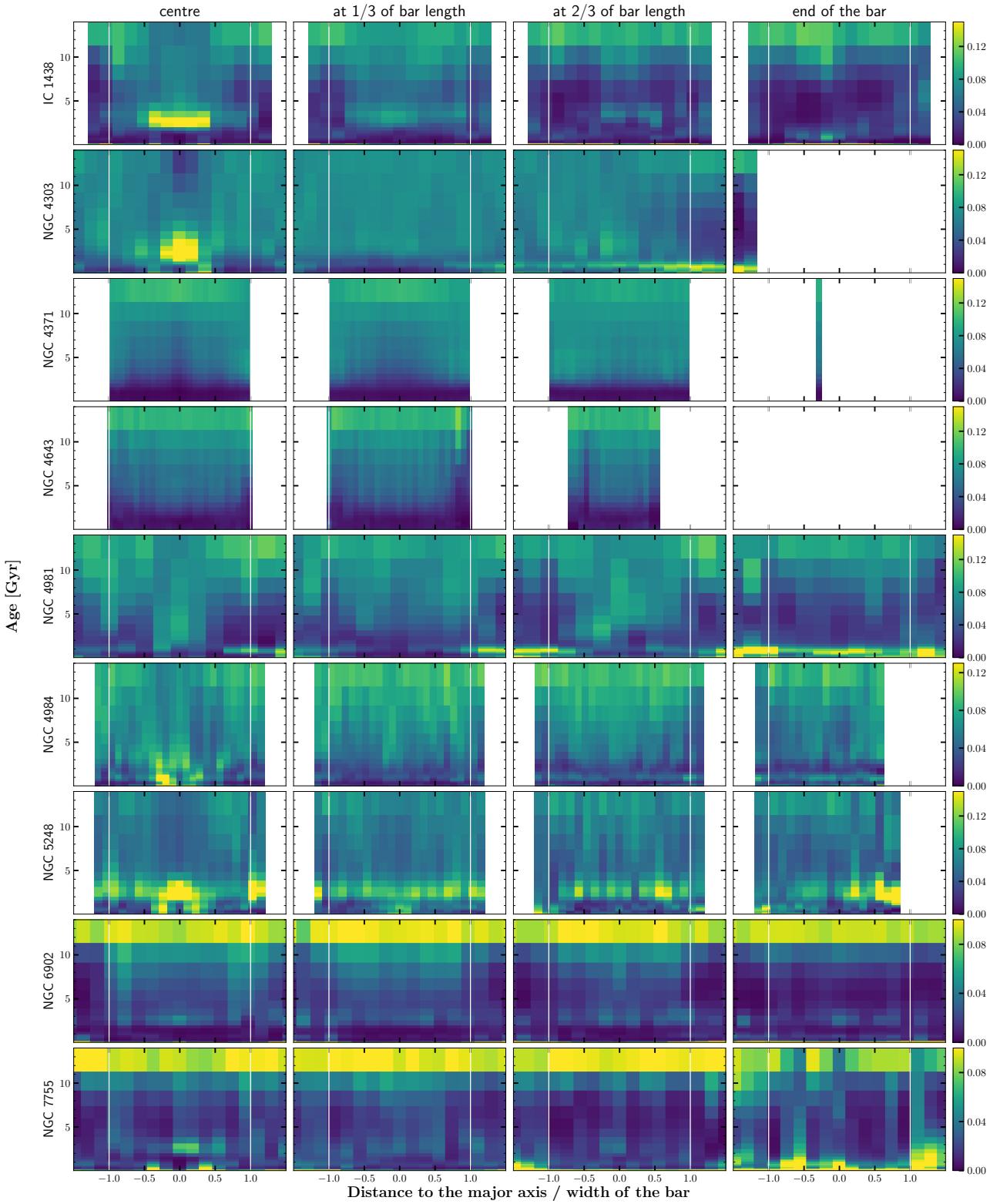

Figure 4.21: SFHs of the complete sample. Details of the figure are the same as in Fig. 4.7. The four panels are shown here from left to right in one row for each galaxy. In some cases the colour bar is stretched in order to show fainter details that allow to recognise the 'V-shape' discussed in the main text.

5 Conclusions and outlook

In this thesis, I used integral field spectroscopy to study internal properties of bars and bulges in disc galaxies to elucidate some of the processes through which secular evolution takes place. Galaxy bulges are the relics of galaxy evolution. The presence of bulges and relative occurrences of the different types put strong constraints on theoretical models of the formation and evolution of galaxies. Bars, on the other side, are the engines of secular evolution. Studying the properties of bars and secularly built structures, such as disc-like bulges, aids in better understanding how and when bars form, i.e. when are the discs dynamically ready to become bar-unstable, as well as what is the role of bars in reshaping the structure of disc galaxies.

The key ingredient to this investigation was the combination of photometry with 2D spatially resolved analyses of dynamics, star formation and stellar populations. This has proven extremely valuable in order to find a new dynamics-based classification method for bulges, to quantify and localise star formation in bars (or the absence thereof), as well as to find trends in the the variation of stellar populations in bars.

The work has been conducted in three different projects as part of three different collaborations: the CALIFA survey, the CARS survey and the TIMER project. All three surveys use IFS to study different aspects of nearby galaxies. In the first project, we used a combination of SDSS images with spatially resolved spectra from PMAS in the CALIFA survey to study bulges. Secondly, in CARS, we were able to take advantage of the strong IFU and (reconstructed) imaging capabilities of MUSE to study the star formation in bars and compare with properties of the host galaxies with both photometry and spectroscopy from observations of a single instrument. Finally, we made further use of the fine spatial sampling and the big FOV of MUSE to investigate in great detail variations of stellar populations in the very nearby barred galaxies in the TIMER survey.

5.1 Summary of the results

5.1.1 Classification and the incidence of bulges

In Chapter 2, we presented a new recipe to separate inner discs from classical bulges based on a combination of photometric and spectroscopic approaches. We performed 2D multi-component image decompositions on SDSS *r*-band images to obtain bulge parameters, such as the Sérsic index $n_{\rm b}$. We further used growth curve measurements to derive the new concentration index $C_{20,50}$, which is the ratio of the radii that contain 20% and 50% of the total light of the galaxy. Finally, we performed full spectral template fitting to the CALIFA IFU data cubes to extract 2D velocity and velocity dispersion maps, from which we derived the inner radial gradient of velocity dispersion $\nabla\sigma$. We tested and compared new classification criteria with other approaches from the literature and proposed a combination of four criteria for a final classification: $n_{\rm b}$, $C_{20,50}$, $\nabla\sigma$, and the Kormendy (1977) relation. With that recipe, we provided a classification of bulges in 45 unbarred CALIFA galaxies, finding 16 pseudobulges, 24 classical bulges, 3 bulge-less galaxies and two galaxies with no clear result. We further found that our new *inner* concentration index $C_{20,50}$ performs considerably better than the traditionally used $C_{50,90}$ and, in combination with the Kormendy relation, provides already a very robust indication of the nature of bulges.

There is still no consensus in the literature about the best method to classify bulges. Additionally to the approaches presented in Chapter 2 and published in Neumann et al. (2017), new studies of bulges emerged, proposing further methods for the classification. For example, Costantin et al. (2018) used the reconstructed 3D instrinsic shape of bulges as a classification criterion, while Luo et al. (2019) proposed the central stellar mass surface density $\Delta\Sigma_1$ within 1 kpc to classify bulges. One of the main problems, that all of these classification attempts face up to, is that the distributions of classical bulges, disc-like bulges and box-peanuts overlap in all of the proposed parameters. A possible solution to find inner discs (as opposed to classical bulges) could be to search for clear evidence of secular processes in action combined with high spatially resolved kinematics of the central structure. This has the potential to unveil small rotating inner discs built through secular evolution in the central part of disc galaxies. Having good evidence for the true nature of these bulges, they would provide an excellent sample to test the performance of any criterion that has been proposed to classify bulges. A study that aims at showing that inner discs in the TIMER galaxies are the same as photometrically indentified disc-like bulges is currently underway and will be published soon (Gadotti et al., in prep.).

5.1.2 Star formation in bars

The absence of star formation in many galaxy bars is yet not well understood. Simulations show that tangential velocity gradients in the bar can be responsible for suppressing star formation even in the presence of high gas densities. Alternatively, bars could efficiently remove all the gas from the bar region and thereby starve star formation within the bar, but there is still sufficiently gas in the centre and outer disc to continue the star formation process in those regions.

In Chapter 3, we studied the star formation in bars of 16 nearby AGN-host disc galaxies in the CARS survey. We combined a very detailed 2D photometric decomposition including up to seven different components with a spatially resolved analysis of SFRs extracted from dust-corrected Hα emission line fluxes. We found a clear separation into eight SF bars and eight non-SF bars; indication of a fast quenching process. Futhermore, we reported the detection of a correlation between the SFR in the bar and the flatness of the surface brightness profile. Only the flattest bars ($n_{\rm bar} \leq 0.4$) are SF, while less flatter bars are quiescent. Both parameters are found to be uncorrelated with Hubble type. However, our sample does not include very late-type galaxies (SBcd-Sm), which have previously been linked to exponential and SF bars. Additionally, owing to the high spatial resolution of the MUSE data cubes, we were able to dissect the SFR within the bars and analyse trends parallel and perpendicular to the bar major axis. We found that star formation is 1.75 times stronger on the leading edge of the bar than on the trailing edge and is decreasing along the major axis. This result constitutes the first quantification of the picture that star formation in rotating bars, if present, occurs preferentially on the leading side.

Finally, we tested an bar-driven AGN feeding scenario by comparing the SFR in the bar with the AGN bolometric luminosity. Active star formation in the bar indicates the presence of gas that is presumably funnelled along the bar towards the centre. If the gas reaches the sphere of influence of the SMBH, it has the potential to ignite or enhance black hole activity. In our study, we did not find a correlation between SFR in the bar and AGN luminosity. There are several possible reasons for the non-correlation. Firstly, it is yet not clear, whether star formation in the bar is only driven by the presence of gas or whether it can also be inhibited by shear. If star formation is suppressed because of shear, non-SF bars will still funnel gas towards the centre. Secondly, in most cases, gas that is pushed by the bar towards the centre is stalled in a nuclear ring at the inner Lindblad resonance, a few 100 pc from the centre, and it requires additional mechanisms, such as nuclear bars or nuclear spirals, to bring the gas further inwards. Finally, a causal connection can easily be washed out due to different timescales of nuclear activity, star formation and the evolution of the bar.

5.1.3 Stellar populations in bars

While the project in Chapter 3 concerns ongoing and localised star formation, the study presented in Chapter 4 focussed on how star formation proceeds in bars on large

spatial and temporal scales. So far, analyses of stellar populations in barred galaxies have mainly studied variations in 1D profiles along the bar major axis and compared them to the disc (Sánchez-Blázquez et al., 2011; Fraser-McKelvie et al., 2019b) or the bar minor axis (Seidel et al., 2016). By using high spatially-resolved MUSE observations of very nearby barred galaxies in the TIMER survey, we were now able to study stellar population properties in bars in much more detail.

In Chapter 4, we presented our detailed IFS analysis of 9 barred galaxies in the MUSE TIMER survey. We derived and analysed spatially resolved maps of stellar ages, metallicities, [α/Fe] abundances, star formation histories, as well as Hα as tracer of star formation. Using these maps, we explored in detail the variations of stellar populations perpendicular to the bar major axis. For the first time, we found observational evidence for a separation of stellar populations supposedly caused by an evolving bar, as it was recently recognised in idealised simulations in Athanassoula et al. (2017), Debattista et al. (2017) and Fragkoudi et al. (2017). In these simulations, the young and kinematically cold component forms an elongated strong bar, while the old and hot component forms a rounder and weaker bar. Our observations showed a recognisable V-shape in the SFH sampled perpendicular to the bar major axis. The same shape also manifested itself as positive gradient of mean mass-weighted stellar ages from the bar major axis outwards. These results are indication of intermediate-age stellar populations (~2-6 Gyr) clustering along the major axis, while old populations are spread further out. When compared to the SFHs in bars in the Auriga magneto-hydrodynamical cosmological zoom-in simulations, we found a similar separation of stellar populations giving rise to the V-shape in the SFHs.

In addition, we found imprints of recent and ongoing star formation along the edges of the bar. Light-weighted mean stellar ages, which are dominated by the light of young stellar populations, show negative gradients from the bar major axis outwards. These gradients are slightly stronger on the leading edge of the bar. We interpreted this as a result of recent star formation on the leading edge, in agreement with our study in Chapter 3, that is partially washed-out due to short dynamical timescales (~100-300 Myr per radial oscillation of the stars along the $x1$ orbits). Furthermore, we found that bars are on average more metal-rich and less α-enhanced than the inner parts of the discs that surrounds them. The part of the disc that we probed is in most cases within the radius of the bar. This region often possesses different properties than the outer disc, it is sometimes termed 'star formation desert' (SFD; James et al., 2009; James & Percival, 2016) and often shows a truncation or down-turn in the SFH both in observations and simulations (James & Percival, 2018; Donohoe-Keyes et al., 2019). In agreement with that, we interpreted our results as indication of a more prolonged or continuous formation of star that shape the bar as compared to shorter formation episodes in the surrounding SFD.

5.2 Future perspectives

5.2.1 Disc-like bulges in unbarred galaxies

The results in Chapter 2 have shown that secularly-built bulges do exist in unbarred galaxies. The consequence of that is that disc-like bulges can be built without bars or/and that bars have built these bulges and were subsequently dissolved. The first scenario requires the existence of another mechanism that redistributes angular momentum in disc galaxies and drives gas to the centre. In fact, such mechanism can be provided by spiral patterns (e.g. Kormendy & Kennicutt, 2004; Sellwood, 2014). This process, however, is much slower than the build-up of disc-like bulges driven by bars. In the second scenario, the disk-like bulge is built by bar-driven secular evolution, but at some point the bar dissolved. Simulations have shown that if the central bulge grows large enough, it can be able to destroy bar-supporting stellar orbits, such that the bar weakens or dissolves. The required bulge mass, however, must be of the order of several percent of the total galaxy mass (Shen & Sellwood, 2004; Debattista et al., 2006). Yet, there is no clear observational evidence that bars dissolve in nature. Kormendy (2013) proposed that lenses may be remnants of dissolved bars. Bars could also be destroyed in minor mergers, but it would be very difficult to avoid the destruction of the disc-like bulge at the same time.

In summary, there are still many open questions regarding unbarred galaxies in general (Berrier & Sellwood, 2016; Bauer & Widrow, 2019) and the existence of disc-like bulges in unbarred galaxies, in particular. A detailed investigation of disc-like bulges in unbarred galaxies would be valuable in several aspects: (1) to further our understanding of the dissolution or the robustness of bars, (2) to investigate the connection between bars and lenses, (3) and to test the efficiency of spiral wave-driven secular evolution.

5.2.2 Star formation in bars with MaNGA

A statistically useful next step for the comparison of star formation activity in bars with properties of the bars and their host galaxies as presented in Chapter 3 is to perform a similar analysis on a much larger and well-defined sample. Specifically, by including AGN-free galaxies, I will be able to test whether the presented results can be extended to the full population of barred galaxies. During my time as 'Research Fellow in IFU Galaxy Evolution' at the University of Portsmouth, I plan to study the star formation in barred galaxies in the Mapping Nearby Galaxies at APO (MaNGA; Bundy et al., 2015) galaxy survey. MaNGA is an IFU survey that aims at observing 10,000 nearby galaxies with almost 5,000 galaxies observed as of today. The sample was selected to have a roughly flat stellar mass distribution and a wide range of colours over a redshift range of $0.01 < z < 0.15$. A classification into barred and unbarred galaxies can be obtained from Galaxy Zoo 2 (GZ2; Willett et al., 2013) or the MaNGA Deep Learning

Morphology Value Added Catalogues (MDLM-VAC; Fischer et al., 2019). Futhermore, bar regions are identified and masks are automatically created in the Galaxy Zoo:3D (GZ:3D; Masters et al, in prep.) project.

One limiting factor is the spatial resolution of $\sim$ 1-4 kpc given that the lengths of bars are on the order of $\sim$ 1-10 kpc. A few studies, however, have already shown the capabilities of MaNGA IFU data in combination with broad-band Sloan images to conduct analyses of barred galaxies in unprecedented sample sizes (Spindler, 2018; Guo et al., 2019; Fraser-McKelvie et al., 2019a,b). The feasibility to detect and classify Hα morphology in bars of MaNGA galaxies was recently demonstrated in (Fraser-McKelvie et al., 2019a). In the study that I intend to conduct, I plan to classify bars into star-forming and non-star-forming. This classification will then be used to compare the star formation within bars to properties of the bars and the host galaxies, similar to the study presented in Chapter 3, but for a much larger statistical sample. Further comparative analyses of the results can easily be conducted given that this sample has already been well studied.

5.2.3 Gas densities and dynamics along bars

The study of star formation in bars presented in Chapter 3 has given rise to the question as to how bars quench star formation in the bar region. Theories have been discussed, e.g. shear within the bar or the depletion of fuelling gas, but observationally this has not yet been systematically analysed.

For this purpose, I propose to use observations from the Atacama Large Millimeter/submillimeter Array (ALMA) for a well-defined sample of SF and non-SF bars to measure molecular gas densities and kinematics. In combination with optical IFU data, it will be possible to analyse whether regions of star formation suppression correlate with decreasing gas densities and/or tangential velocity gradients. Furthermore, it would be beneficial to complement this study with spatially resolved H I observations. In very strong flows along bars, molecular gas can get unbound and convert partially into atomic gas (Sormani et al., 2018). In these cases, observations of atomic gas would add valuable additional information. In addition, ALMA observations can also be used for independent star formation estimation as well as to constrain feedback efficiency.

5.2.4 High-redshift bars with JWST

As discussed in various parts of this thesis, one important objective of galaxy evolution studies is to determine the time when galaxy discs dynamically settle, thus, leading to the formation of bars. Furthermore, spatially resolved observations of young high-redhift bars would improve our understanding of bar formation and evolution.

With the upcoming launch of the James Webb Space Telescope (JWST, currently scheduled for 2021), investigations of high-redshift bars will be pushed to new heights. The use of JWST's Near Infrared Camera (NIRCam), Near InfraRed Spectrograph (NIRSpec) and Mid-Infrared Instrument (MIRI) combines very high spatial resolution with a much larger light collecting area than can be achieved with the HST. The instruments will be able to observe at wavelength ranging between 0.6 μm-5.6 μm and 5 μm-28.5 μm. This opens up an unprecedented opportunity for the detailed research of structure and kinematics of galaxies by being sensitive to faint signatures and being able to observe stellar components of high redshift galaxies at rest-frame optical wavelengths, which could lead to the detection of the earliest barred galaxies ever observed.

Bibliography

Abazajian K. N., et al., 2009, ApJS, 182, 543
Abraham R. G., Valdes F., Yee H. K. C., van den Bergh S., 1994, ApJ, 432, 75
Aguerri J. A. L., Balcells M., Peletier R. F., 2001, A&A, 367, 428
Aguerri J. A. L., Elias-Rosa N., Corsini E. M., Muñoz-Tuñón C., 2005, A&A, 434, 109
Aguerri J. A. L., Méndez-Abreu J., Corsini E. M., 2009, A&A, 495, 491
Alam S., et al., 2015, ApJS, 219, 12
Albrecht A., Steinhardt P. J., 1982, Physical Review Letters, 48, 1220
Algorry D. G., et al., 2017, MNRAS, 469, 1054
Allen P. D., Driver S. P., Graham A. W., Cameron E., Liske J., de Propris R., 2006, MNRAS, 371, 2
Alonso S., Coldwell G., Lambas D. G., 2014, A&A, 572, A86
Alonso S., Coldwell G., Duplancic F., Mesa V., Lambas D. G., 2018, A&A, 618, A149
Alpher R. A., Herman R., 1948, Nature, 162, 774
Anderson J. P., James P. A., 2009, MNRAS, 399, 559
Andrae R., Jahnke K., Melchior P., 2011, MNRAS, 411, 385
Athanassoula E., 1992a, MNRAS, 259, 328
Athanassoula E., 1992b, MNRAS, 259, 345
Athanassoula E., 2002, ApJ, 569, L83
Athanassoula E., 2003, MNRAS, 341, 1179
Athanassoula E., 2005, MNRAS, 358, 1477
Athanassoula E., 2013, Bars and secular evolution in disk galaxies: Theoretical input. Cambridge University Press, p. 305
Athanassoula E., Beaton R. L., 2006, MNRAS, 370, 1499
Athanassoula E., Bureau M., 1999, ApJ, 522, 699
Athanassoula E., Misiriotis A., 2002, MNRAS, 330, 35
Athanassoula E., Sellwood J. A., 1986, MNRAS, 221, 213
Athanassoula E., Bienayme O., Martinet L., Pfenniger D., 1983, A&A, 127, 349
Athanassoula E., Machado R. E. G., Rodionov S. A., 2013, MNRAS, 429, 1949
Athanassoula E., Laurikainen E., Salo H., Bosma A., 2015, MNRAS, 454, 3843
Athanassoula E., Rodionov S. A., Prantzos N., 2017, MNRAS, 467, L46
Babusiaux C., et al., 2010, A&A, 519, A77
Bacon R., et al., 2001, MNRAS, 326, 23
Bacon R., et al., 2010, in Ground-based and Airborne Instrumentation for Astronomy III. p. 773508, doi:10.1117/12.856027
Bacon R., et al., 2017, A&A, 608, A1
Baldwin J. A., Phillips M. M., Terlevich R., 1981, PASP, 93, 5
Barazza F. D., Jogee S., Marinova I., 2008, ApJ, 675, 1194
Barazza F. D., et al., 2009, A&A, 497, 713
Bauer J. S., Widrow L. M., 2019, MNRAS, 486, 523
Belfiore F., et al., 2016, MNRAS, 461, 3111
Bennett C. L., et al., 2003, ApJS, 148, 1
Bennett C. L., Larson D., Weiland J. L., Hinshaw G., 2014, ApJ, 794, 135
Berentzen I., Athanassoula E., Heller C. H., Fricke K. J., 2003, MNRAS, 341, 343
Berentzen I., Athanassoula E., Heller C. H., Fricke K. J., 2004, MNRAS, 347, 220
Berrier J. C., Sellwood J. A., 2016, ApJ, 831, 65
Bershady M. A., Verheijen M. A. W., Swaters R. A., Andersen D. R., Westfall K. B., Martinsson T., 2010, ApJ, 716, 198
Bertin E., Arnouts S., 1996, A&AS, 117, 393
Bertram T., Eckart A., Fischer S., Zuther J., Straubmeier C., Wisotzki L., Krips M., 2007, A&A, 470, 571
Binney J., Tremaine S., 1987, Galactic dynamics. Princeton University Press
Bittner A., et al., 2019, A&A, 628, A117
Böker T., Laine S., van der Marel R. P., Sarzi M., Rix H.-W., Ho L. C., Shields J. C., 2002, AJ, 123, 1389
Bournaud F., Combes F., Semelin B., 2005, MNRAS, 364, L18
Bundy K., et al., 2015, ApJ, 798, 7
Bureau M., Athanassoula E., 1999, ApJ, 522, 686
Bureau M., Athanassoula E., 2005, ApJ, 626, 159
Bureau M., Freeman K. C., 1999, AJ, 118, 126
Busch G., et al., 2014, A&A, 561, A140
Buta R., 1986, ApJS, 61, 609
Buta R., Combes F., 1996, Fundamentals Cosmic Phys., 17, 95
Buta R. J., Zhang X., 2009, ApJS, 182, 559
Buta R. J., et al., 2015, ApJS, 217, 32
Cacho R., Sánchez-Blázquez P., Gorgas J., Pérez I., 2014, MNRAS, 442, 2496
Calzetti D., Kinney A. L., Storchi-Bergmann T., 1994, ApJ, 429, 582
Calzetti D., Armus L., Bohlin R. C., Kinney A. L., Koornneef J., Storchi-Bergmann T., 2000, ApJ, 533, 682
Caon N., Capaccioli M., D'Onofrio M., 1994, A&AS, 106, 199
Cappellari M., Copin Y., 2003, MNRAS, 342, 345
Cappellari M., Emsellem E., 2004, PASP, 116, 138
Cappellari M., et al., 2011, MNRAS, 413, 813
Catalán-Torrecilla C., et al., 2017, ApJ, 848, 87
Cheung E., et al., 2013, ApJ, 779, 162
Cheung E., et al., 2015a, MNRAS, 447, 506
Cheung E., et al., 2015b, ApJ, 807, 36
Chung A., Bureau M., 2004, AJ, 127, 3192
Cisternas M., et al., 2013, ApJ, 776, 50
Coelho P., Gadotti D. A., 2011, ApJ, 743, L13
Cole S., Lacey C. G., Baugh C. M., Frenk C. S., 2000, MNRAS, 319, 168
Collaboration P., et al., 2011, A&A, 536, A1
Combes F., 1994, in Shlosman I., ed., Mass-Transfer Induced Activity in Galaxies. p. 170
Combes F., 1996, in Buta R., Crocker D. A., Elmegreen B. G., eds, Astronomical Society of the Pacific Conference Series Vol. 91, IAU Colloq. 157: Barred Galaxies. p. 286
Combes F., 2014, A&A, 571, A82
Combes F., Sanders R. H., 1981, A&A, 96, 164
Combes F., Debbasch F., Friedli D., Pfenniger D., 1990, A&A, 233, 82
Combes F., et al., 2019, A&A, 623, A79
Comerón S., Knapen J. H., Beckman J. E., Laurikainen E., Salo H., Martínez-Valpuesta I., Buta R. J., 2010, MNRAS, 402, 2462
Comerón S., et al., 2014, A&A, 562, A121
Contopoulos G., 1980, A&A, 81, 198
Contopoulos G., Papayannopoulos T., 1980, A&A, 92, 33
Corsini E. M., 2011, Memorie della Societa Astronomica Italiana Supplementi, 18, 23
Cortese L., Catinella B., Boissier S., Boselli A., Heinis S., 2011, MNRAS, 415, 1797
Cortese L., et al., 2014, ApJ, 795, L37
Costantin L., Méndez-Abreu J., Corsini E. M., Eliche-Moral M. C., Tapia T., Morelli L., Dalla Bontà E., Pizzella A., 2018, A&A, 609, A132
Croom S. M., et al., 2012, MNRAS, 421, 872
Davies R. L., et al., 2016, MNRAS, 462, 1616

De Rosa A., et al., 2018, MNRAS, 480, 1639
Debattista V. P., Sellwood J. A., 2000, ApJ, 543, 704
Debattista V. P., Shen J., 2007, ApJ, 654, L127
Debattista V. P., Mayer L., Carollo C. M., Moore B., Wadsley J., Quinn T., 2006, ApJ, 645, 209
Debattista V. P., Ness M., Gonzalez O. A., Freeman K., Zoccali M., Minniti D., 2017, MNRAS, 469, 1587
Di Matteo P., Haywood M., Combes F., Semelin B., Snaith O. N., 2013, A&A, 553, A102
Di Matteo P., et al., 2014, A&A, 567, A122
Di Matteo P., Fragkoudi F., Khoperskov S., Ciambur B., Haywood M., Combes F., Gómez A., 2019, A&A, 628, A11
Díaz-García S., Salo H., Laurikainen E., Herrera-Endoqui M., 2016, A&A, 587, A160
Djorgovski S., Davis M., 1987, ApJ, 313, 59
Doi M., Fukugita M., Okamura S., 1993, MNRAS, 264, 832
Domínguez A., et al., 2013, ApJ, 763, 145
Donohoe-Keyes C. E., Martig M., James P. A., Kraljic K., 2019, MNRAS, 489, 4992
Dressler A., Lynden-Bell D., Burstein D., Davies R. L., Faber S. M., Terlevich R., Wegner G., 1987, ApJ, 313, 42
Drory N., Fisher D. B., 2007, ApJ, 664, 640
Du M., Shen J., Debattista V. P., 2015, ApJ, 804, 139
Efstathiou G., Lake G., Negroponte J., 1982, MNRAS, 199, 1069
Eggen O. J., Lynden-Bell D., Sandage A. R., 1962, ApJ, 136, 748
Einstein A., 1916, Annalen der Physik, 354, 769
Eisenhauer F., et al., 2003, in Iye M., Moorwood A. F. M., eds, Society of Photo-Optical Instrumentation Engineers (SPIE) Conference Series Vol. 4841, Instrument Design and Performance for Optical/Infrared Ground-based Telescopes. pp 1548–1561 (arXiv:astro-ph/0306191), doi:10.1117/12.459468
Elmegreen B., 1996, in Buta R., Crocker D. A., Elmegreen B. G., eds, Astronomical Society of the Pacific Conference Series Vol. 91, IAU Colloq. 157: Barred Galaxies. p. 197
Elmegreen B. G., Elmegreen D. M., 1985, ApJ, 288, 438
Elmegreen D. M., Elmegreen B. G., Bellin A. D., 1990, ApJ, 364, 415
Elmegreen B. G., Elmegreen D. M., Chromey F. R., Hasselbacher D. A., Bissell B. A., 1996, AJ, 111, 2233
Elmegreen B. G., Bournaud F., Elmegreen D. M., 2008, ApJ, 688, 67
Emsellem E., et al., 2011, MNRAS, 414, 888
Emsellem E., Renaud F., Bournaud F., Elmegreen B., Combes F., Gabor J. M., 2015, MNRAS, 446, 2468
Englmaier P., Shlosman I., 2004, ApJ, 617, L115
Erwin P., 2005, MNRAS, 364, 283
Erwin P., 2010, preprint, (arXiv:1002.1445)
Erwin P., 2015, ApJ, 799, 226
Erwin P., 2018, MNRAS, 474, 5372
Erwin P., 2019, arXiv e-prints
Erwin P., Debattista V. P., 2013, MNRAS, 431, 3060
Erwin P., Sparke L. S., 2003, ApJS, 146, 299
Erwin P., Beckman J. E., Pohlen M., 2005, ApJ, 626, L81
Erwin P., Pohlen M., Beckman J. E., 2008, AJ, 135, 20
Erwin P., et al., 2015, MNRAS, 446, 4039
Eskridge P. B., et al., 2000, AJ, 119, 536
Faber S. M., 1977, in Tinsley B. M., Larson D. Campbell R. B. G., eds, Evolution of Galaxies and Stellar Populations. p. 157
Faber S. M., Jackson R. E., 1976, ApJ, 204, 668
Fabricius M. H., Saglia R. P., Fisher D. B., Drory N., Bender R., Hopp U., 2012, ApJ, 754, 67
Falcón-Barroso J., et al., 2006, MNRAS, 369, 529
Falcón-Barroso J., et al., 2017, A&A, 597, A48
Fall S. M., Efstathiou G., 1980, MNRAS, 193, 189
Federrath C., et al., 2017, MNRAS, 468, 3965
Feldmann R., Mayer L., 2015, MNRAS, 446, 1939
Ferrarese L., Merritt D., 2000, ApJ, 539, L9
Ferrari F., de Carvalho R. R., Trevisan M., 2015, ApJ, 814, 55
Ferrers N., 1877, Quart. J. Pure and Appl. Math., 14, 1
Fischer J.-L., Domínguez Sánchez H., Bernardi M., 2019, MNRAS, 483, 2057
Fisher D. B., Drory N., 2008, AJ, 136, 773
Fisher D. B., Drory N., 2010, ApJ, 716, 942
Fisher D. B., Drory N., 2011, ApJ, 733, L47
Fisher D. B., Drory N., 2016, Galactic Bulges, 418, 41
Fisher D. B., Drory N., Fabricius M. H., 2009, ApJ, 697, 630
Font J., et al., 2017, ApJ, 835, 279
Förster Schreiber N. M., et al., 2009, ApJ, 706, 1364
Fragkoudi F., Athanassoula E., Bosma A., 2016, MNRAS, 462, L41
Fragkoudi F., Di Matteo P., Haywood M., Gómez A., Combes F., Katz D., Semelin B., 2017, A&A, 606, A47
Fragkoudi F., Di Matteo P., Haywood M., Schultheis M., Khoperskov S., Gómez A., Combes F., 2018, A&A, 616, A180
Fraser-McKelvie A., Merrifield M., Aragón-Salamanca A., Masters K., the MaNGA Survey Team 2019a, arXiv e-prints
Fraser-McKelvie A., et al., 2019b, MNRAS, 488, L6
Freeman K. C., 1970, ApJ, 160, 811
Freeman K. C., 1975, in Hayli A., ed., IAU Symposium Vol. 69, Dynamics of the Solar Systems. p. 367
Friedli D., Martinet L., 1993, A&A, 277, 27
Friedli D., Benz W., Kennicutt R., 1994, ApJ, 430, L105
Friedmann A., 1922, Zeitschrift fur Physik, 10, 377
Gadotti D. A., 2008, MNRAS, 384, 420
Gadotti D. A., 2009, MNRAS, 393, 1531
Gadotti D. A., 2011, MNRAS, 415, 3308
Gadotti D. A., Athanassoula E., Carrasco L., Bosma A., de Souza R. E., Recillas E., 2007, MNRAS, 381, 943
Gadotti D. A., Seidel M. K., Sánchez-Blázquez P., Falcón-Barroso J., Husemann B., Coelho P., Pérez I., 2015, A&A, 584, A90
Gadotti D. A., et al., 2019, MNRAS, 482, 506
Galloway M. A., et al., 2015, MNRAS, 448, 3442
Gamow G., 1946, Physical Review, 70, 572
Ganda K., et al., 2007, MNRAS, 380, 506
Gao H., Ho L. C., 2017, ApJ, 845, 114
García-Barreto J. A., Franco J., Carrillo R., Venegas S., Escalante-Ramírez B., 1996, Rev. Mex. Astron. Astrofis., 32, 89
García-Benito R., et al., 2015, A&A, 576, A135
García-Burillo S., Combes F., 2012, in Journal of Physics Conference Series. p. 012050 (arXiv:1205.0758), doi:10.1088/1742-6596/372/1/012050
Gaspari M., Sądowski A., 2017, ApJ, 837, 149
Gebhardt K., et al., 2000, ApJ, 539, L13
George K., Subramanian S., Paul K. T., 2019, A&A, 628, A24
Gerin M., Combes F., Athanassoula E., 1990, A&A, 230, 37
Giavalisco M., Steidel C. C., Macchetto F. D., 1996, ApJ, 470, 189
Goulding A. D., et al., 2017, ApJ, 843, 135
Graham A. W., Driver S. P., Petrosian V., Conselice C. J., Bershady M. A., Crawford S. M., Goto T., 2005, AJ, 130, 1535
Grand R. J. J., et al., 2017, MNRAS, 467, 179
Guo R., Mao S., Athanassoula E., Li H., Ge J., Long R. J., Merrifield M., Masters K., 2019, MNRAS, 482, 1733
Guth A. H., 1981, Phys. Rev. D, 23, 347
Hakobyan A. A., Mamon G. A., Petrosian A. R., Kunth D., Turatto M., 2009, A&A, 508, 1259
Hakobyan A. A., et al., 2016, MNRAS, 456, 2848
Hammer F., Flores H., Elbaz D., Zheng X. Z., Liang Y. C., Cesarsky C., 2005, A&A, 430, 115
Harrison C. M., 2017, Nature Astronomy, 1, 0165
Häussler B., et al., 2007, ApJS, 172, 615
Häußler B., et al., 2013, MNRAS, 430, 330
Hawarden T. G., Mountain C. M., Leggett S. K., Puxley P. J., 1986, MNRAS, 221, 41P
Haywood M., Lehnert M. D., Di Matteo P., Snaith O., Schultheis M., Katz D., Gómez A., 2016, A&A, 589, A66
Heisenberg W., 1927, Zeitschrift fur Physik, 43, 172
Hernquist L., Weinberg M. D., 1992, ApJ, 400, 80
Herrera-Endoqui M., Díaz-García S., Laurikainen E., Salo H., 2015, A&A, 582, A86
Herrero-Illana R., Pérez-Torres M. Á., Alberdi A., 2012, A&A, 540, L5
Hinshaw G., et al., 2007, ApJS, 170, 288
Ho L. C., Filippenko A. V., Sargent W. L. W., 1997, ApJ, 487, 591
Hohl F., 1971, ApJ, 168, 343
Holmes L., et al., 2015, MNRAS, 451, 4397
Hoyle F., Tayler R. J., 1964, Nature, 203, 1108
Hubble E. P., 1925, Popular Astronomy, 33
Hubble E. P., 1926, ApJ, 64, 321

Hubble E., 1929, Proceedings of the National Academy of Science, 15, 168
Hubble E. P., 1936, Realm of the Nebulae
Husemann B., Wisotzki L., Sánchez S. F., Jahnke K., 2013a, A&A, 549, A43
Husemann B., et al., 2013b, A&A, 549, A87
Husemann B., Jahnke K., Sánchez S. F., Wisotzki L., Nugroho D., Kupko D., Schramm M., 2014, MNRAS, 443, 755
Husemann B., Bennert V. N., Scharwächter J., Woo J.-H., Choudhury O. S., 2016, MNRAS, 455, 1905
Husemann B., et al., 2017, The Messenger, 169, 42
Immeli A., Samland M., Gerhard O., Westera P., 2004a, A&A, 413, 547
Immeli A., Samland M., Westera P., Gerhard O., 2004b, ApJ, 611, 20
James P. A., Percival S. M., 2016, MNRAS, 457, 917
James P. A., Percival S. M., 2018, MNRAS, 474, 3101
James P. A., Bretherton C. F., Knapen J. H., 2009, A&A, 501, 207
Jarvis B. J., 1986, AJ, 91, 65
Kalnajs A. J., 1972, ApJ, 175, 63
Kalnajs A. J., 1976, ApJ, 205, 751
Kalnajs A. J., 1978, in Berkhuijsen E. M., Wielebinski R., eds, IAU Symposium Vol. 77, Structure and Properties of Nearby Galaxies. pp 113–125
Kaspi S., Smith P. S., Netzer H., Maoz D., Jannuzi B. T., Giveon U., 2000, ApJ, 533, 631
Katz N., Gunn J. E., 1991, ApJ, 377, 365
Katz N., Weinberg D. H., Hernquist L., 1996, ApJS, 105, 19
Kauffmann G., Colberg J. M., Diaferio A., White S. D. M., 1999, MNRAS, 303, 188
Kauffmann G., et al., 2003a, MNRAS, 341, 33
Kauffmann G., et al., 2003b, MNRAS, 346, 1055
Kautsch S. J., Grebel E. K., Barazza F. D., Gallagher III J. S., 2006, A&A, 445, 765
Kelz A., et al., 2006, PASP, 118, 129
Kennicutt Jr. R. C., 1994, in Shlosman I., ed., Mass-Transfer Induced Activity in Galaxies. p. 131
Kennicutt Jr. R. C., 1998, ARA&A, 36, 189
Kennicutt R. C., Evans N. J., 2012, ARA&A, 50, 531
Kent S. M., 1985, ApJS, 59, 115
Kewley L. J., Dopita M. A., Sutherland R. S., Heisler C. A., Trevena J., 2001, ApJ, 556, 121
Khoperskov S., Haywood M., Di Matteo P., Lehnert M. D., Combes F., 2018, A&A, 609, A60
Kim W.-T., Seo W.-Y., Stone J. M., Yoon D., Teuben P. J., 2012, ApJ, 747, 60
Kim T., et al., 2014, ApJ, 782, 64
Kim T., et al., 2015, ApJ, 799, 99
Kim E., Hwang H. S., Chung H., Lee G.-H., Park C., Cervantes Sodi B., Kim S. S., 2017, ApJ, 845, 93
Knapen J. H., Shlosman I., Peletier R. F., 2000, ApJ, 529, 93
Komatsu E., et al., 2009, ApJS, 180, 330
Kormendy J., 1977, ApJ, 217, 406
Kormendy J., 1980, in Crane P., Kjär K., eds, Two Dimensional Photometry. p. 191
Kormendy J., 1993a, in Beckman J., Colina L., Netzer H., eds, The Nearest Active Galaxies. pp 197–218
Kormendy J., 1993b, in Dejonghe H., Habing H. J., eds, IAU Symposium Vol. 153, Galactic Bulges. p. 209
Kormendy J., 2013, Secular Evolution in Disk Galaxies. p. 1
Kormendy J., 2016, in Laurikainen E., Peletier R., Gadotti D., eds, Astrophysics and Space Science Library Vol. 418, Galactic Bulges. p. 431 (arXiv:1504.03330), doi:10.1007/978-3-319-19378-6˙16
Kormendy J., Gebhardt K., 2001, in Wheeler J. C., Martel H., eds, American Institute of Physics Conference Series Vol. 586, 20th Texas Symposium on relativistic astrophysics. pp 363–381 (arXiv:astro-ph/0105230), doi:10.1063/1.1419581
Kormendy J., Illingworth G., 1982, ApJ, 256, 460
Kormendy J., Kennicutt Jr. R. C., 2004, ARA&A, 42, 603
Krajnović D., et al., 2011, MNRAS, 414, 2923
Kraljic K., Bournaud F., Martig M., 2012, ApJ, 757, 60
Kroupa P., 2001, MNRAS, 322, 231
Kruk S. J., et al., 2018, MNRAS, 473, 4731
Kuijken K., Merrifield M. R., 1995, ApJ, 443, L13
Kunder A., et al., 2016, ApJ, 821, L25
Kuntschner H., et al., 2010, MNRAS, 408, 97
Laine S., Shlosman I., Knapen J. H., Peletier R. F., 2002, ApJ, 567, 97
Laurikainen E., Salo H., 2017, A&A, 598, A10
Laurikainen E., Salo H., Buta R., 2005, MNRAS, 362, 1319
Laurikainen E., Salo H., Buta R., Knapen J. H., 2007, MNRAS, 381, 401
Laurikainen E., Salo H., Buta R., Knapen J. H., 2009, ApJ, 692, L34
Laurikainen E., Salo H., Buta R., Knapen J. H., Comerón S., 2010, MNRAS, 405, 1089
Laurikainen E., Salo H., Buta R., Knapen J. H., 2011, MNRAS, 418, 1452
Lemaître G., 1927, Annales de la Société Scientifique de Bruxelles, 47, 49
Lemaître G., 1931, Nature, 127, 706
Li C., Gadotti D. A., Mao S., Kauffmann G., 2009, MNRAS, 397, 726
Li Z., Shen J., Kim W.-T., 2015, ApJ, 806, 150
Lin Y., Cervantes Sodi B., Li C., Wang L., Wang E., 2014, ApJ, 796, 98
Lin L., Li C., He Y., Xiao T., Wang E., 2017, ApJ, 838, 105
Linde A. D., 1982, Physics Letters B, 108, 389
Linde A. D., 1986, Physics Letters B, 175, 395
Loh E. D., Biel J. D., Chen J.-J., Davis M., Laporte R., Loh O. Y., 2004, in Moorwood A. F. M., Iye M., eds, Proc. SPIEVol. 5492, Ground-based Instrumentation for Astronomy. pp 1644–1652, doi:10.1117/12.551808
Łokas E. L., 2018, ApJ, 857, 6
Łokas E. L., Athanassoula E., Debattista V. P., Valluri M., Pino A. d., Semczuk M., Gajda G., Kowalczyk K., 2014, MNRAS, 445, 1339
Łokas E. L., Ebrová I., del Pino A., Sybilska A., Athanassoula E., Semczuk M., Gajda G., Fouquet S., 2016, ApJ, 826, 227
Luo Y., et al., 2019, arXiv e-prints
Lynden-Bell D., 1979, MNRAS, 187, 101
Lynden-Bell D., Kalnajs A. J., 1972, MNRAS, 157, 1
Madau P., Dickinson M., 2014, ARA&A, 52, 415
Marino R. A., et al., 2016, A&A, 585, A47
Marinova I., et al., 2009, ApJ, 698, 1639
Marinova I., et al., 2012, ApJ, 746, 136
Martig M., et al., 2013, MNRAS, 432, 1914
Martinet L., Friedli D., 1997, A&A, 323, 363
Martinez-Valpuesta I., Shlosman I., 2004, ApJ, 613, L29
Martinez-Valpuesta I., Shlosman I., Heller C., 2006, ApJ, 637, 214
Masters K. L., et al., 2011, MNRAS, 411, 2026
McDermid R. M., et al., 2015, MNRAS, 448, 3484
Melvin T., et al., 2014, MNRAS, 438, 2882
Méndez-Abreu J., Aguerri J. A. L., Corsini E. M., Simonneau E., 2008a, A&A, 478, 353
Méndez-Abreu J., Corsini E. M., Debattista V. P., De Rijcke S., Aguerri J. A. L., Pizzella A., 2008b, ApJ, 679, L73
Méndez-Abreu J., Simonneau E., Aguerri J. A. L., Corsini E. M., 2010a, A&A, 521, A71
Méndez-Abreu J., Sánchez-Janssen R., Aguerri J. A. L., 2010b, ApJ, 711, L61
Méndez-Abreu J., Debattista V. P., Corsini E. M., Aguerri J. A. L., 2014, A&A, 572, A25
Méndez-Abreu J., et al., 2017, A&A, 598, A32
Méndez-Abreu J., et al., 2019, MNRAS, 482, L118
Menéndez-Delmestre K., Sheth K., Schinnerer E., Jarrett T. H., Scoville N. Z., 2007, ApJ, 657, 790
Merritt D., Sellwood J. A., 1994, ApJ, 425, 551
Milgrom M., 1983, ApJ, 270, 365
Minchev I., Famaey B., 2010, ApJ, 722, 112
Miwa T., Noguchi M., 1998, ApJ, 499, 149
Mo H. J., Mao S., White S. D. M., 1998, MNRAS, 295, 319
Moffett A. J., et al., 2016, MNRAS, 462, 4336
Moore B., Katz N., Lake G., Dressler A., Oemler A., 1996, Nature, 379, 613
Moorwood A., Cuby J.-G., Lidman C., 1998, The Messenger, 91, 9
Mulchaey J. S., Regan M. W., 1997, ApJ, 482, L135
Naab T., Burkert A., 2003, ApJ, 597, 893
Navarro J. F., Steinmetz M., 1997, ApJ, 478, 13
Navarro J. F., Steinmetz M., 2000, ApJ, 538, 477
Ness M., et al., 2013a, MNRAS, 430, 836
Ness M., et al., 2013b, MNRAS, 432, 2092

Neumann J., et al., 2017, A&A, 604, A30
Neumann J., et al., 2019, A&A, 627, A26
Newnham L., Hess K., Masters K., Kruk S., Penny S., Lingard T., Smethurst R., 2019, arXiv e-prints
Noguchi M., 1987, MNRAS, 228, 635
Noguchi M., 1996, ApJ, 469, 605
Noguchi M., 1998, Nature, 392, 253
Noguchi M., 1999, ApJ, 514, 77
Ocvirk P., Pichon C., Lançon A., Thiébaut E., 2006a, MNRAS, 365, 46
Ocvirk P., Pichon C., Lançon A., Thiébaut E., 2006b, MNRAS, 365, 74
Oesch P. A., et al., 2016, ApJ, 819, 129
Oh S., Oh K., Yi S. K., 2012, ApJS, 198, 4
Ohta K., 1996, in Buta R., Crocker D. A., Elmegreen B. G., eds, Astronomical Society of the Pacific Conference Series Vol. 91, IAU Colloq. 157: Barred Galaxies. p. 37, http://adsabs.harvard.edu/abs/1996ASPC...91...370
Ostriker J. P., Peebles P. J. E., 1973, ApJ, 186, 467
Pasquini L., et al., 2000, in Iye M., Moorwood A. F., eds, Society of Photo-Optical Instrumentation Engineers (SPIE) Conference Series Vol. 4008, Optical and IR Telescope Instrumentation and Detectors. pp 129–140
Patra N. N., Jog C. J., 2019, MNRAS, 488, 4942
Patsis P. A., Athanassoula E., Grosbøl P., Skokos C., 2002, MNRAS, 335, 1049
Peebles P. J. E., 1968, ApJ, 153, 1
Peletier R. F., et al., 2007, MNRAS, 379, 445
Peng C. Y., Ho L. C., Impey C. D., Rix H.-W., 2002, AJ, 124, 266
Peng C. Y., Ho L. C., Impey C. D., Rix H.-W., 2010, AJ, 139, 2097
Peng Y.-j., Lilly S. J., Renzini A., Carollo M., 2012, ApJ, 757, 4
Penzias A. A., Wilson R. W., 1965, ApJ, 142, 419
Pérez I., Sánchez-Blázquez P., 2011, A&A, 529, A64
Pérez I., Sánchez-Blázquez P., Zurita A., 2007, A&A, 465, L9
Pérez I., Sánchez-Blázquez P., Zurita A., 2009, A&A, 495, 775
Perlmutter S., et al., 1999, ApJ, 517, 565
Peschken N., Łokas E. L., 2019, MNRAS, 483, 2721
Pfenniger D., 1984, A&A, 134, 373
Pfenniger D., Friedli D., 1991, A&A, 252, 75
Phillips A. C., 1993, PhD thesis, UNIVERSITY OF WASHINGTON.
Phillips A. C., 1996, in Buta R., Crocker D. A., Elmegreen B. G., eds, Astronomical Society of the Pacific Conference Series Vol. 91, IAU Colloq. 157: Barred Galaxies. p. 44, http://adsabs.harvard.edu/abs/1996ASPC...91...44P
Pietrinferni A., Cassisi S., Salaris M., Castelli F., 2004, ApJ, 612, 168
Pietrinferni A., Cassisi S., Salaris M., Castelli F., 2006, ApJ, 642, 797
Pietrinferni A., Cassisi S., Salaris M., Percival S., Ferguson J. W., 2009, ApJ, 697, 275
Pietrinferni A., Cassisi S., Salaris M., Hidalgo S., 2013, A&A, 558, A46
Piner B. G., Stone J. M., Teuben P. J., 1995, ApJ, 449, 508
Planck Collaboration et al., 2016, A&A, 594, A13
Pohlen M., Trujillo I., 2006, A&A, 454, 759
Polyachenko E. V., 2004, MNRAS, 348, 345
Polyachenko E. V., 2013, Astronomy Letters, 39, 72
Press W. H., Teukolsky S. A., Vetterling W. T., Flannery B. P., 1992, Numerical recipes in FORTRAN. The art of scientific computing
Raha N., Sellwood J. A., James R. A., Kahn F. D., 1991, Nature, 352, 411
Rautiainen P., Salo H., 2000, A&A, 362, 465
Rautiainen P., Salo H., Laurikainen E., 2008, MNRAS, 388, 1803
Regan M. W., Teuben P. J., 2004, ApJ, 600, 595
Renaud F., et al., 2015, MNRAS, 454, 3299
Reynaud D., Downes D., 1998, A&A, 337, 671
Rich R. M., Reitzel D. B., Howard C. D., Zhao H., 2007, ApJ, 658, L29
Riess A. G., et al., 1998, AJ, 116, 1009
Romero-Gómez M., Masdemont J. J., Athanassoula E., García-Gómez C., 2006, A&A, 453, 39
Romero-Gómez M., Athanassoula E., Masdemont J. J., García-Gómez C., 2007, A&A, 472, 63
Roth M. M., et al., 2005, PASP, 117, 620
Ryder S. D., Dopita M. A., 1993, ApJS, 88, 415
Saha K., Elmegreen B., 2018, ApJ, 858, 24
Salo H., et al., 2015, ApJS, 219, 4
Salpeter E. E., 1955, ApJ, 121, 161
Sánchez-Blázquez P., Ocvirk P., Gibson B. K., Pérez I., Peletier R. F., 2011, MNRAS, 415, 709
Sánchez-Blázquez P., et al., 2014, A&A, 570, A6
Sánchez S. F., et al., 2012, A&A, 538, A8
Sánchez S. F., et al., 2016, A&A, 594, A36
Sarzi M., et al., 2006, MNRAS, 366, 1151
Schwarz M. P., 1984, MNRAS, 209, 93
Scoville N., et al., 2007, ApJS, 172, 1
Seidel M. K., Falcón-Barroso J., Martínez-Valpuesta I., Díaz-García S., Laurikainen E., Salo H., Knapen J. H., 2015, MNRAS, 451, 936
Seidel M. K., Falcón-Barroso J., Martínez-Valpuesta I., Sánchez-Blázquez P., Pérez I., Peletier R., Vazdekis A., 2016, MNRAS, 460, 3784
Seifert W., et al., 2003, in Iye M., Moorwood A. F. M., eds, Proc. SPIEVol. 4841, Instrument Design and Performance for Optical/Infrared Ground-based Telescopes. pp 962–973, doi:10.1117/12.459494
Sellwood J. A., 1980, A&A, 89, 296
Sellwood J. A., 1981, A&A, 99, 362
Sellwood J. A., 1985, MNRAS, 217, 127
Sellwood J. A., 2013, Dynamics of Disks and Warps. p. 923, doi:10.1007/978-94-007-5612-0˙18
Sellwood J. A., 2014, Reviews of Modern Physics, 86, 1
Sellwood J. A., Binney J. J., 2002, MNRAS, 336, 785
Sellwood J. A., Evans N. W., 2001, ApJ, 546, 176
Sellwood J. A., Wilkinson A., 1993, Reports on Progress in Physics, 56, 173
Seo W.-Y., Kim W.-T., Kwak S., Hsieh P.-Y., Han C., Hopkins P. F., 2019, ApJ, 872, 5
Sérsic J. L., 1963, Boletin de la Asociacion Argentina de Astronomia La Plata Argentina, 6, 41
Sersic J. L., 1968, Atlas de Galaxias Australes
Sharples R., et al., 2013, The Messenger, 151, 21
Shen J., Debattista V. P., 2009, ApJ, 690, 758
Shen J., Sellwood J. A., 2004, ApJ, 604, 614
Shen J., Rich R. M., Kormendy J., Howard C. D., De Propris R., Kunder A., 2010, ApJ, 720, L72
Sheth K., Vogel S. N., Regan M. W., Teuben P. J., Harris A. I., Thornley M. D., 2002, AJ, 124, 2581
Sheth K., et al., 2008, ApJ, 675, 1141
Sheth K., et al., 2010, PASP, 122, 1397
Sheth K., Melbourne J., Elmegreen D. M., Elmegreen B. G., Athanassoula E., Abraham R. G., Weiner B. J., 2012, ApJ, 758, 136
Shlosman I., Frank J., Begelman M. C., 1989, Nature, 338, 45
Shlosman I., Begelman M. C., Frank J., 1990, Nature, 345, 679
Simard L., et al., 2002, ApJS, 142, 1
Simmons B. D., et al., 2014, MNRAS, 445, 3466
Singh R., et al., 2013, A&A, 558, A43
Skibba R. A., et al., 2012, MNRAS, 423, 1485
Skokos C., Patsis P. A., Athanassoula E., 2002a, MNRAS, 333, 847
Skokos C., Patsis P. A., Athanassoula E., 2002b, MNRAS, 333, 861
Smoot G. F., et al., 1992, ApJ, 396, L1
Sormani M. C., Binney J., Magorrian J., 2015, MNRAS, 449, 2421
Sormani M. C., Treß R. G., Ridley M., Glover S. C. O., Klessen R. S., Binney J., Magorrian J., Smith R., 2018, MNRAS, 475, 2383
Spergel D. N., et al., 2007, ApJS, 170, 377
Spindler A., 2018, PhD thesis, The Open University
Spinoso D., Bonoli S., Dotti M., Mayer L., Madau P., Bellovary J., 2017, MNRAS, 465, 3729
Steinmetz M., Müller E., 1995, MNRAS, 276, 549
Steinmetz M., Navarro J. F., 1999, ApJ, 513, 555
Steinmetz M., Navarro J. F., 2002, New Astronomy, 7, 155
Stott J. P., et al., 2016, MNRAS, 457, 1888
Taylor E. N., et al., 2011, MNRAS, 418, 1587
Thomas D., Greggio L., Bender R., 1999, MNRAS, 302, 537
Tiret O., Combes F., 2008, in Funes J. G., Corsini E. M., eds, Astronomical Society of the Pacific Conference Series Vol. 396, Formation and Evolution of Galaxy Disks. p. 259
Toomre A., 1964, ApJ, 139, 1217
Toomre A., 1966, in Geophysical Fluid Dynamics, Notes on the 1966 Summer Study Program at the Woods Hole Oceanographic Institution, ref. no. 66-46. p. 111
Toomre A., 1977, in Tinsley B. M., Larson D. Campbell R. B. G., eds,

Evolution of Galaxies and Stellar Populations. p. 401
Toomre A., 1981, in Fall S. M., Lynden-Bell D., eds, Structure and Evolution of Normal Galaxies. pp 111–136
Toomre A., Toomre J., 1972, ApJ, 178, 623
Tremaine S., 1989, in Sellwood J. A., ed., Dynamics of Astrophysical Discs. pp 231–238
Tremaine S., Weinberg M. D., 1984, ApJ, 282, L5
Trujillo I., Graham A. W., Caon N., 2001, MNRAS, 326, 869
Valdes F., Gupta R., Rose J. A., Singh H. P., Bell D. J., 2004, ApJS, 152, 251
Vazdekis A., Sánchez-Blázquez P., Falcón-Barroso J., Cenarro A. J., Beasley M. A., Cardiel N., Gorgas J., Peletier R. F., 2010, MNRAS, 404, 1639
Vazdekis A., et al., 2015, MNRAS, 449, 1177
Veilleux S., Osterbrock D. E., 1987, ApJS, 63, 295
Verley S., Combes F., Verdes-Montenegro L., Bergond G., Leon S., 2007, A&A, 474, 43
Wagoner R. V., Fowler W. A., Hoyle F., 1967, ApJ, 148, 3
Walcher C. J., et al., 2014, A&A, 569, A1
Walcher C. J., Coelho P. R. T., Gallazzi A., Bruzual G., Charlot S., Chiappini C., 2015, A&A, 582, A46
Wandel A., Peterson B. M., Malkan M. A., 1999, ApJ, 526, 579
Weaver J., et al., 2018, A&A, 614, A32
Weilbacher P. M., Streicher O., Urrutia T., Jarno A., Pécontal-Rousset A., Bacon R., Böhm P., 2012, in Software and Cyberinfrastructure for Astronomy II. p. 84510B, doi:10.1117/12.925114
Weinzirl T., Jogee S., Khochfar S., Burkert A., Kormendy J., 2009, ApJ, 696, 411
White S. D. M., Rees M. J., 1978, MNRAS, 183, 341
Whitmore B. C., Schechter P. L., Kirshner R. P., 1979, ApJ, 234, 68
Willett K. W., et al., 2013, MNRAS, 435, 2835
Wisnioski E., et al., 2015, ApJ, 799, 209
Wisotzki L., Christlieb N., Bade N., Beckmann V., Köhler T., Vanelle C., Reimers D., 2000, A&A, 358, 77
Wozniak H., 2015, A&A, 575, A7
Wozniak H., Pierce M. J., 1991, A&AS, 88, 325
York D. G., et al., 2000, AJ, 120, 1579
Zeldovich Y. B., Kurt V. G., Syunyaev R. A., 1968, Zhurnal Eksperimentalnoi i Teoreticheskoi Fiziki, 55, 278
Zwicky F., 1933, Helvetica Physica Acta, 6, 110
de Lorenzo-Cáceres A., Vazdekis A., Aguerri J. A. L., Corsini E. M., Debattista V. P., 2012, MNRAS, 420, 1092
de Lorenzo-Cáceres A., Falcón-Barroso J., Vazdekis A., 2013, MNRAS, 431, 2397
de Lorenzo-Cáceres A., et al., 2019, MNRAS, 484, 5296
de Souza R. E., Dos Anjos S., 1987, A&AS, 70, 465
de Souza R. E., Gadotti D. A., dos Anjos S., 2004, ApJS, 153, 411
de Vaucouleurs G., 1948, Annales d'Astrophysique, 11, 247
de Vaucouleurs G., 1959, Handbuch der Physik, 53, 311
de Vaucouleurs G., 1974, in Shakeshaft J. R., ed., IAU Symposium Vol. 58, The Formation and Dynamics of Galaxies. p. 335
de Vaucouleurs G., 1977, in Tinsley B. M., Larson D. Campbell R. B. G., eds, Evolution of Galaxies and Stellar Populations. p. 43
de Zeeuw P. T., et al., 2002, MNRAS, 329, 513
van de Sande J., et al., 2017, ApJ, 835, 104

Publications

First-author publications

1. **J. Neumann**, L. Wisotzki, O. S. Choudhury, et al., "A combined photometric and kinematic recipe for evaluating the nature of bulges using the CALIFA sample", A&A, 604, A30, July 2017

2. **J. Neumann**, D. A. Gadotti, L. Wisotzki, et al., "The Close AGN Reference Survey (CARS). Comparative analysis of the structural properties of star-forming and non-star-forming galaxy bars", A&A, 627, A26, July 2019

Co-author publications

3. R. Leaman, ..., **J. Neumann**, et al., "Survival of molecular gas in a stellar feedback-driven outflow witnessed with the MUSE TIMER project and ALMA", MNRAS, 488, 3904–3928, September 2019

4. A. Bittner, ..., **J. Neumann**, et al. "The GIST pipeline: A multi-purpose tool for the analysis and visualisation of (integral-field) spectroscopic data", A&A, 628, A117, August 2019

5. D. A. Gadotti, ..., **J. Neumann**, et al., "Time Inference with MUSE in Extragalactic Rings (TIMER): properties of the survey and high-level data products", MNRAS, 482, 506–529, January 2019

Submitted articles and articles in preparation

6. **J. Neumann**, F. Fragkoudi, I. Pérez, D.A. Gadotti, et al., "Stellar populations across galaxy bars in the TIMER project", to be submitted to MNRAS within the next few months

Non-refereed publications

7. D. Gadotti, ..., **J. Neumann**, et al. "Investigating the Formation and Evolution of Massive Disc Galaxies with the MUSE TIMER Project", The Messenger, vol. 173, p. 28-32., September 2018

8. B. Husemann, ..., **J. Neumann**, et al., "The Close AGN Reference Survey (CARS)", The Messenger, vol. 169, p. 42-47., September 2017

9. A. Kelz, T. Jahn, **J. Neumann**, et al., "Development of deployable fibre integral-field-units for the E-ELT", Proceedings of SPIE, vol. 9151, 915151, July 2014

10. A. Kelz, ..., **J. Neumann**, et al., "VIRUS: assembly, testing and performance of 33,000 fibres for HETDEX", Proceedings of SPIE, vol. 9147, 914775, July 2014

Acknowledgements

I am deeply grateful for the huge support of Dimitri Gadotti who agreed to supervise me during my two-years studentship at ESO in Santiago de Chile and ended up being my biggest support during the whole four years of my PhD. Dimitri, you not only taught me endless aspects of galaxies, bars and bulges, but you were always there to keep motivating me in the moments of stress, doubts and exhaustion. You noticed when this was necessary and you always found the right words to keep pushing me forward and to remember me of my enthusiasm for astrophysics. The circumstances for the supervision were not always easy, given the physical distance, but your permanent availability through other channels made this almost irrelevant. Finally, with your personality, you made me always feel comfortable to talk to you as your student but also as your friend.

Furthermore, I would like to thank my supervisor Lutz Wisotzki for the support during my PhD, but especially, I am grateful for the time and circumstances that made these doctoral studies possible in the first place. You taught me about extragalactic astrophysics and pushed me to a successful completion of my undergraduate studies. You created a friendly and relaxed environment in the galaxy group of the AIP that always supported me on my way. Finally, thanks to your initiative and support, I was able to get in contact with Dimitri and to start the ESO studentship, which smoothed the way to get to the point were I am now.

The writing of this thesis and, to be honest, in general, to pursue my dream of being an astronomer would be impossible without the infinite love and selfless support of my incredible wife, Karina. You stand always by my side, you love me, you help me and you motivate me. During the time as PhD student you never stopped listening to me babbling about bulges and bars and you could easily give a presentation of my work all by yourself. Part of this thesis would definitely deserve your credit, because you always helped me to find the best titles, the best phrases or to reorganise my mess. Gracias por todo tu apoyo en toda mi vida y aquí especialmente durante los largos días y las largas noches para terminar esta tesis. Te amo!

Moreover, I am deeply thankful for the hospitality and kind support from Isabel Pérez and Jesus Falcón-Barroso who made the stay in Granada and Tenerife earlier this year a very nice and fruitful experience. Muchísimas gracias! I also thank all members of the CALIFA, CARS and TIMER surveys who have been somehow involved in my work during my PhD on one level or another. Especially, I would like to thank Bernd Husemann, Francesca Fragkoudi, Patricia Sánchez-Blázquez and Jairo Méndez-Abreu for the nice and interesting scientific discussions along the way.

Finally, a big thanks to the whole AIP galaxy group, including Josie, Khadiga, Sanja, Anika, Sabine, Rikke, Yohana, Daniel, Omar, Simona, Christian, Kasper, Tanya, Mirko, Peter, Mark, Jakob, Davor, Joseph and my student colleagues and office mates from ESO: James, Alessandro, Callum, Javier, Daniela, Alejandra and Blake.

Erklärung

Gemäß §12 der Promotionsordnung der Mathematisch-Naturwissenschaftlichen Fakultät der Universität Potsdam vom 18. September 2013 erkläre ich, dass diese Arbeit an keiner anderen Hochschule eingereicht sowie selbstständig von mir und nur mit den angegebenen Mitteln angefertigt wurde.

Potsdam, den 18. September 2019